# Performance and degradation of solid oxide cells for steam electrolysis

by

**James Peter William Watton**

A thesis submitted to
The University of Birmingham
for the degree of

**DOCTOR OF PHILOSOPHY**

The Centre for Hydrogen and Fuel Cell Research
Chemical Engineering
University of Birmingham
January 2016

# Abstract

In this thesis testing of solid oxide cells in fuel cell and electrolysis operation have been performed. Attempts to fabricate fuel cells are described, equipment for testing solid oxide electrolysis cells has been constructed and the development process for this described.

Cells of a number of different types have been tested in which initial work was performed using microtubular cells. Work on the fabrication of planar solid oxide cells is described, anode supports were prepared by pellet pressing however the application of a suitably dense electrolyte was unsuccessful which resulted in a poor cell OCV.

The initial degradation of commercial solid oxide cells has been investigated. During cyclic testing at low current density the cells were found to degrade at twice the rate in electrolysis operation compared to fuel cell operation. This leads to the conclusion that the degradation observed in electrolysis is reversible and that there is a disconnect between the electrolysis and fuel cell degradation processes.

During testing at different current densities the cells were found to undergo severe degradation when operated with very low water content supplied to the cells. The degradation was 512 mV $kh^{-1}$ at 2.5 vol% $H_2O$ and reduced to 45mV $kh^{-1}$ at 50 vol% $H_2O$. Over the timescales investigated in this work and due to the reversible nature of the electrolysis degradation identifying a degradation mechanism was very difficult.

# Acknowledgements

There are many people who I would like to thank for their support and guidance through my PhD, too many to thank individually so I would like to thank them all here − Thanks.

I would especially like to thank Robert for his guidance and for picking up the pieces of my project when he joined the university. I would also like to thank Aman for his guidance through the DTC.

I would like to thank my family for their support and patience through the many years of my PhD.

Apparently Lauren thinks she deserves a special mention in this part and she does, I appreciate all the support you've given me during while I've been writing the thesis.

# Contents

# Abbreviations

**SOE** – Solid oxide electrolysis /electrolyser
**SOFC** – Solid oxide fuel cell
**FC** – Fuel cell
**EL** – Electrolysis
**GWP** – Global Warming Potential
**PV** – Photovoltaic
**PEM** – Polymer electrolyte membrane
**RSOFC** – Reversible Fuel cell
**$\Delta H$** – Change in enthalpy
**$\Delta G$** – Change in Gibbs energy
**$\eta$** – Efficiency
**E** – Potential
**$E^{o}$** – Standard potential
**R** – Gas Constant
**T** – Temperature
**n** – Moles
**F** – Faradays constant
**$PH_2$** – $H_2$ partial pressure
**$PH_2O$** – $H_2O$ partial pressure
**$PO_2$** – $O_2$ partial pressure
**HHV** – Higher heating value
**LHV** – Lower heating value
**kh** – thousand hours
**OCV** – Open Circuit Voltage
**LSM** – Lanthanum strontium manganite
**YSZ** – Yittria stabilised zirconia
**TPB** – Triple phase Boundary
**EIS** – Electrochemical impedance spectroscopy
**AH** – Absolute humidity
**RC** – Resistor−Capacitor
**CPE** – Constant Phase Element
**CEM** – Controlled Evaporator Mixer
**TGA** – Thermogravimetric analysis

# Figures:

# 1 Introduction

The current worldwide crisis regarding the use of fossil fuels has been well documented and there is worldwide agreement that emissions from fossil fuels need to be replaced. Whether an argument is based on $CO_2$ emissions, emissions of other pollutants or sustainability of supply, there is a consensus that a new energy vector is required. If the world is to reach a point where there is no longer reliance on fossil fuels and emissions of $CO_2$ among other pollutants are reduced; the current energy landscape will have to undergo a major revolution. While a wide range of renewable technologies will be required to fulfil the current and expanding world energy market [1], wind and solar power are likely to be major sources of energy. As both are intermittent energy producers there will become a much greater reliance on energy storage, especially the storage of electrical energy. Batteries are the most efficient electricity storage devices, however they are limited by their performance and cost in large scale stationary applications [2]. Hydrogen is another energy storage vector which has been proposed; hydrogen is a storable, transportable, highly versatile, efficient and clean energy carrier [3].

There is a massive worldwide demand for hydrogen which will expand enormously if fuel cells become commonplace. It has been predicted that demand for hydrogen from non−traditional demands will grow from 168 million kg in 2013 to 3.5 billion kg in 2030 [4]. Current worldwide consumption of hydrogen is currently around 50 million metric tonnes per year [5]. Research into the global hydrogen market has found that the production of hydrogen as a chemical constituent and energy source was valued at $120 billion in 2010, and is

expected to reach $163 billion in 2015 [6], although more recent reports suggest the market value was $96.6 billion in 2013 and is predicted to be $141.1 billion by 2020 [7].

The majority of the hydrogen currently produced is from steam reforming of methane which is reliant on fossil fuels. Clean hydrogen production is desirable if the potential of fuel cells to de−carbonise the transport industry is to be realised. Hydrogen production from water is potentially a very clean source of hydrogen. The main way in which hydrogen is produced from water is via electrolysis. Electrolysis requires a supply of water and electricity. The purity of hydrogen produced from electrolysis is highly dependent on the source of the electricity which is used to produce the hydrogen. While in the near term hydrogen produced from electrolysis will use electricity produced from fossil fuels, a major benefit of a hydrogen economy is in the separation of fossil fuels and transport or energy storage. Once energy storage and transport is done using hydrogen the increase in renewable energy production will result in an immediate reduction in the use of fossil fuels for transport. There are also significant advantages in the centralised production of $CO_2$ and other pollutants associated with the burning of fossil fuels. In this thesis the production of hydrogen by solid oxide electrolysis will be investigated. Solid oxide electrolysis is one type of electrolysis for the production of hydrogen. It has potential advantages due to the thermodynamics of its operation.

While the use of hydrogen in the de−carbonisation of transport is vital, it may play an even greater role in the balancing of power grids and the de−carbonisation of gas. The next section will briefly introduce the UK's energy market and its future trends, and the use of power to gas to de−carbonise domestic heating. Hydrogen production will then be introduced.

## 1.1 UK energy use

The UK is committed by law to reducing its greenhouse gas emissions by 80% compared to 1990 levels by 2050 [8]. This is a highly ambitious target and will require massive changes to the way in which the country's energy sector operates, produces and stores energy. This will require an increasing rate of decarbonisation of the energy sector. There have been a number of projections made on possible pathways in which a reduction of emissions of the order required can be made and all possible pathways would indicate that there will be an increasing use of either renewable electricity or nuclear power [9]. Increasing the use of either renewable energy or nuclear power will lead to an increase in the need for energy storage, this is due to both the intermittency of demand and the intermittency of supply [2,10–13].

Intermittency with renewable energy is unavoidable. We have no control over when the wind blows or sun shines, therefore strategies are needed to ensure that we have a stable overall power supply. The use of a wide range of renewable energies with lots of small generators over large areas can solve some of the issues with intermittency however there will still be periods of excess or shortfall in energy supply. With nuclear power a similar problem exists, nuclear power plants are very effective at producing a steady amount of electricity however they can't match the fluctuating demand of the UK electricity grid. Figure 1 shows the UK gas and electricity use over a 3-year period which shows a daily and seasonal variation in the electrical requirements. The UK has a number of strategies to combat these problems [8,9], with an increasing nuclear base load the current strategies wouldn't be enough to maintain a stable power supply.

The variation in the UK's electricity demand through the year isn't the main observation made from Figure 1. The main conclusion is that the UK's electricity use is far outweighed by

the UK's gas use. This is especially true during the winter. The variation in demand of gas is also very large; The UK's electricity has very little seasonal variation when compared to the seasonal variation in gas use. The majority of the winter gas use is for heating the home. This presents large problems for the decarbonisation of the UK's energy supply. De−carbonisation of electricity is a far easier challenge than the decarbonisation of heating.

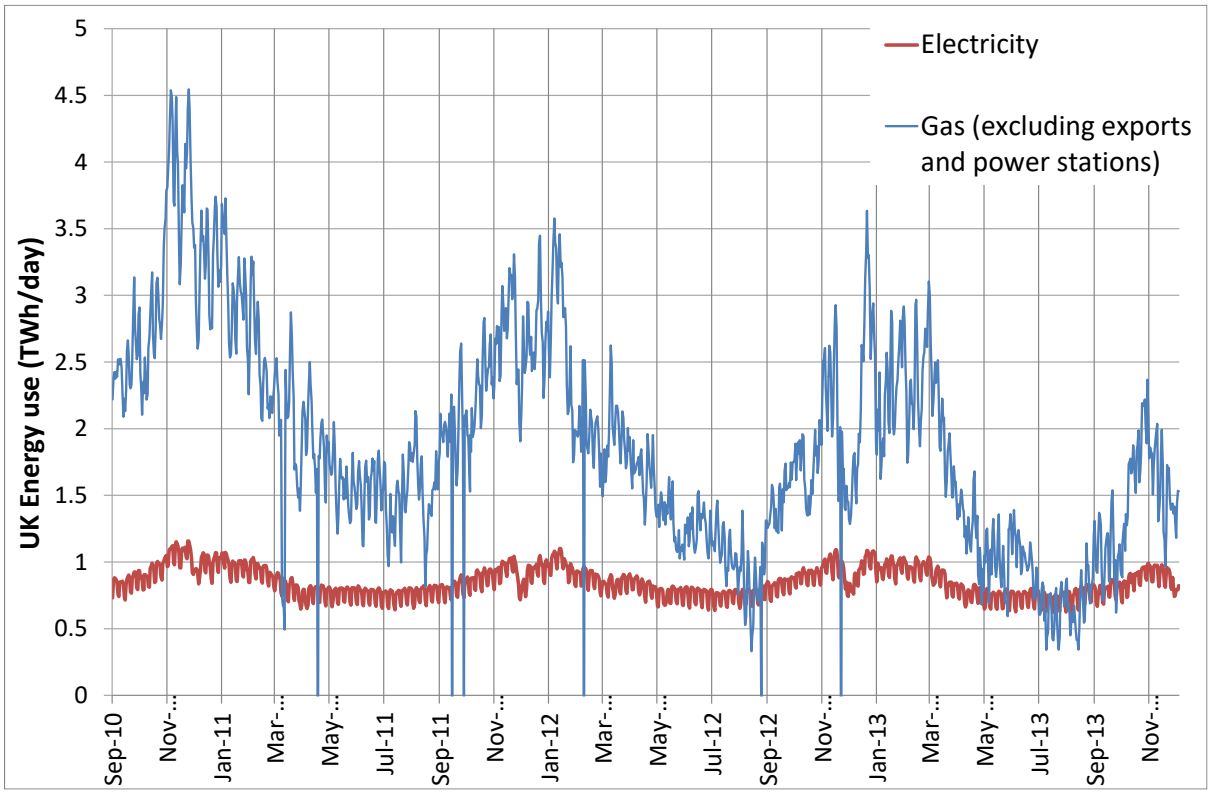


**Figure 1: UK's gas and electricity use in TWh/day. The data for this figure was obtained from the National Grid website [14,15], reproduced from a figure in [16].**

### 1.1.1 Power to gas

Power to gas is a term used for a process which converts electrical power to a gas fuel[17–19], this is normally done in two steps using electrolysis of water with electrical energy, and then the reaction of hydrogen and CO or $CO_2$ to methane. The gas, either hydrogen or methane can then be pumped directly into the gas grid. If this can be performed with surplus renewable electrical energy the gas supply can be decarbonised and energy storage combined with the goal of moving towards a smart grid[20]. The gas which is pumped into the grid can

either be Hydrogen or Methane. When hydrogen is injected into the natural gas grid there are limits on the quantity which can be injected safely. There are two main reasons for this [21]:

- Transport; injecting hydrogen into gas pipes designed for methane not hydrogen can lead to a number of problems, either gas leakage or hydrogen damaging pipelines
- End use; appliances designed to burn methane can handle small quantities of hydrogen without issue; however, could become damaged, inefficient or dangerous if large hydrogen quantities are used.

There are also national limits on the amount of hydrogen which can be injected into the gas grid, which are depending on the country between 0 – 11% [16]. There are a number of power to gas projects which are currently being performed [22,23]. These projects use PEM electrolysers to produce hydrogen. There is then a subsequent methanation step, such as the Sabatier reaction Equation 1, to produce methane for injection into the natural gas grid [18].

$$CO_2 + 4H_2 \rightarrow CH_4 + 2H_2O \qquad \textit{Equation 1}$$

$$\Delta H_{298} = -165 \text{ kJ mol}^{-1}$$

While there isn't any work performed in this thesis on co−electrolysis it is possible to use a solid oxide electrolyser to perform co−electrolysis of water and carbon dioxide to produce syn−gas (a CO and $H_2$ mixture) [24–26]. Co−electrolysis may be a deceptive term as the process may actually be a two stage reaction involving the electrolysis of water and subsequent reaction of water and $CO_2$ to produce hydrogen and CO. If integrated into a power to gas system this has the potential to reduce the amount and complexity of equipment required for a power to gas plant. While this work does not cover any co−electrolysis a solid oxide electrolyser performing only water electrolysis may be suitable for integration with a power−to−gas system as a solid oxide electrolyser with the heat produced by the Sabatier

reaction, Equation 1, which takes place at 300 − 400ºC to vaporise water and heat inlet gasses, as discussed later integration of a solid oxide electrolyser with a heat source lowers the electrical energy required for hydrogen production.

## 1.2 $H_2$ production

In this section a brief introduction to the main types of hydrogen production will be presented. The focus of this work is on solid oxide electrolysis therefore a more detailed description will follow the other hydrogen production techniques. Hydrogen production techniques have been broadly separated into three main categories, production from fossil fuels, production from biomass and production from water.

### 1.2.1 Hydrogen production from fossil fuels

Currently the vast majority of the world's hydrogen is produced by methane steam reforming; 80% of the hydrogen produced in the U.S. is produced by this method [27]. Further details on hydrogen production methods will be discussed in the next chapter. Steam reforming requires fossil fuels and produces large quantities of greenhouse gasses.

Methane steam reforming (Equation 2) produces hydrogen and carbon monoxide in a gas mixture known as syngas. The water−gas shift reaction (Equation 3) boosts the hydrogen yield by adding hydrogen from water;

**Steam Reforming:**

$$CH_4 + H_2O \leftrightarrow 3H_2 + CO \qquad \textit{Equation 2}$$

$$\Delta H_{298} = +206 \text{ kJ mol}^{-1}$$

**Water−Gas shift reaction:**

$$CO + H_2O \leftrightarrow H_2 + CO_2 \qquad \textit{Equation 3}$$

$$\Delta H_{298} = -40.4 \text{ kJ mol}^{-1}$$

Steam reforming can also be performed using other fossil fuels, although efficiency of hydrogen production per mole of $CO_2$ produced is reduced. For a generic hydrocarbon the steam reforming reaction can be written as in Equation 4:

$$C_m H_n + mH_2O \leftrightarrow (m + \frac{1}{2}n)H_2 + mCO \qquad \textit{Equation 4}$$

$$\Delta H = \text{ dependant on hydrocarbon}$$

Hydrogen can also be produced from methane by dry reforming and partial oxidation Equation 5 and Equation 6.

**Dry Reforming:**

$$CH_4 + CO_2 \leftrightarrow 2H_2 + 2CO \qquad \textit{Equation 5}$$

$$\Delta H_{298} = +247 \text{ kJ mol}^{-1}$$

**Partial Oxidation:**

$$CH_4 + \frac{1}{2}O_2 \leftrightarrow 2H_2 + CO \qquad \textit{Equation 6}$$

$$\Delta H_{298} = -8.5 \text{ kJ mol}^{-1}$$

In this section the main routes of hydrogen production from fossil fuels have been outlined, however many more reaction mechanisms and pathways are possible, for more information refer to the review on hydrogen production technologies by Holladay et al [28].

The hydrogen produced by this processes is contaminated with a variety of different impurities which are incompatible with use in fuel cells, therefore significant steps are required to purify and desulphurise the hydrogen. There are also large quantities of $CO_2$ emitted. Steam reforming of methane produces approximately 9.7 kg($CO_2$) kg$^{-1}$($H_2$)[29] which is a major contributor to the greenhouse effect. If other emitted greenhouse gasses such

as $CH_4$, $NO_2$ , and $CO_2$ are taken into account the equivalent $CO_2$ emitted is 13.7 kg($CO_2$) $kg^{-1}$($H_2$) in global warming potential (GWP) over a 100 year timescale [30].

### 1.2.2 Hydrogen production from biomass:

Biomass may play a significant role in the transfer from fossil fuels to a hydrogen economy. There are a wide variety of sources for biomass from crops grown specifically for energy to wastes from agriculture, forestry, industrial and municipal sources [28,31–33]. The processes for utilising the biomass fall into two categories; thermochemical processes which are similar to those described for methane steam reforming but using higher hydrocarbons and will not be further discussed for more information refer to the review of hydrogen production from biomass by Ni et al [33]; and biological production where microorganisms play a role in the production of hydrogen.

There are two main routes for biological hydrogen the first is using photolysis, by an algae or bacteria. Bacteria and algae naturally photosynthesis to produce carbohydrates and oxygen from water and sunlight, some also produce hydrogen to varying degrees, the aim is to increase the production of hydrogen by the organisms. This is currently very inefficient <1% [28] therefore large areas are required. However, efficiency may increase to become more competitive with other solar harvesting techniques. The second route to produce hydrogen is via fermentation. This can either be dark or light assisted fermentation. Fermentation requires a source of carbohydrate which is easily digested, ideally in the form of simple sugars, which places limits on the possible biomass sources which can be utilised. These undergo fermentation reactions which produce hydrogen as a by−product. Again aims to selectively modify the organisms for hydrogen production are being researched. There are also other

products such as organic acids which are produced and would limit production if not removed from the system.

With the right waste streams thermochemical production of hydrogen from biomass may play a significant role in future hydrogen production. Hydrogen produced from biomass via biological routes could also play a significant role however increases in efficiency and technology maturity are required.

### 1.2.3 Hydrogen production from water:

There are a number of processes which produce hydrogen from water, depending on the source of energy for the splitting. These may be very clean without $CO_2$ production. There are three main water splitting processes; photoelectrolysis, thermolysis and electrolysis, however, electrolysis is the most commonly used.

#### 1.2.3.1 Photoelectrolysis:

In photoelectrolysis a cell similar to an electrolysis cell is used. A diagram showing photoelectrolysis is shown in Figure 2. Two electrodes are separated by an electrolyte. The anode is made up of a multilayer photovoltaic (PV) material, photons of the correct energy for the PV material produce a hole−electron pair. The hole causes the decomposition of water on the anode. Hydrogen ions pass through the electrolyte where they recombine with the electrons transported through an external circuit. This requires materials choices for the photoanode and photocathode to accept energy from within a wide a range of the spectrum as possible for maximum efficiency. They must then also have band edges which match with the breakdown potential of water to provide the correct energy for splitting. There are also significant issues with material stability and cost which means that photoelectrolysis is still at the investigatory stage, and commercialisation is only expected in the long term [28,34].

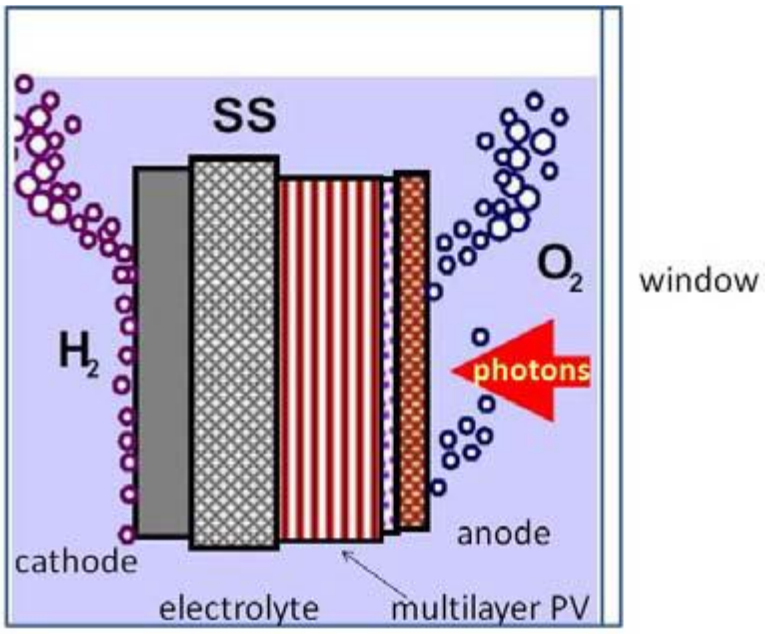


**Figure 2: Generic diagram of a photoelectrolysis where SS is a stainless steel electrolyte. Taken from [35].**

### 1.2.3.2 Thermochemical cycles:

There are a number of thermochemical cycles which can be used to produce hydrogen. These cycles are used to produce hydrogen using heat with a much reduced or completely eliminated electrolytic step. While water will be decomposed at 2500$^{o}$C the availability of stable materials and a suitable sustainable heat source is rare at these temperatures. Therefore, chemical cycles are used to reduce the temperature at which water splitting will occur, while temperature is lower and the pressure required is generally higher. There are more than 300 water splitting cycles referenced for more information on these please refer to the review by Holladay et at [36]. Thermochemical cycles are attractive as they reduce the steps and therefore increase the efficiency of heat to hydrogen conversion. Below two cycles are shown, the Copper−Chlorine cycle which operates at low temperature and the Westinghouse sulphur process.

#### 1.2.3.2.1 Copper−Chlorine (Cu−Cl) Cycle:

$$2Cu + 2HCl \rightarrow 2CuCl + H_2\ (450^oC)$$

$$4CuCl + 4Cl^- \rightarrow 4CuCl_2^-\ (30^oC)$$

$$4CuCl_2^- \rightarrow\ 2CuCl_2 + 2Cu + 4Cl^-(30^oC)$$

$$2CuCl_2(aq) \rightarrow 2CuCl_2(s)(100^oC)$$

$$2CuCl_2 + H_2O \rightarrow CuO + CuCl_2 + 2HCl\ (400^oC)$$

$$CuO + CuCl_2 \rightarrow 2CuCl + \frac{1}{2}O_2\ (500^oC)$$

This process is operated at lower temperature than other thermochemical cycles. Therefore, it is compatible with current low temperature nuclear reactors and has fewer problems with material and corrosion issues at 500$^o$C. The energy efficiency of this process is projected to be 40–45%. This process has only been studied at the bench top level so far.

#### 1.2.3.2.2 Westinghouse Sulphur Process:

This is a hybrid high temperature thermochemical and electrolytic process.

$$H_2SO_4 \rightarrow SO_2 + H_2O + \frac{1}{2}O_2(800^oC)$$

$$2H_2O + SO_2 \rightarrow H_2SO_4 + H_2(80^0C)$$

The high temperature step is separated from the electrolytic step. Therefore, the high temperature step can be located close to the nuclear power plant with the electrolytic hydrogen production step. The electrolytic step for the reaction of $H_2O$ and $SO_2$ only requires a potential of 0.17V, significantly lower than the 1.23V required to split water.

The thermochemical cycles require a significant amount of work before they are commercially viable as current processes have mainly been studied at bench top scale in the lab. They also use hazardous chemicals and significant work on the materials which can handle these materials at high temperatures is needed.

### 1.2.3.3 Electrolysis

Electrolysis is a process in which a DC electrical current is used to drive a reaction. There are many different types of electrolysis from the production of sodium hydroxide in the chloralkali process to the production of aluminium. This will focus on the electrolysis of water of which there are also many different techniques. There are three main types of water electrolysis; Polymer Electrolyte Membrane (PEM), Alkaline and Solid Oxide Electrolysis (SOE). Alkaline and PEM electrolysis are low temperature techniques with water in a liquid form up to temperatures around 90°C. Solid oxide electrolysis is a high temperature technique operating between 500 and 800°C. Electrolysis is the electrochemical breakdown of water into hydrogen and oxygen; this is shown in the overall reaction in Equation 7.

**Overall Reaction**

$$2H_2O_{(aq)} \rightarrow 2H_{2(g)} + O_{2(g)} \qquad \textit{Equation 7}$$

$$\Delta H_{298} = 285.83 \text{ kJ}$$

#### 1.2.3.3.1 Alkaline Electrolysis:

Alkaline electrolysis is performed at temperature around 80°C. In alkaline electrolysis the anode and cathode are submerged in an alkaline solution normally potassium hydroxide, KOH. The two cells are separate by a membrane. A voltage is applied across the anode and cathode. At the cathode water is reduced to form $OH^-$ and $H_2$, the $OH^-$ passes through

solution and membrane to the anode where it is oxidised to reform water with the release of oxygen. Equation 8 and Equation 9 show the half cells including base for the reaction.

**Cathode half-cell reaction**

$$2H_2O_{(aq)} + 2e^- \rightarrow 2OH^-_{(aq)} + 2H_{2(g)} \qquad \textit{Equation 8}$$

**Anode half-cell reaction**

$$4OH^-_{(aq)} \rightarrow O_{2(g)} + 2H_2O_{(aq)} + 4e^- \qquad \textit{Equation 9}$$

There are advantages and disadvantages to the use of alkaline electrolysis. Almost all of the hydrogen currently produced by electrolysis is produced by alkaline electrolysis, therefore the technology is well advanced and has been well optimised. For alkaline electrolysis the energy required for the reaction is obtained solely from electricity and the electrical demands are high. The use of a strong alkaline is undesirable while essential. It makes material choice more complicated and can be dangerous in an industrial environment.

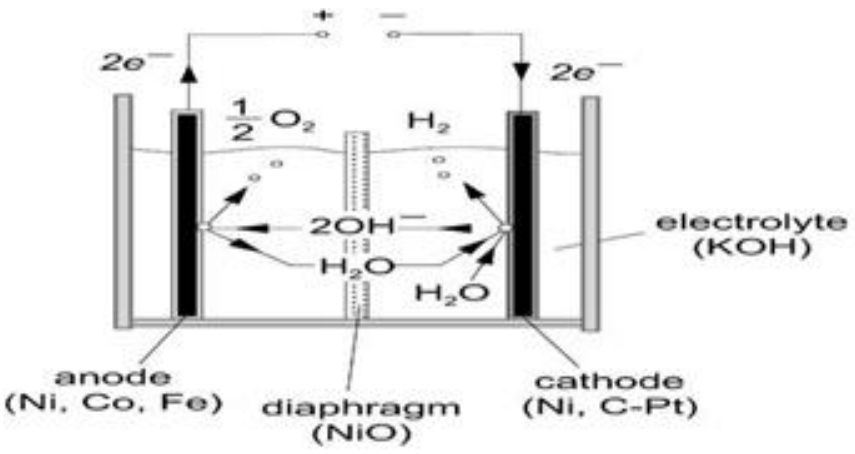


**Figure 3: Diagram of an alkaline electrolyser taken from Ulleberg [11]**

### 1.2.3.3.2 Polymer electrolyte membrane electrolysis:

A polymer electrolyte membrane (PEM) electrolyser, is another low temperature electrolyser. A PEM electrolyser is a PEM fuel cell which is used in reverse operation. In a PEM cell there are three main components; two electrodes the anode and cathode; and an electrolyte. As a

PEM cell operates at low temperature the anode and cathode must be very electrochemically active, therefore a highly active catalyst, platinum, is used. The catalyst is supported on a polymer membrane, commonly made of Nafion. The electrodes must be electronically conductive and be porous to gases. The electrolyte is positioned between the two electrodes. The electrolyte is made of a polymer membrane which is also commonly made of Nafion, the electrolyte membrane must be electronically isolating while allowing the conduction of protons, and the electrolyte must also be gas tight.

Water enters at the anode where it dissociates to form hydrogen ions and oxygen gas with the release of electrons. The hydrogen ions pass through the electrolyte to the cathode. An external voltage is applied across the anode and cathode which forces the electrons around the external circuit to reform with the hydrogen ions at the cathode to form hydrogen gas.

A PEM electrolyser is a more efficient electrochemical process than an alkaline electrolyser, however there are disadvantages. Current PEM electrolysers are low temperature devices, with operating limits of 90°C. Therefore, there is no contribution to the overall required energy from heat, and therefore there is a high electrical demand.

**Cathode half−cell reaction**

$$2H^{+}_{(aq)} + 2e^{-} \rightarrow H_{2(g)} \quad E^{o}_{red} = 0.00 \text{ V} \qquad \textit{Equation 10}$$

**Anode half−cell reaction**

$$2H_2O_{(l)} \rightarrow O_{2(g)} + 4H^{+}_{(aq)} + 4e^{-} \quad E^{o}_{ox} = -1.23 \text{ V} \qquad \textit{Equation 11}$$

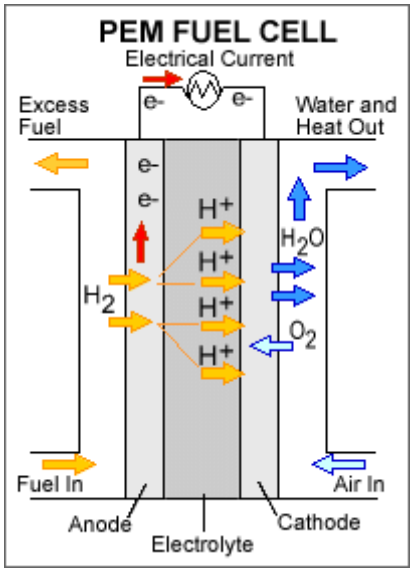


**Figure 4: Diagram of a PEM electrolyser [37]**

#### 1.2.3.3.3 Solid oxide electrolysis:

Here a very brief introduction to Solid oxide electrolysis (SOE) will be provided as it will be discussed in detail in Chapter 2. SOE functions in a very similar way to PEM electrolysis, apart from materials considerations. The main differences are:

- The temperature, SOE operates at high temperature 650$^{o}$C to 800$^{o}$C and has been operated at 1000$^{o}$C in some work. The temperature of operation allows higher efficiency and use of less expensive materials than in PEM, however the increased complexity of high temperature operation means there are no commercial SOE systems currently in use.
- The ion conduction through the electrolyte, while PEM electrolysis is limited to the conduction of protons through the electrolyte. High temperature materials for solid oxide electrolysis allow the conduction of either protons or oxide ions through the electrolyte.

# 2 Solid oxide electrolysis

A solid oxide electrolyser (SOE) is a device which converts water into hydrogen and oxygen via an electrochemical process. SOE is a high temperature process, operating between 500 and 800$^{o}$C. The water is present as steam therefore this is also known as steam electrolysis. The device is identical to a fuel cell but run in reverse and can be switched from one mode of operation to the other. Therefore, SOE cells are also known as reversible solid oxide fuel cells, RSOFC.

An SOE cell has three main components, the electrolyte and two electrodes; the anode and cathode, as shown in Figure 5. The electrolyte is an oxide material, giving rise to the device's name, which conducts oxygen ions but is electronically insulating and gas tight. The anode and cathode, also known as the oxygen electrode and hydrogen electrode, are electronically conductive and porous to gas. The designation of anode and cathode is dependent on whether electrons are entering or leaving the electrode. They are the opposite way around in a fuel cell i.e. a fuel cell anode is an electrolysis cathode as the electrons are moving in the opposite direction. A cathode can be defined as the electrode where electrons enter the cell and reduction occurs. An anode can be defined as the electrode where electrons leave the cell and oxidation occurs. To avoid confusion in the rest of this report the cathode will be referred to as the hydrogen electrode and the anode as the oxygen electrode.

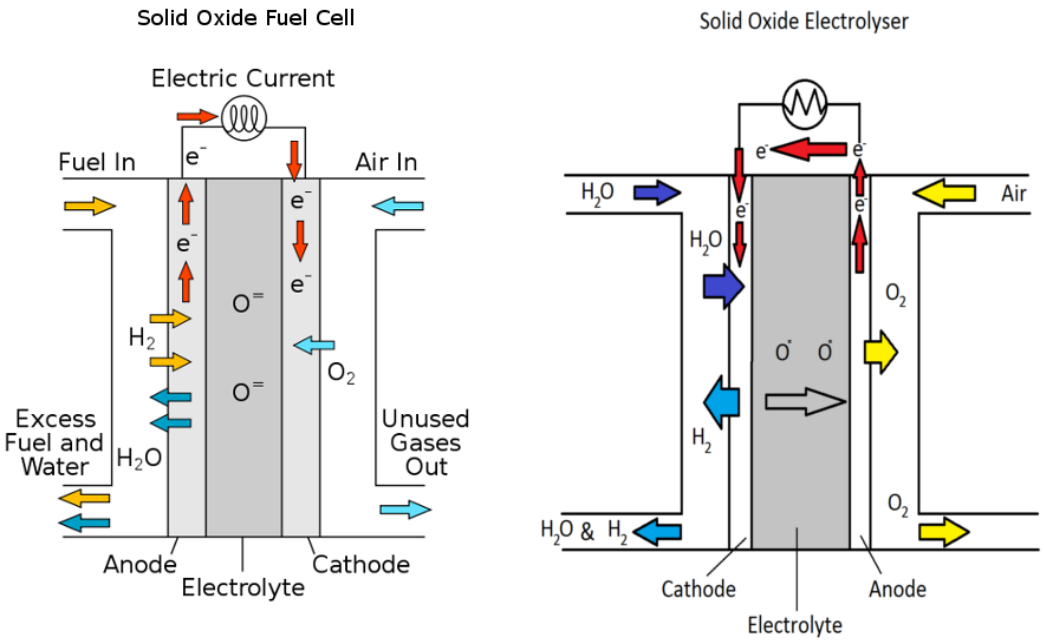


**Figure 5: Diagram of a solid oxide cell operating in electrolysis and fuel cell modes of operation [38].**

The "fuel" (water), enters the electrolyser on the hydrogen electrode, where it dissociates into hydrogen and oxygen ions. The oxygen ions travel through the electrolyte and upon reaching the oxygen electrode they form a molecule of oxygen with the release of two electrons, (Equation 12). The electrons travel around the external circuit to the hydrogen electrode where they reform with two hydrogen ions to form a molecule of hydrogen (Equation 13). In a solid oxide electrolyser the electrons are forced to the negative electrode, hydrogen electrode, by the application of an external voltage.

**Oxygen electrode half−cell reaction**

$$O^{2-} \rightarrow \frac{1}{2}O_2 + 2e^- \qquad \textit{Equation 12}$$

**Hydrogen electrode half−cell reaction**

$$H_2O \quad + 2e^- \rightarrow O^{2-} + H_2 \qquad \textit{Equation 13}$$

## 2.1 Thermodynamics:

There are thermodynamic advantages to running an electrolyser at high temperature, especially if there is a high temperature source of energy which can be utilised to displace some of the electrical requirement of the cell. The U.S. Department of Energy has reviewed hydrogen production using nuclear power and has identified SOE as the leading candidate for integration with a next generation nuclear plant in 2021 [39].

One of the major advantages of SOE over conventional water electrolysis, either PEM or alkaline based, is the change in the thermodynamics of the process at higher temperature. The enthalpy change, ΔH, required to split water is shown in Equation 14.

$$\Delta H = \Delta G + T\Delta S \qquad \textit{Equation 14}$$

**H =Enthalpy of formation; G= Gibbs free energy; T = Temperature; S= Entropy**

The total enthalpy change required for water splitting has a thermal and electrical component. The Gibbs free energy is the electrical energy required, and TΔS is the thermal energy required.

The Gibbs free energy is related to the electrical requirement of the system and cell potential as shown in Equation 15. A reduction in the Gibbs energy results in a reduction in the cell potential E.

$$\Delta G = -nFE \qquad \textit{Equation 15}$$

**Where n is the number of electrons involved, F is Faradays constant (98,485 C mol−1) and E is the equilibrium voltage.**

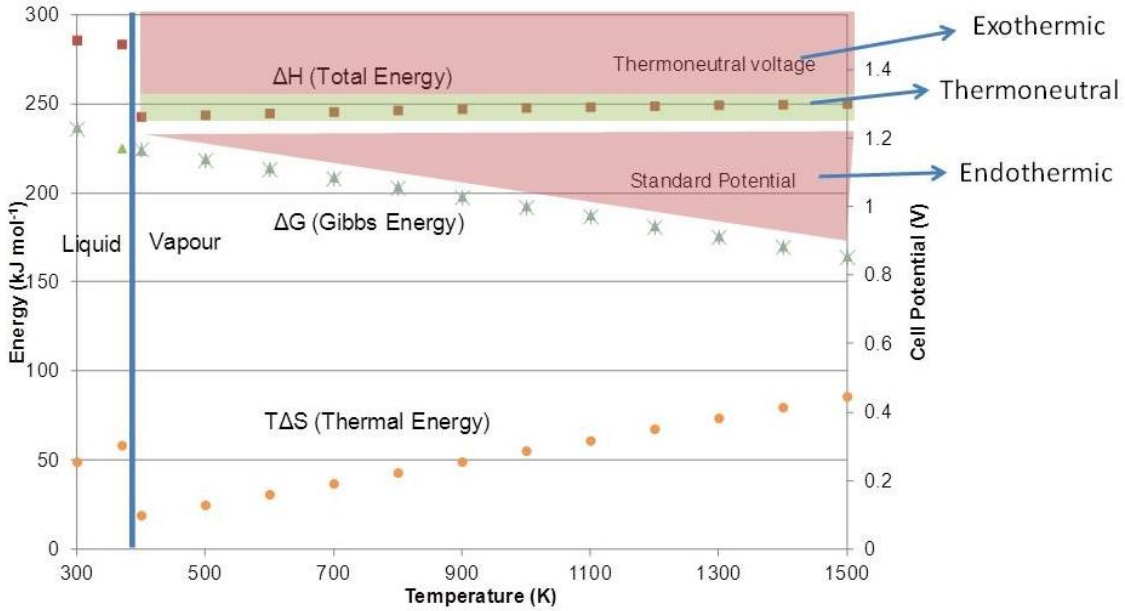


**Figure 6: Electrical (ΔG), thermal (temperature and entropy change, TΔS) and total energy change (ΔH) required for electrolysis of water, and the potential at which this occurs, as a function of the temperature of operation. Figure also shows regions of operation for a solid oxide electrolyser. Operation at voltages below $U_{th}$ is endothermic, operation at $U_{th}$ gives a thermoneutral operation and operation at voltage over $U_{th}$ results in exothermic operation. $U_{th}$ can be calculated from Equation 16 assuming no losses. Data obtained from[40], based on figure redrawn from [41].**

The thermodynamics of operation during electrolysis have a significant effect on the operation of cells, especially in a stack. The cell will behave exothermically, endothermically or thermoneutrally depending on the voltage of operation (Figure 6). At voltages between ΔH and ΔG the cell will operate endothermically and require heat to be supplied to the cell. If the voltage is greater than ΔH the cell will be operating exothermically. If the voltage is equal to ΔH the cell will operate isothermally/thermoneutrally. The voltage of thermoneutral operation ($U_{th}$) is temperature dependant and is 1.285V at 800°C which can be calculated using Equation 16. Using the value of ΔH to calculate voltage assumes that there is a sufficient heat source to evaporate the water required. Without the excess heat to evaporate water the thermoneutral voltage for the reaction is calculated from the hydrogen higher heating value (HHV) as 1.481V using Equation 17.

$$U_{th} = \frac{\Delta H}{nF}$$ ***Equation 16***

$$E = \frac{HHV\ (H_2)}{nF}$$ ***Equation 17***

Solid oxide cells operated in electrolysis mode can be operated over a large voltage range [42]. With a high $pH_2O$ the OCV can come down to approaching 0.7V at 800ºC as described in section 0. With an external heat source for water evaporation (low temperature) and cell heating (high temperature) the cell can be operated to the thermoneutral voltage 1.285V at 800ºC. If the cell is operated exothermically and the excess heat used to evaporate water the cell can be operated up to 1.48V. This gives a very large range over which the cell can operate. Therefore, it may be possible that cells operated in electrolysis mode can sustain a higher degradation rate than a fuel cell. Figure 7 shows potential degradation rates and cell lifetimes. It is possible to obtain a cell lifetime over 20,000h with cell degradations as high as 2% $kh^{-1}$ [42]. The Solid State Energy Conversion Alliance (SECA) has stated a target SOFC degradation rate of 0.2% $kh^{-1}$. Due to the greater range of operation available for an SOE the required degradation rate for an SOE could be much larger >1% to achieve a 40,000 hour lifetime.

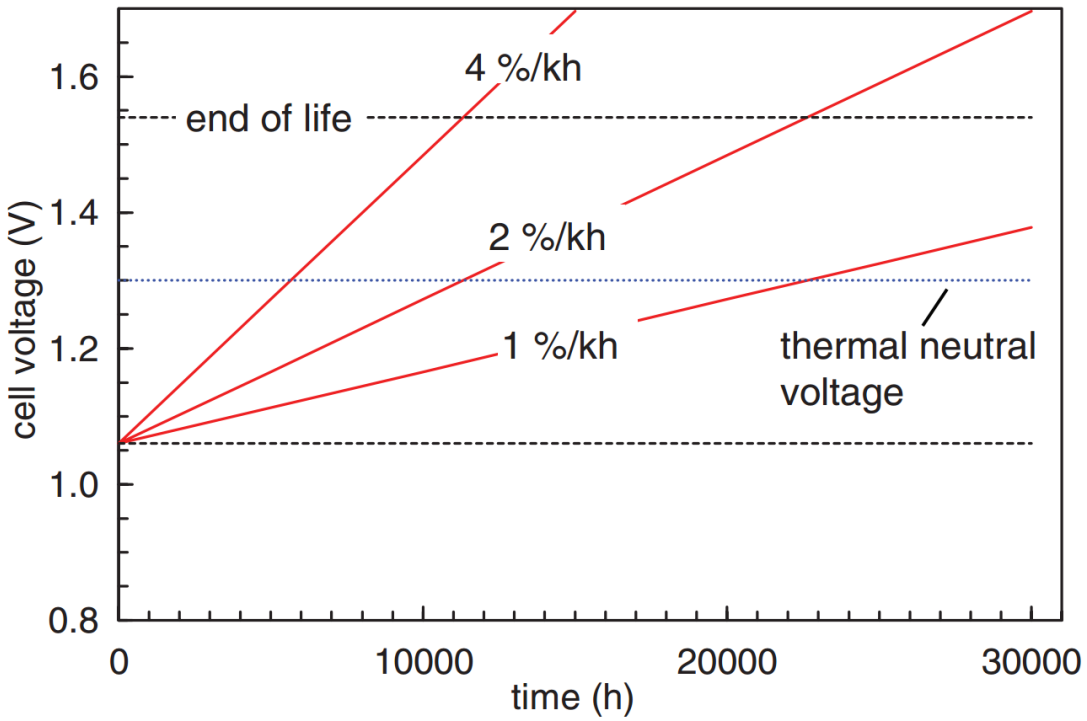


**Figure 7: Potential SOE degradation rates with a starting voltage of 1.06V and a lifetime end of 1.48V taken from [42] without permission.**

## 2.2 Nernst potential

The Nernst voltage or open circuit voltage can be calculated from Equation 18.

$$E = E^{\theta} + \frac{RT}{nF}\ln\left(\frac{p_{H_2} \cdot p_{O_2}^{\frac{1}{2}}}{p_{H_2O}}\right)$$ ***Equation 18***

**Where $E^{\theta}$:**

$$E^{\theta} = \frac{\Delta G}{nF}$$ ***Equation 19***

From this the theoretical Nernst potential can be calculated for 800°C as shown in Figure 8. There is a decisive variation in Nernst potential dependant on the inlet $H_2O$ ratio. This has a very large influence on the cell voltage and should be given careful consideration when comparison of performance at different $H_2O$ partial pressure in made. If a cell is operated with a 95% steam supply at thermoneutral voltage 1.3V the cell will be operating with a bias of

0.5V from the OCV of 0.8V. With a 20% steam supply the cell will be operating with a bias of 0.3V at thermoneutral voltage from the OCV of 1.0V.

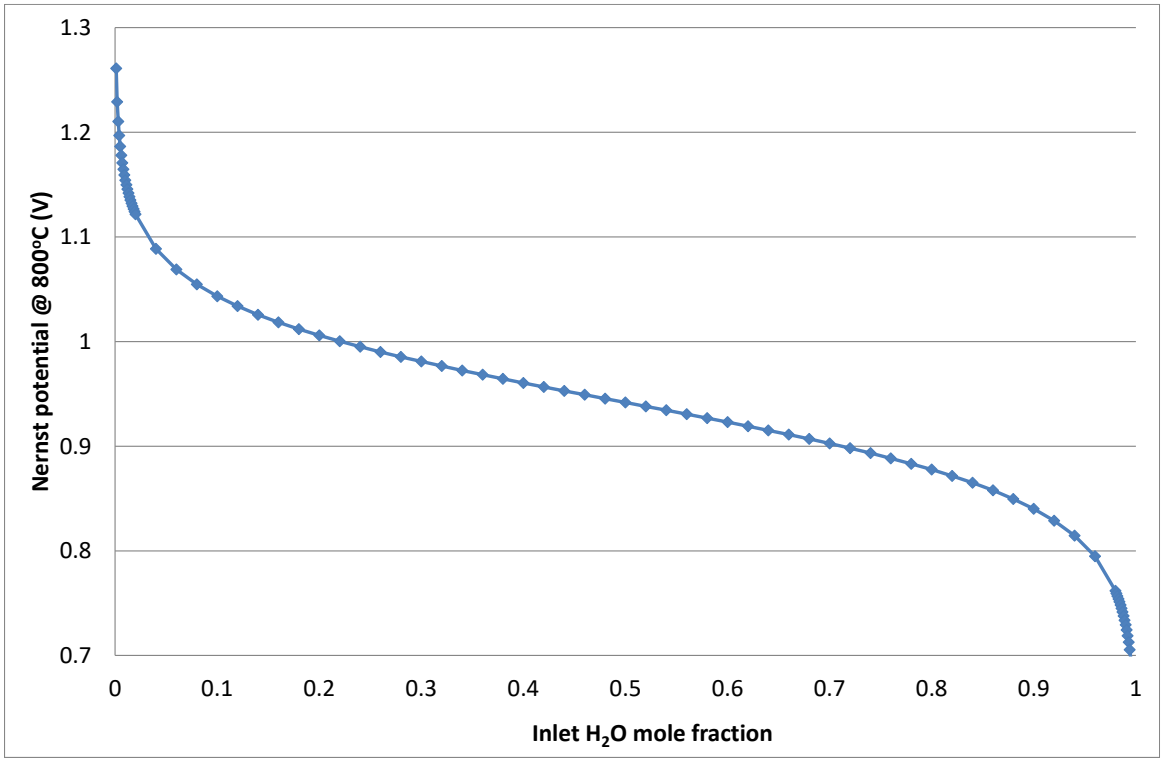


**Figure 8: Graph of Nernst potential vs $H_2O$ gas inlet fraction at 800°C.**

### 2.2.1 Fuel utilisation

The fuel utilisation is calculated by converting the fuel ($H_2$ or $H_2O$) flow rate to a molar flow rate per second using the ideal gas law Equation 23:

$$n = \frac{PV}{RT} \qquad \textit{Equation 20}$$

The molar flow of electrons per second calculated from the current as shown in Equation 21:

$$n_{e^-} = \frac{I}{F} \qquad \textit{Equation 21}$$

The utilisation at the specified current is then calculated as shown in Equation 22; the molar flow rate of electrons divided by the molar flow of hydrogen atoms in the fuel:

$$U = \frac{Electron\ flow\ rate}{Hydorgen\ atom\ flow\ rate} x100 \qquad \textit{Equation 22}$$

## 2.3 Operational considerations for SOE

For a number of reasons the operation of solid oxide cells requires careful thought. The exothermic/isothermal/endothermal nature of the operational voltage will have a small, but noticeable, effect on the performance of a single cell. The effect magnified over a stack will be very noticeable and possibly destructive to the cell. There may also be advantages of the ability to operate the stack in a wide range of voltages. It may be possible to use voltage changes in the cells as a means of temperature control within a stack. If a stack is too warm, the voltage can be dropped to cool it down and vice versa [43]. However, this could potentially lead to much greater difficulty in managing the stack temperature. As far as the author is aware the issues with controlling the stack temperature has not been studied in any level of detail.

Whether the cell/stack is operated either galvanically or potentially controlled should also be given careful consideration. Controlling the cell potential allows good thermal management of the cells however this will result in a loss of control in the current through the cell. As will be discussed in chapter 3.2 the current of the cell and therefore the oxygen flux through the cell can play a very large role in the degradation of the cell. High current densities will normally result in higher rates of cell degradation. Therefore, it may be desirable to put current limits on the cell to avoid excessive degradation.

The degradation at higher currents presents one of the greatest control issues in SOE. As cell performance improves so does the cell current at thermoneutral voltage. Currents over 1 A

$cm^{-2}$ have been achieved at thermoneutral voltage [44]. These high currents can lead to increased cell degradation and this effect may be magnified if cells improve and therefore currents keep increasing. Operating at low cell voltages isn't a problem while the cell has a limitless supply of external heat however if there is no external heat supply the cell would have to operate exothermically and this may lead to the stage where, as ridiculous as it sounds, it may be desirable to reduce cell performance so that the cell can operated exothermically without undesirable cell degradation. With more knowledge of the mechanisms of cell degradation it may be possible to design cells which perform at high current densities without degradation.

On a more general note, when studying degradation whether the cell is operated with constant current or constant voltage has to be decided. In this work we have chosen to operate the cell in constant current operation. Without voltage control the thermal conditions (exo−/endo−thermic) can't be controlled. It should be noted that it has been assumed that the lack of cell temperature control will play a much smaller role in a small button cell than in a large cell and especially a stack. In constant current the oxygen flux across the cell is constant however as the cell performance changes the voltage will change. Operating with a constant current is desirable for calculation of voltage degradation rates, also as the oxygen flux across the cell has a large influence on the cell degradation rate for different cells to be compared. If two cells had different performance operating with a constant voltage would result in different currents and the degradation rates wouldn't be comparable.

In this work it has also been possible to operate without much regard for the exothermic/endothermic nature of the operational voltage as the cell is housed within an externally controlled furnace and gasses are preheated in the furnace and water evaporated externally. There would need to be much greater thought given to the voltage of operation if

the furnace weren't externally heated and evaporated water wasn't available. These operational conditions are not considered further within the scope of this thesis.

### 2.3.1 Round trip efficiency

The round trip efficiency of a solid oxide cell can be calculated from the voltage at the same current density in fuel cell and electrolysis operation as shown in Equation 23.

$$\eta = \left(\frac{V_{fuel\,cell}}{V_{electrolysis}}\right) \quad - \text{at the same current} \qquad \textit{Equation 23}$$

Table 1 shows data from Figure 9 on the round trip efficiency of a solid oxide cell. The efficiency drops as the current of operation increases. Operating the cells at the lowest possible current density is ideal. However, this presents problems when operating an electrolysis cell. As the cell operates thermoneutrally at 1.29V operating below 1.29V requires an input of energy from an external source to keep the cell temperature constant.

**Table 1: Calculation of round trip efficiency**

| Current (A $cm^{-2}$) | Voltage – electrolysis (V) | Voltage −fuel cell (V) | Round trip Efficiency |
|---|---|---|---|
| −0.1 / 0.1 | 1.13 | 0.84 | 0.74 |
| −0.2 / 0.2 | 1.29 | 0.7 | 0.54 |

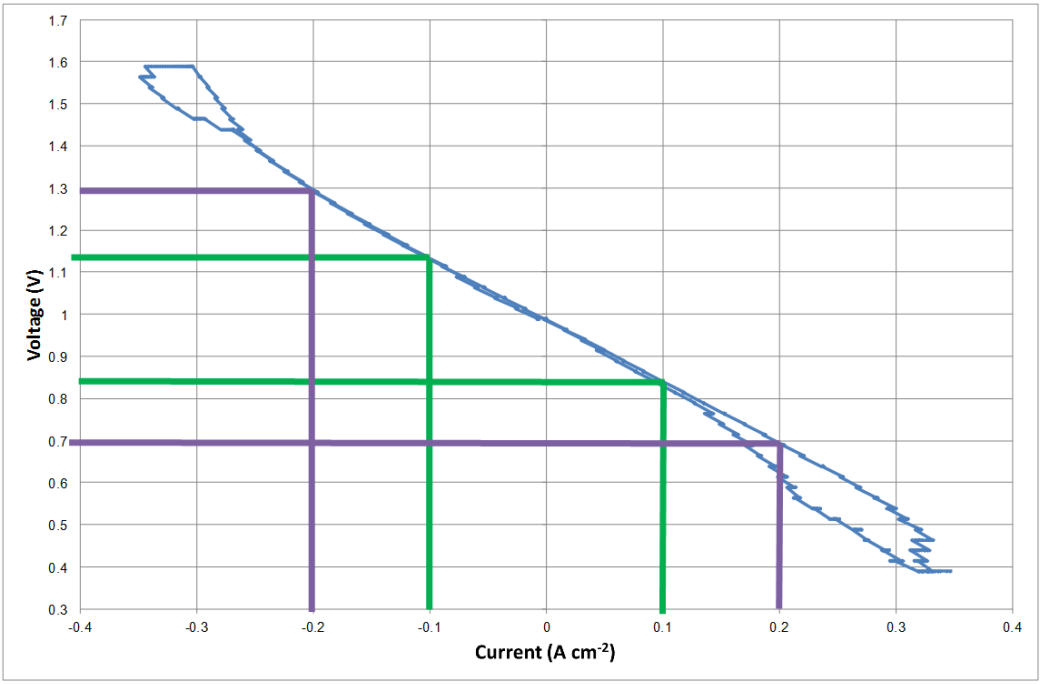


**Figure 9: An example jV curve to calculate the round trip efficiency of a solid oxide cell at −0.2/0.2 and −0.1/0.1 A $cm^{-2}$.**

### 2.3.1.1 Source of electricity and heat

For commercial SOE operation the source of heat and electricity must be considered. While it would be possible to run an SOE on electricity alone it would be advantageous if a waste source of heat could be found. Using either high or low temperature heat should improve the efficiency and the hotter the heat available the greater the improvement in electrical efficiency would be.

A low temperature source of heat above 100–200ºC could be used to evaporate water. There is a large latent heat associated with the evaporation of water and anything which is able to

overcome this barrier would significantly reduce the electrical demand. There are also projects which are investigating the integration with a solid oxide electrolysis stack with a steel plant [45] and an ammonia production plant [46].

If a high temperature source of heat 800–1000ºC , such as nuclear or solar [47–54], can be used to heat the electrolyser there would be a much greater reduction in thermal demand. There are currently very few high temperature heat sources available. However, there are many which may be able to provide an intermediate range of heat 200–800ºC, i.e. by supplying steam. This should reduce the demand for thermal heating from electricity but won't remove it altogether.

## 2.4 Efficiency:

When looking at the overall efficiency of SOE cell it is important to realise that the heat energy provides a significant quantity of the energy for the process, depending on the source of electricity. Only looking at the electrical efficiency of a system could be misleading with electrical efficiencies over 100% achievable. For comparing cells it is useful to use the electrical energy required for the reaction but it must be remembered that this will be affected by temperature. The efficiency of low temperature electrolysis is calculated in terms of electricity per unit of $H_2$. For high temperature electrolysis electrical to hydrogen efficiencies over 100% can be achieved as the heat supplied to the reaction reduces the electrical requirement of the cell. Using a thermal to hydrogen efficiency allows fair comparisons of low and high temperature electrolysis to be made however becomes misleading if the source of electricity is from wind or solar. Many authors quote electrical to hydrogen efficiency when performing efficiency calculations of SOE. Unless the heat would otherwise be wasted this gives an unequal playing field in comparison to low temperature electrolysis.

Various researchers [36,55,56] have looked at the possible efficiencies with which hydrogen can be produced. Thermal to hydrogen efficiencies ranging from 32 to 59% have been found depending on the temperature used and component efficiencies of electrical generation, heat recuperation and electrolyser efficiency. Each found that the efficiency of electrical generation was the factor with the greatest influence on the overall efficiency of hydrogen production. Bo et al [57] found that the overall efficiency of hydrogen production in SOE was dominated by the efficiency of electricity production, 70% of the overall number was determined by this value. If the efficiency of electricity production is negated, system efficiency for an SOE can be very high. Wang, Mori and Araki [58] achieved a system efficiency with a 300 $Nm^3$ hydrogen production system of 98% HHV (83% LHV). The cost of hydrogen produced by high temperature electrolysis will depend on the price of the electrolysis stack, the amount of heat available and the cost of electricity. It has been calculated that hydrogen can potentially be produced by SOE for a price of 3.23 \$ $kg^{-1}$ [59]. This price was achieved assuming heat and electricity from a high temperature helium−cooled nuclear power plant. This almost reaches the DOE target of 2—3 \$ $kg^{-1}$ for hydrogen to be a direct competitor for conventional fuels [60,61].

Donitz and Erdle [62] reported an efficiency of hydrogen production in a solid oxide electrolyser of 2.57 kWh $Nm^{-3}$ at 995$^o$C temperature. More recently a hydrogen production efficiency of 3.16 kWh $Nm^{-3}$ has been reported for a 720 cell stack at 800$^o$C [63].

# 3 Literature review:

In this literature review three areas will be discussed, materials choices for solid oxide electrolysis, degradation of solid oxide cells during electrolysis, and performance of cells operated in electrolysis and during transient and cyclic operation.

There are significant materials issues with SOE. SOFC development has received much greater attention than SOE development. Currently most SOE work is performed with SOFC's run in reverse, however the resistances are higher in SOE than SOFC mode. Bo et al [57] found that the polarisation resistance for a Ni−YSZ/YSZ/LSM cell was 0.76 Ω $cm^2$ in SOFC mode but when used in SOE mode the polarisation resistance increased to 3.7 Ω $cm^2$. However, this is an extreme example and when comparing SOE and SOFC performance care should be taken to ensure the conditions for each are the same. The polarisation resistance in SOE is strongly dependant on the water content of the flow to the cell. Brisse at al [64] report a cell ASR for electrolysis operation increasing from 0.42 Ω $cm^2$ at 82 vol% absolute humidity (AH) to 0.69 $cm^2$ at 30 vol% AH. There are also greater degradation issues observed with SOE cells compared to an SOFC. The main source of degradation when operating at high current densities is at the oxygen electrode due to delamination of the oxygen electrode, however other degradations mechanisms have equally been observed.

## 3.1 Materials:

There is constant research on materials for SOFC and SOE applications [65–70]. In this review the most common materials are reviewed. It was deemed that novel materials were beyond the scope of this review. While many promising materials are proposed the state of development of these is far behind the established materials. For these materials there is a lot of work needed into their long term stability along with the performance data.

### 3.1.1 Electrolyte

#### 3.1.1.1 Zirconia

In its un−stabilised form Zirconia undergoes phase transitions which lead to large changes in volume and would be destructive to fuel cell or electrolysis operation. The cubic form of zirconia is the most preferable for use in a solid oxide cell. There are a number of dopants which are used to stabilise the cubic form of zirconia for SOFC or SOE operation. Figure 10 shows a few examples and the variation of conductivity with doping level.

##### 3.1.1.1.1 YSZ

Yttria stabilised zirconia, YSZ, is the most commonly used material in SOFC and therefore is the most commonly studied as the electrolyte for an SOE too. The function of the electrolyte is very similar for both a SOFC and SOE and therefore YSZ has been the material of choice for most studies of SOE so far. The main disadvantage in the use of YSZ is its lower conductivity than that of Scandia doping which results in high temperature operation [71].

#### 3.1.1.1.2 ScSZ

Scandia stabilised Zirconia, ScSZ, is rarely used as an electrolyte material for electrolysis. While doping with Scandia provides the highest ionic conductivity it is rarely used as an electrolyte due to its cost, which is significantly higher than that for Yittria [72].

As shown in Figure 10 its ionic conductivity is higher than that of YSZ therefore it is often used at lower temperatures than for YSZ. The number of studies on ScSZ is limited, as far as the authors are aware there is only one paper on the use of a Ni−ScSZ hydrogen electrode supported cell [73], however there are a number of studies with Scandia electrolyte supported cells [74–80].

### 3.1.1.2 Proton conducting electrolytes

The author felt a brief mention of proton conducting materials, while not common, was worthy of mention. In−depth reviews on materials and reversible operation can be found in [67,69]. A proton conducting electrolyte has a few possible advantages over an oxide conducting membrane. A proton conducting membrane performs gas separation by design, as protons travel through the electrolyte. The hydrogen side is pure hydrogen, therefore there is the requirement for purification of hydrogen from water. This also leads to the main advantage of proton conducting oxides which is that the environment of the hydrogen electrode is pure hydrogen, therefore there is no exposure of Ni in the hydrogen electrode to oxidising water containing atmospheres. It has also been suggested that the optimal configuration for a proton conducting cell is hydrogen electrode supported for both SOE and SOFC, while for an oxide conducting cell the hydrogen electrode support is desirable in SOFC operation but a disadvantage in electrolysis operation [81].

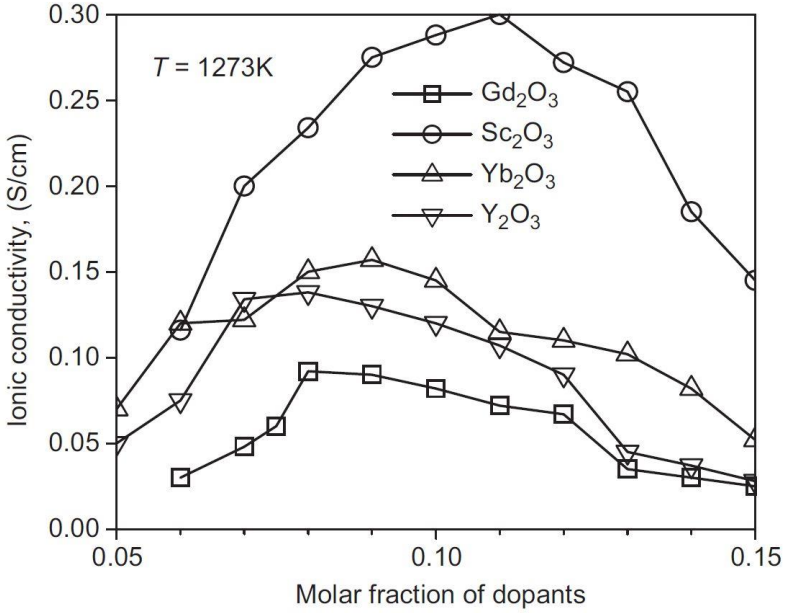


**Figure 10: The dependence of ionic conductivity in Zirconia on the dopant and dopant concentration [82].**

### 3.1.2 Hydrogen electrode

#### 3.1.2.1 Nickel based

Ni is by far the most common material for SOE and SOFC hydrogen electrodes. Ni has been found to be the best electrochemical noble metal for $H_2$ oxidation [83]. Ni is an electronic conductor, but can't conduct ionically, therefore reactions take place at the triple phase boundary (TPB) between Ni and the electrolyte. The thermal expansion co−efficient of Ni is also much greater than that of YSZ and would cause mechanical damage to the cell if a pure Ni hydrogen electrode was used due to the mismatch in expansion. To increase the area of TPB available for reaction and reduce the thermal stresses in the cell the Ni is mixed with YSZ to form a cermet [83]. The most common cell configuration is to have a cell supported on a thick hydrogen electrode.

Much of the research performed on hydrogen electrodes has been on the microstructure of the Ni/YSZ cermet electrode aimed at improving redox behaviour. During redox cycles a Ni/YSZ hydrogen electrode expands as seen in Figure 11. When NiO is reduced it undergoes a volume

reduction when it forms Ni metal. When the metallic Ni is reoxidised the volume is increased but the NiO formed has extra pores and is not as dense as the starting NiO and therefore there is a continuous expansion of the material following repeated cycles [84]. The poor redox behaviour of Ni is one potential problem for its application in an SOE. At high humidity an oxidising environment would form at the hydrogen electrode [85] and while the reduction of nickel is slower in $H_2O$ environments than $O_2$ environments [86] the cell would still suffer from damage. Hydrogen is added to the fuel inlet of an SOE cell to prevent Ni oxidation, as far as the author is aware there is no detailed study on the addition of $H_2$ to prevent nickel oxidation in an electrolysis environment.

There are other materials which have been investigated as alternatives to YSZ within a Ni based electrode such as samaria−doped ceria SDC [79,87–90] with Ni dispersed on the surface. SDC is a mixed ionic electronic conductors (MIEC's). However, long term stability of these materials has not been proven and they are not currently a viable alternative to Ni−YSZ.

### 3.1.2.2 Redox stable anodes

There are a number of reasons why a hydrogen electrode material stable in oxidising and reducing atmospheres would be an advantage. During an unexpected shutdown there would be no need for a protective atmosphere on the hydrogen electrode. In commercial systems this would significantly reduce the cost and complexity of the systems [91]. For electrolysis the use of a redox stable anode would remove any concerns with the re−oxidation of Ni with high water content of hydrogen electrode fuel supply, and the need to add hydrogen to the water supply to the hydrogen electrode. There has been work performed on achieving redox stability with conventional Ni based electrodes [91–93]. There is also a lot of research on the use of

perovskite materials for use as a hydrogen electrode[94–99], which could be more resistant to redox cycling.

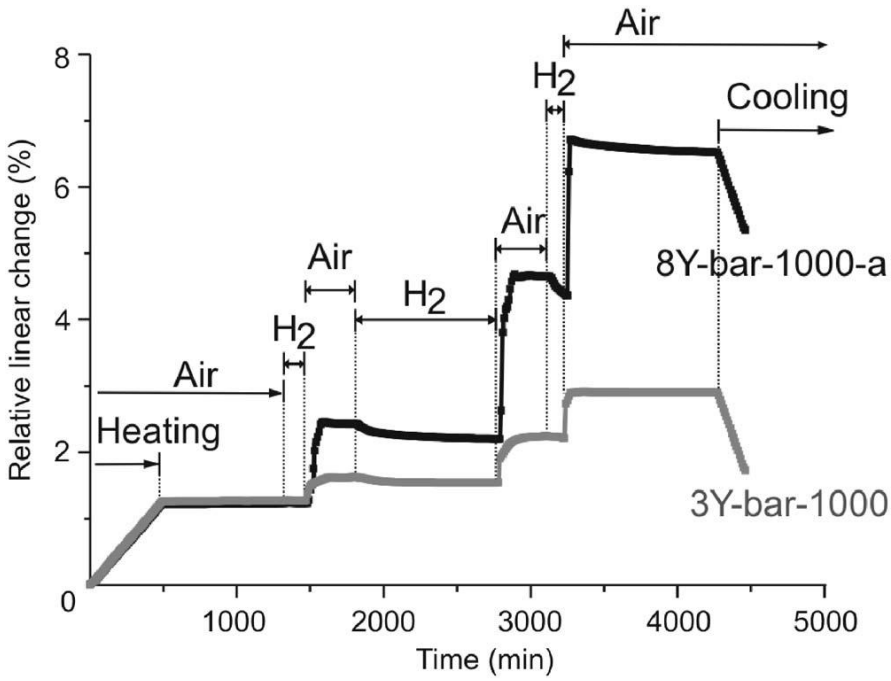


**Figure 11: Work by Klemensoe et al [84] − Dilatometry profile of Ni−YSZ samples, two different YSZ doping levels were used. 8Y−bar−1000−a (black curve) and 3Y−bar−1000 (grey curve) during changing reducing atmosphere (marked $H_2$) and oxidizing atmosphere (marked Air). Shows the volume change when redox cycling occurs.**

### 3.1.3 Oxygen electrode

#### 3.1.3.1 LSM

The most common material used for SOFC and SOE oxygen electrodes is Sr doped $LaMnO_3$ (LSM). LSM is an electronic conductor and is unable to conduct ionically. Like the hydrogen electrode materials the reactions occur at the TPB between LSM and YSZ, therefore the TPB is extended by using a mixed LSM−YSZ material for the oxygen electrode. There are degradation issues with LSM as an oxygen electrode, especially in the delamination of the oxygen electrode from the YSZ surface which will be discussed in more detail in section (3.2.3).

LSM has been reported to undergo an initial improvement in performance while operating under electrolysis conditions[100,101]. There are two mechanisms which have been suggested to account for this effect. Wang and Jiang[100] suggested this to be due to the incorporation of SrO into the LSM lattice. This results in the removal of cation vacancies and the creation of oxygen vacancies. Oxygen vacancies in LSM would increase its ionic conductivity therefore increasing its reactivity. Backhaus−Ricoult et al [101] proposed that during electrolysis, $Mn^{2+}$ migrated from the TPB over the surface of the YSZ electrolyte. This enrichment of the surface by $Mn^{2+}$ led to direct incorporation of $O_2$ into the electrolyte therefore increasing the surface area for reaction.

### 3.1.3.2 LSCF

The main alternative to LSM as an oxygen electrode is Lanthanum Strontium Cobalt Ferrite, LSCF. This material has been used by a number of researchers for solid oxide electrolysis [42,73,102]. LSCF is incompatible with YSZ as there is a reaction which forms an insulating Strontium Zirconate layer on the YSZ−LSCF interface [103]. Therefore intermediate layers such as CGO or SDC are used. LSCF is often used as an intermediate temperature oxygen electrode. The conductivity of LSCF is higher than that of LSM at lower temperatures, LSM providing good performance at 800$^{o}$C while LSCF performs better below 750$^{o}$C. LSCF is a mixed ionic electronic conductor (MIEC) therefore there is no YSZ or other ionic conductor used in the oxygen electrode structure.

### 3.1.3.3 Other

There are a number of other materials which are also being investigated for use as oxygen electrodes for both SOE and SOFC. Wang et al [104] have investigated YSZ with Sr doped $LaCoO_3$ (LSCo), Sr doped $LaFeO_3$ (LSF) and LSM as oxygen electrodes for SOE cells. They

found that the LSM−YSZ had the best performance after oxygen electrode activation, which was caused by partial reduction of the LSM. However this activation was lost during electrolysis. They found that LSCo and LSF showed impedance values which are almost independent of current and operated equally well under both anodic and cathodic polarisations. This makes them more attractive as an oxygen electrode for SOE cells than LSM/YSZ. However they have also been seen to undergo reactions with the YSZ over time at high temperature; more work is required on the long term stability of these materials.

## 3.2 Degradation:

One of the largest problems faced with solid oxide electrolysers is the degradation which the cells experience. The degradation of SOE's has been studied in far less detail than the degradation in SOFC's, although there have recently been significant investigations made in the degradation in electrolysis mode [105–111]. While some of the degradation mechanisms may be very similar there are significant differences between the two. Initial work on electrolysis indicated that degradation is significantly higher for a solid oxide cell, SOC, working in electrolyser mode than fuel cell mode, and this suggests that the operation of a solid oxide electrolyser presents unique problems compared to that of a fuel cell. However, mitigation strategies have been proposed [106], and long−term testing has proven cells to be robust [26,42]. There are also differences in degradation between single cells and cell stacks. In this review the degradation of stacks has not been investigated and the author directs readers to the review by P. Mocoteguy and A. Brisse [108] for more information on degradation in stacks.

SECA (the Solid State Energy Alliance) has given guidelines for operating parameters of fuel cells; the guidance requires a minimum lifetime of 40,000 hours and a power degradation of ≤

0.2% per 1000 hours [112], it may be imagined that the requirements for an SOE cells will be similar. Currently the best long term performance has been reported by Hauch et al [113] who found a voltage increase of 2% $kh^{-1}$ obtained on a Ni/YSZ−YSZ−LSM/YSZ cell at 850°C at a current of −0.5A $cm^{-2}$,and $p(H_2O)/p(H_2) = 0.5/0.5$.

### 3.2.1 Long term testing

A number of studies have been performed on the long term durability of SOE cells:

J.Schefold et al [42] reported a test on a solid oxide cell in steam electrolysis for 9000h, the cell was a Ni−YSZ/YSZ/LSCF cell operated at 780°C and −1A $cm^{-2}$. The feed gas had an AH of 80 vol% and a steam utilisation of 36%. The average voltage loss over the whole experiment was 3.8% (40mV) $kh^{-1}$. However, during a period with no experimental interruptions a degradation rate of 1.7% was observed over a 3600h period. J. Schefold et al [114] also performed long term testing on two stacks. A 5 cell hydrogen electrode supported stack, degradation rate 3% $kh^{-1}$; and a 5 cell electrolyte supported stack, degradation rate 2.6% $kh^{-1}$.

P. Hjalmarsson et al [115] reported a test on a Ni/YSZ−YSZ−CGO−LSC/CGO hydrogen electrode supported cell tested for 2700h in $H_2O$ and $CO_2$ co−electrolysis at 800°C and −1 A $cm^{-2}$. The voltage loss was 0.9% (<12mV) $kh^{-1}$.

Mougin et al [116] have tested a 3 cell stack at 700°C. The feed had an AH of 90 vol%. The cell was operated at a variety of operational currents with the degradation strongly related to the current density. Degradation rates of ~2% $kh^{-1}$ were obtained at 0.5A $cm^{-2}$ at 1 A $cm^{-2}$ the degradation rate was 6.6% $kh^{-1}$.

### 3.2.2 Causes of degradation

The major causes of degradation in a solid oxide electrolysis cell are [117]:

- Delamination of the oxygen electrode and bond layer on the steam/oxygen side
- Deposition of contaminants (e.g. Ni, Cr, Si, etc.) on reaction sites
- Loss of electrical/ionic conductivity of electrolyte
- Change in microstructure of electrodes

The rate of degradation is highly dependent on the current density through the cell as shown by Mougin et al [116]. At low current density, i.e.< 1 A $cm^{-2}$, the degradation observed can mostly be attributed to impurities in the cell. At higher current densities the degradation becomes due to structural changes in the cell.

Graves [25] investigated the durability during co−electrolysis of $H_2O$ and $CO_2$ and found that at low current densities (0.25 A $cm^{-2}$) the degradation was predominantly at the hydrogen electrode whereas at higher current densities (0.5 and 1 A $cm^{-2}$) the hydrogen electrode degradation was still apparent but there was a greater contribution from the degradation at the oxygen electrode.

In the next section the causes of degradation are discussed separately depending on whether they occur at the oxygen electrode, electrolyte or at the hydrogen electrode.

### 3.2.3 Degradation of the oxygen electrode

Delamination of the oxygen electrode from the electrolyte is a major issue for YSZ/LSM cells operated at high current density [25,105,109,110,118–123]. However, as shown by Hauch et al [113], it is possible to operate LSM cells for long time scales with reasonable performance.

The stability of LSM based electrodes can be enhanced by the extension of the reaction zone [108].

It is thought that the delamination occurs due to a build−up of gaseous oxygen between the electrolyte and electrode which causes the electrode to peel off from the surface of the electrolyte [119,124,125]. Virkar [119] found that under certain conditions the chemical potential of oxygen in the YSZ electrolyte could exceed the chemical potential of oxygen in the oxygen electrode. The chemical potential is related to the partial pressure. The result is that high pressure regions can form between the oxygen electrode and YSZ electrolyte resulting in delamination as seen in Figure 12 which shows a Ni/YSZ – YSZ – LSM/YSZ microtubular cell investigated by Laguna – Bercero et al [109,126].

Rashkeev and Glazoff [125] modelled the degradation in a solid oxide cell and also found that a pressure build up at the electrode−electrolyte interface caused the degradation. Their models indicated that there was inter diffusion of La and Sr into the Zirconia leading to the formation of SrZr and LaZr which may cause a change in oxygen transport leading to the delamination. Li et al [127] studied the effect of applying an interlayer of Mn−YSZ between the YSZ and LSM. This was found to reduce the delamination observed. Their results showed a decrease in the formation of LaZr on the Mn−YSZ surface which is thought to have prevented the build−up of high oxygen pressure.

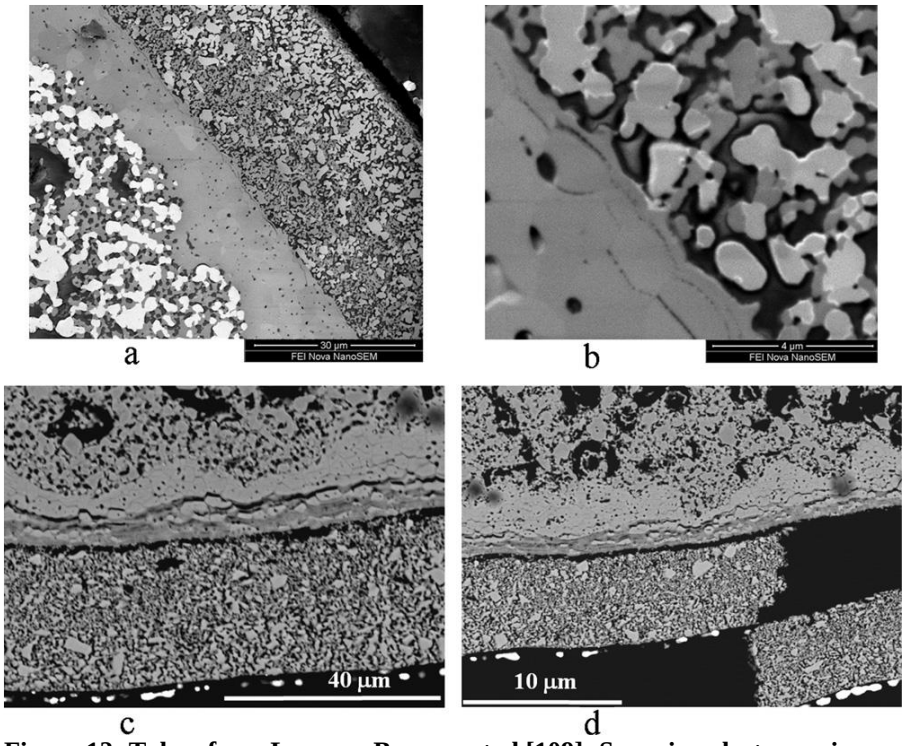


**Figure 12: Taken from Laguna−Bercero et al [109]: Scanning electron microscopy, SEM, micrographs showing different stages of damage for the same cell (a) general view of the cell; (b) origin of the degradation at the YSZ grain boundaries; (c) cracking of the YSZ electrolyte and (d) delamination of the LSM–YSZ electrode.**

There are a number of approaches which can be used to mitigate the effects of delamination. These generally involve extending the electrolyte−electrode interface further into the electrode or operation at lower current density. For an LSM based electrode the use of a composite oxygen electrode of LSM/YSZ may be enough to prevent delamination [128]. The use of a mixed ionic electronic conductor such as LSCF is another possible way of preventing the delamination of the oxygen electrode as the oxygen is less likely to form at the electrode−electrolyte interface [42,108,118].

### 3.2.4 Hydrogen electrode degradation

There are a number of mechanisms which may cause degradation at the Ni/YSZ hydrogen/steam electrode.

At the inlet of a fuel cell the water partial pressure will be low, commonly ~4% water will be used in the inlet hydrogen. Across the cell the water partial pressure will increase and depending on the utilisation of the cell may get to 50—60% at the outlet of the cell. In an electrolyser this will be different. For optimal performance the water partial pressure at the inlet to the cell would be as high as possible, approaching 100% water. It has been stated that without hydrogen to the hydrogen electrode the nickel would oxidise. While ~1% hydrogen in the gas stream is enough to prevent re oxidation of nickel [129,130] the effects of high humidities on an SOE hasn't been studied in great detail.

Hauch et al [107] studied the degradation at a p($H_2O$) of 0.2, 0.4 and 0.6 atm. During fuel cell operation they found a faster degradation rate at higher $H_2O$ partial pressures.

Matsui et al [131] investigated the degradation of a Ni−ScSZ cermet at different humidification's for fuel cell operation on electrolyte supported cells. Cells showed high degradation over 5 hours at 40% humidity.

Osinkin et al [132] performed work on a Ni cermet with the addition of some Cu and Ce in fuel cell operation. They found that the performance of a solid oxide cell degrades at a faster rate at higher $H_2O$ concentrations and that at $H_2O$:$H_2$ ratios of 65:35 and 75:25 the electrode suffers from very rapid degradation.

Kim at al [133] investigated the effect of gas composition on SOE performance with a Ni/YSZ based cell. Their cell suffered from a severe failure when operating at high $H_2O$ concentrations ($H_2$:$H_2O$ 1:20); this was attributed to low $H_2$ partial pressure at the hydrogen electrode causing electrode damage through re−oxidation of the electrode.

Evaluation of the 9000h test performed by J.Schefold et al [42] and by Tietz et al [105] found that the overall contribution to cell degradation by the Ni/YSZ electrode was small compared

to the contribution by the electrolyte. Post−test investigation of the cell showed minimal degradation and little morphological change. It would be expected that nickel coarsening would play a significant part in the degradation especially with high water content [108] but this was not observed.

Hauch et al [134] have looked at the degradation of a Ni/YSZ hydrogen electrode when used in fuel cell mode. Electrolysis was performed at various current densities and steam concentrations. They found that passivation, and reversible loss in performance, had occurred over the first few days of testing. At low cell polarisations only the polarisation resistance increased, however higher cell polarisations caused an increase in both polarisation resistance and ohmic resistance. Comparison of the cell and reference cells of the same batch were performed using SEM and EDS. They observed that silicon, as sodium silicate glass, was present on the electrolyte/hydrogen electrode boundary. The silicon was limited to the ~8μm of electrode closest to the electrolyte, with the first 2μm containing the majority. The presence of silicon at the electrode/electrolyte boundary led to increases in the ohmic resistance of the cell. Increasing the cell polarisation resulted in a greater degree of silicon deposition in the cell. The silicon was found to have come from the glass sealant. As silicon becomes more mobile at higher $H_2O$ concentrations this form of poisoning is a much greater issue for electrolysis operation than fuel cell operation.

Hauch et al [135] investigated the Ni/YSZ structures in the hydrogen electrode and found that they could be optimised for increased electrolysis performance and durability. This was done by minimising the ability of Ni to move within the structure by making the structure dense, with small pores and particle size distribution. Through this degradation was reduced to 0.35% $kh^{-1}$, which shows the importance of the hydrogen electrode in the cell degradation.

### 3.2.5 Electrolyte degradation

The degradation of the electrolyte when operated in SOE is different than during fuel cell operation. In part this is due to a difference in the oxygen potential across the electrolyte [136]. At OCV the oxygen potential across the electrolyte is small but greater at the oxygen electrode. During fuel cell operation the oxygen potential across the electrolyte is reduced as the potential at the hydrogen electrode increases. During fuel cell operation the oxygen ions are traveling in the direction of the oxygen potential across the cell. During electrolysis operation the oxygen potential is increased as oxygen is forced towards the oxygen electrode and oxygen ions travel against the direction of oxygen concentration across the cell. Figure 13 shows the oxygen present across the electrolyte, the degraded sample operated in electrolysis shows much higher oxygen content close to the oxygen electrode (LSM/YSZ) than the blank sample; it also shows that an oxygen gradient has formed across the electrolyte. Formation of oxygen in the electrolyte has been reported by Tietz et al [137] and Knibbe et al [110]. This has been associated with the delamination of the oxygen electrode. It also causes pore formation in the electrolyte close to the oxygen electrode and therefore degradation of the cell, due to increased grain boundary resistance in the electrolyte. Tietz et al [137] studied the degradation on a cell which had been operated for 9000h in electrolysis at −1 A $cm^{-2}$. Analysis of the cell cross section showed ‘trans−granular longitudinal porosity’ as well as pore formation near grain boundaries in the electrolyte.

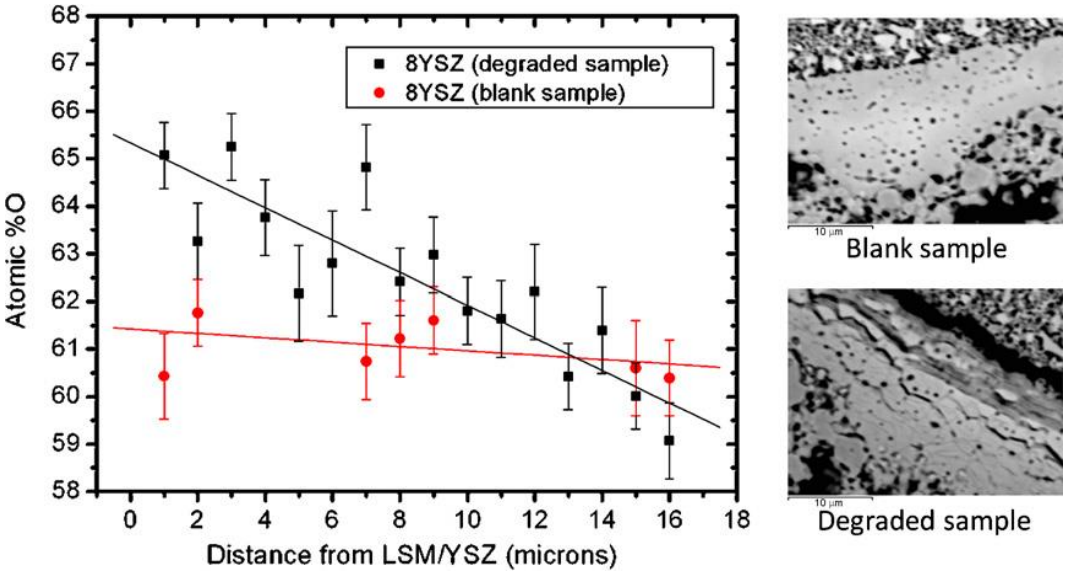


**Figure 13: Taken from Laguna−Bercero et al [109]. Oxygen content across YSZ measured by energy dispersive x−ray spectroscopy, EDS, for a degraded, after SOE, and blank sample, also shows SEM images of the analysed regions.**

It has been reported by a number of researchers including Laguna−Bercero et al [138], and Schefold et al [139] that the voltage saturates at voltages of about 1.9V during electrolysis operation, shown in Figure 14. This is attributed to the electrolyte becoming electronically conductive. The voltage at which the electrolyte becomes conductive is lower during electrolysis, and with a low oxygen partial pressure on the hydrogen side, is lower than the YSZ reduction potential of 2.2V at 1000$^{o}$C [140]. While the voltage at which the electrolyte becomes conductive is greater than that which would normally be found during electrolysis operation, the electronic conduction should not affect normal cell performance. During normal operation if the electrolyte were to become electronically conductive through normal IV measurements the cell would appear to improve in performance. The fact that the cell improvement was due to electronic conduction through the electrolyte would only become apparent through analysis of the gas composition of the cell outlet.

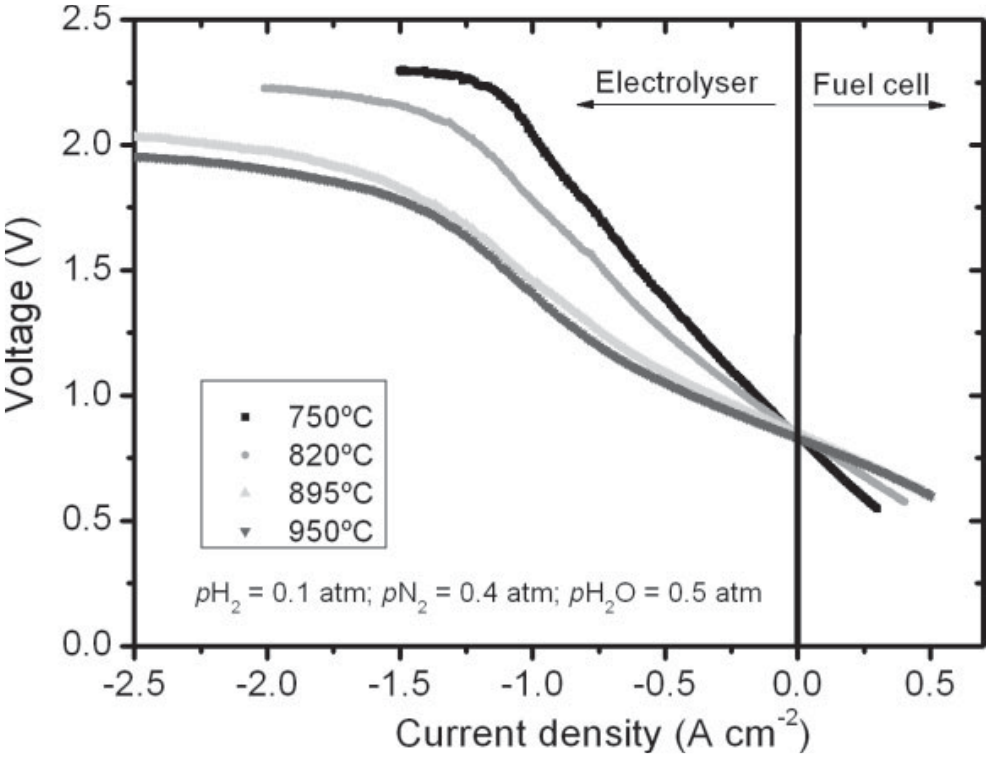


**Figure 14: Voltage saturation due to electronic conduction through the electrolyte of cells operated in electrolysis operation taken from [141]**

## 3.3 Reversible cell operation

While cells have the ability to perform in either direction they may not have an equivalent performance in both directions. The performance of a cell in electrolysis mode is commonly worse than cell performance when operated in fuel cell mode, this is especially true for an LSCF electrode and is caused by depletion of oxygen vacancies at the electrode/electrolyte boundary [142–144].

Marina et al [142] looked at a number of oxygen electrode materials for SOFC and SOE and found that the performance in SOE was worse than SOFC. They found that the MIEC type conductors; lanthanum strontium copper ferrite (LSCuF) and lanthanum strontium cobalt ferrite (LSCoF); showed a greater difference between fuel cell and electrolysis performance than an LSM cell.

Ni Leung and Leung [143] modelled a number of electrode for RSOFC operation and found that the fuel cell concentration overpotentials were higher on the oxygen electrode whereas the electrolysis concentration over−potentials were greater in electrolysis operation. This would suggest a hydrogen electrode supported cell may be optimal for SOFC operation whereas an oxygen electrode supported cell may be better for electrolysis operation.

Hughes et al [145], looked at the cyclic operation of a symmetrical solid oxide cell with LSM electrodes. They found very high rates of degradation for a cell which was held at constant current 1.5 A $cm^{-2}$ however the cells cycled at 12 and 1 hour periods showed much smaller degradation rates. The degradation observed was due to delamination with much less delamination on the cells cycled at 1 hour periods than the 12 hour periods or constant operation.

Versa power [146] have performed cyclic tests on a solid oxide cell. Cell degradation in fuel cell operation was about 0.45% $kh^{-1}$ whereas the degradation rate in SOE mode was 3.8% $kh^{-1}$. In cyclic operation for 100days with switching every 12 hours they found that the cells degraded at roughly 90 mV $kh^{-1}$ SOFC and 70 mV $kh^{-1}$ SOE operation, the cell degradation was about four times greater in cyclic operation than in pure fuel cell operation. It is also interesting to note that the fuel cell degradation was greater than the electrolysis degradation. As this is provided as a presentation rather than paper little further information about the testing can be gleamed. The test was performed at 750$^{o}$C, 0.5A $cm^{-2}$ and 50% utilisation.

Hauch et al [147] performed testing of solid oxide cells in electrolysis mode. While they did not perform cyclic operation on cells they reported that the performance of a cell operated, and passivated, by operation in electrolysis can be reactivated by subsequent operation as a

fuel cell. However they did not re−cycle the cell into electrolysis operation after testing as a fuel cell.

Petipas et al [148] investigated the transient operation of a commercial Ni/YSZ−YSZ−LSCF/GDC fuel cell from SOFC power. The cell was operated transiently between 0 and 0.44 A $cm^{-2}$, 0.44 A $cm^{-2}$ corresponding to the thermoneutral voltage of 1.28V. They observed a voltage degradation of 5% (70mV) $kh^{-1}$. They mention that the edges of the cell are oxidised and reduced during transient operation, oxidation occurring in the absence of or at low current. No speculation is given as to whether this is due to the increased hydrogen flow during electrolysis or due to the lower water utilisation at OCV or low currents.

Nguyen et al [149] tested a 2 cell planar stack in both fuel cell and electrolysis operation for ~8000h. During fuel cell operation the stack degraded at 0.6% $kh^{-1}$. During electrolysis (50% $H_2O$:$H_2$ 0.3 A $cm^{-2}$) operation there was a slight improvement in performance. This was attributed to the fact that the stack was moved from one furnace to another between fuel cell and electrolysis tests resulting in a change in contacting. Close to the OCV the cell operation in fuel cell and electrolysis operation was smooth showing very similar performance in both modes of operation.

Graves et al [106] have investigated the cyclic (galvanic) performance of a solid oxide cell and found that the degradation observed in SOE operation could be prevented. This links to various other work performed on solid oxide electrolysis degradation [25,110,150]. The cyclic studies used a fuel cell current of 0.5 A $cm^{-2}$ and an electrolysis current of 1 A $cm^{-2}$. The cell remained for 1 hour in electrolysis before cycling to fuel cell for 5 hours. During fuel cell and OCV operation the cell was operated with 50:50 $H_2O$:$H_2$ fuel mixture; for electrolysis this

was altered to a 90:10 $H_2O$:$H_2$ mixture. Compared to an electrolysis cell operated at a constant 1 A $cm^{-2}$, which showed a high rate of degradation, the electrolysis cell showed no degradation.

### 3.3.1 Modelling

Depending on the load and voltage between which the cells are cycled there will be some transient temperature changes in the cell. Cai et al [151] modelled the transient behaviour of a solid oxide cell. They found that the cell temperature dropped within 200s of a reduction in operating current. For small current changes (1–0.75 A $cm^{-2}$) the temperature stabilisation period was around 9 min. For larger current changes (1–0.2 A $cm^{-2}$) the temperature drop can be large (88 K over 300s). Experimental work on the temperature profile of a solid oxide electrolyser has been performed by Cumming and Elder [152] and it would be interesting if this could be expanded to include the changes in temperature experienced during cyclic operation.

Petipas et al [153] modelled the operation of an electrolyser stack operated without an external heat source. They found that the cell operational range was limited to regions between 60−100% of full operation. This is in part due to the need to operte the cell close to the thermoneutral volage due to sensitivity to thermal graadients.

Yoon et al [154] modelled the performance of hydrogen electrode supported cells in SOFC and SOE operation, they found the performance in SOE was limited by the porosity in the hydrogen electrode to a greater extent than in fuel cell operation and that increasing the porosity of the hydrogen electrode increased the cell performance. The design of the hydrogen electrode, for a hydrogen electrode supported cell, is more important for SOE operation than SOFC operation.

## 3.4 Cyclic/transient operation (load cycling)

It is likely that a solid oxide electrolysis system will be operated as part of an energy storage system, possibly as energy storage for intermittent power supplies. With this in mind it is unlikely that solid oxide electrolysis will be performed at constant current. The cells will either be cycled between electrolysis and OCV or electrolysis and fuel cell operation. There has been very little reported work on the load cycling of solid oxide electrolysis cells however the work which has been reported presents very interesting results [106,148].

This work is reviewed in detail in Chapter 6.

# 4 Experimental

In this section the cells used in this work are introduced. The experimental test set−up for cell testing and the associated development process are then described. Finally the electrochemical measurements by which the cell was characterised have been introduced.

## 4.1 Cells used

There were three types of cell used in this work. Microtubular cells were used for some of the initial work. The project moved on to focus on planar cells, these were a combination of ‘in house’ fabricated cells and commercial button cells.

### 4.1.1 Microtubular

The microtubular cells had a 2.3mm I.D. and were supplied by AMI. Further details on the cell can be found in [155]. The cells were Ni/YSZ supported with a YSZ electrolyte. The oxygen electrode was applied by brush painting ink onto the cells. The ink for the oxygen electrode was a water based LSM ink which was prepared as described by Howe et al [156]. The formulation for the inks are show below in Table 2. The ink was applied in two layers with an LSM/YSZ layer and an LSM layer.

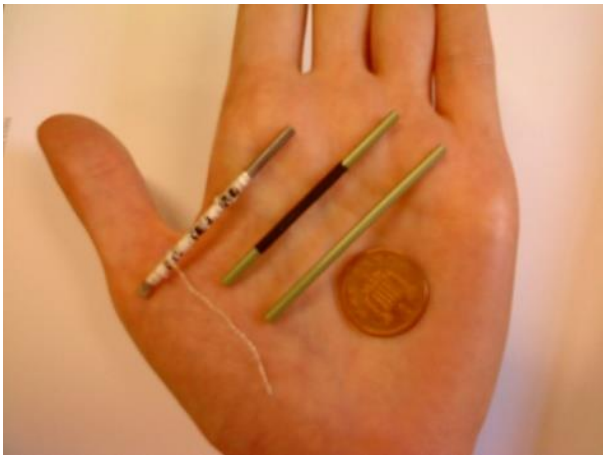

**Figure 15:Images of microtubular cell courtesy of Howe [157]. Far right tube as received, centre tube with oxygen electrode applied, left reduced tube with interconnections applied.**

**Table 2: Recipe for oxygen electrode inks used for microtubular cells [156].**

| Component | Cathode ink 1 | | Cathode ink 2 | |
|---|---|---|---|---|
| LSM (Merk 0.82/0.18) | | | 10.00 | g |
| LSM (SSC 0.5/0.5) | 3.25 | g | | |
| TOSCH (TZ8Y) | 3.25 | g | | |
| PVA Polyvinyl acetate (binder − 12% of powder weight) | 0.78 | g | 1.20 | g |
| Water | 8.00 | ml | 7.00 | ml |
| PVP Polyvinylpyrrolidone (dispersant − 3.7% of powder weight) | 0.24* | g | 0.37* | |
| #Milling beads used | 7 | | 8 | |

The ink was applied by painting as described by Dhir [155]. The LSM ink was applied to the cell by hand painting and was painted over the central 40 mm of the cell. The 1st ink was allowed to dry for 24 hours before the application of the 2nd ink. Once the ink was applied the cells were sintered, at 1150 $^{o}$C. The sintering profile is shown in Figure 16, and was performed in a Carbolite furnace.

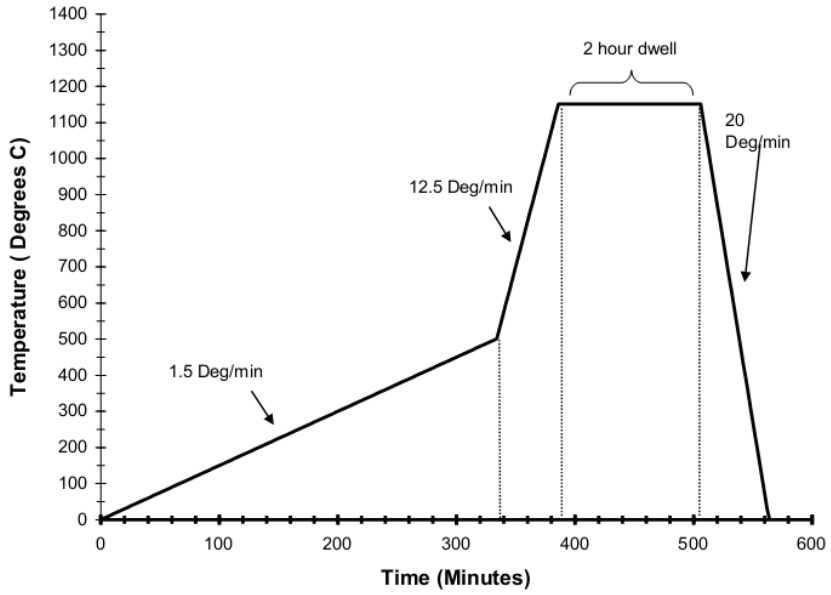


**Figure 16: Sintering profile for the LSM oxygen electrode [155].**

The hydrogen electrode was exposed on the outside of the cell by the removal of a 3mm band of YSZ. The oxygen electrode electrical connections were attached over the painted oxygen electrode. 3mm bands of silver ink were painted onto the cell, 3 bands for the oxygen electrode, a single band for the hydrogen electrode. Silver wire (Goodfellow, 0.25mm, 99.99%) was wrapped around the silver ink bands to form the electrical connections. The electrical connections were positioned at the fuel inlet end of the cell. The active, oxygen electrode area of the cell was around 1 $cm^2$.

### 4.1.2 Planar

There were two types of planar cells used; one was homemade, the other was obtained from a commercial supplier.

#### 4.1.2.1 Homemade

The fabrication of cells is described in the Chapter 5.

#### 4.1.2.2 Commercial

Commercial cells produced by the Ningbo Institute of Materials Technology and Engineering were also tested for electrolysis and fuel cell operation. The cells were anode supported with a Ni/YSZ $H_2$ electrode, a YSZ electrolyte and a LSM/YSZ cathode. These were supplied as either; anode supports (anode support with active anode), half cells (anode support, active anode and electrolyte), or full cells. The cells were 3 cm in diameter. The full cells were supplied with a 3 $cm^2$ oxygen electrode.

## 4.2 Experimental test set up

In this work there have been two test setups used. The main difference between the two test rigs was the way in which the humidity was created. The Mk1 set up used a bubbler humidifier to create a wet gas stream by bubbling dry gasses through a water bath at a set temperature. The Mk2 set up used a commercial water evaporator to provide a gas stream with greater control over the water content of the gas.

For all cells testing was performed in a tubular furnace (Elite thermal solutions THH12/90). The furnace temperature was controlled using a PID controller (Eurotherm, 2408). Gases supplied were hydrogen and nitrogen (BOC). Compressed dry air from a compressor in the lab was supplied to the oxygen electrode with no purification.

In the next section the two test set−ups used for testing and the development work which was performed to optimise their use will be described.

### 4.2.1 Microtubular

A photo of the test set−up for the testing of microtubular cells is shown in Figure 17 and a schematic in Figure 18. The testing of microctubular cells was performed using a bubbler humidifier. Gas was bubbled through a heated water bath at a set temperature; all gas lines following the humidifier were insulated and heated with line heaters to prevent condensation. The set−up was equipped with a humidity sensor (HMT 335, Vaisala) which was used to monitor the amount of water in the gas stream. The probe for the humidity sensor was housed within a heated box and either the inlet or outlet gasses of the cell could be measured to enable measurement of the utilisation by comparison of the inlet and outlet gas humidities. This method of humidification was effective at low levels of humidification, at water bath temperature below 60$^{o}$C 15% RH, however became very unstable as the water bath temperature increased above 70$^{o}$C.

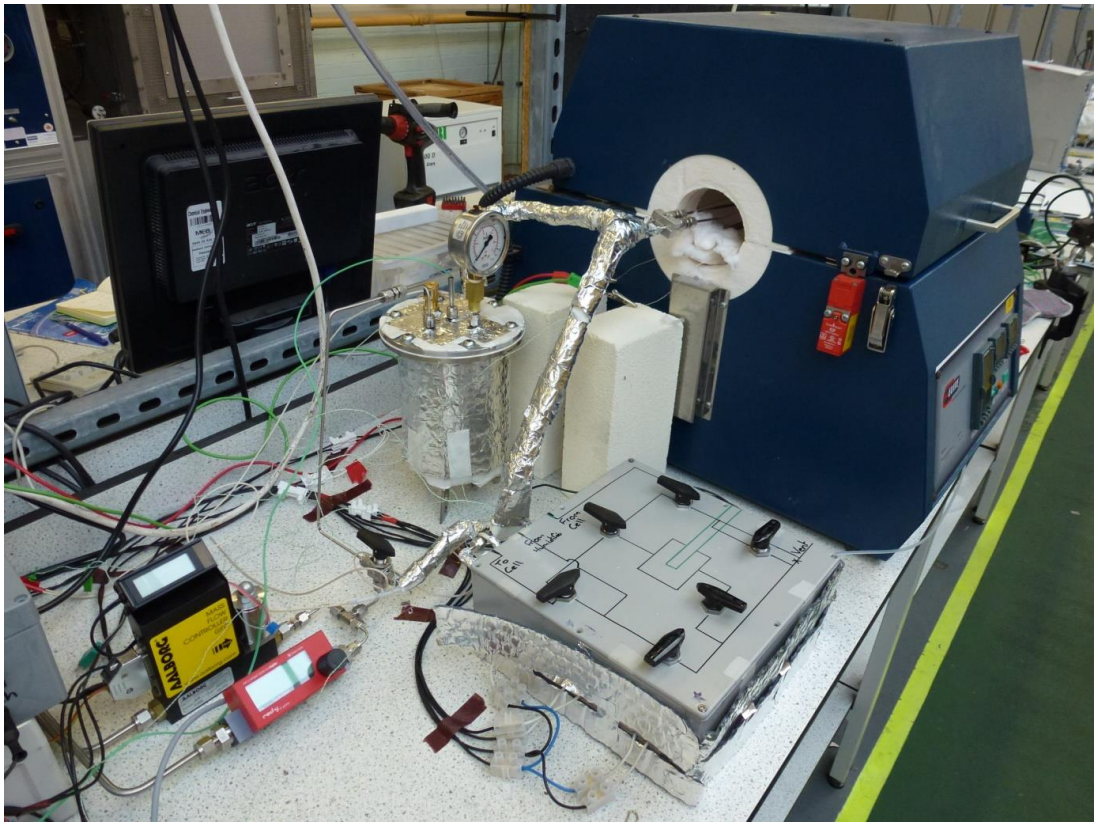

**Figure 17: Test set up for the testing of microtubular cells. The gasses from mass controllers on the left pass through the humidifier. There is a humidity sensor. With probe mounted in a heated box, which is used to measure the quantity of water in the gas stream.**

Figure 19 shows the effect of increasing water bath temperature on the performance of cells operated at constant current. The electrolysis performance is reasonably stable until a water bath temperature of 70$^{o}$C is reached at which point condensation causes large instability in the cell performance.

Figure 20 shows the calibration of the Mk1 test set up. The maximum mixing ratio is 0.24 $m^3/m^3$ ($H_2O_{(g)}$/air) with a maximum stable relative humidity (with a water bath temperature of 60$^{o}$C) of 15%RH. Attempts were made to increase the stability of the gas stream through increased insulation and temperature of the heated pipes however this made no difference to the stability of the water in the gas stream.

Initial experiments were performed using this test stand on microtubular cells, however the decision was made to redesign the test stand with a different humidity generator to enable a greater level of humidity and an increased control over the humidity generated. Running in electrolysis operation with 15%RH is non ideal and would severely limit the work which could be performed.

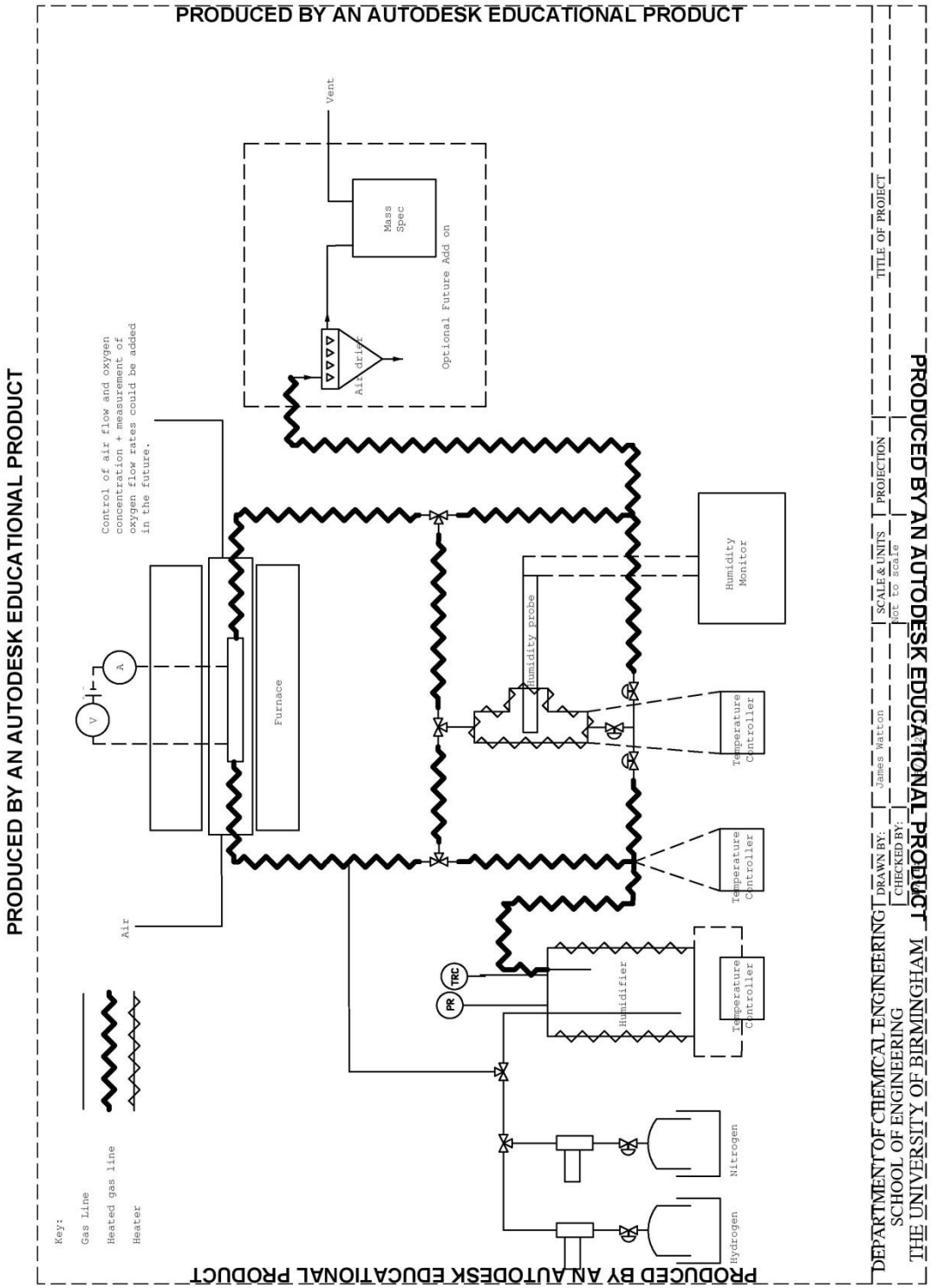


**Figure 18: Schematic of the experimental test setup for microtubular cell testing.**

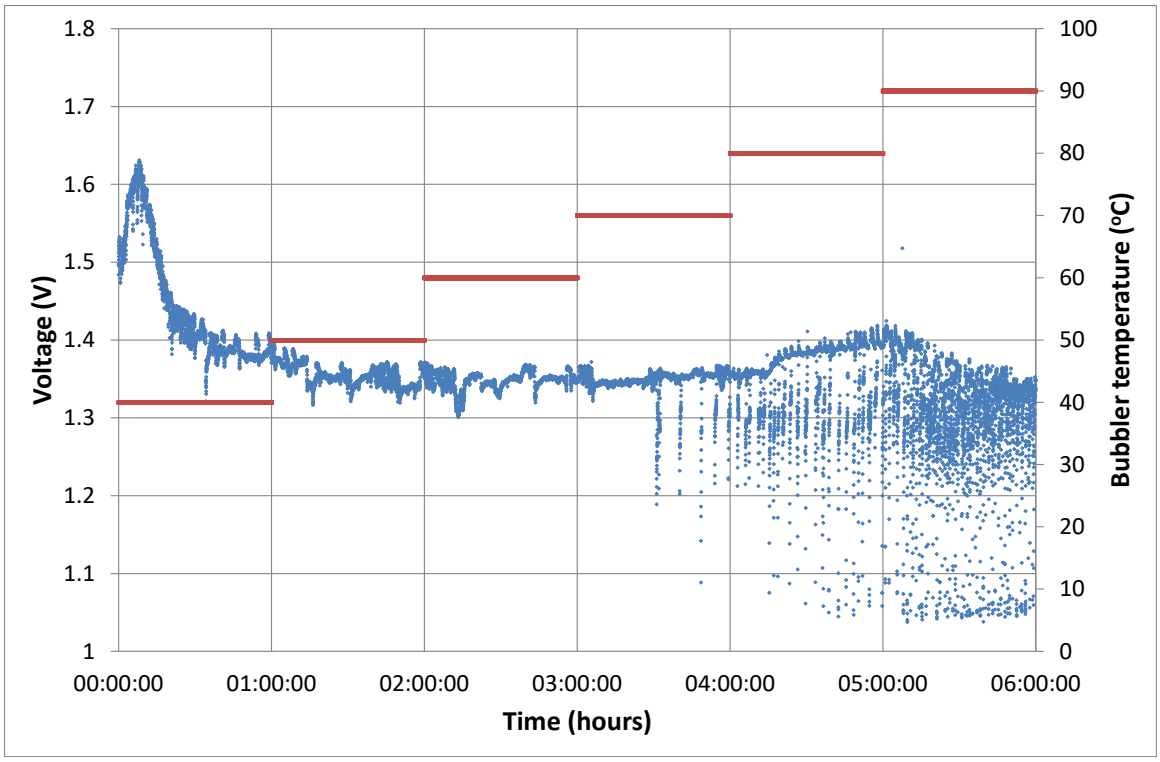


**Figure 19: Effect of water bath temperature on the stability of fuel cell measurements. Experiment performed a constant current of −0.377 A cm$^{-2}$. Temperature of water bath increased every hour by 10°C with the increase started at the beginning of the hour and taking 10−20 mins. The voltage at the start of the 40°C period was very high due to insufficient water in the cell, which decreased rapidly as the water bath heated up. The blue line indicated the cell voltage and the red line shows the cell current.**

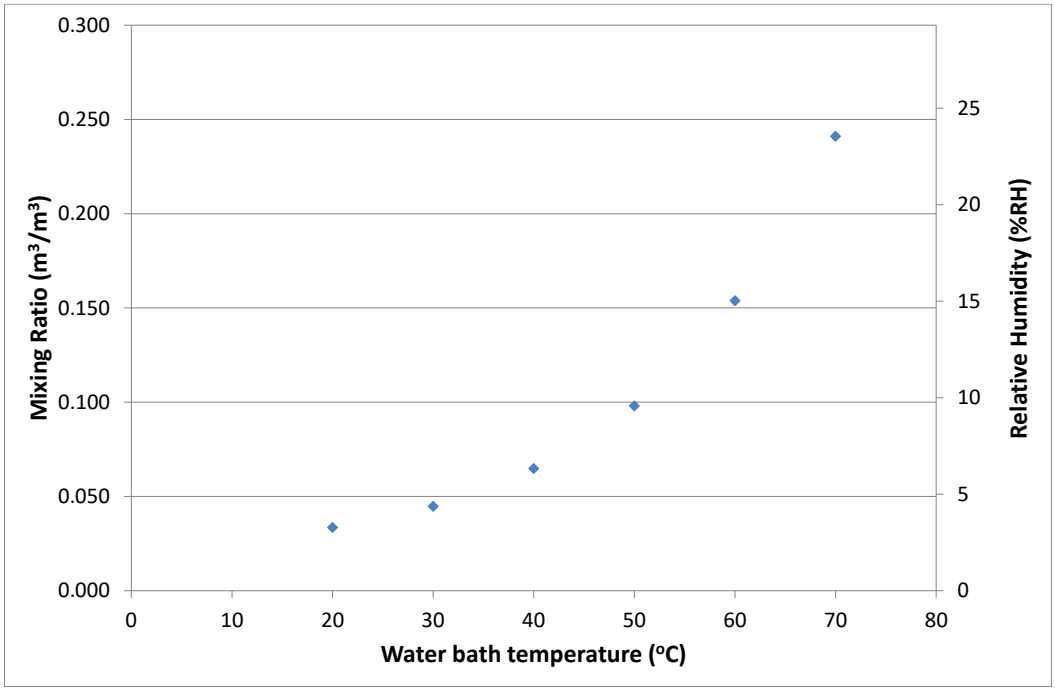


**Figure 20: Graph showing the mixing ratio and relative humidity against the water bath temperature for the Mk1 test set−up. This shows that the maximum stable achievable gas mixture using this setup is ~15%.**

### 4.2.2 Planar

For testing of planar cells, which comprises the majority of the work in this thesis, the test set−up was redesigned to house planar cells and increase the rage of humidities achievable. The gas supply to the hydrogen electrode was controlled using the system shown in Figure 21. Gasses were controlled by mass flow controllers (Aalborg GFCS). Steam was added to the gas stream using a controlled evaporator mixer (CEM) produced by Bronkhorst, this comprised a heated compartment with a water to allow liquid water in and a liquid water mass flow controller. The CEM allows a fine control of the water added to the gas stream and finer control over the flow rate than was possible using the Mk1 bubbler humidifier. After the CEM all gas lines were insulated and heated with line heaters to prevent steam condensation. A disadvantage of this set−up is that there was no humidity sensor which prevented the measurement of the outlet humidity and a verification of the measured cell efficiency.

### 4.2.3 Gas delivery and cell sealing

When operating the microtubular cells gas delivery and sealing the cells was simple, the cells were placed onto an Inconel (Inconel 600, Alloyshop.com) pipe to prevent corrosion of stainless steel. The end of the Inconel tube which had been machined to give a tight fit to the tube and a small amount of sealing agent used to seal the remainder (Ceramabond, 552) (Figure 22). This provided a reliable method of sealing the cell, however, the cell was likely to break during removal and reusing the cell was difficult.


**Figure 21: Test set−up Mk2. This was used for the testing of planar button cells and comprised mass flow controllers and a controlled evaporator mixer (CEM – Bronkhorst) unit for humidification of the gas stream.**

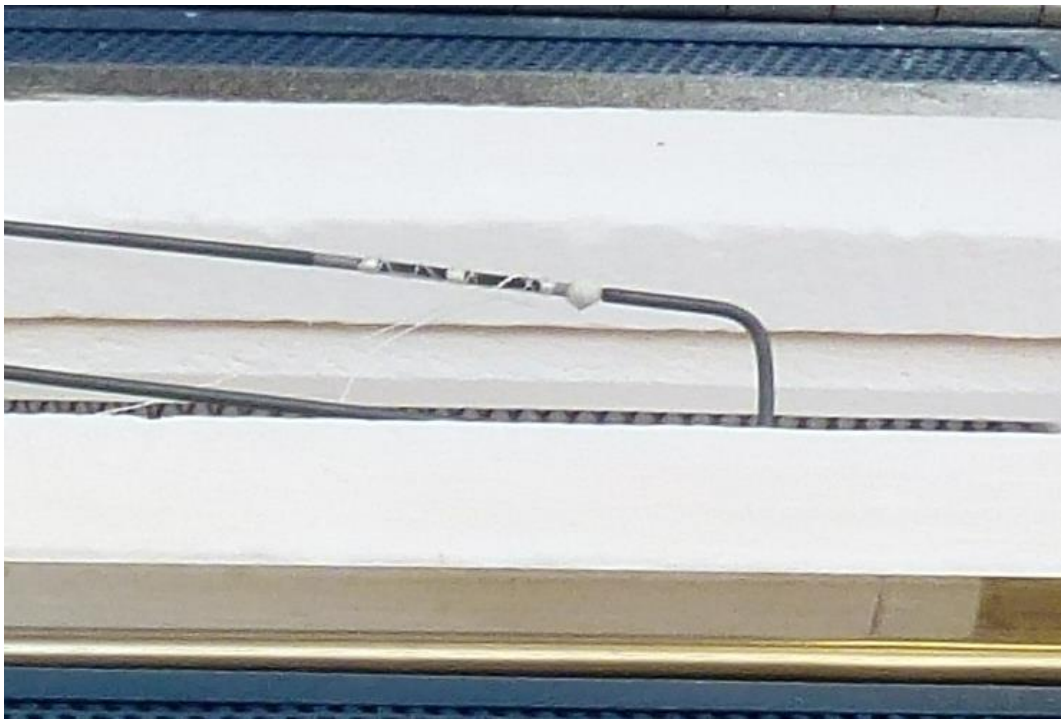

**Figure 22: The sealing of microtubular cells to Inconel feed and outlet pipes, ceramic seals formed of ceramabond.**

The sealing of planar cells presents greater problems, a number of techniques were used to provide a good seal. In this work Alumina tubes were used as the feed tubes onto which the cell was mounted. The first technique used involved the use of ceramabond to adhere the cell to the end of the tube. This technique is shown in Figure 24, for the oxygen electrode interconnections the cell had silver wires (99.9% purity, Scientific Wires) attached to the cell using silver ink (SPI 05002−AB). The silver ink was also used to paint a current collection pattern to the surface (Figure 24). For the hydrogen electrode the cell was placed onto a Ni mesh (Hart materials). This technique proved problematic as the cells once attached to the tube were very hard to remove and the cells broke during removal, the tubes also became damaged very quickly due to the removal of the ceramic adhesive. The ceramabond also caused issues with the cell cracking during cell heat up. This was due to the contraction of ceramabond during the furnace heating leading to cracking of the cell. Therefore a new cell sealing system was developed. This used a gasket made of Thermiculite 866 (Flexitallic) 1mm thickness as a sealing gasket between the cell and the alumina tube. This was chosen because it is a gasket material which was easy to cut using a sharp blade, Thermiculite is also slightly flexible and compressible which means it is possible to have wires protruding between the cell and the gasket and achieve a reasonable seal. For Thermiculite to provide a seal it needs to be held under compression therefore the test stand was redesigned to allow the cell to be compressed between two alumina tubes, as shown in Figure 25.

The current collector for the oxygen electrode (Figure 26) was a gold mesh (Gold M_Grid$^{tm}$, Fiaxell), which was soldered to two silver wires (0.71mm diameter 99.99% silver, Scientific wire company). These acted as current collection and voltage sensing wires. The hydrogen electrode (Figure 27) had a silver mesh with two silver wires (0.71mm diameter 99.99% silver, Scientific wire company) acting as current collection and voltage sense wires. Figure

28 shows an example of a cross section of a polished planar cell used in this work. The hydrogen electrode is Ni/YSZ ~500µm thick; the electrolyte is YSZ 9–10 µm thick; the oxygen electrode is LSM/YSZ 40µm thick; the oxygen electrode current collection layer LSM 10–50 µm thick.


**Figure 23: Compression housing for planar cells. The tubes which house the cell are spring loaded to apply pressure to the cell gasket.**

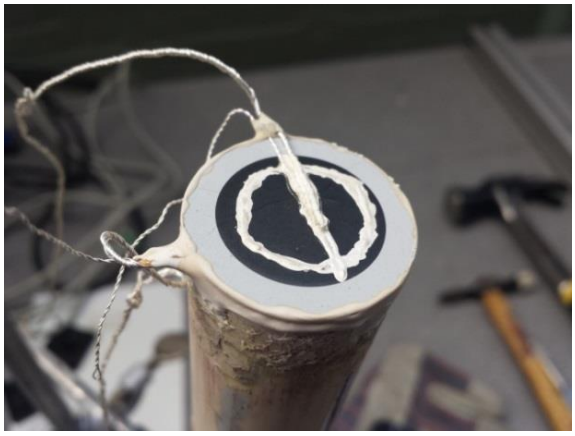

**Figure 24: Button cell attached to tube holder with ceramabond. The white paste is a silver ink used for contacting, the hydrogen electrode contacting was performed using a nickel mesh. This design led to cell cracking due to ceramabond shrinkage.**

**Figure 25: Cell placed within a compression setup. Cell is placed within two Thermiculite gaskets with anode and cathode connections between the cell and the gasket.**

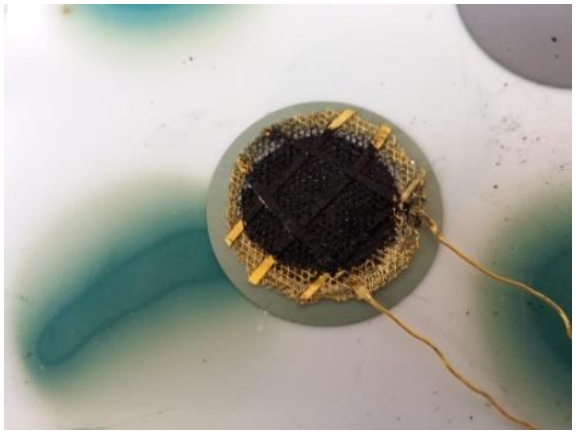

**Figure 26: Oxygen electrode current collector M_Grid gold mesh (Fiaxell). The two gold wires were welded to silver wires for current collection.**

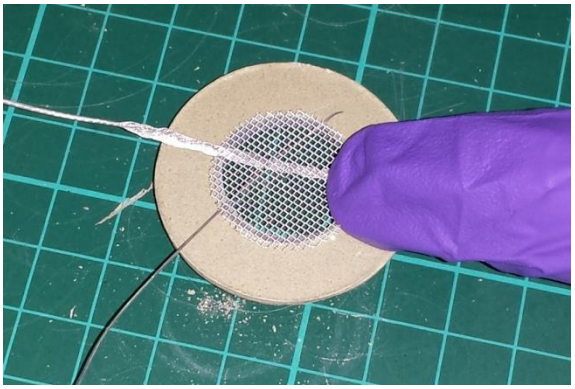

**Figure 27: Hydrogen electrode current collector, silver mesh with silver wires attached.**

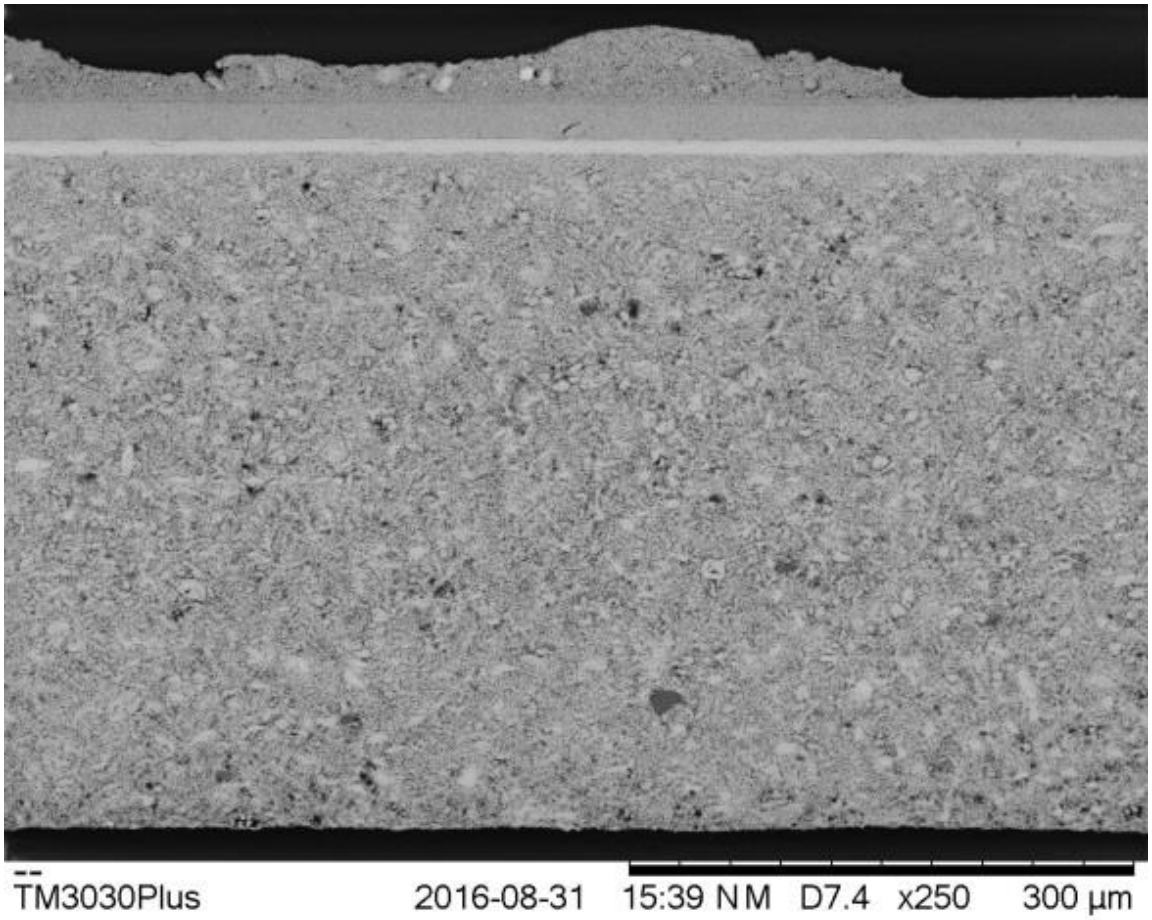


**Figure 28: SEM of cell cross section after polishing. The layers from bottom to top are; hydrogen electrode (Ni/YSZ) ~500µm; electrolyte (YSZ) 9 – 10 µm; oxygen electrode (LSM/YSZ) 40µm; and current collection layer (LSM) 10−50 µm.**

## 4.3 Electrochemical testing

In this work all electrochemical testing was recorded and controlled using a potentiostat (Model 1470E, Solatron). This was connected to a frequency response analyser (1455 FRA, Solatron) for impedance measurements.

### 4.3.1 Polarisation curve

Basic cell performance was evaluated by recording a polarisation curve (IV curve). Unless otherwise stated, the IV curve was performed as a stair−step with a 25mV step and a stair (duration) of 30s. The duration of 30s was found to be ample for the cells to reach a steady

state. Before the addition of water to the gas stream the IV curve was performed in the following order: OCV →0.4V→OCV. After the addition of water to the gas stream the IV curve was performed in both fuel cell and electrolysis operation in the following order OCV →0.4V→OCV→1.6V→OCV.

The IV curve provides information on the resistance of the cell and shows the current at various voltages. The IV curve is a very useful way of comparing the performance of different cells and gives some indication of the main losses in the cell. However, this information is limited. An example IV curve for fuel cell and electrolysis is shown in Figure 29. The IV curve shows the size of the activation overpotential, the ohmic resistance and the mass transport overpotential of the cell. The high operating temperature of a SOFC results in very small activation energy and which results in an almost straight line from the OCV. The area specific resistance (ASR) of the cell can be calculated as the gradient of a linear region of the curve, outside the activation or concentration overpotential regions of the cell. Figure 30 shows an example IV curve using real data and the region of fuel cell and electrolysis data used to calculate the ASR of the cell.

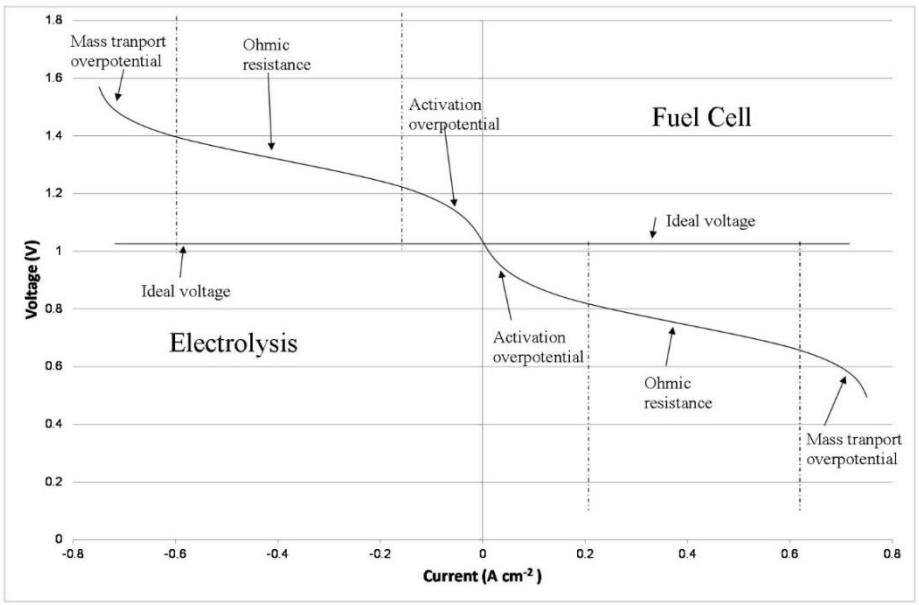


**Figure 29: Example IV curve showing expected losses observable for fuel cell and electrolysis operation.**

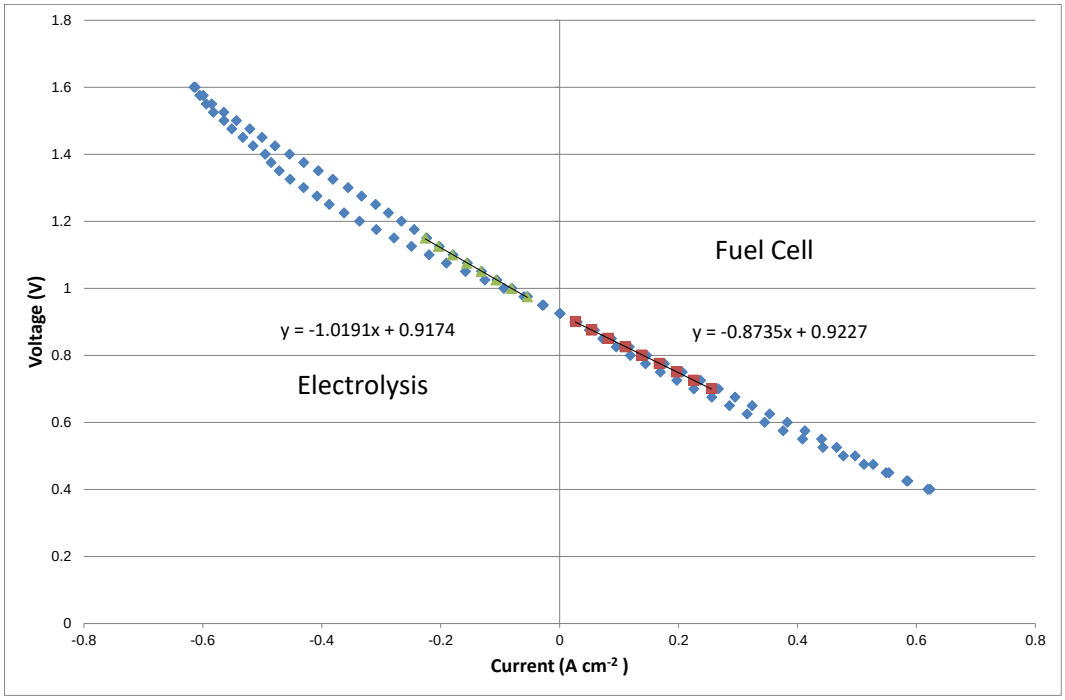


**Figure 30: Example IV curve using real data showing an example of the region used to calculate cell ASR, the ASR is slightly higher in electrolysis operation than fuel cell operation. The cell shows no discernible activation overpotential for electrolysis or fuel cell operation. There are very slight mass transport losses visible in the electrolysis data but none in the fuel cell data. The experiment was performed at 800ºC with a 50:50 $H_2O$:$H_2$ mixture.**

### 4.3.2 Electrochemical Impedance Spectroscopy

The use of IV curves provides limited information about the losses in the cell and the only measurement which can be made is the cell ASR. Electrochemical impedance spectroscopy (EIS) is commonly used as a diagnostic tool for SOE cells [44,158–161]. A review of EIS for solid oxide electrolysis is provided by Nachache, Cassir and Ringuede [159]. In this work EIS was performed in an attempt to quantify the different losses associated with the cell. EIS allows the separation of processes which occur at different timescales. There are four main processes which lead to losses in a fuel cell, these are ohmic resistance, activation overpotential, charge transfer overpotentials, and mass transport overpotentials.

Unless otherwise stated the following settings were used for the EIS measurements. Measurements were made between 100,000 Hz and 0.1 Hz as a logarithmic frequency sweep with 10 steps per decade. The EIS was voltage controlled with an applied potential of −0.1V (fuel cell) or 0.1V (electrolysis) against the cell OCV. An AC amplitude of 10mV was applied to the cell. An automatic averaging was performed with duration of 1 second.

#### 4.3.2.1 Equivalent Circuit fitting

For further analysis of the EIS spectra an equivalent circuit has been used to equate the various features observed in the impedance spectra to components of an electrical circuit. The equivalent circuit used in this work is shown in Figure 31. As the system doesn't perform in an ideal way the capacitor usually used in the resistor−capacitor (RC) element has been replaced with a constant phase element (CPE). Figure 31 is shown with an inductor ($L_1$). If there is no inductance observed in the impedance spectra, then this is omitted for the equivalent circuit fitting.

The resistor ($R_{ohm}$) represents the purely ohmic resistances in the cell such as the resistance of ion or electron movement through the cell, these processes do not store charge and have no time dependence. The high frequency and low frequency R−CPE elements represent the resistances which are time dependant. The high frequency region is commonly ascribed to charge transfer processes while the low frequency domain is commonly attributed to mass transfer processes [159,162].

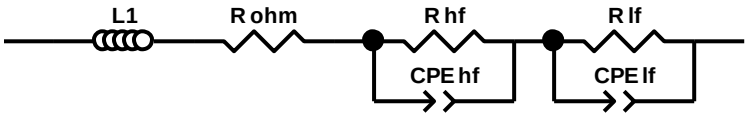


**Figure 31: Equivalent circuit model, capacitors have been changed to constant phase elements. $L_1$ − induction, $R_{ohm}$ − ohmic resistance, $R_{hf}$ – high frequency resistance, $CPE_{hf}$ – high frequency capacitance, $R_{lf}$ – low frequency resistance, $CPE_{lf}$ – low frequency capacitance.**

The majority of the fitting work was performed using the equivalent circuit shown above. There were some impedance spectra which showed very large disturbance in the low frequency region of the impedance. This made fitting an equivalent circuit with two RC elements impossible. Therefore, an equivalent circuit with only the high frequency RC element was used as shown in Figure 32. It will be made clear in the text where this is used instead of the circuit in Figure 31. Again the inductor $L_1$ was omitted if the impedance showed no inductance.

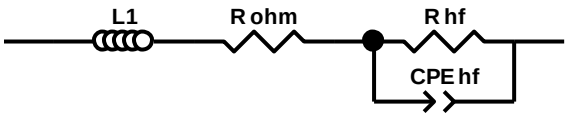


**Figure 32: Equivalent circuit used if the impedance at low frequency is too scattered to be modelled.**

## 4.4 Structural investigation

The structural change of the fuel cells was investigated by optical and SEM microscopy. This was either performed on the surface of the cells, on a fracture cross section, or on a polished cross section.

### 4.4.1 Polished cross sections

To investigate the structure of the fuel cells cross sections of the fuel cell were cut using a diamond wheel. After being washed in distilled water and dried the cross sections were mounted in a resin and polished. The mounting was performed in a Buehler Cast N' Vac. The samples were introduced in to the vacuum chamber, a vacuum of −0.8 bar was applied for 2 minutes before the resin (Epo thin, Buehler) was added slowly. After a further 5 minutes to remove any further air bubbles the samples were removed from the vacuum and allowed to set overnight.

The mounted cross sections were polished to reveal a representative cross section of the bulk of the cell. The following polishing procedure was used. Diamond grinding discs (125 μm followed by 75 μm and 45 μm) were used to remove excess resin and cut past any damage created by the cutting wheel. The cell was then polished initially using 15 μm, 9 μm and 3 μm diamond suspension (MetaDi Supreme, Buehler) on TriDent cloths (Buehler) followed by 1μm and 0.05 μm diamond suspension on Microcloth (Buehler). After each stage of polishing the sample quality was checked under an optical microscope.

### 4.4.2 Optical microscopy

Optical Microscopy (Axio Lab A1, Zeiss) was performed on the samples. Images were obtained using Q−Imaging Micropublisher 3.3 (Photometrics) with Image Pro software

(Mediacy). Image analysis was also performed using the open source software packages Image J [163] and Fiji [164].

### 4.4.3 SEM

SEM imaging was performed using a tabletop SEM (TM3030Plus, Hitachi). The SEM was equipped with Energy Dispersive X−ray (EDX) detection (Quantax70, Bruker Nano GmbH). Further information on the SEM techniques used is provided in section 7.4.

# 5 Cell fabrication

## 5.1 Introduction

In this chapter the work performed on the fabrication of solid oxide cells will be described. The testing procedures and optimisation studies on the cell fabrication will also be detailed. A lot of the work on the fabrication of an anode substrate has been performed with the assistance of Nikkia McDonald and her thesis contains more information in some areas. The aim of this work was to produce solid oxide cells fully in−house. This would provide the group with the ability to change materials and cell configuration in the future. As a starting point in this work we were aiming to produce a conventional hydrogen electrode supported cell Ni/YSZ−YSZ−LSM/YSZ. This was produced using powder pressing to produce the anode support, and screen printing to apply the electrolyte. In this work we are aiming for an electrolyte 10−20 μm thick. The oxygen electrode was applied by brush painting with the aim to replace this technique with screen printing. However, curvature of the cells resulted in cracking of the cell when screen printing was attempted.

## 5.2 Hydrogen electrode substrate

### 5.2.1 Pellet fabrication

Solid oxide fuel cells were fabricated from powders by uniaxial pressing. Powders, NiO, YSZ, tapioca starch, and PVB binder were weighed in the desired ratios and mixed with ethanol to form a slurry. The slurry was ball milled for 12 hours with Zirconia milling media.

The resultant slurry was dried slowly. The powder was then ball milled again dry to break down large agglomerates and sieved through a sieve to produce a powder for pressing.

The powder was placed into a 40mm diameter die, which was gently shaken to level the powder. The follower was placed into the die and rotated to further level the powder. The die was pressed to 10 tons in a uniaxial press. The effect of die pressing pressure on the pellet is shown in Figure 33. Pressing of the pellet to < 10 tons resulted in a poor pellet structure. In Figure 33 pressing to 10 tons shows some flaking at the edges which is due to handling issues, this was not present on a freshly pressed pellet. Above 10 tons the flaking of the cell became worse but unfortunately no image was taken.

| | | | |
|---|---|---|---|
| 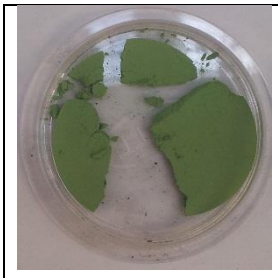 | 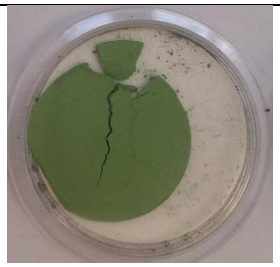 | 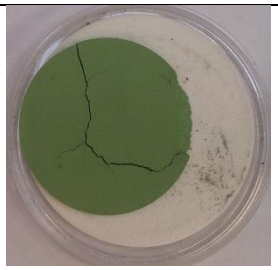 | 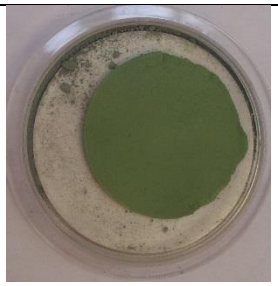 |
| 4 tons | 6 tons | 8 tons | 10 tons |

**Figure 33: Powder pressure testing to achieve good cell quality.**

## 5.2.2 Pellet firing

The pellet formed was subjected to a pre−firing as shown in the firing schedule below. The pre firing to 1200$^{o}$C was used to increase the strength of the pellet to enable easier handling and screen printing. The pre fired pellet is shown in Figure 35. During the pre−firing phase there is a significant shrinkage of the cell of 13−14%. There is also a colour change as the binder burns out leaving a green cell. The cell is heated slowly and there are two binder burn−out periods at 325$^{o}$C and 500$^{o}$C. The temperatures at which the different organic constituents were removed from the cell are shown in Figure 36, these were measured using

thermogravimetric analysis (TGA). 325ºC was chosen as a point after the removal of starch which is the major constituent which had to be removed and therefore would create the most gas and most likely cause damage to the cell as it was burnt off. 500ºC was chosen as it is beyond the burn off temperature of all the carbon which had to be removed and ensured that there was no more burn−out occurring before the rest of the heating cycle occurred.

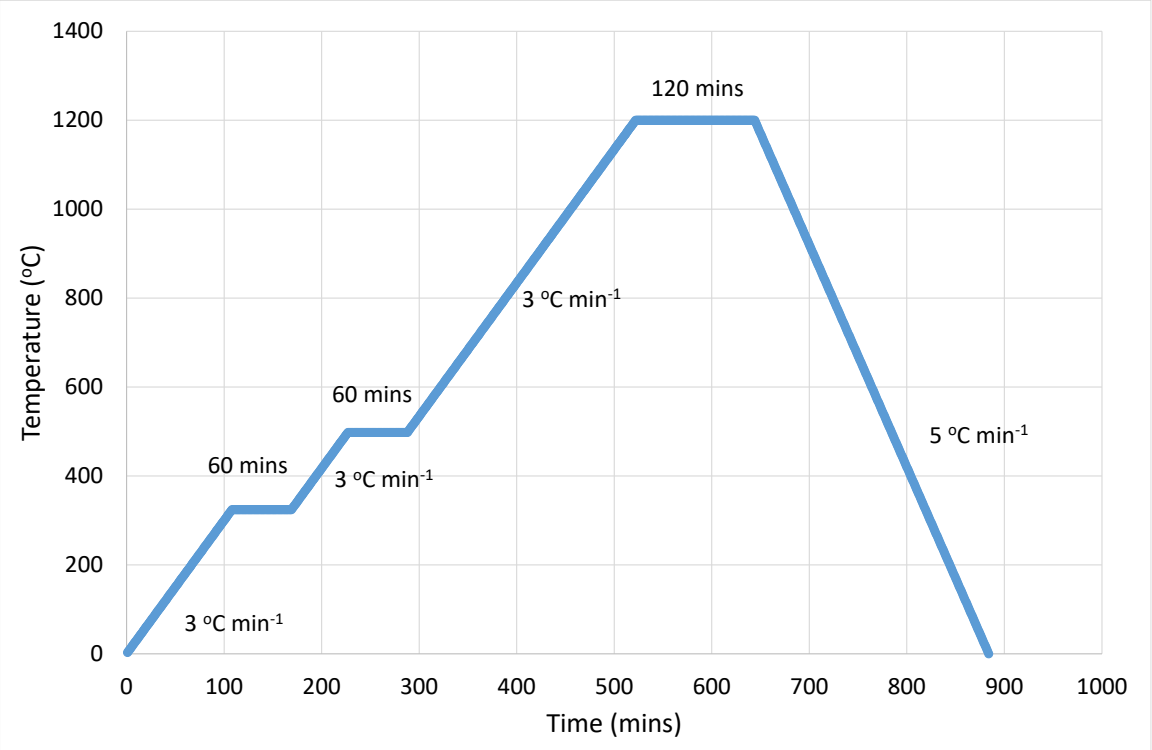


**Figure 34: Anode support pre fire firing schedule**

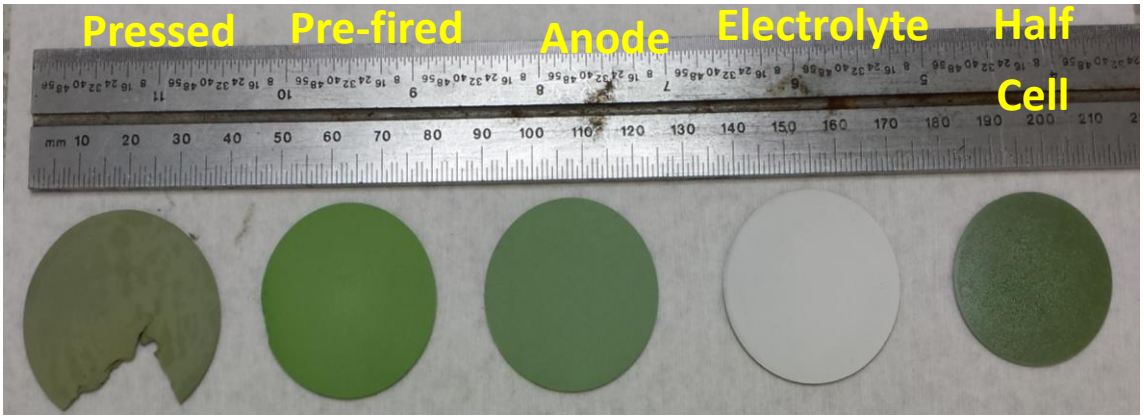


**Figure 35: Images of the cell during the fabrication steps to produce a half cell.**

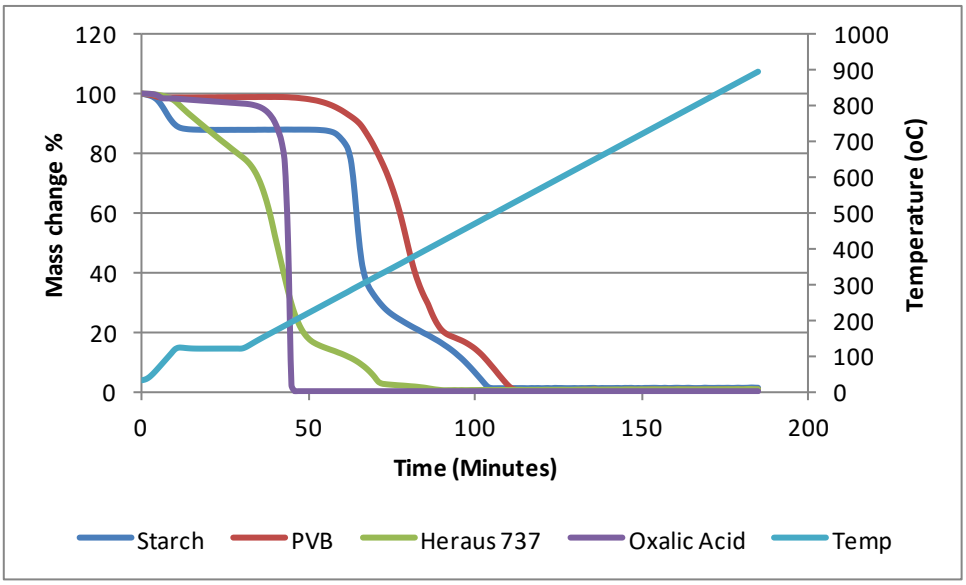


**Figure 36: Burn out temperatures for organic constituents of the pressed cell measured by TGA.**

## 5.3 Screen printing:

### 5.3.1 Paste preparation

Paste for screen printing was prepared by mixing powders (YSZ, NiO, LSM on their own or as a combination) with a vehicle (Heraus 737V). The ingredients were initially roughly mixed by stirring then homogenised using a three roll mill (Exact, 50I). The viscosity of the pastes was measured using a rheometer and these are shown in Figure 37. The loading was calculated as a volume % of the solids in the vehicle. The rheometry data was collected using a TA instruments AR−G2 Rheometer. As expected, the solids increased the viscosity of the resulting mixture. The highest possible solids loading was desired as a high solids loading reduced the amount of vehicle which needed to be removed. It also increased the particle packing in the electrolyte layer which increases the likelihood of a gas tight layer forming. However, there was a limit on the viscosity of the ink which could be printed. If the loading is too high the paste becomes difficult to print and there is an increased likelihood of the pellet sticking to the screen while printing. This reduces the print quality and a rough surface forms.

The cell can also break if it becomes attached to the screen. As described in 5.3.2 during the screen printing process the paste is pressed through a mesh. This results in a mesh pattern on the surface of the pellet. If the viscosity were too high the paste would not be able to flow to fill the pattern left by the mesh. This is demonstrated in Figure 38. With low solids loading there is an increased risk of pores forming through the electrolyte as the vehicle is burnt off.

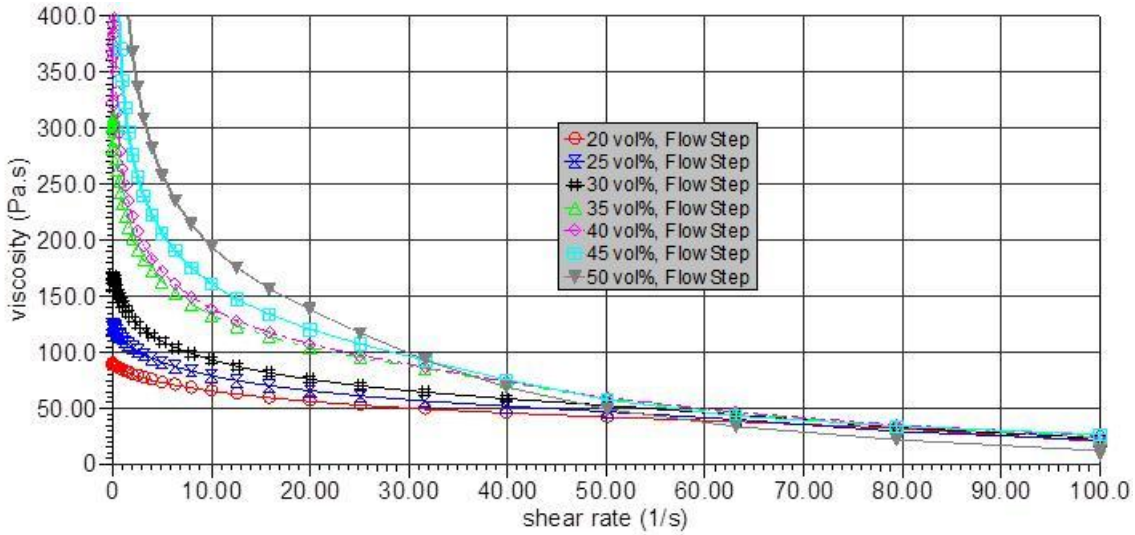


**Figure 37: Viscosity of electrolyte paste with a YSZ solids loading between 20 and 50 vol% in an organic vehicle.**

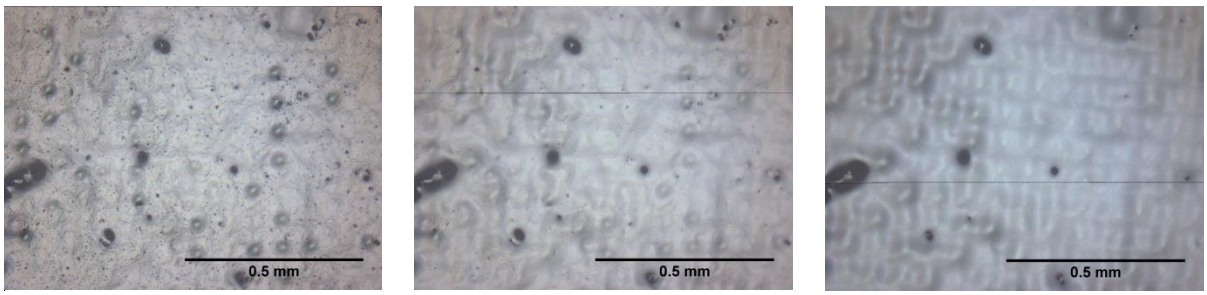


**0 secs** **5 mins** **10 mins**

**Figure 38: Air drying of a screen printed electrolyte layer at 0, 5 and 10mins., paste used 40 vol% YSZ in vehicle. After printing the paste spreads to fill small gaps in the surface. This isn't an example of a perfect print quality as there are large holes in the surface however the spreading of the paste is demonstrated.**

## 5.3.2 Screen printing process:

Screen printing was performed using a DEK 248 screen printer equipped with a 125 micron stainless steel mesh (DEK). Samples were printed once then rotated by 90$^{o}$ and printed again to form one layer. Subsequent layers were applied after the previous layer had undergone a

drying procedure. Before printing each layer the surface of the cell was cleaned and dust/loose particles removed using an antistatic roller and compressed gas. The schematic of a screen printer is shown in Figure 39. During screen printing a paste is placed onto a screen and the majority of the screen is blocked off with an emulsion giving control of the area onto which the paste is applied. The substrate to be printed on is placed below the screen and held in place using a vacuum from below. The squeegee pressed down onto the screen forces the paste through the open parts of the screen. This leaves behind a paste on the substrate the thickness of which is determined by a large range of parameters, including but not limited to: mesh size, emulsion thickness, paste viscosity, squeegee; pressure, speed, angle; and screen gap. The mesh size and emulsion thickness were fixed. As the loading for the paste was altered the experimental factors based on the machine (speed, pressure applied and gap between screen and substrate) were systematically adjusted to provide a good print quality for the paste loading. A good quality print was one which was evenly spread across the surface of the pellet with no visible marks on the surface.

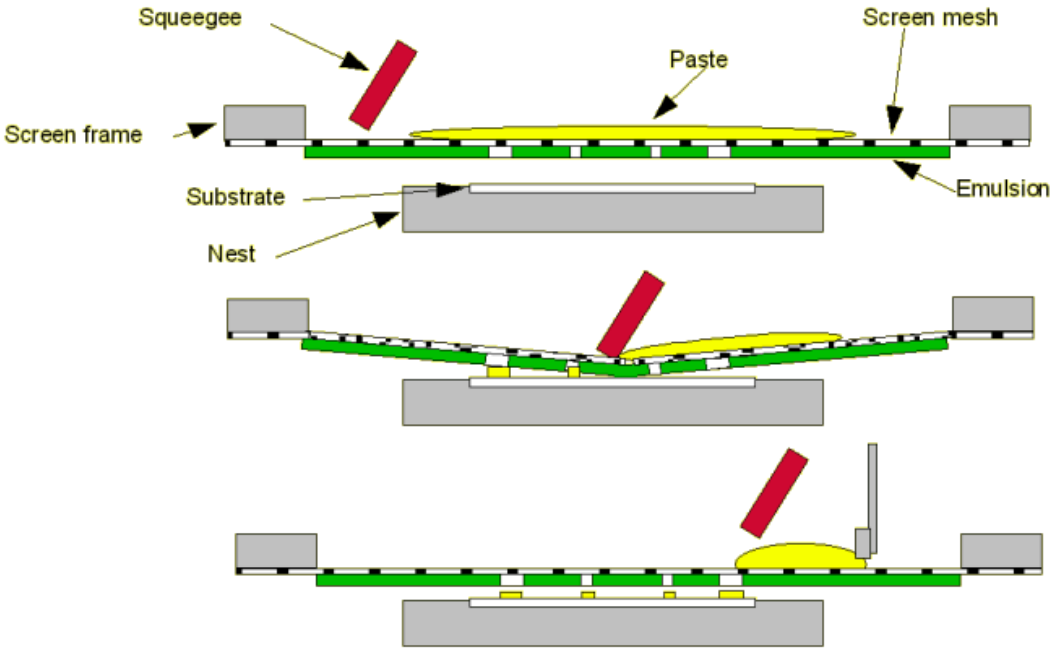


**Figure 39: Schematic of the screen printing process taken from A. Hobby [165] without permission.**

### 5.3.3 Optimisation of printed layers:

There were a number of layers printed onto the cell. Onto the pre fired pellet surface 1 to 3 anode active layers were printed. These layers served a multiple purposes; They acted as a layer with increased YSZ loading to provide a better interface between the electrolyte and the anode for both oxide ion conduction and a closer match of thermal expansion coefficient between the anode and electrolyte. A mismatch in thermal expansion coefficient results in a significant mechanical strain being placed on the cell.

The drying of screen printed layers was found to make a difference to the quality of the printed surface. While a dry surface was required before the next layer could be applied the rate of drying had to be minimised to achieve a uniform layer, and to prevent the boiling of vehicle creating pores through the electrolyte. It was decided that a temperature controlled drying step would be too time intensive and it was found that drying at room temperature for 20 minutes before oven drying at 80$^{o}$C for 40 mins achieved a suitable surface for further layers to be printed. Attempting to dry the surface faster at higher temperatures was found to

create pores in the surface. It was found that a number of thin layers was required to create a suitably thick electrolyte layer. As shown in Figure 40 each subsequent layer resulted in a better surface quality with less marking seen on each layer. The marking observed in the images of 1 layer and 2 layers, Figure 40, is thought to arise from the surface quality of the anode pellet.

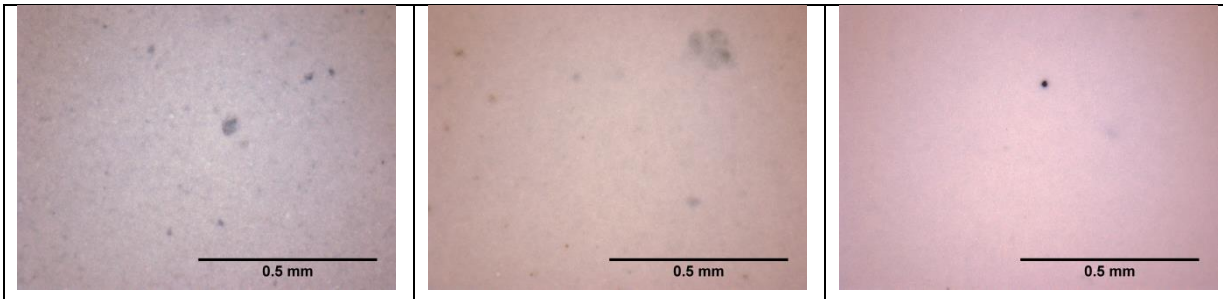


| 1 layer | 2 layers | 3 layers |
|---|---|---|

**Figure 40: Images showing the surface of the electrolyte at 10x magnification with different numbers of air dried electrolyte layers.**

The electrolyte layer was fired according to the schedule shown in Figure 41. This consisted of a slow ramp rate to 1400ºC. During this firing period the cell was held at 325ºC and 500ºC to allow the burn−off of organics.

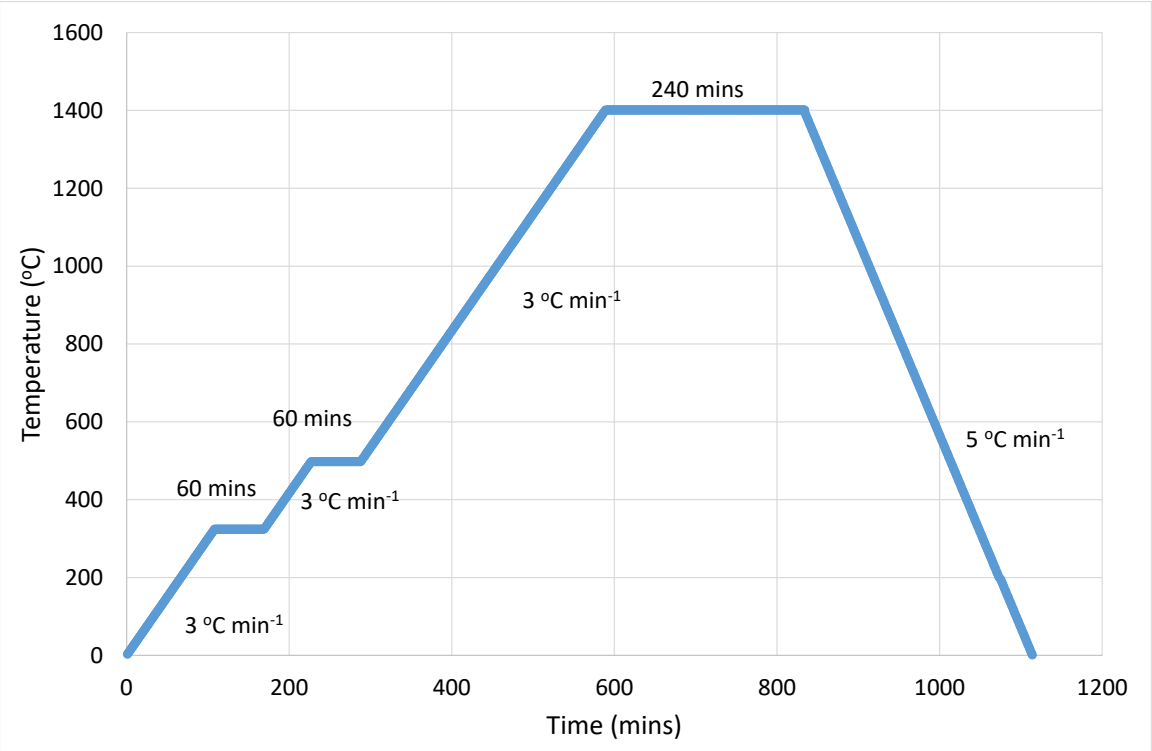


**Figure 41: Shows the firing schedule used for co sintering the hydrogen electrode and electrolyte. Temperature increases at 3°C min$^{-1}$ to 1400°C with a 60-minute hold period at 320 and 500°C. Cell was held at 1400°C for 4 hours. Cooling was performed at 5°C min$^{-1}$ but limited to the cooling rate of the furnace.**

## 5.4 Leak testing – Pressure drop measurement

A quick method was required to test the quality of the electrolyte to decide whether or not it was worth applying an oxygen electrode to the cell. An ethanol drop test was used to perform a very rough quality check on the electrolyte by dropping ethanol onto the surface of the electrolyte. A reasonable electrolyte should show no signs of the ethanol soaking into the electrolyte. This was a reasonable initial test, however, a more rigorous test was later established to determine the layer quality. Therefore, a simple test set up to perform pressure drop measurements was made, schematic shown in Figure 42. The sample to be tested is placed with the electrolyte down onto a rubber gasket to form a seal at the edges of the electrolyte, a vacuum pump was used to reduce the pressure behind the sample to −1 atm. The time taken for the vacuum to reduce by 0.8 atm was measured, if this took more than an hour

the pressure drop within the hour was measured. The gas tightness of the system was verified using a piece of plastic which showed no pressure drop over 2 hours. Using the vacuum pump available the starting vacuum was −0.9 bar and the end vacuum was dependant on the quality of the electrolyte. A very poor electrolyte may lose its vacuum within a minute. A good electrolyte would fall to −0.8 bar in ~ 2 hours. The leak rate is calculated from Equation 24 [166] normalised to the area of the test sample:

$$\frac{\Delta P}{V} = \frac{P_1 - P_2}{tA} \qquad \textit{Equation 24}$$

**Where:**
**ΔP = Pressure change**
**V= volume of test sample**
**P1 = initial pressure**
**P2 = final pressure**
**t = time**
**A = leakage area**

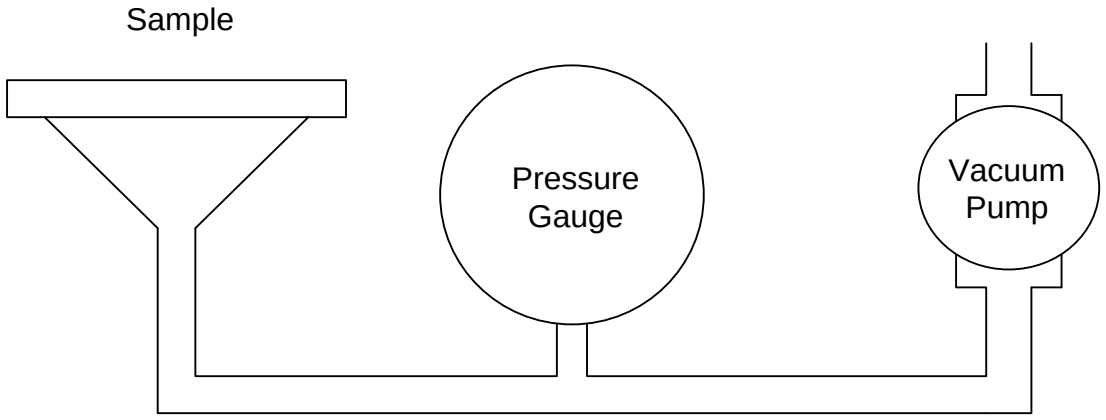


**Figure 42: Leak testing experimental set−up.**

The volume of the system is unknown however should be constant for each experiment. The area is defined by the area within the rubber ring which was 2.5cm$^2$. The pressure gauge used was not a high resolution device therefore a large pressure differential was used to allow the most accurate reading. Depending on the quality of the electrolyte either a pressure drop from −0.9 to −0.2 atm or the amount the pressure dropped in 1−2 hours was used as indicator. The

rubber ring reduces the available area of the cell for testing. If a pinhole is under the rubber ring the cell would appear reasonable via this test. It is therefore possible to have a pin−hole which reduces the cell OCV but still shows a good pressure drop result.

The leak rate against OVC measurement is shown in Figure 43. There is generally a correlation between OCV and leak rate, plotting this shows that a minimum value of $5x10^{-4}$ $Nm^3$ hPa $sec^{-1}$ $cm^{-2}$ is required before a cell achieves a good OCV, however this still doesn't ensure a good OCV is achieved. Any cells which don't meet this criterion would not be used for further testing. However, this is not a guarantee of a good OCV as several cells meet the criteria and show poor OCV.

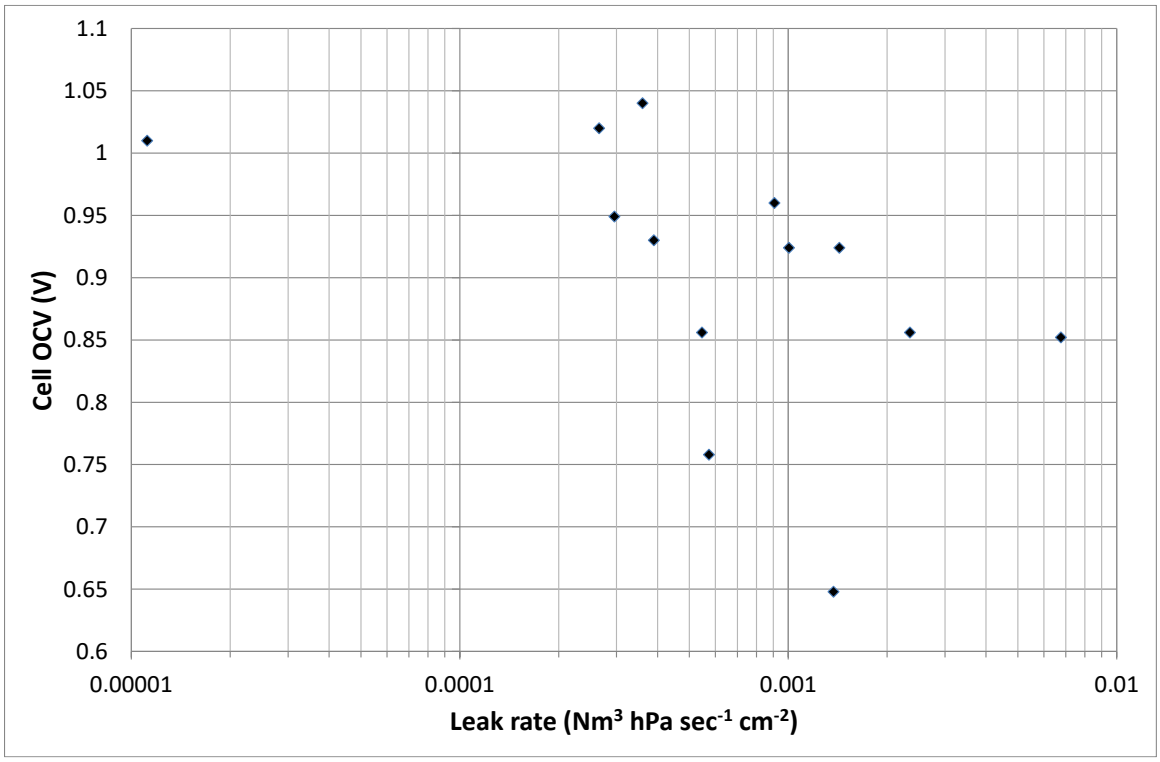


**Figure 43: Graph showing the cell OCV vs leak rate measured by the pressure drop leak testing method.**

If a cell passes the leak rate test and a good initial OCV is found a pinhole in the surface can rapidly cause the degradation of the cell. Figure 44 shows the OCV during heating of a homemade cell. This cell shows a reasonable OCV of 0.96V at 530°C. However after this the cell OCV becomes unstable and degrades rapidly with a final OCV of 0.87V. The degradation

of the cell is thought to be due to a pin−hole which expands during heat up and leads to a worsening of the cell OCV.

The use of gas leakage testing is a useful first step in quality control of the cells. However, a good gas leakage result is not a guarantee of a successful cell.

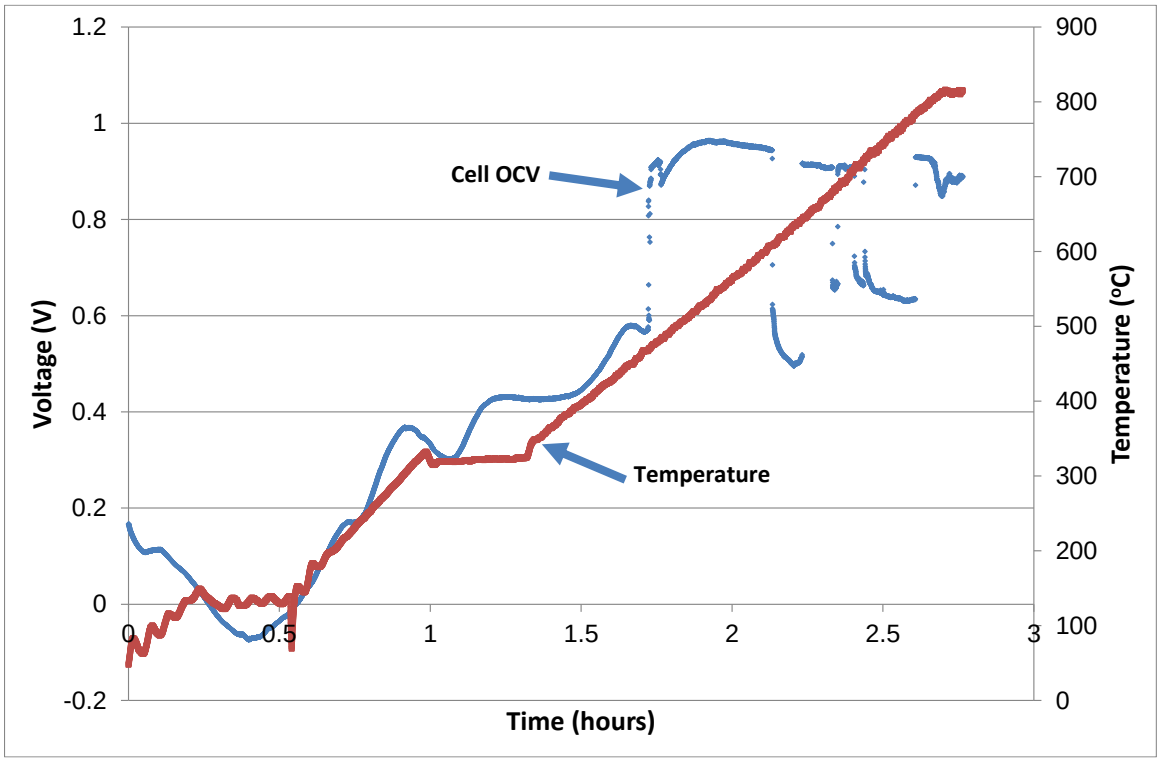


**Figure 44: Cell degradation during heat up the red line shows the temperature measured at the cell, the blue line shows the cell OCV. The cell was heated at 5°C min$^{-1}$ with 60ml min $H_2$ and 120ml min $N_2$.**

### 5.4.1 Electrolyte thickness vs applied layers

The effect of the number of applied electrolyte layers on the electrolyte thickness was investigated. This was done to ensure that each electrolyte application resulted in an even layer and there was a linear increase in layer size with each application. Electrolyte thickness for two paste formulations was tested, one was 50 wt.% YSZ the other 40wt % YSZ. An anode pellet was prepared as described before. The cell was printed with different numbers of layers, with each layer dried as described earlier. The initial applied layer thickness was very

similar for the two cells, however, with a larger solid loading the electrolyte grows faster per layer applied. After three applied electrolyte layers the 40 vol% electrolyte reaches 20µm which is the maximum electrolyte thickness set as a requirement for this cell.

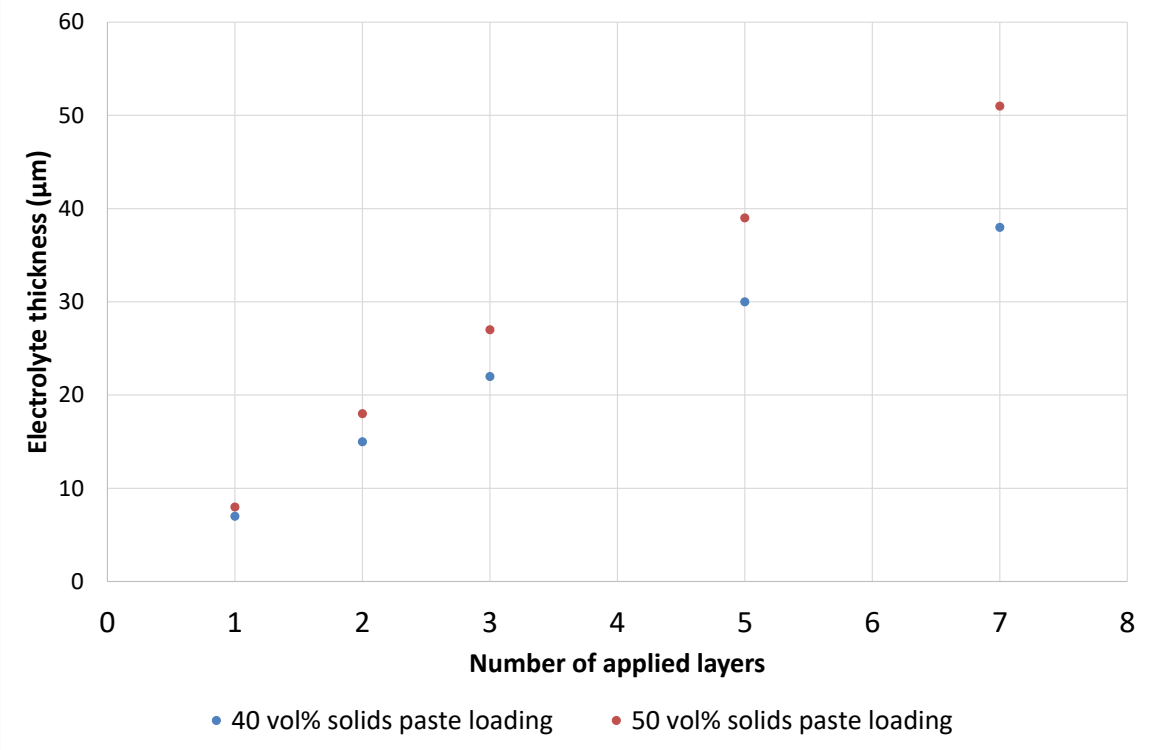


**Figure 45: Fired electrolyte thickness vs the number of layer applied for two paste loadings, 40 vol% solids and 50 vol% solids.**

## 5.4.2 Leak rate vs electrolyte paste loading

The effect of paste loading on the leak rate of the cell was investigated and the results are shown in Figure 46. In this work the cell had 1 anode functional layer added. There were then 3 electrolyte layers added and the effect on the air leakage rate investigated. The cells were fired using the standard regime described above. The leakage rate was heavily dependent on the paste solids loading. The results show a minimum value of 4.4 $Nm^3$ hPa $sec^{-1}$ $cm^{-2}$ for a cell with 35% volume loading of solid in the vehicle. The cells showed a greater cell leakage below and above 35 vol% solid loading. From this it was decided to use a 35 vol% paste loading for the rest of the experiments. The reason for a poor leakage rate below 35 vol% was

a lack of solid material on the cell surface. Above 35 vol% the print quality became poorer resulting in a greater cell leakage. Attempts were made to improve the print quality through variation of print parameters such as print speed, pressure and screen gap however an improved print quality was unsuccessful. There were also issues with cell breakage at 50 vol% solid loading in the paste due to adhesion between the screen and the pellet breaking the cell.

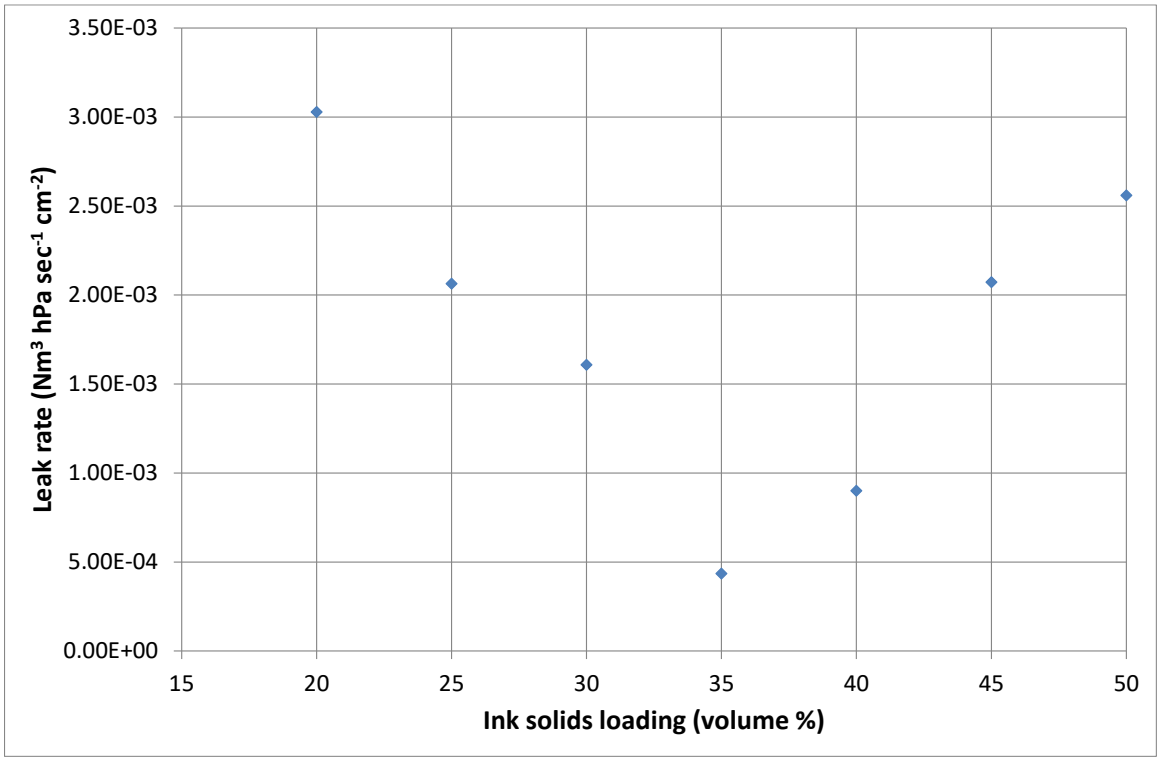


**Figure 46: Cell leakage rate measured from the pressure drop technique vs electrolyte paste solids loading. This shows that the optimal loading for the electrolyte ink is 35%.**

### 5.4.3 Leak rate vs electrolyte layers

In this test the number of layers required to produce a gas tight electrolyte was investigated. All cells were made in the same manner and visual checks to ensure integrity were performed. The cells had one anode functional layer applied after which the cells had electrolyte layers added. The solid loading in the electrolyte paste was 35 vol% in these experiments. Each

layer, as described above was printed twice with a 90° rotation after each print. The cells were dried in the standard manner. The cells were fired at the same time. The cells were then tested to investigate the air leak rate of the cells. The results are shown in Figure 47. They show that three layers are required to satisfy the minimum requirement for cell leakiness of $5x10^{-4}$ $Nm^3$ hPa $sec^{-1}$ $cm^{-2}$. There is no improvement of the cell with over 3 layers applied.

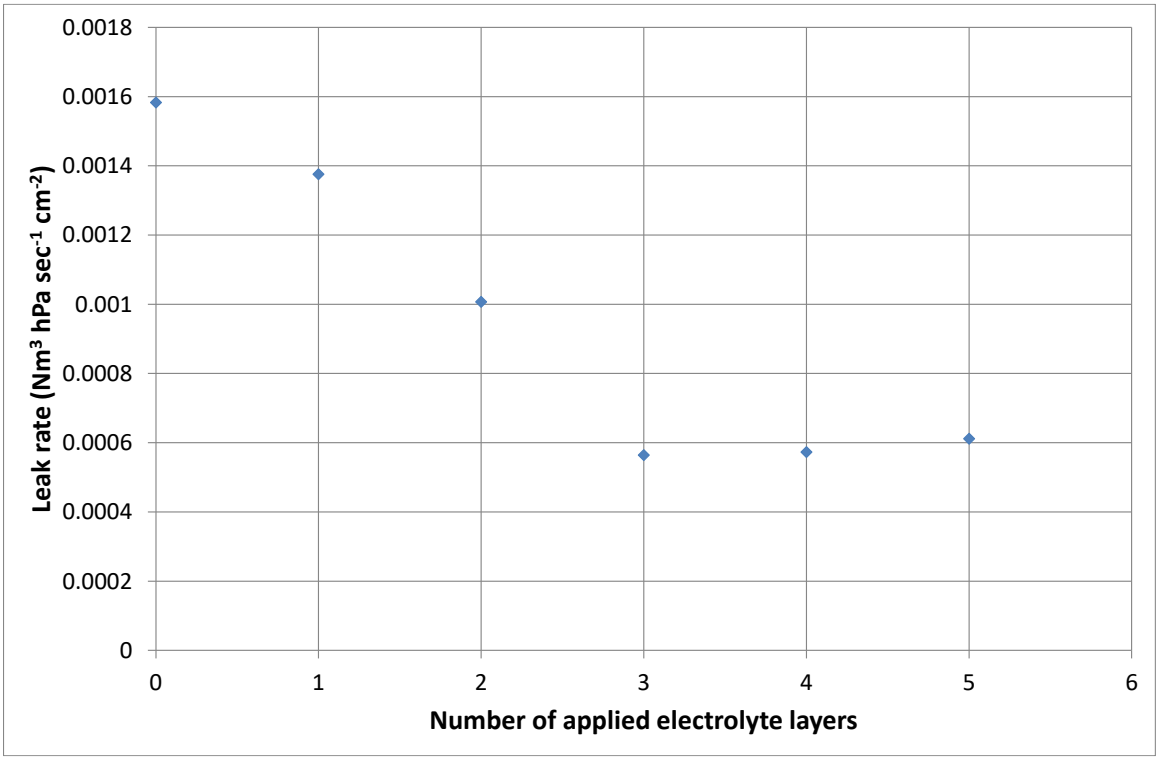


**Figure 47: Performance of cells under air leak testing with different numbers of electrolyte layers added, leak testing performed using the pressure drop leak testing method.**

### 5.4.4 Cell flattening:

During the electrolyte sintering step significant curvature of the cell was experienced. This presented severe problems with the tape casting steps. A weight could be placed on the cells to increase the cells flatness however this presented further problems with the cells cracking due to the extra strain in the cell caused by the restrictions on its movement. The electrolyte also suffered from the weight placed on top as some of the surface was transferred to the electrolyte surface. Experiments were performed on the flattening of the cells in an attempt to

create a flat surface. A cell was prepared with three electrolyte layers, the cell was then sintered and significant curvature was observed (Figure 48−A). The maximum cell thickness (including the curvature) was 2.4mm. The cell was then placed into a furnace, sandwiched between two alumina plates and a weight applied to the top (Figure 48−B). The cell was then heated successively to higher temperatures and the amount of flattening which occurred measured. The cell was heated at 5$^{o}$C min$^{-1}$ and the cell held at the target temperature for 2 hours. The cell was heated to temperatures between 900$^{o}$C and 1400$^{o}$C. The results are shown in Figure 49. Below 1200$^{o}$C there was no evidence of cell flattening; after 1200$^{o}$C there was evidence of flattening however the cell wasn't completely flat even after firing to 1400$^{o}$C. Figure 48−C shows the cell after the final flattening. There is a slight curvature which can be observed. Due to the time and difficulty required to undertake cell flattening and the non−ideal results obtained even after firing to 1400$^{o}$C it was decided that this would not be used as a further technique. Further work was undertaken in the prevention of the cell curvature and in the application of a weight during the electrolyte sintering process.

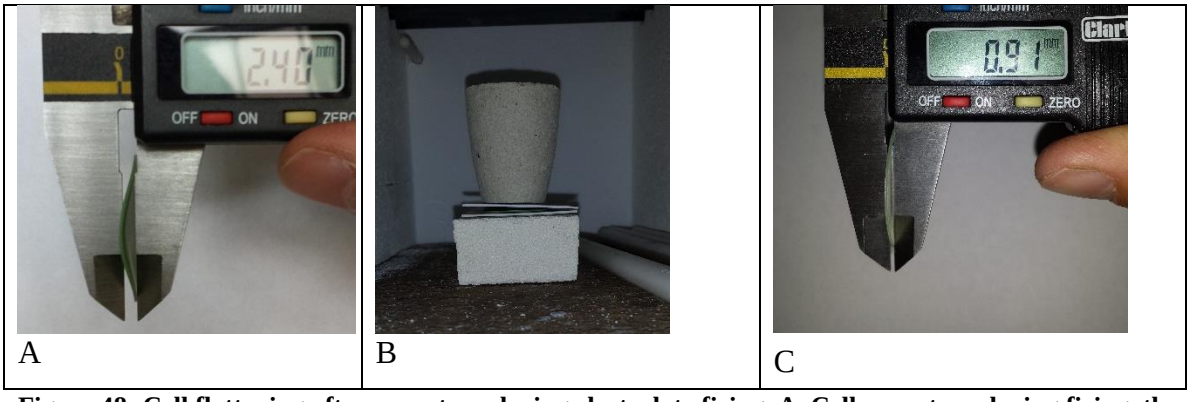


A B C

**Figure 48: Cell flattening after curvature during electrolyte firing. A. Cell curvature during firing, the cell shows significant curvature. B. Cell with weight placed in to flatten cell. C. Cell after flattening tests to 1400$^{o}$C the cell is almost completely flat however a slight bend was observed.**

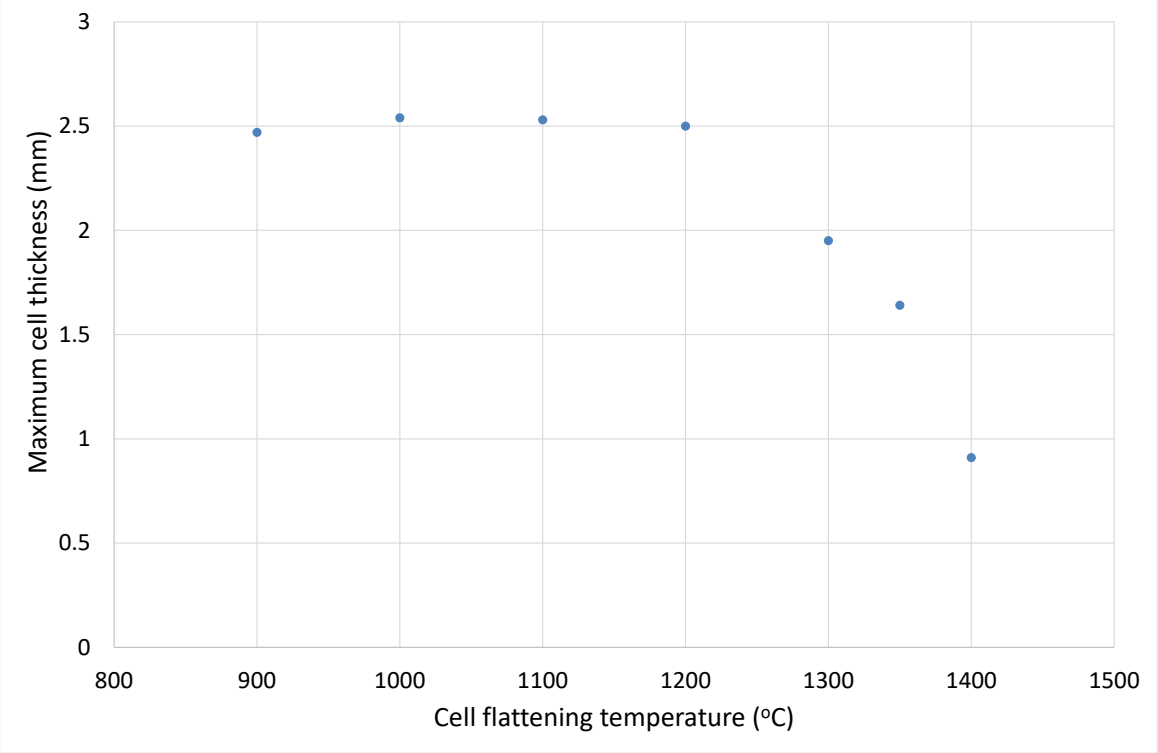


**Figure 49: The maximum thickness (including curvature) of a cell which had electrolyte applied and curved during sintering. The cell was weighted and a re−fired to increasing temperature to obtain a flat cell and the cell thickness is shown.**

## 5.5 Oxygen electrode optimisation:

In this section experiments were performed to investigate the performance of various LSM based electrolytes applied to the surface of a cell. As the electrolytes produced in the preceding sections did not show good leak testing or OCV performance in this section commercial half cells with a sintered electrolyte were used. The half cells used are hydrogen electrode supported Ni−YSZ / YSZ cells. The cathode inks used in this work were prepared into a vehicle for printing in a three roll mill. Powders of the correct quantity were manually mixed, then roughly mixed with a vehicle in a 50:50 vol% ratio. The resulting mixture was then put through a three roll mill to homogenise the paste. A circle with an area of $3cm^2$ was masked in the centre of the cell. The ink was hand painted onto the surface. This was allowed to air dry for 10 mins before drying in an oven at 80°C for 1 hour. If a second layer was being applied this was then painted and the drying repeated. The cells were all fired to 1200°C at

3°C $min^{-1}$. The cell was held at 325°C and 500°C for 1 hour. Testing was performed in the standard manner with a gold grid attached to the oxygen electrode surface with an LSM paste, and a silver grid on the hydrogen electrode. For each oxygen electrode three cells were tested and the average values provided, the three cells tested showed good agreement with each other.

Four different oxygen electrodes were tested;

1. LSM−YSZ
2. LSM−YSZ / LSM (with both layers fired at the same time)
3. LSM−YSZ / LSM (with each layer undergoing a separate firing step)
4. LSM−ScSZ / LSM (with both layers fired at the same time)

The performance of these electrodes is compared in fuel cell operation (Figure 50) and in electrolysis operation (Figure 51). The error increases as the temperature decreases as the IV curve becomes less linear therefore reading the ASR for the cell becomes more difficult.

For both fuel cell and electrolysis operation over the whole temperature range the LSM−YSZ cell shows significantly worse performance than the other cells. There was no significant difference in performance between the LSM−YSZ cells co fired and fired separately throughout the temperature range. In both modes of operation the LSM−ScSZ / LSM cell showed no difference in performance at >700°C than the bi−layer LSM−YSZ / LSM cells. However, the performance of the ScSZ cell was slightly worse than the bi layer YSZ cells at 650°C.

The ASR for the cells is very similar at 700°C and 750°C. At 800°C the electrolysis performance is slightly worse than the fuel cell performance and at 650°C the electrolysis

performance shows an improvement compared to the fuel cell performance measured in terms of ASR.

The rate of a reaction is governed by the Arrhenius equation (Equation 25). This shows that ln ASR α 1/T, these experiments all show a straight line for ln ASR vs 1/T.

$$k = Ae^{-E_a/(RT)}$$ ***Equation 25***

**Where; k=the reaction rate constant, A=the pre exponential factor, $E_a$=activation energy, T=temperature and R=universal gas constant.**

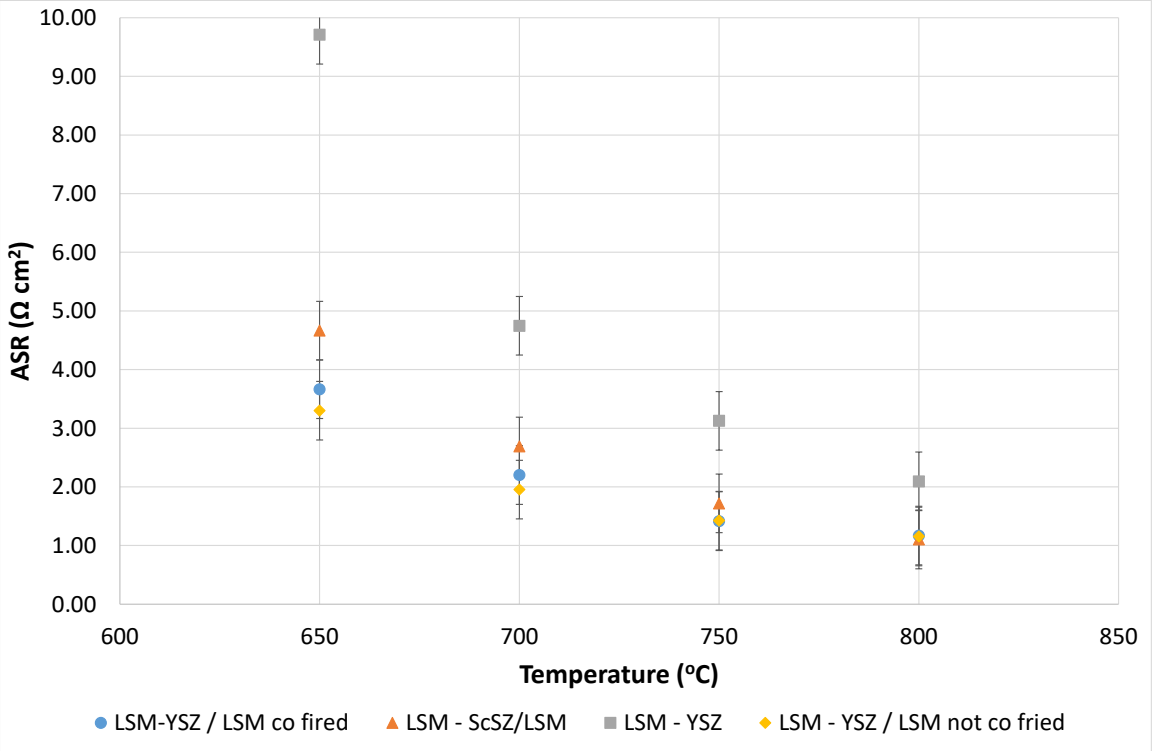


**Figure 50: Performance of different oxygen electrode sintered to commercial half cells in fuel cell operation at various temperatures.**

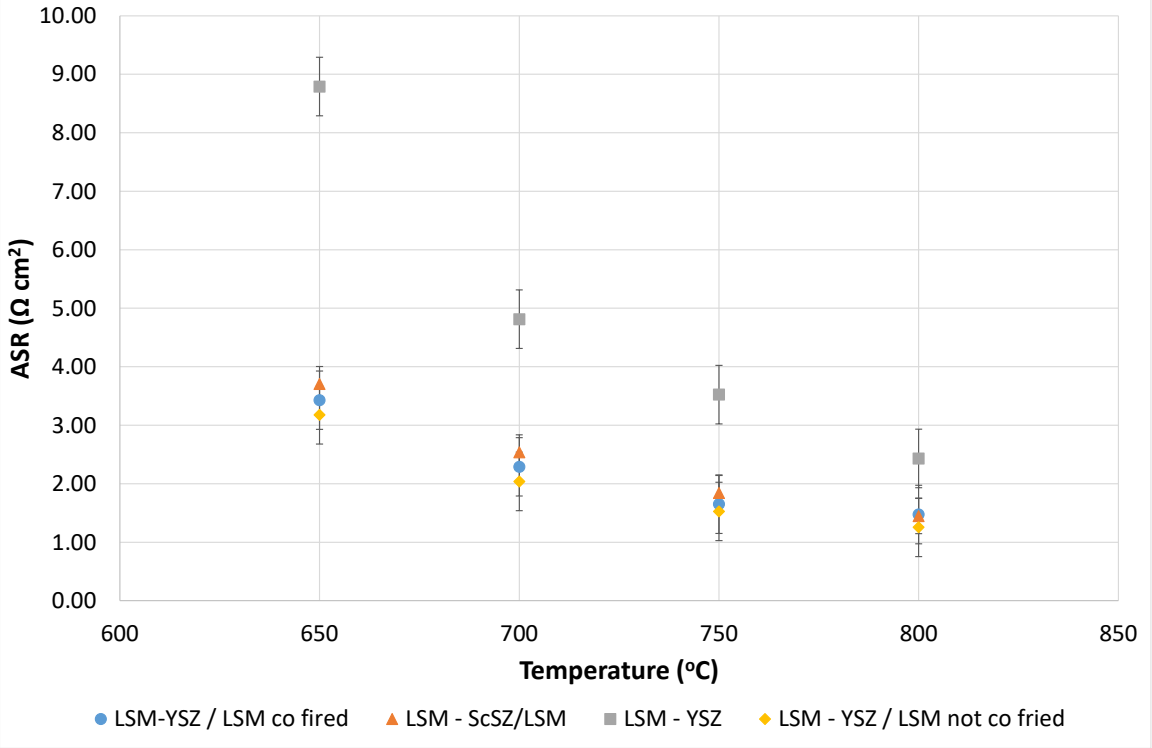


**Figure 51: Performance of different oxygen electrode sintered to commercial half cells in electrolysis operation at various temperatures.**

## 5.6 Conclusions:

In this section work was performed to fabricate anode supported cells and apply an electrolyte to these cells. Anode supports were successfully produced by powder pressing, however the production of a suitable electrolyte proved much more difficult. A leak testing set up was constructed for the testing of electrolyte quality. The leak testing showed a correlation with the achievable OCV for the cell. However a good leak test result did not necessarily result in a good cell OCV. Various techniques were attempted to optimise the process to produce a suitable electrolyte while significant improvements were made in the electrolyte quality. None showed a suitable performance for a cell. In Figure 43 the point on the far left of the graph shows a commercial cell which was tested, a leak rate of $4.7 \times 10^{-5}$ $Nm^3$ hPa $sec^{-1}$ $cm^{-2}$. This shows that the best electrolyte achieved by screen printing in this work is an order or magnitude worse than the electrolyte of a commercial cell. Due to the poor reproducibility

and quality of the electrolytes achieved in this work it was decided that the purchase of commercial cells would be a more viable method to get the desired results in a feasible length of time.

# 6 Reversible operation

## 6.1 Introduction:

In the first part of this chapter solid oxide cells which are operated in either fuel cell (FC) or electrolysis (EL) operation will be discussed. These results are then compared to the degradation observed when the cells are operated in cyclic manner between fuel cell and electrolysis operation, reversible operation.

The ability of a cell to perform well in both fuel cell and electrolysis operation would be an advantage as it would reduce the capital costs for a system if it could be configured to operate for as much of the time as possible. A cell operated in a cyclic manner could utilise excess energy during times of high production and low demand then produce electricity during low production and high demand. This would be the case if it were coupled to a wind or solar source with intermittent supply, or to a nuclear source with constant output and variable demand.

While the use of water electrolysis is one way to reduce the carbon intensity of a hydrogen economy, the use of a reversible fuel cell in a renewable energy storage system would also have benefits due to reduced capital costs and performance of load management in a power grid.

There has been a large amount of work done on the degradation in either SOFC or SOE operation. However, few studies have investigated the ability of an SOFC cell to operate

cyclically between SOFC and SOE operation. This aspect has been receiving greater attention recently [106,144,148,149,151,167–169]. Modelling work has been done at a stack level which has shown that temperature changes caused by switching currents can lead to degradation of the cells [151]. Therefore, the rate of switching would have to be managed. However, this is not a fundamental restriction on operation of the cells in a cyclic manner. There has also been some work performed on the cyclic operation of cells which suggests that there is the possibility to operate a cell in transient electrolysis and fuel cell operation without degradation, while operation in electrolysis alone would result in high rates of degradation [106]. The work performed by Graves [106] assumes that it is the partial pressure of oxide ions at the oxygen electrode−electrolyte interface which leads to some of the degradation in electrolysis operation due to pore formation in the electrolyte and delamination of the oxygen electrode. Their work has found that if the time period for electrolysis operation is shorter than the fuel cell period of operation, there is apparently no cell degradation as the oxygen partial pressure at the oxygen electrode−electrolyte interface is regularly reduced therefore it does not cause cell damage. While this is a useful verification of the theory that oxygen partial pressure build−up contributes to the cell degradation, in actual operation this will be less useful. The time period over which this effect was studied was short, they operated in electrolysis operation between 1 and 5 hours with a fuel cell period of 5 hours. When the electrolysis time period was less than the fuel cell time period the degradation rate was low. The degradation rate increased when the EL and FC time periods were the same. In a real system it is likely that the electrolysis operation would have to be occurring for much longer time periods

It is interesting to note that the cell was operated for ~1100h undergoing 120 cycles without showing signs of degradation. This indicates that there is nothing inherent in the switching of

the cell which causes degradation. Operation for short time scales in FC and EL may also be useful for load balancing on a system which is in flux i.e. with a very intermittent wind source. However, in many systems this load balancing would be performed by a battery. A fuel cell and electrolyser combination is likely to be useful over longer time scales, e.g. electrolysis during the day when there is surplus solar electricity and fuel cell operation overnight. It may also be needed over longer time scales, operating preferentially in one direction for a week or month depending on weather conditions and time of year.

In the work presented in this chapter the EL or FC each last for 20 hours. There are also some initial results presented on varying the rate of switching. Further work on this is required though. The degradation of the cells will be studied using the galvanostatic data, IV curves and impedance measurements.

### 6.1.1 Current and rate of change from EL to FC:

In this work the experiments were performed at constant current operation of ±0.166 A $cm^{-2}$ for both fuel cell and electrolysis. Constant current was selected to ensure a constant ion flux through the cell. Therefore, degradation rates could be compared, and measurements of voltage degradation made. The current was chosen to give an operation of ~0.7V in fuel cell operation and 1.3V in electrolysis. However, the current was chosen when cell performance was poor, therefore the voltages in this work are actually higher than 0.7V in fuel cell and lower than 1.3V in electrolysis operation. This does not present a problem for fuel cell operation, however, for electrolysis operation the cell is operating in endothermic operation rather than thermoneutral. The cell is within a temperature controlled furnace therefore the temperature changes should be minimised. Nevertheless, while a thermocouple was positioned close to the cell this was not sensitive enough to measure any changes in cell

temperature. The effect of temperature changes due to endothermic operation was assumed to be minimal for the small cells used in this work however the effect of thermal changes in the cell should not be discarded entirely.

In this experiment changes to the cell current are performed as a step change, this includes changes from electrolysis to fuel cell and vice versa. However, often there would have been an IV curve and impedance measurements between electrolysis and fuel cell steps. While it is known that temperature changes from OCV to electrolysis operation can damage a stack, as far as the author is aware very little work has been performed on the temperature management of a stack when altering the current from electrolysis to fuel cell operation. Upon a change in current from fuel cell to electrolysis there will be a temperature change, especially if the electrolysis is performed in endothermic operation. The temperature changes will produce expansion/contraction of the materials and could lead to stresses which harm the cell performance. There is a lot of flexibility in the materials and test stand which should allow for some of the expansion/contraction without damaging the cell on a large scale. However, there would be induced stresses between the materials in the stack and the effect at a small scale isn't known and may play a role in degradation.

## 6.2 Experimental:

For these tests the Ni−YSZ/YSZ/LSM−YSZ solid oxide cells produced at the Ningbo Institute were used. Hydrogen electrode contacting was made using a silver mesh with silver wires for current and voltage sense connection. Oxygen electrode contacting was performed using a gold mesh (Fiaxell) pressed into a wet LSM paste which dried during the cell heat up. The gold mesh was connected to silver wires for connection out of the furnace. Gas and water control as described before in section 4.2.2, utilising a Bronkhorst water evaporator. The cell

was placed in a compression test stand with gaskets. (Flexitallic Thermiculite 866) in the test rig described in section 4.2.3.

### 6.2.1 Testing schedule

The initial period of cell treatment was the same for each cell. Initially the cell was heated to 800ºC at 5ºC $min^{-1}$ with 120ml $min^{-1}$ $N_2$ and 60ml $min^{-1}$ $H_2$. Once at 800ºC the cell was left to reduce for 1 hour before performing an initial IV curve. After the initial IV curve had been performed, 60 $ml_{(g)}$ $min^{-1}$ (2.9 g $hour^{-1}$) $H_2O_{(g)}$ was added. The cell was left for a further 2 hours as the steam supply stabilised. After this initial period the experiment continued at 800ºC with 1:1:2 $H_2$:$H_2O_{(g)}$:$N_2$ at a total flow rate of 240 ml $min^{-1}$ for the rest of the experiment. Once finished the cell was cooled under the experimental gas conditions at 5ºC $min^{-1}$.

### 6.2.2 Electrochemical testing:

All electrochemical measurements have been performed on a Solatron 1470E with 1455 FRA.

IV curves were performed using voltage control as a stair step. Starting from OCV the cell tested between 0.4V and 1.6V with 25mV steps and a step duration of 30 seconds. The point on the IV curve is the average voltage for the 30 seconds.

Impedance analysis was performed between 100,000 Hz or 10,000 Hz and 0.1 Hz with 10 steps/decade. The applied potential from OCV was −0.1V for fuel cell and 0.1V for electrolysis with an AC amplitude of 10mV unless otherwise stated.

## 6.3 Results:

In the next two chapters the cells are labelled as Ningbo as the source of the cells was the Ningbo institute and the cell number tested.

### 6.3.1 Fuel cell degradation

Ningbo 56 was operated for 300 hours at 800ºC with a volume ratio of 1:1:2 $H_2$:$H_2O$:$N_2$. With a total flow rate of 240 ml $min^{-1}$, there was an air supply of 1 L $min^{-1}$ to the oxygen electrode. The cell was operated at 0.166 A $cm^2$ with a galvanostatic step duration of 20 hours after which IV curves and impedance spectra were recorded.

The galvanostatic data is shown in Figure 52. Over the first 20 hours there was a rapid increase in cell performance. After this initial settling period each subsequent period showed similar features. The first 20 hours were not included in any degradation analysis as this behaviour was thought to be due to some initial conditioning of the cell.

From 20 to 150 hours during each constant current step there was a large initial increase in performance over the course of 1 to 2 hours there was then a steadier phase for the rest of the step 18 to 19 hours. After performing IV and impedance measurements between the steps which would have taken ~40 minutes the cell operation was restarted at the same voltage in each step (within ±2mV).

The cell resumed at the same voltage, but after each step the size of the initial rapid increase was reduced. The rapid increase in performance reached the level at which the cell finished the previous step and over the course of the experiment an almost continual degradation was observed. The rapid increase in performance occurred over 1 to 2 hours.

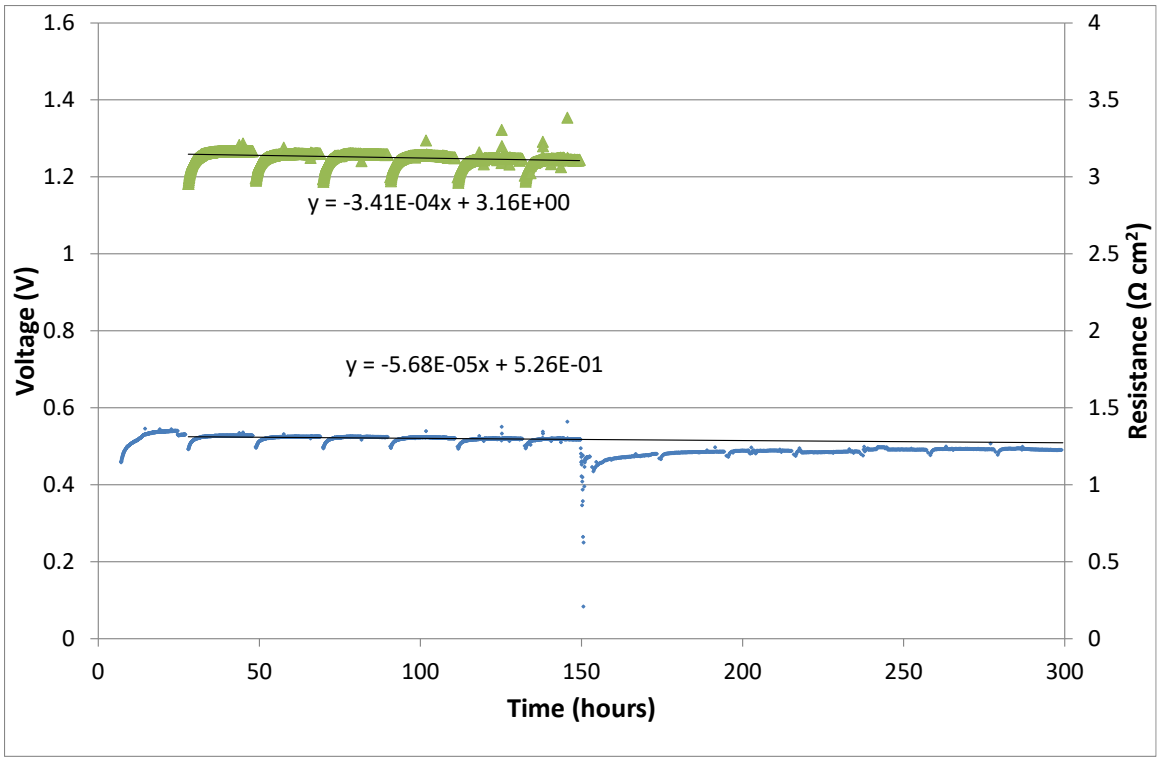


**Figure 52: Ningbo 56 fuel cell degradation rate at 800°C 1:1:2 $H_2$:$H_2O$:$N_2$ with a total flow rate of 240ml $min^{-1}$ and current of 0.16 A $cm^{-2}$. The y−axis scale was chosen for continuity and ease of comparison with electrolysis results throughout the chapter. The blue line shows the cell voltage, the green line shows the cell resistance.**

After 150 hours the cell suffered a brief interruption of the gas supply which caused a loss in performance. The cell underwent a recovery over the next 90 hours. After the recovery the cell started to degrade again. The average fuel cell degradation rate from 240 to 300 hours was 54 mV $kh^{-1}$ although this was at an offset from the original degradation rate.

The IV curves obtained throughout the experiment are show in Figure 53. The OCV was around 0.916V which is slightly lower than the expected Nernst voltage of 0.942V, this may be due to inadequate sealing of the cell. The OCV however stayed stable throughout the experiment indicating the $H_2$:$H_2O$ ratio in the gas stream was constant throughout the experiment. The curves for both fuel cell and electrolysis are almost linear showing no obvious performance loss due to mass transport or activation overpotentials. Overall the ASR is slightly higher in electrolysis than fuel cell operation, 2.83 Ω $cm^2$ vs 2.56 Ω $cm^2$. It is difficult to identify a trend from the IV curves as the data is very similar. However, the ASR

for fuel cell and electrolysis has been calculated from the initial linear part of the IV curve for fuel cell and electrolysis operation and this data is presented in Figure 54. The IV curves of both electrolysis and fuel cell operation show an initial decrease in cell ASR of about 0.3 Ω $cm^2$ between 6 and 27 hours. From 27 to 132 hours the rate of ASR degradation is similar for both electrolysis and fuel cell operation, 0.62 Ω $cm^2$ $kh^{-1}$ and 0.84 Ω $cm^2$ $kh^{-1}$.

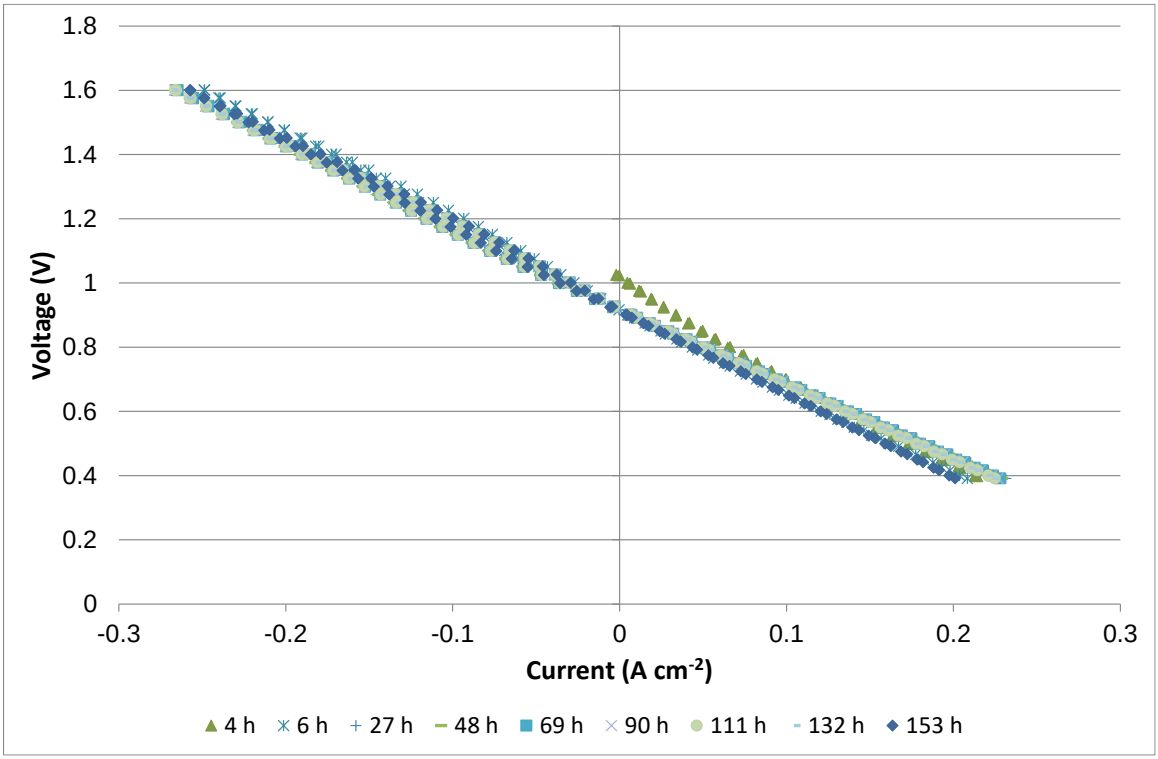


**Figure 53: Ningbo 56 IV curves performed at 800°C 1:1:2 $H_2$:$H_2O$:$N_2$ with a total flow rate of 240ml $min^{-1}$, apart from 4 h which had 50:50 $H_2$:$N_2$ with a total flow of 120ml $min^{-1}$.**

The fuel cell and electrolysis impedance spectra are shown in Figure 56 and Figure 55 respectively. From the impedance spectra the total fuel cell resistance appears to be larger than the total electrolysis impedance. This is the opposite to that observed in the IV curves where the FC ASR is lower than the EL ASR. This may indicate that the impedance data don't show represent what's happening during operation. Impedance measurements were made at ±0.1V from OCV, at low current density. During operation the cell is operating at a higher current density which may result in the EIS not showing the degradation observed

during constant current operation. Another possibility is that the cell ASR doesn't represent the cell operation close to OVC. The cell may perform better in electrolysis operation than fuel cell operation with a small voltage difference from OCV but become lose performance more quickly in electrolysis than fuel cell operation as the voltage difference from OCV increases.

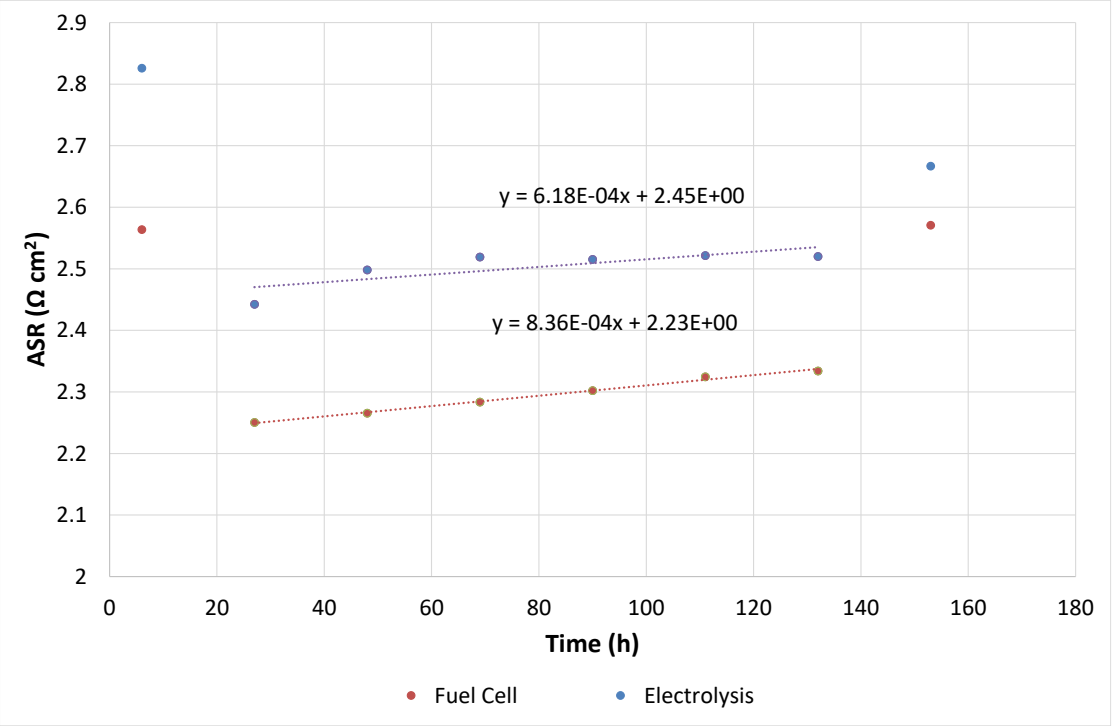


**Figure 54: Ningbo 56 ASR calculated from IV curve slope. performed at 800°C 1:1:2 $H_2$:$H_2O$:$N_2$ with a total flow rate of 240ml $min^{-1}$, apart from 4 h which had 50:50 $H_2$:$N_2$ with a total flow of 120ml $min^{-1}$.**

In the fuel cell impedance spectra, Figure 56, there is a 4-hour curve (labelled 4 B) which is the dry hydrogen impedance spectrum which is very different from the impedance with water. Without water the total gas flow rate is lower than with water. Equivalent circuit fitting using the model shown in Figure 31 gave a resistance for the low frequency region (<100 Hz) of 0.96 Ω $cm^2$ without water which increased to 1.23 Ω $cm^2$ with water showing the diluting effect of the water addition. The high frequency response of the cell is the main reason for the increased cell performance with water, the high frequency resistance decreased from 1.56 Ω $cm^2$ to 1.14 Ω $cm^2$.

Between 7 and 28 hours there is a further large reduction in the total ASR. There is a very small decrease in the lower intercept which would indicate a slight reduction in ohmic resistance. However, there is a very large reduction in the total impedance of the cell; a large contribution to this improvement in performance is a reduction in the high frequency arc which indicates that the process is linked to charge transfer.

For the rest of the impedance spectra there is very little change in the impedance. The only noticeable change is at 153 hours where a large increase in mass transport which is probably due to the gas interruption is observed.

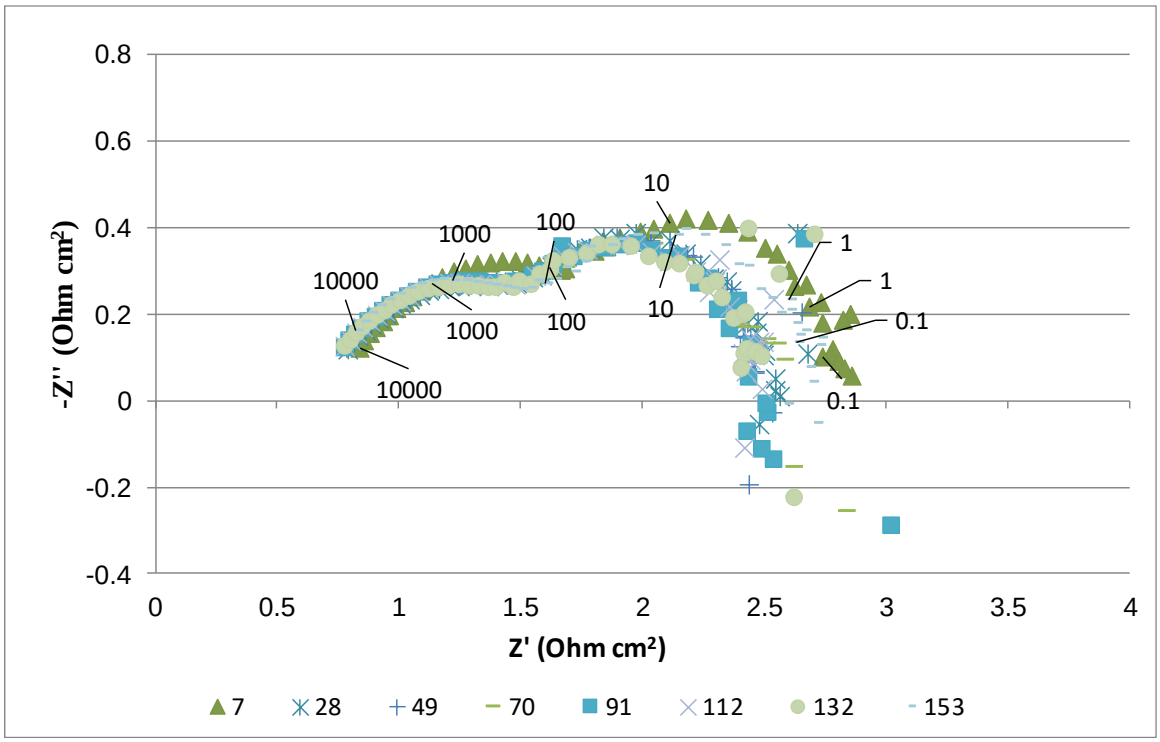


**Figure 55: Ningbo 56 impedance electrolysis, the frequency markers are shown for 7 and 153 hours. Measurements made at 800ºC with 1:1:2 $H_2$:$H_2O$:$N_2$ total flow rate of 240ml $min^{-1}$, at applied voltage of 0.1V above OCV. Axis label indicates time since start of experiment.**

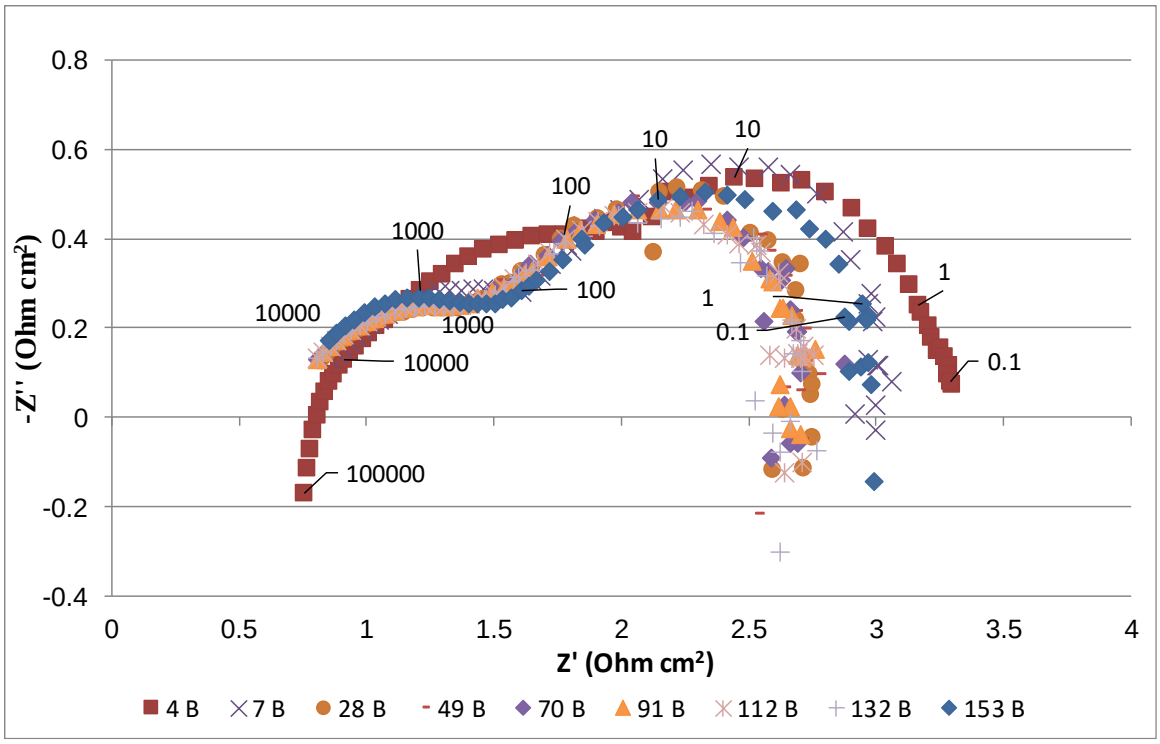


**Figure 56: Ningbo 56 impedance fuel cell. The frequency markers are shown for 4 hours and 153 hours. Measurements made at 800ºC 1:1:2 $H_2$:$H_2O$:$N_2$ with a total flow rate of 240ml $min^{-1}$, apart from 4 B which was performed at 800ºC 50:50 $H_2$:$N_2$ with a total flow of 120ml $min^{-1}$. Axis label indicates time since start of experiment.**

Figure 57 shows the impedance spectra for Ningbo 56 in fuel cell and electrolysis operation at 7 hours. This shows that the total impedance for the cell is very similar for fuel cell and electrolysis operation. There are however differences in the curves to reach the impedance. The fuel cell curve shows a smaller high frequency impedance than the electrolysis mode. The fuel cell impedance at low frequency (100−0.1Hz) is then much larger than for the electrolysis mode.

In Figure 58 the FC and EL impedance spectra at 91 and 153 hours are compared to see the effect of the damage due to the gas interruption. It can be seen that for both the fuel cell impedance is higher than the electrolysis impedance. The high frequency curve is slightly higher in electrolysis than fuel cell operation but this difference is larger at 91 hours than at 153 hours. There is a larger increase in the low frequency arc for both fuel cell and electrolysis. It is harder to be exact by how much as at the low frequency end there is a large

amount of scatter which makes interpreting the impedance spectra harder. However, it appears that the increase in impedance between 91 and 153 hours is greater in fuel cell operation than in electrolysis operation.

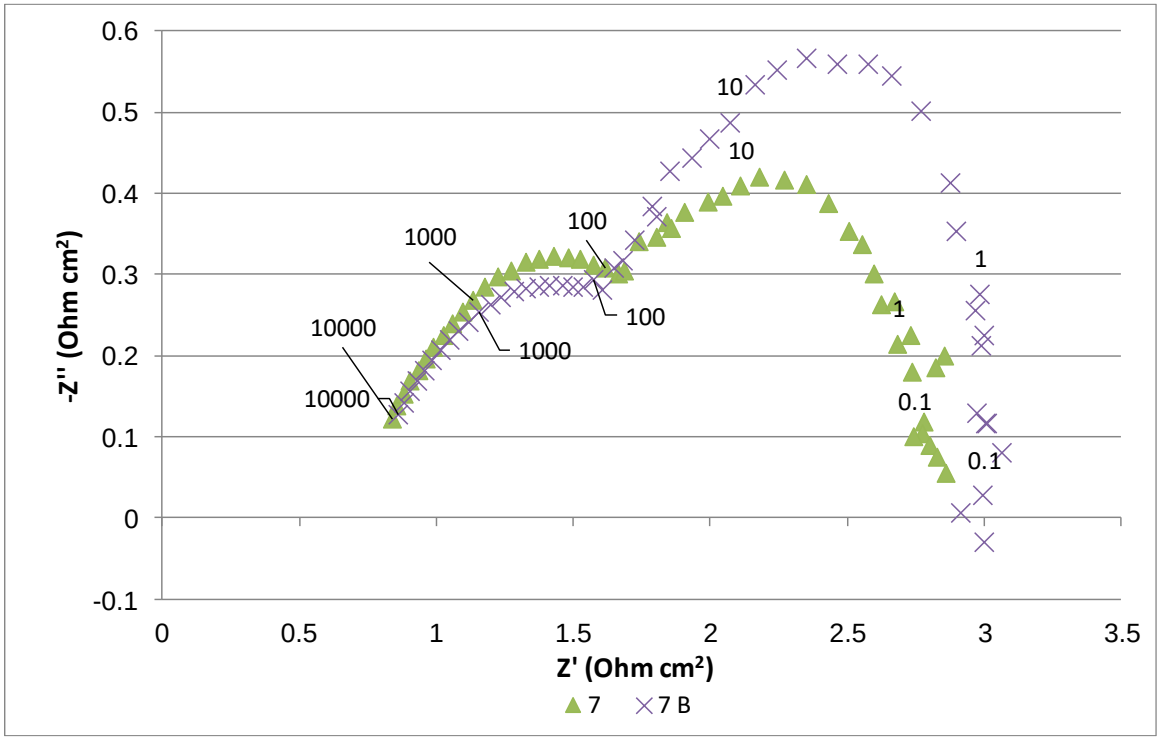


**Figure 57: Comparison of electrolysis (green triangles) and fuel cell (purple crosses) impedance at 7 hours for Ningbo 56. Performed at 800°C 1:1:2 $H_2$:$H_2O$:$N_2$ with a total flow rate of 240ml $min^{-1}$.**

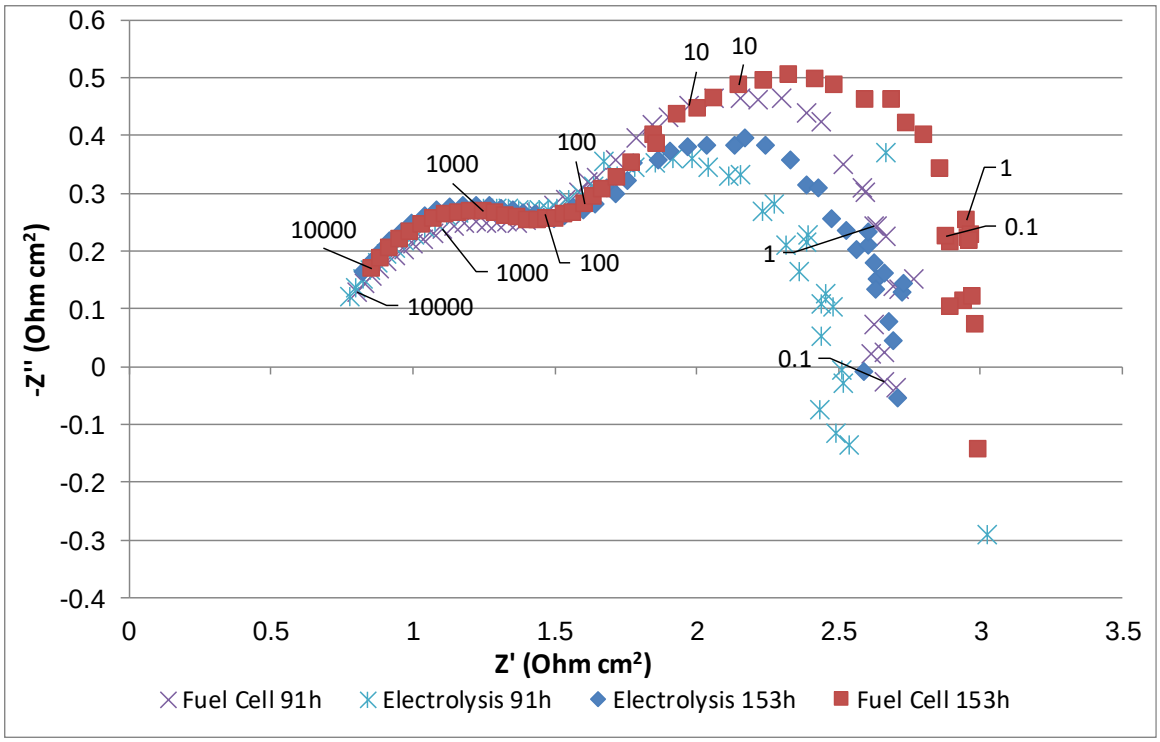


**Figure 58: Comparison of electrolysis and fuel cell impedance spectra at 91 and 153 hours, before and after the gas interruption for Ningbo 56. Frequency labels given for fuel cell mode at 91 and 153 hours. Performed at 800°C 1:1:2 $H_2$:$H_2O$:$N_2$ with a total flow rate of 240ml $min^{-1}$. This shows a large reduction in the low frequency are but very little change in the high frequency arc.**

### 6.3.2 Electrolysis degradation

Ningbo 50 was operated for 150 hours at 800°C with a 1:1:2 $H_2$:$H_2O_{(g)}$:$N_2$ fuel mixture and a total flow rate of 240 ml $min^{-1}$. The cell was operated at −0.16 A $cm^2$ with a galvanostatic duration of 20 hours after which IV curves and impedance spectra were recorded.

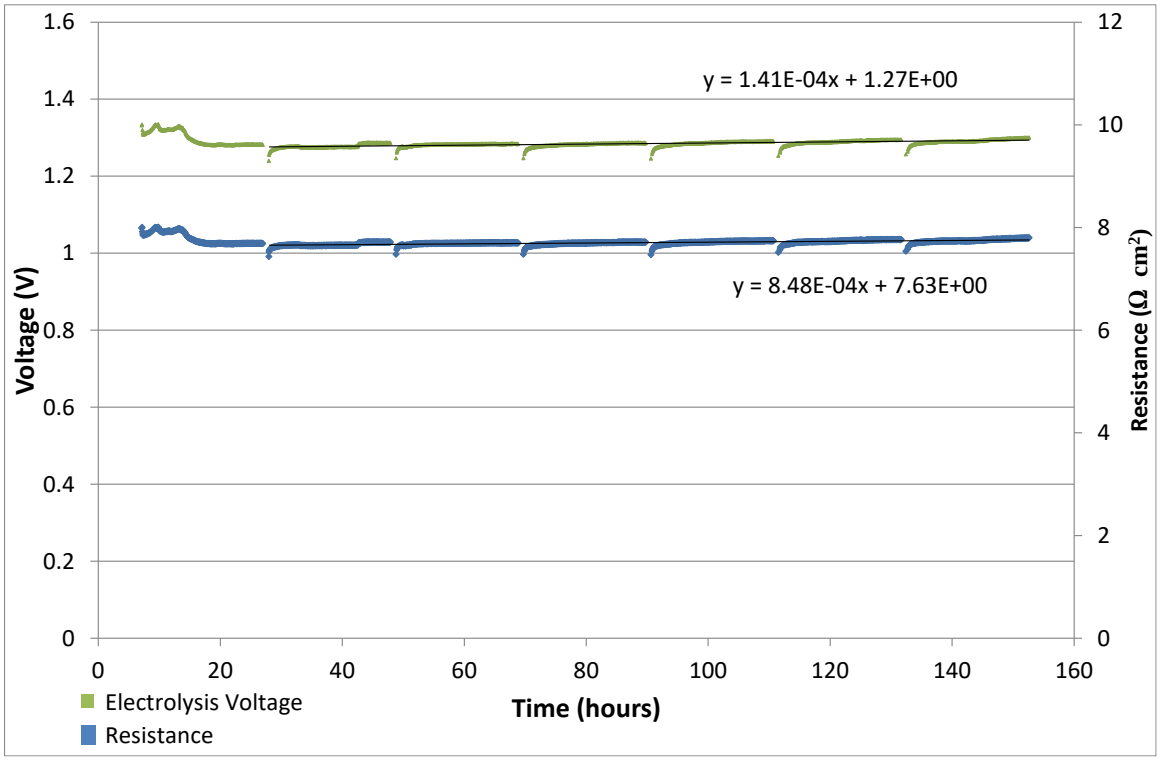


**Figure 59: Ningbo 50 electrolysis degradation rate performed at 800°C 1:1:2 $H_2$:$H_2O$:$N_2$ total flow rate 240ml $min^{-1}$ at −0.16 A $cm^{-2}$. The cell has an average degradation rate of 141 mV $kh^{-1}$. The green line shows the voltage evolution with time, the blue line shows the resistance evolution with time.**

The galvanostatic data for the electrolysis degradation is shown in Figure 59. There was some settling of the voltage during the first 10−20 hours of the experiment: initially the voltage was high before dropping to become more stable.

After the first 20-hour period the degradation rate of the cell appeared to be constant at 141 mV $kh^{-1}$. As has been seen during the fuel cell operation there were different features during each electrolysis step. There is an initial short period which lasts ~5−10 mins of rapid voltage increase which is then followed by a more gradual increase in voltage. The increase in voltage during these periods is much higher than the overall rate of degradation at 400 – 900 mV $kh^{-1}$.

The more rapid increase in voltage lasts for 2−4 hours at which point the cell reaches the voltage at the end of the previous galvanostatic step and the degradation is continued at the average rate.

The IV curves for the cell are shown in Figure 60. The cell OCV is 0.92V which is consistent with other results, while still lower than the expected OCV for the given gas conditions. The cell ASR is lower for fuel cell operation (1.8 Ω $cm^2$) than for electrolysis operation (2.3 Ω $cm^2$). There is no evidence of any major mass transport losses in the cell. The ASR has been calculated for each of the IV curves performed on the cell and the data is displayed in Figure 61. The electrolysis data shows an increase of 0.42 Ω $cm^2$ $kh^{-1}$. The fuel cell data shows a decrease in ASR of 0.27 Ω $cm^2$ $kh^{-1}$.

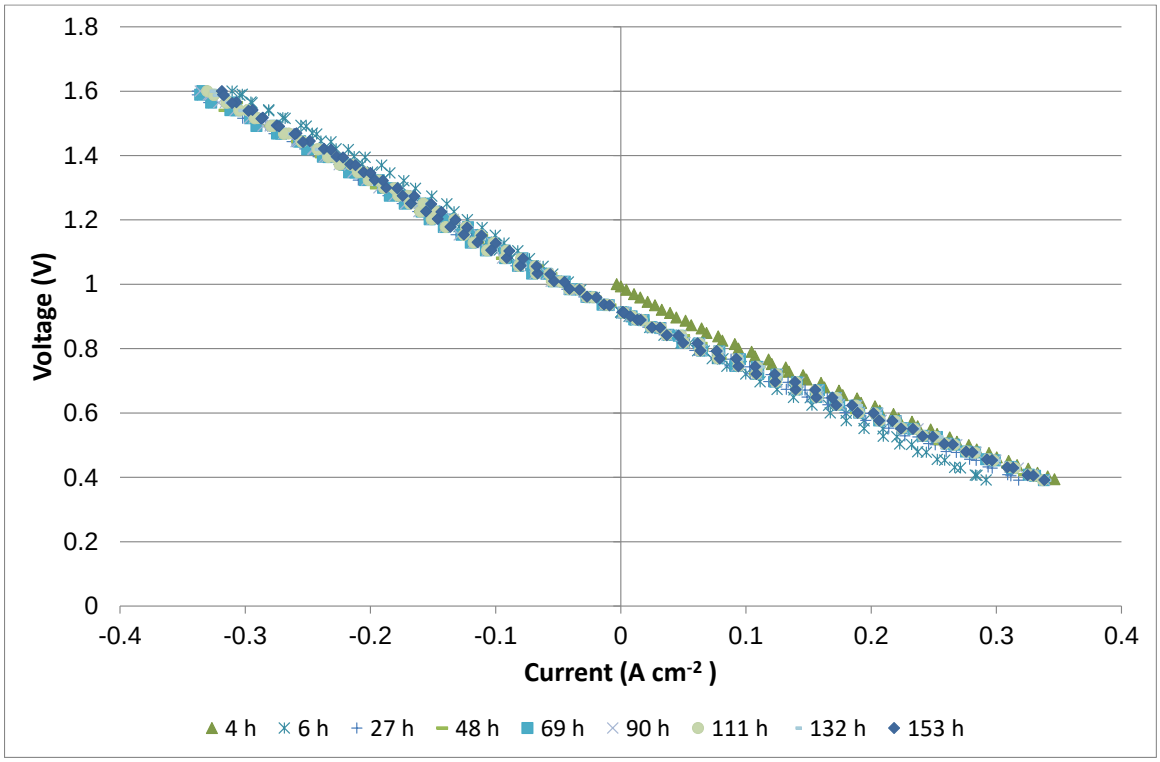


**Figure 60: Ningbo 50 IV curves performed at 800 ºC 1:1:2 $H_2$:$H_2O$:$N_2$ with a total flow rate of 240ml $min^{-1}$, apart from the initial 4h curve (green triangles) which was operated with 1:2 $H_2$:$N_2$ with a total flow rate of 180 ml $min^{-1}$.**

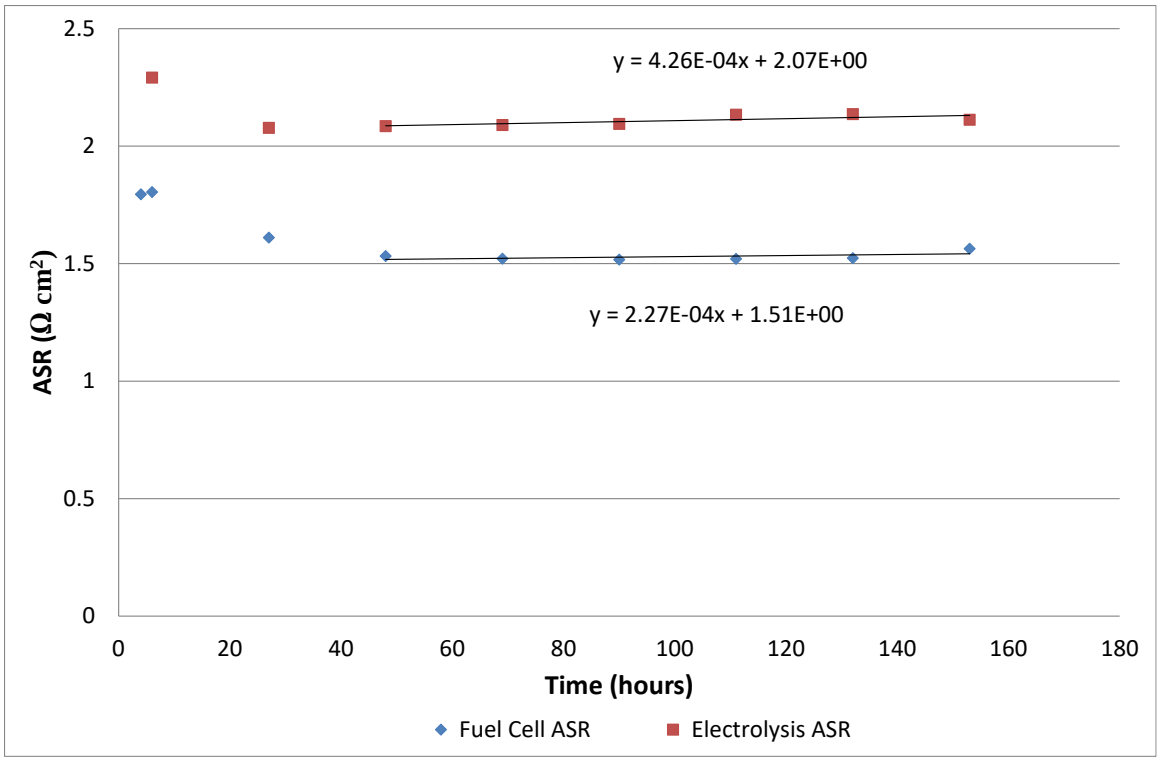


**Figure 61: Ningbo 50, values for ASR calculated from the IV. The electrolysis data shows an increase of 42 Ω $cm^2$ $kh^{-1}$. The fuel cell data shows a decrease in ASR of 27 Ω $cm^2$ $kh^{-1}$. Performed at 800 ºC 1:1:2 $H_2$:$H_2O$:$N_2$ with a total flow rate of 240ml $min^{-1}$, apart from the initial 4h measurement which was operated with 1:2 $H_2$:$N_2$ with a total flow rate of 180 ml $min^{-1}$.**

The impedance spectra recorded for the cell are shown in Figure 62 for fuel cell operation and Figure 63 for electrolysis operation. In Figure 64 the impedance spectra for fuel cell and electrolysis operation are compared. The impedance spectra comparing fuel cell and electrolysis impedance spectra show identical ohmic resistance. The high frequency fuel cell impedance shows improved performance over the electrolysis performance. However, the low frequency <100 Hz electrolysis performance is better than the low frequency fuel cell performance. The overall cell resistance for fuel cell and electrolysis operation appears to be very similar, however the impedance is dominated by scatter at frequencies <1Hz.

The impedance spectra show a large reduction in cell ohmic resistance after the first 20 hours of electrolysis operation where the cell conditioning is occurring. After the initial improvement in ohmic resistance there is no further systematic change which is observable in the impedance spectra. As there is a trend in the IV curve data and the galvanostatic data it

was expected that the impedance spectra would give further information about the resistance within the cell. There are a few possible reasons that the cell degradation isn't reflected in the impedance spectra:

- There is a lot of scatter in the results at low frequencies. There may be some changes occurring to the mass transport in the cell which is disguised as the fluctuations in performance mask the effect. The cell degradation over the timescales studied in this work is low, therefore the scatter may disguise the degradation.
- After each galvanostatic step the cell starts at a very similar voltage. The impedance spectra are measured after performing an IV curve on the cell. The IV curve may perform some conditioning on the cell which results in the cell being in a very similar state for each impedance measurement disguising the changes in the cell.

Figure 64 shows a comparison of the performance at 7 hours for fuel cell and electrolysis operation. The graphs show an identical total impedance however the curves for each are different. The fuel cell operation shows lower high frequency impedance than the electrolysis mode. The low frequency impedance (100−0.1Hz) is higher for fuel cell operation than electrolysis operation.

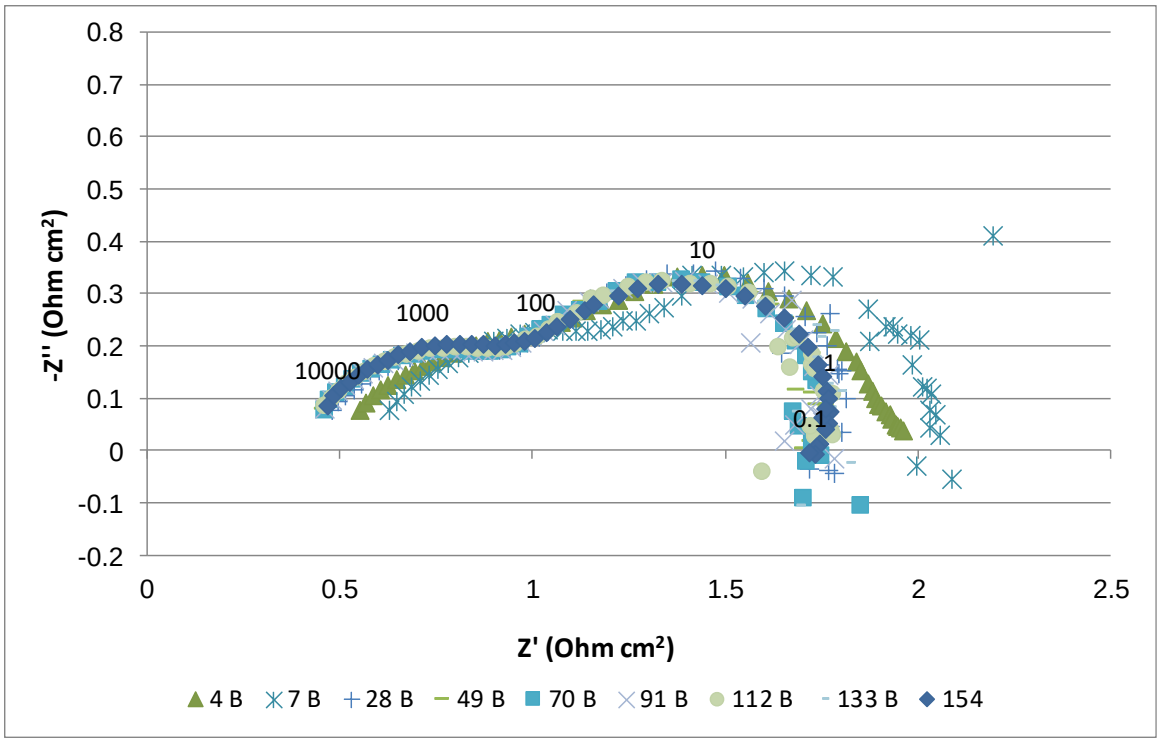


**Figure 62: Ningbo 50 Fuel cell impedance. The labels indicate time since the start of the experiment. Performed at 800ºC 1:1:2 $H_2$:$H_2O$:$N_2$ with a total flow rate of 240ml $min^{-1}$, apart from the initial 4 B measurement which was operated with 1:2 $H_2$:$N_2$ with a total flow rate of 180 ml $min^{-1}$.**

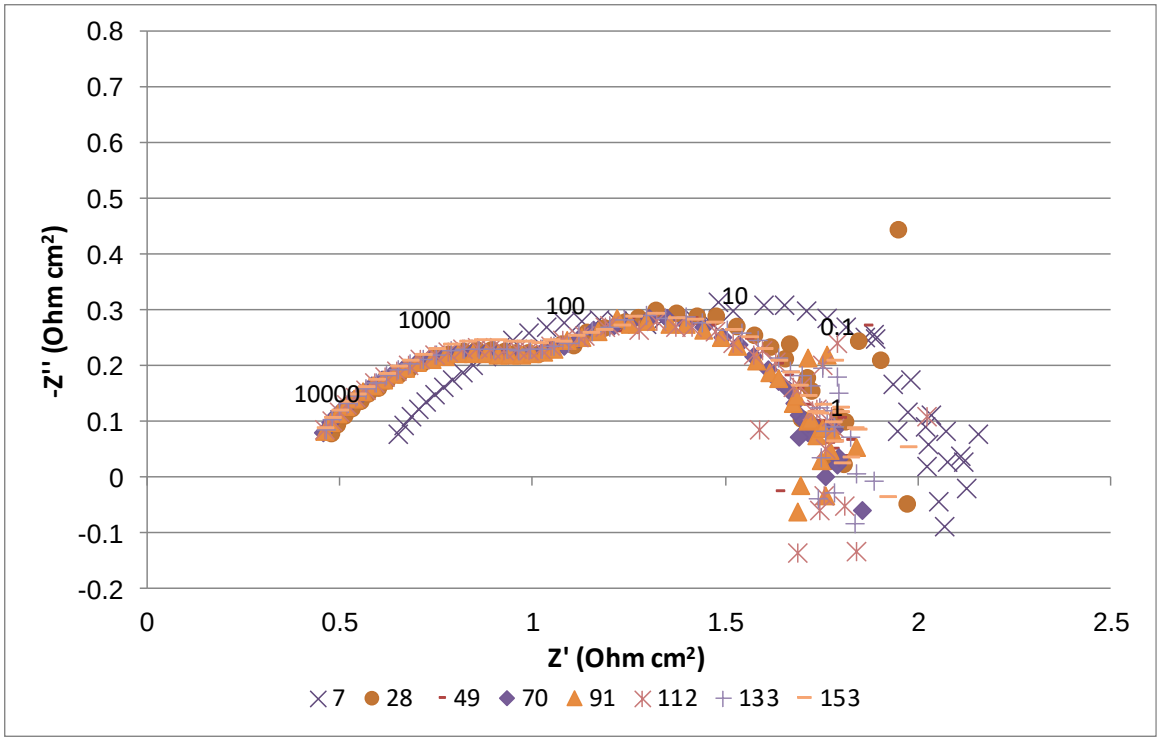


**Figure 63: Ningbo 50 electrolysis impedance. The labels indicate time since the start of the experiment. Performed at 800 ºC 1:1:2 $H_2$:$H_2O$:$N_2$ with a total flow rate of 240ml $min^{-1}$.**

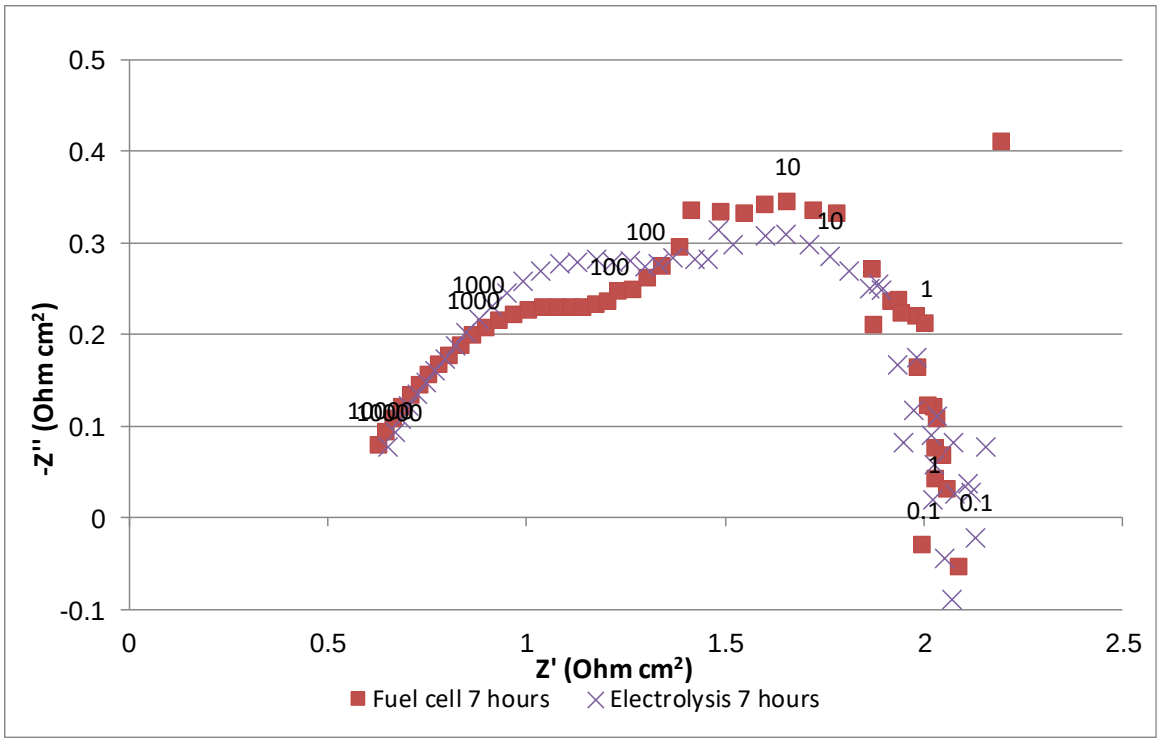


**Figure 64: Ningbo 50 comparison of fuel cell and electrolysis impedance at 7 hours into the experiment. Performed at 800ºC 1:1:2 $H_2$:$H_2O$:$N_2$ with a total flow rate of 240ml $min^{-1}$. The electrolysis impedance was recorded at OCV + 0.1V. The fuel cell impedance was measured at OCV − 0.1V.**

## 6.4 Cyclic performance from SOE to SOFC

In this section the cells were cycled between fuel cell and electrolysis operation and the rates of degradation were measured. In all tests the current for fuel cell and electrolysis operation was 0.166A and −0.166A respectively. The first two cells studied, Ningbo 81 and Ningbo 82 have been cycled between fuel cell and electrolysis operation with a 20 hour galvanostatic period. Subsequently other cells which have been cycled with different time scales have been studied.

### 6.4.1 Ningbo 81

Figure 65 shows the results of Ningbo 81 operated cyclically between fuel cell and electrolysis operation for 160 hours. This shows an electrolysis degradation rate of 145 mV $kh^{-1}$ and a fuel cell degradation rate of 77mV $kh^{-1}$.

There are large jumps in the electrolysis voltage during electrolysis operation. This is due to instability in the water supply to the hydrogen electrode causing changes in the cell voltage. Due to the spikes in voltage the degradation in each electrolysis step is difficult to measure. It can be seen that there is a higher rate of degradation at the beginning of each electrolysis step than for the rest of the electrolysis period. The fuel cell voltage does not show any of the instability shown in the electrolysis steps which leads to the conclusion that the instability in the electrolysis steps is due to instability in the water supply to the cell. The resistance degradation rate measured from the galvanostatic data is 0.75 $\Omega$ $cm^2$ $kh^{-1}$ in fuel cell operation whereas the electrolysis degradation rate is 1.01 $\Omega$ $cm^2$ $kh^{-1}$.

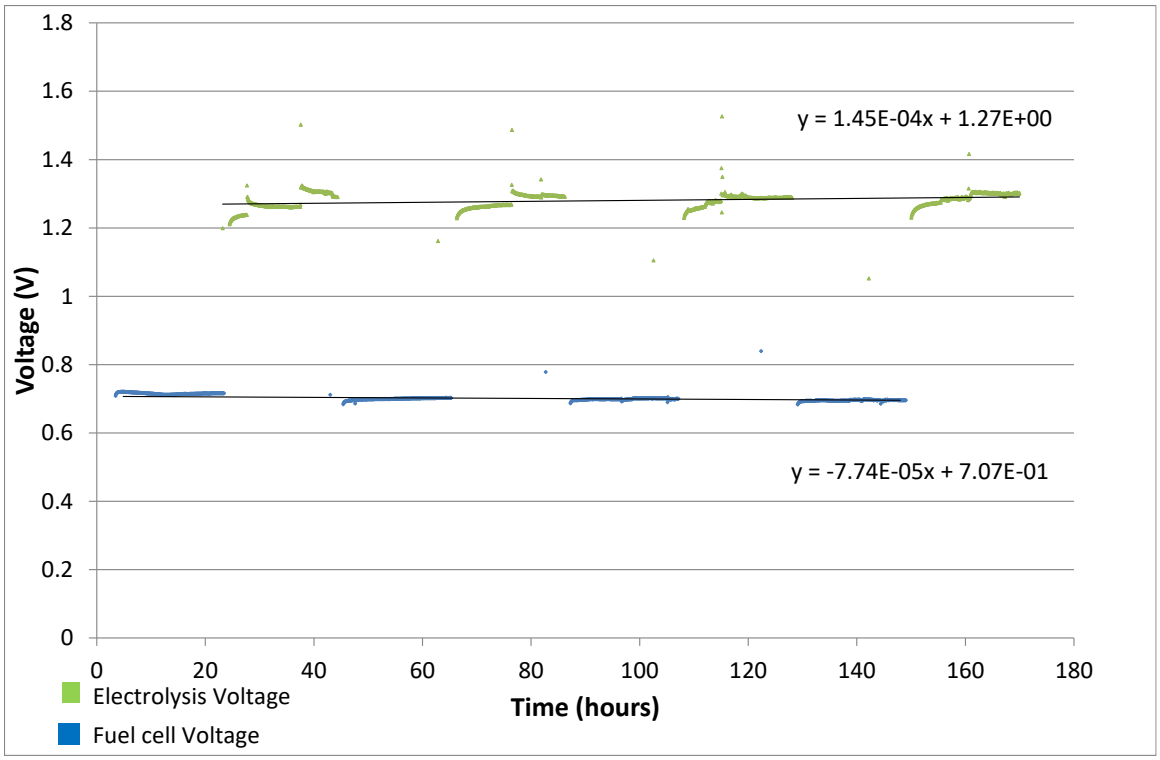


**Figure 65: Ningbo 81 electrolysis degradation rate at 800°C 1:1:2 $H_2$:$H_2O$:$N_2$ total flow rate 240ml $min^{-1}$ cyclic operation between electrolysis −0.16 A $cm^{-2}$ (green line) and fuel cell 0.16 A $cm^{-2}$ (blue line). The cell has an average degradation rate of 145mV $kh^{-1}$ in electrolysis operation and 77mV $kh^{-1}$ in electrolysis operation.**

The IV curves for the cell are shown in Figure 66 and the calculated ASR's are shown in Figure 67. The ASR for fuel cell operation 1.19 Ω $cm^2$ is slightly smaller than the electrolysis ASR 1.31 Ω $cm^2$. The rate of ASR degradation is lower in fuel cell operation than electrolysis operation 1.31 Ω $cm^2$ $kh^{-1}$ and 1.47 Ω $cm^2$ $kh^{-1}$ respectively. The ASR degradation rate during. The ASR degradation rates measured from the IV curves are slightly higher than the ASR degradation rates measured from the galvanostatic data.

The IV data shows the ASR is very dependent on whether a fuel cell or electrolysis step was performed before the IV curve. The ASR for both fuel cell and electrolysis sides of the IV curve are higher after a galvanostatic electrolysis step has been performed than after a galvanostatic fuel cell step has been performed. This suggests that performing a galvanostatic step causes some conditioning of the cell which is evident in the IV curve after the galvanostatic step has stopped.

The impedance data is also presented. The fuel cell and electrolysis impedance spectra after the fuel cell galvanostatic step is presented in Figure 68 and Figure 69 respectively. The fuel cell and electrolysis impedance spectra after electrolysis operation are presented in Figure 70 and Figure 71 respectively.

A comparison of the impedance data at the same time period shows the ohmic resistance is the same. The very high frequency impedance of the cell >10,000 Hz is dominated by inductance but is the same for both cells. The impedance in fuel cell operation shows a lower high frequency impedance than the electrolysis operation however the low frequency impedance <100Hz of both modes of operation is the same.

The impedance spectra after fuel cell galvanostatic steps for both fuel cell (Figure 68) and electrolysis (Figure 69) show the same trends. Both show an increase in the ohmic resistance component of the impedance after each cycle. The curve for polarisation resistance is the same for each subsequent spectra, and they show the same shape which is shifted to the right. Comparison of the impedance spectra taken at the beginning and end of a fuel cell galvanostatic step shows no change in the polarisation resistance.

The impedance spectra, after the electrolysis galvanostatic steps, also show the same trends for fuel cell (Figure 70) and electrolysis (Figure 71). Each step shows an increase in ohmic resistance however the shape of the curve also changes. The high frequency response of the cell shows a reduction for the curves in fuel cell and electrolysis. Analysis of the impedance spectra before and after an electrolysis step shows that there is an increase in the cells ohmic resistance.

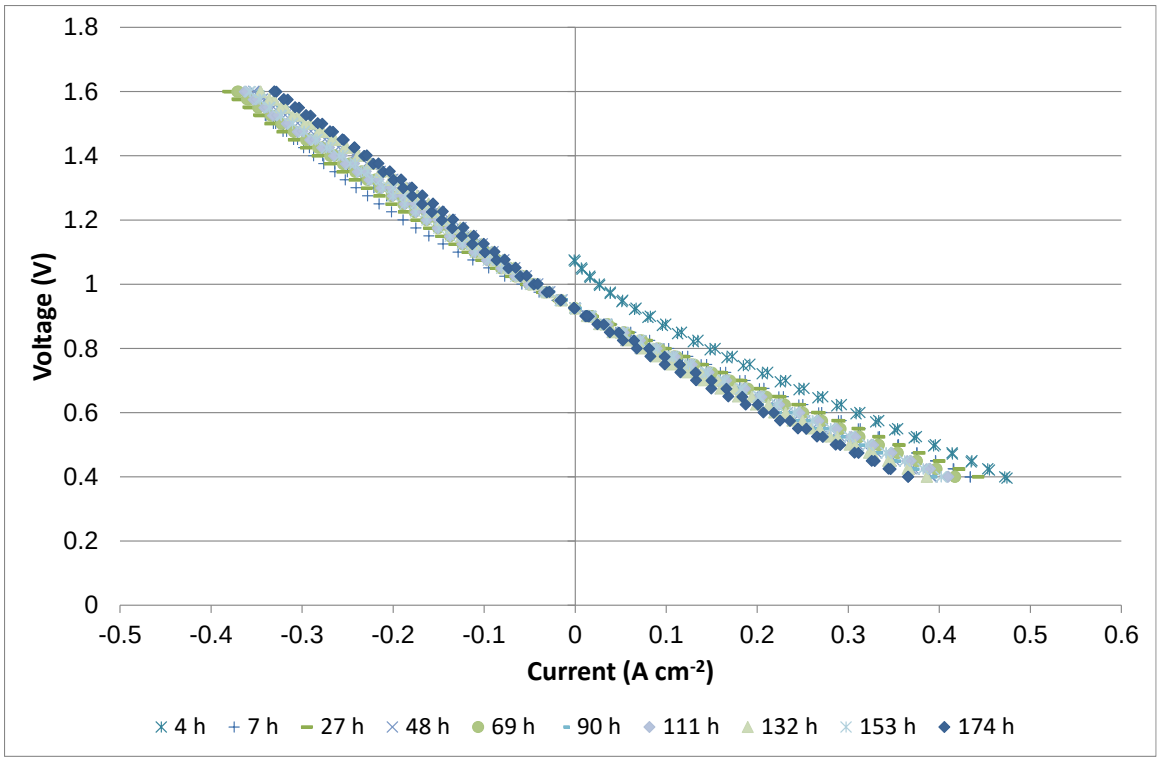


**Figure 66: Ningbo 81 IV curves performed at 800ºC 1:1:2 $H_2$:$H_2O$:$N_2$ with a total flow rate of 240ml $min^{-1}$, apart from the initial 4h curve (blue cross) which was operated with 1:2 $H_2$:$N_2$ with a total flow rate of 180 ml $min^{-1}$.**

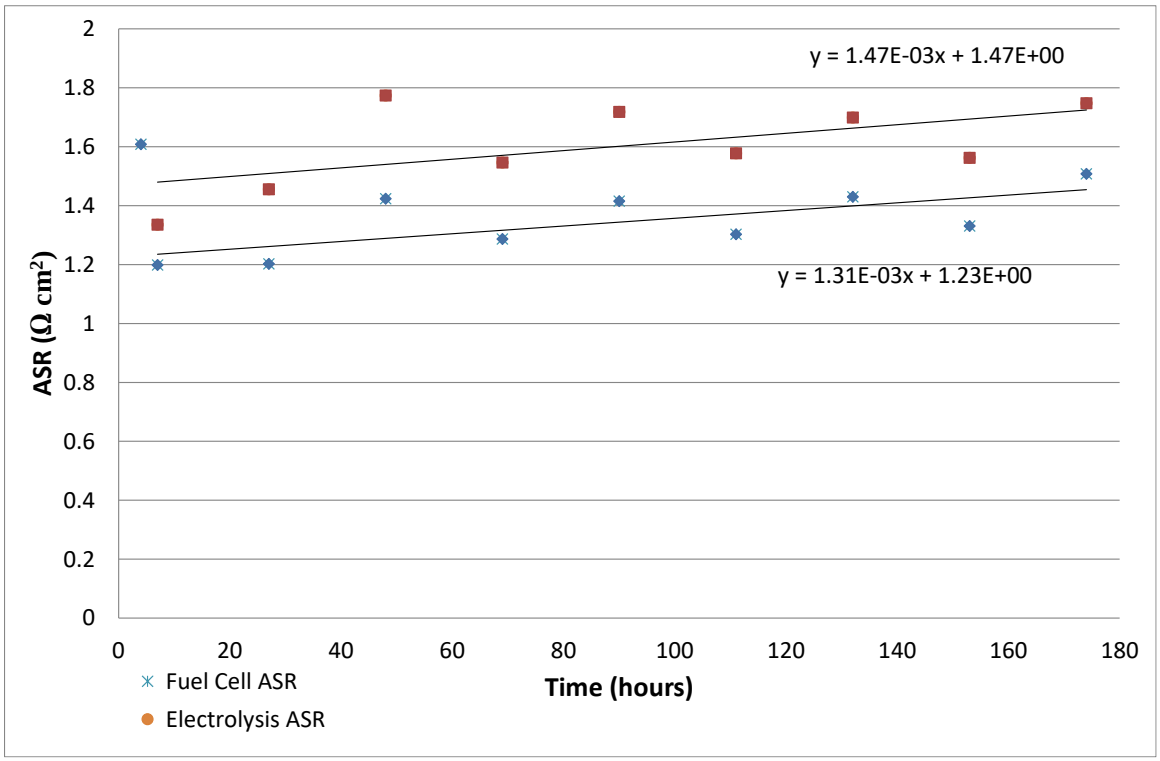


**Figure 67: The ASR for fuel cell and electrolysis operation calculated from slope of IV curve. The ASR is strongly dependant on the period of operation before it was performed. The ASR for both fuel cell and electrolysis is higher after a period of electrolysis operation than a period of fuel cell operation. Performed at 800ºC 1:1:2 $H_2$:$H_2O$:$N_2$ with a total flow rate of 240ml $min^{-1}$, apart from the initial measurement at 4h which was operated with 1:2 $H_2$:$N_2$ with a total flow rate of 180 ml $min^{-1}$.**

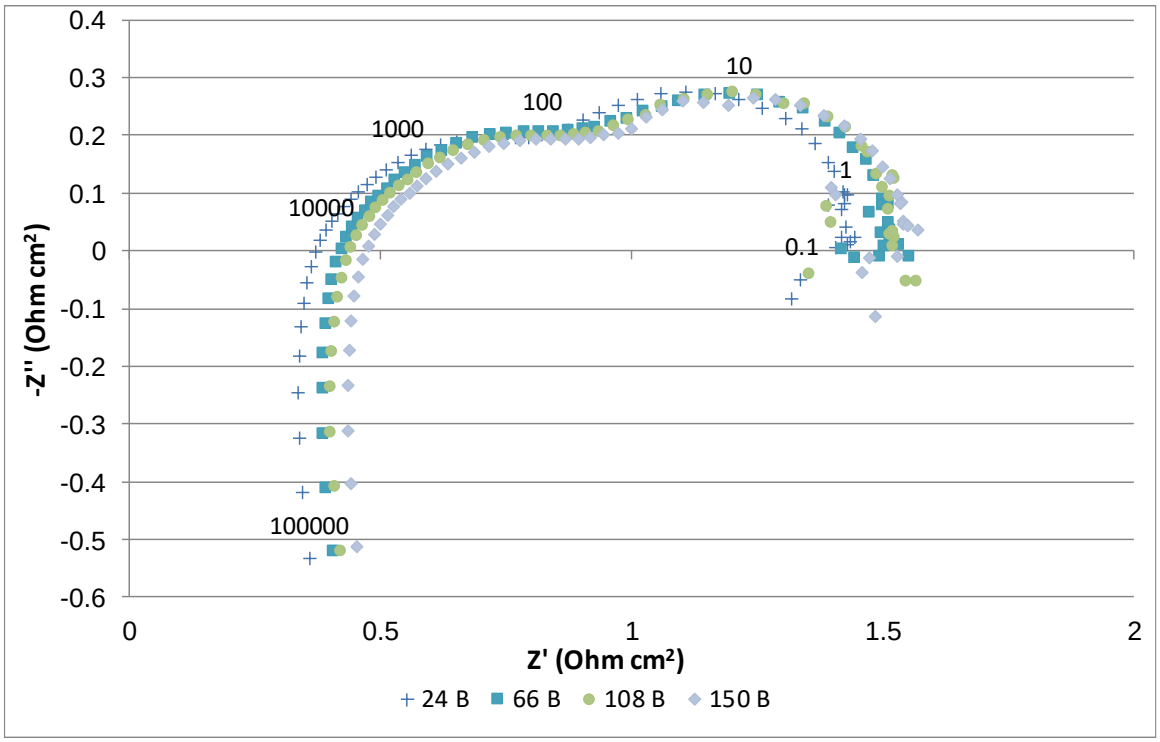


**Figure 68: Ningbo 81 Fuel Cell impedance spectra measurement performed after a fuel cell galvanostatic period. Performed at 800ºC 1:1:2 $H_2$:$H_2O$:$N_2$ with a total flow rate of 240ml $min^{-1}$.**

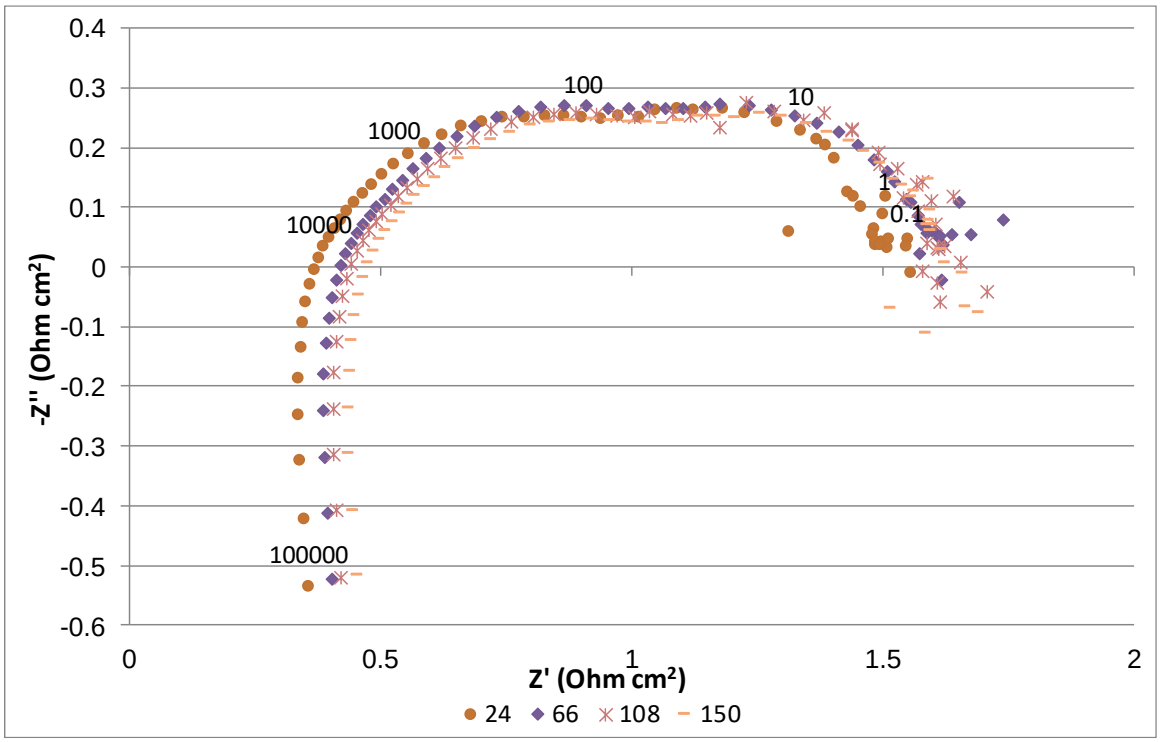


**Figure 69: Ningbo 81 Electrolysis impedance spectra measurement performed after a fuel cell galvanostatic period. Performed at 800ºC 1:1:2 $H_2$:$H_2O$:$N_2$ with a total flow rate of 240ml $min^{-1}$.**

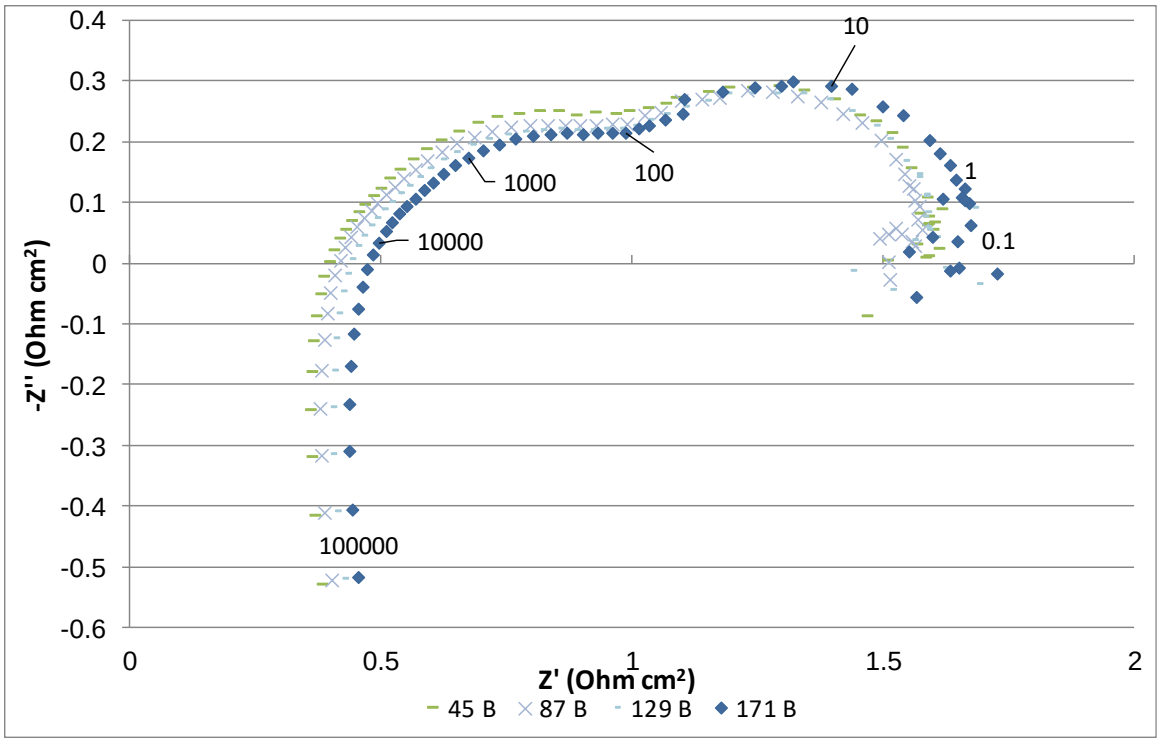


**Figure 70: Ningbo 81 fuel cell impedance performed after electrolysis galvanostatic period. Performed at 800ºC 1:1:2 $H_2$:$H_2O$:$N_2$ with a total flow rate of 240ml $min^{-1}$.**

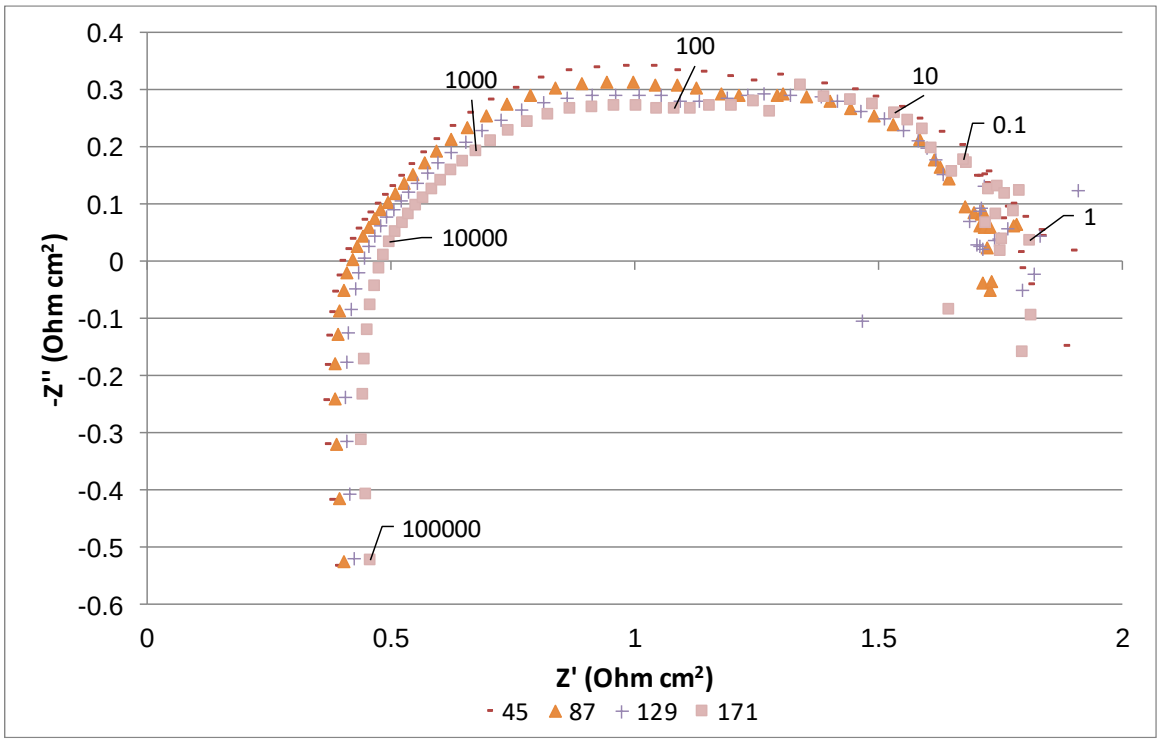


**Figure 71: Ningbo 81 electrolysis impedance performed after electrolysis galvanostatic period. Performed at 800ºC 1:1:2 $H_2$:$H_2O$:$N_2$ with a total flow rate of 240ml $min^{-1}$.**

### 6.4.2 Ningbo 82

Figure 72 shows the results of Ningbo 82 operated cyclically for 160 hours. This shows an electrolysis degradation rate of 61 mV $kh^{-1}$ and a fuel cell degradation rate of 32mV $kh^{-1}$.

The cell shows a much smaller degradation rate compared to Ningbo 81 for both fuel cell and electrolysis operation, however the electrolysis degradation rate is still twice the degradation rate observed in fuel cell operation. The electrolysis step shows a small rapid voltage increase at the beginning of each step. Subsequently each step shows a slower voltage degradation. The rate of degradation in each step is higher than the overall rate of degradation. Fuel cell operation also shows a small spike at the beginning of each step however the period after this shows very little degradation. The rate of degradation in each step and the overall degradation rate for fuel cell operation are very similar.

The IV curves and the calculated ASR for each are shown in Figure 73 and Figure 74. The ASR is lower for both fuel cell, and electrolysis operation for this cell is lower than for Ningbo 81, while there is also very little difference between the cell ASR. In fuel cell operation the ASR was 0.69 Ω $cm^2$ and in electrolysis operation the ASR was 0.71 Ω $cm^2$. While the difference is smaller for Ningbo 82 than that in Ningbo 81 the ASR data shows the same trend in the IV data as was shown for Ningbo 81. The cell ASR after an electrolysis galvanostatic step is greater than the cell ASR after a fuel cell galvanostatic step. This is true for the ASR of both the electrolysis and fuel cell operation. The ASR degradation rate is higher for electrolysis 0.37 Ω $cm^2$ $kh^{-1}$ than fuel cell operation 0.25 Ω $cm^2$ $kh^{-1}$.

The impedance for both fuel cell (Figure 75) and electrolysis (Figure 76) operation shows very little change throughout the experiment. There is no evidence of the dependence on the previous galvanostatic step in the impedance spectra. The electrolysis operation shows a

higher resistance for the intermediate frequency to high frequency range (10,000 – 100Hz) than in the fuel cell operation. The total resistances for both fuel cell and electrolysis are very similar. The initial impedance spectra, after water was added to the gas stream, show an increase in the ohmic resistance, with a large reduction in the intermediate – high frequency resistance of the cell.

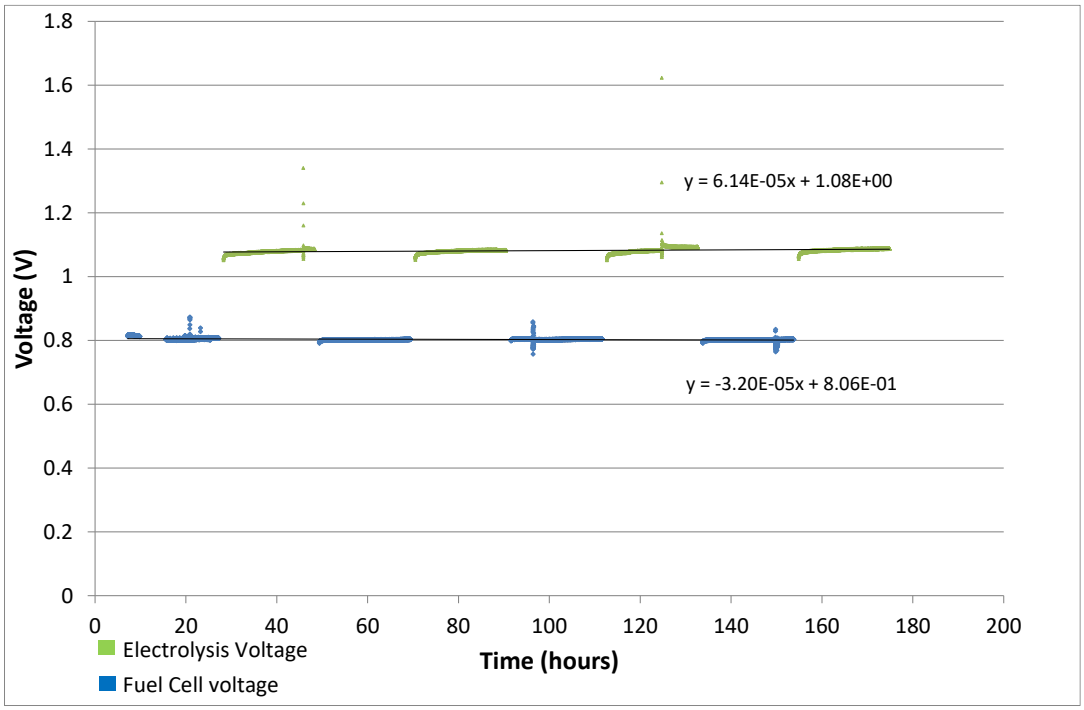


**Figure 72: Ningbo 82 electrolysis degradation rate at 800°C 1:1:2 $H_2$:$H_2O$:$N_2$ with a total flow rate of 240ml $min^{-1}$ cyclic operation between electrolysis −0.16 A $cm^{-2}$ (green line) and fuel cell 0.16 A $cm^{-2}$ (blue line). The cell has an average degradation rate of 61 mV $kh^{-1}$ in electrolysis operation and 32 mV $kh^{-1}$ in electrolysis operation.**

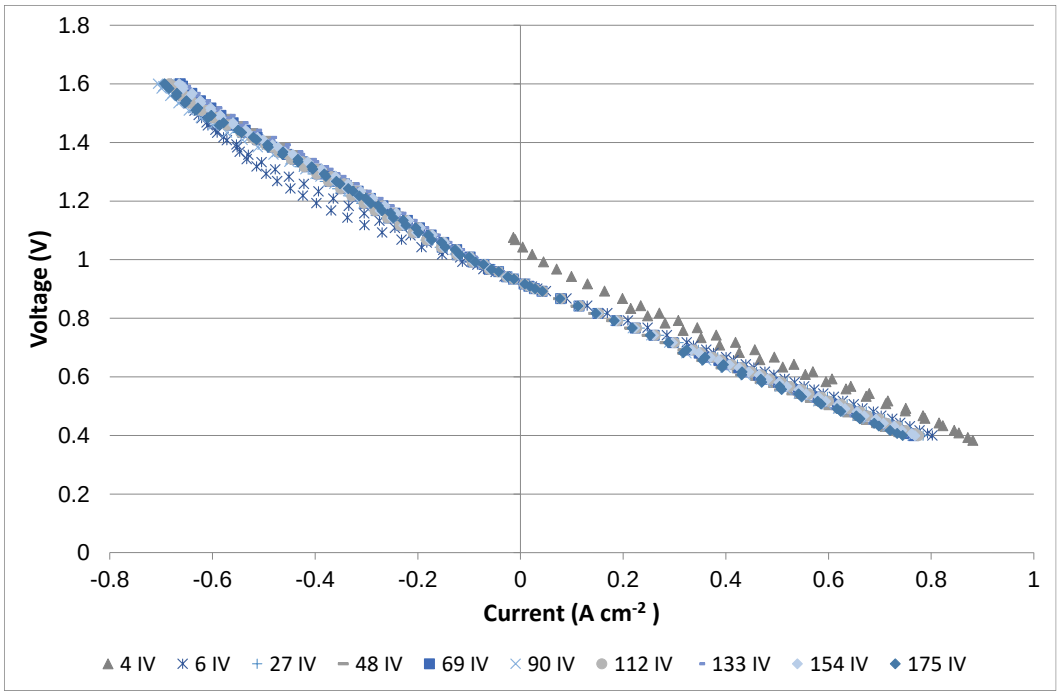


**Figure 73: Ningbo 82 IV curves performed at 800ºC 1:1:2 $H_2$:$H_2O$:$N_2$ with a total flow rate of 240ml $min^{-1}$, apart from the initial 4h curve (grey triangle) which was operated with 1:2 $H_2$:$N_2$ with a total flow rate of 180 ml $min^{-1}$.**

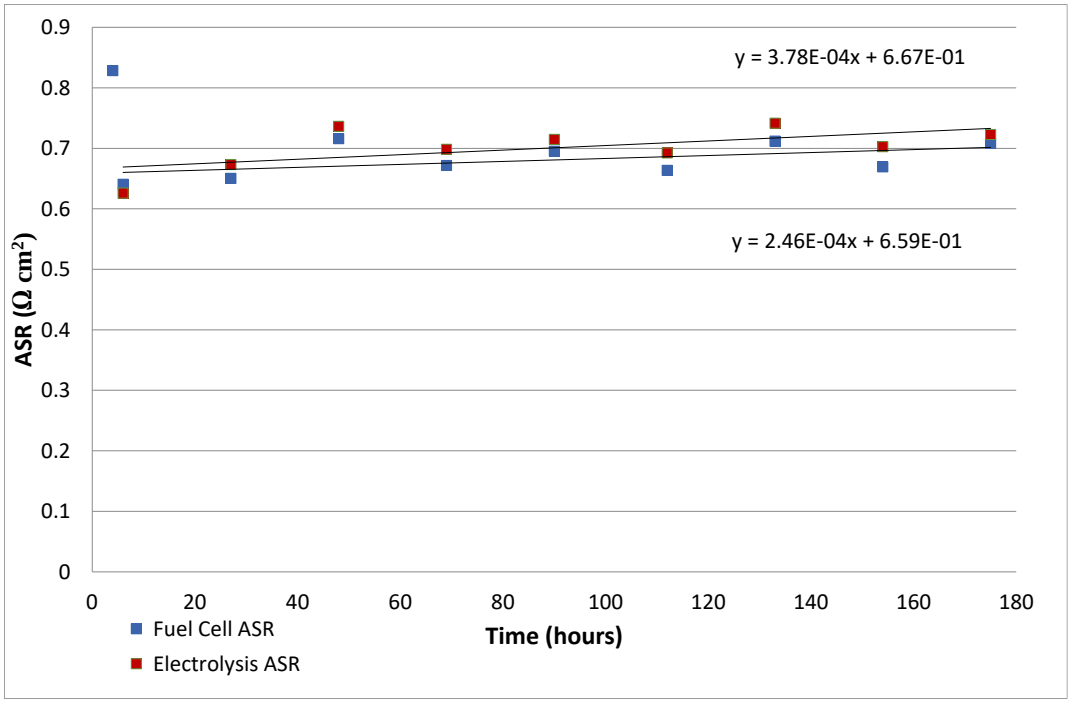


**Figure 74: Evolution of ASR for Ningbo 82 in fuel cell and electrolysis mode. ASR calculated from the IV curves in Figure 73.**

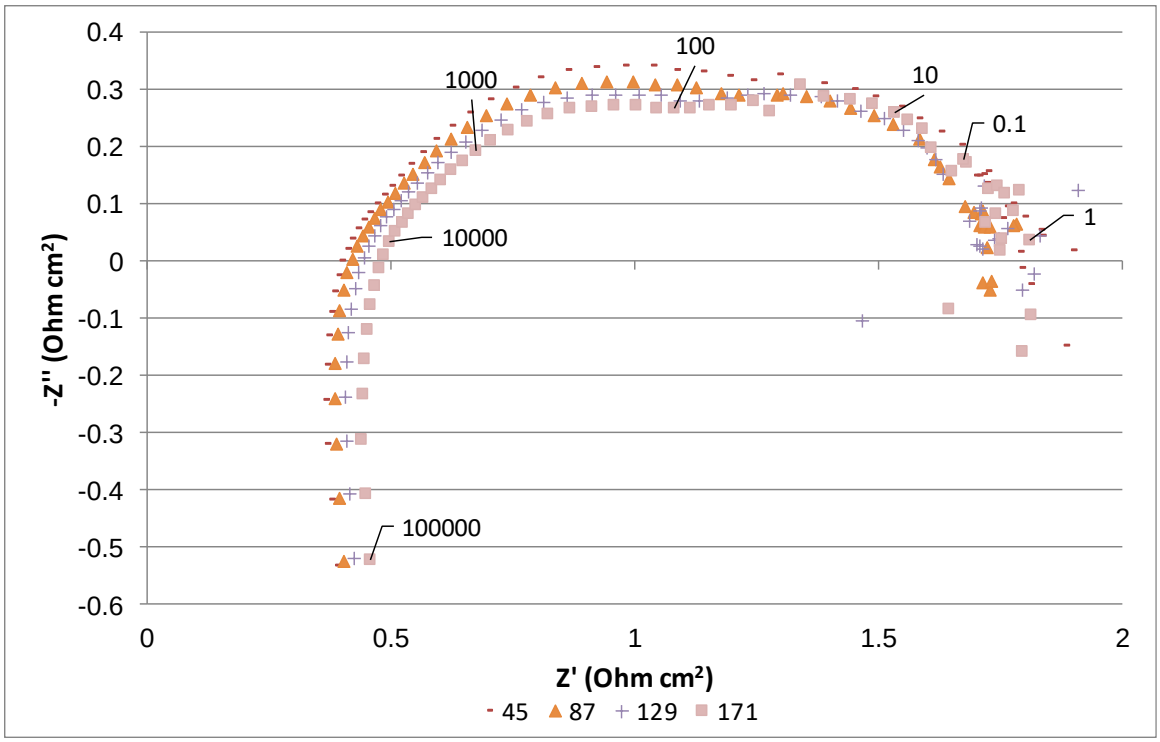


**Figure 75: Ningbo 82 fuel cell impedance spectra. Labels indicate time since start of experiment. Performed at 800°C 1:1:2 $H_2$:$H_2O$:$N_2$ with a total flow rate of 240ml $min^{-1}$, apart from the initial 4h spectrum which was operated with 1:2 $H_2$:$N_2$ with a total flow rate of 180 ml $min^{-1}$. Frequency markers are provided for 4h and 176 h.**

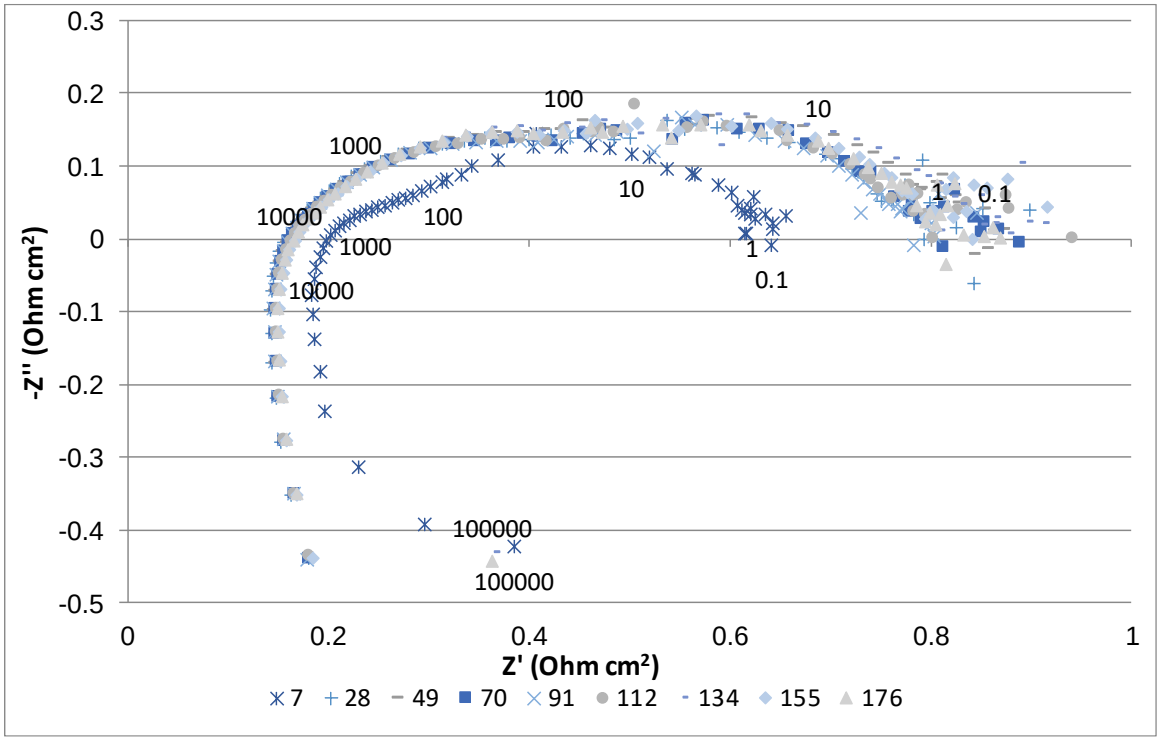


**Figure 76: Ningbo 82 electrolysis impedance spectra. Labels indicate time since start of experiment. Performed at 800°C 1:1:2 $H_2$:$H_2O$:$N_2$ with a total flow rate of 240ml $min^{-1}$. Frequency markers are provided for 7 and 176 h spectra.**

## 6.5 Rate of cycling

In the next two experiments (Ningbo 39 and Ningbo 44) the time period for electrolysis and fuel cell steps was different therefore they have been separated. It should also be noted that for Ningbo 39 the water content in the feed flow to the cell was reduced therefore comparisons should be treated with caution.

### 6.5.1 Ningbo 39 cyclic performance SOFC to SOE 100 hours

It was intended that the cell would be operated with a 50:50 water to hydrogen mixture. However, after the test an issue with the water supply was identified which resulted in a tenfold reduction in the water supply to the cell. This cell was operated with 60ml $min^{-1}$ $H_2$ and 6ml $min^{-1}$ $H_2O_{(g)}$ with 120 ml $min^{-1}$ $N_2$. The reduction in water is reflected in both the cell OCV and performance in electrolysis operation. The results from the cell have been included, however, the results have been interpreted with respect to the reduced water supply to the cell.

In this test the cell was operated for 15 hours in fuel cell operation and 15 hours in electrolysis before going through 6 cycles of fuel cell and electrolysis operation with a period of 5 hours. The overall rate of degradation in fuel cell operation was 44 mV $kh^{-1}$ and the electrolysis degradation was 320 mV $kh^{-1}$.

The fuel cell degradation appeared to be constant throughout the experiment with a sharp increase in voltage at the start of each step. The electrolysis voltage was very unstable and showed large voltage fluctuations. It is thought that the voltage fluctuations were due to the water supply fluctuating wildly as it was operating at the edge of its ideal range and struggled to keep a constant flow rate. The fluctuating water supply appears to have no effect on the

fuel cell voltage which is interesting as the OCV should be changing slightly and it would be expected that this would alter the fuel cell operation voltage.

The IV curve shown in Figure 78 indicates the lack of water to the cell, with very large mass transport losses in the electrolysis performance. The fuel cell performance appears very good, due to the ample supply of hydrogen to the cell. Unfortunately, due to the unavailability of the frequency response analyser no impedance spectra were recorded for this cell therefore further investigation of the cell's superior performance can't be performed. During the electrolysis operation the cell is operating in a region of water starvation. The cell shows a reduction in both fuel cell and electrolysis performance over the experiment.

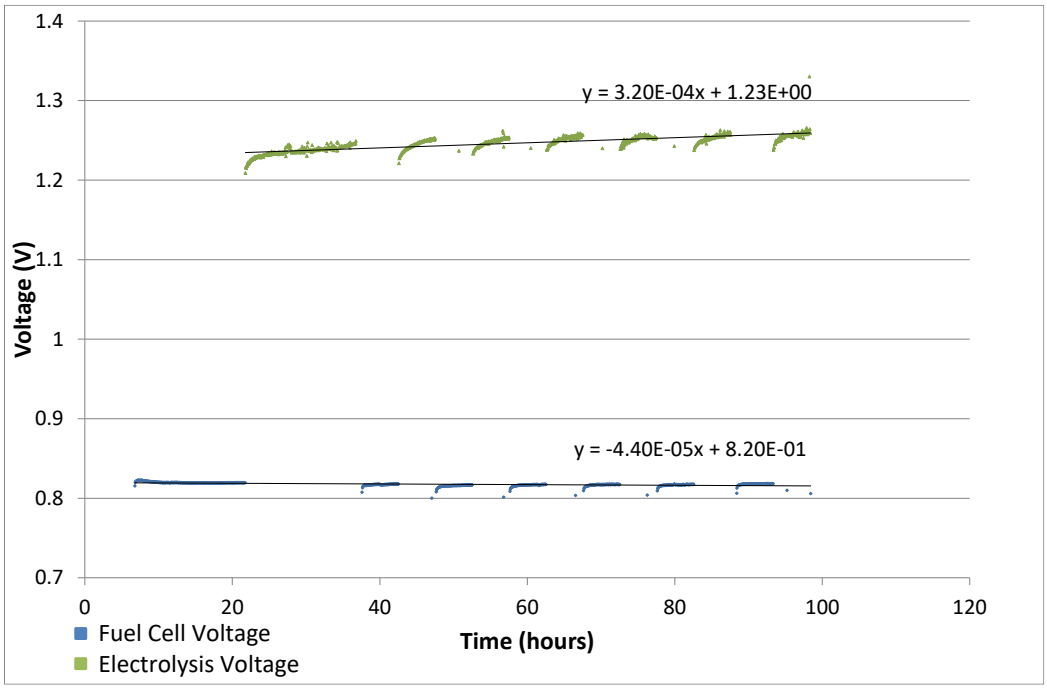


**Figure 77: Ningbo 39 cyclic operation between electrolysis −0.16 A $cm^{-2}$ (green line) and fuel cell 0.16 A $cm^{-2}$ (blue line). Experiment performed at 800ºC with 32:3:65 $H_2$:$H_2O$:$N_2$ total flow rate 186ml $min^{-1}$. The cell has an average degradation rate of 320mV $kh^{-1}$ in electrolysis operation and 44mV $kh^{-1}$ in electrolysis operation.**

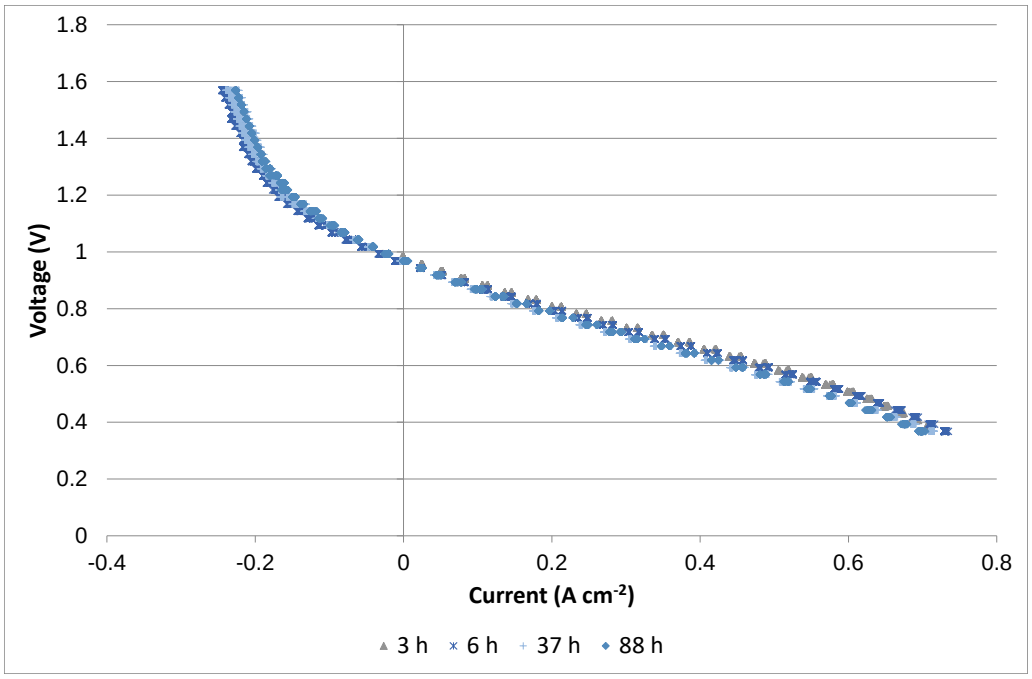


**Figure 78: IV curves for Ningbo 39, the cell was operated with low water content due to problems with the water controller. Thee experiment performed at 800ºC with 32:3:65 $H_2$:$H_2O$:$N_2$ total flow rate 186ml $min^{-1}$.**

### 6.5.3 Ningbo 44

This was run to the same testing regime at the previous cell (Ningbo 39), however, the period of operation was longer and the water supply issues had been corrected. In this experiment the cell was operating with a 60ml $min^{-1}$ $H_2$, 60ml $min^{-1}$ $H_2O$ and 120 ml $min^{-1}$ $N_2$ gas feed. The galvanostatic data is shown in Figure 79. The electrolysis degradation appears constant throughout the experiment at 126 mV $kh^{-1}$. The fuel cell degradation appears constant for the first 110 hours at 64 mV $kh^{-1}$. After 110 hours there is a sudden drop in performance, but no equivalent decrease in electrolysis performance is observed. While the fuel cell data after 110 hours will be excluded from the results an attempt will be made to explain what happened using the available IV and impedance data.

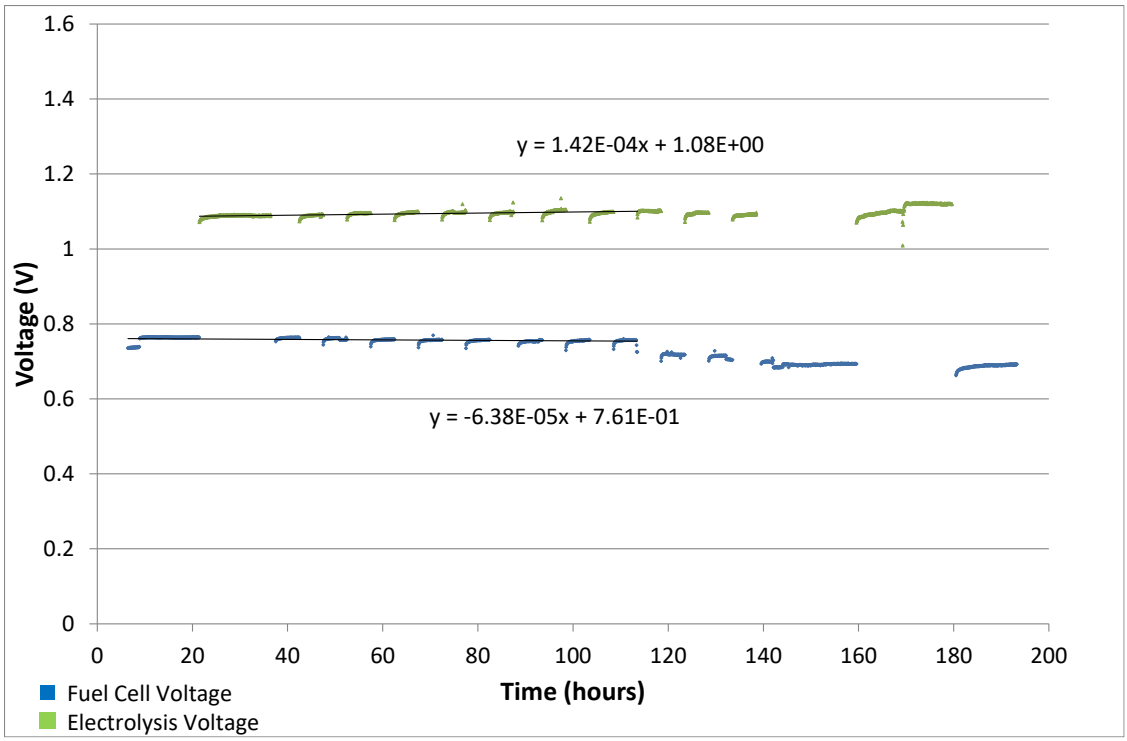


**Figure 79: Ningbo 44 cyclic operation between electrolysis −0.16 A $cm^{-2}$ (green line) and fuel cell 0.16 A $cm^{-2}$ (blue line). Performed at 800ºC with 1:1:2 $H_2$:$H_2O$:$N_2$ total flow rate 240ml $min^{-1}$. The degradation in this cell has been measured over the first 110 hours as after this there was a change in the experimental conditions resulting in changes in performance. The degradation rate for fuel cell and electrolysis operation has been measured in the region before 110 hours. The cell has an average degradation rate of 140mV $kh^{-1}$ in electrolysis operation and 64mV $kh^{-1}$ in electrolysis operation.**

The curves for fuel cell and electrolysis degradation show that the electrolysis degradation is about twice as high as the fuel cell degradation. While each electrolysis step shows a high rate of degradation the overall rate of degradation is similar to that observed with a longer electrolysis and fuel cell step.

#### 6.5.3.1 Reason for the drop in fuel cell performance:

The IV curve shows an increase in ASR for both fuel cell and electrolysis, in the curve recorded at 140 hours compared to the 80-hour curve. While the increase in ASR for the fuel cell curve is 0.2 Ω $cm^{-2}$ the increase in electrolysis ASR is 0.1 Ω $cm^{-2}$ half that of the fuel cell ASR increase. The impedance at low frequency is too scattered to reliably fit to an equivalent circuit therefore the equivalent circuit with a single RCPE element is used for the equivalent circuit shown in Figure 32. The impedance spectra show an increase in ohmic resistance between 80 and 140 hours. The increase in ohmic resistance is 0.082 Ω $cm^{-2}$ for both electrolysis and fuel cell operation. There is also an increase in the high frequency impedance of 0.045 Ω $cm^{-2}$ for electrolysis and 0.039 Ω $cm^{-2}$ for fuel cell operation. The impedance spectra account for the increase in ASR observed in the IV curve for electrolysis operation but do not account for the increase in ASR observed in the fuel cell operation. Below 100 Hz the impedance spectra become very scattered due to fluctuations in the cell voltage, therefore it is impossible to draw any conclusions about the contribution of low frequency impedance to the overall ASR. Table 3 summarised the increase in resistance between 80 and 140 hours from the IV curves and impedance data.

**Table 3: Increase in resistance observed between 80 and 140 hours for Ningbo 44. The low frequency region showed too much scatter to model using EIS therefore the equivalent circuit shown in Figure 32 has been used.**

| | Increase between measurements at 80 and 140 hours. | | |
|---|---|---|---|
| | IV curve | Impedance | |
| | | Ohmic ($\Omega$ cm$^2$) | High Frequency Arc ($\Omega$ cm$^2$) |
| Fuel cell | 0.195 | 0.082 | 0.039 |
| Electrolyis | 0.108 | 0.082 | 0.045 |

The high frequency and ohmic parts of the impedance spectra account for the increase in ASR observed in the IV curve for electrolysis operation but not for fuel cell operation. The increase in fuel cell operation may be a low frequency response of the system, which could indicate that it is mass transport based. It is hypothesised that the decrease in voltage during fuel cell operation (decrease in performance) is due to a decrease in hydrogen flow which does not affect the electrolysis performance. There is limited evidence of an increase in the mass transport in the IV curve at 140 hours however there also appears to be a larger increase in the ohmic resistance of the cell, which wouldn't have been caused by a lack of hydrogen to the cell. There were no problems observed with the equipment which would explain a decrease in the hydrogen supply. Although the mass flow controllers are sensitive to the supply pressure. An intermittent drop in the supply pressure would have resulted in a decrease in flow to the cell. This may have led to oxidation of the hydrogen electrode, causing the drop in ohmic resistance observed. This wouldn't however account for the difference between the electrolysis and fuel cell impedance and IV curves.

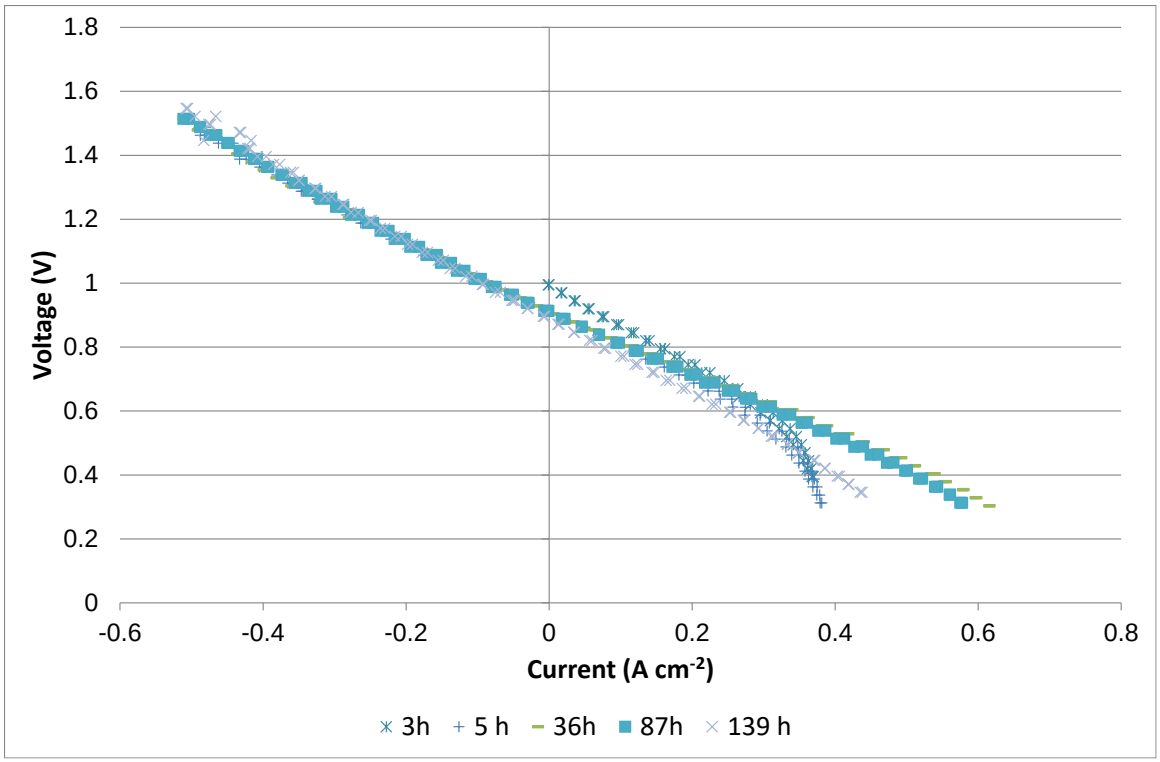


**Figure 80: IV curves for Ningbo 44. Performed at 800°C with 1:1:2 $H_2$:$H_2O$:$N_2$ total flow rate 240ml $min^{-1}$, apart from the 3h curve which has 1:1 $H_2$:$N_2$ total flow rate 120ml $min^{-1}$.**

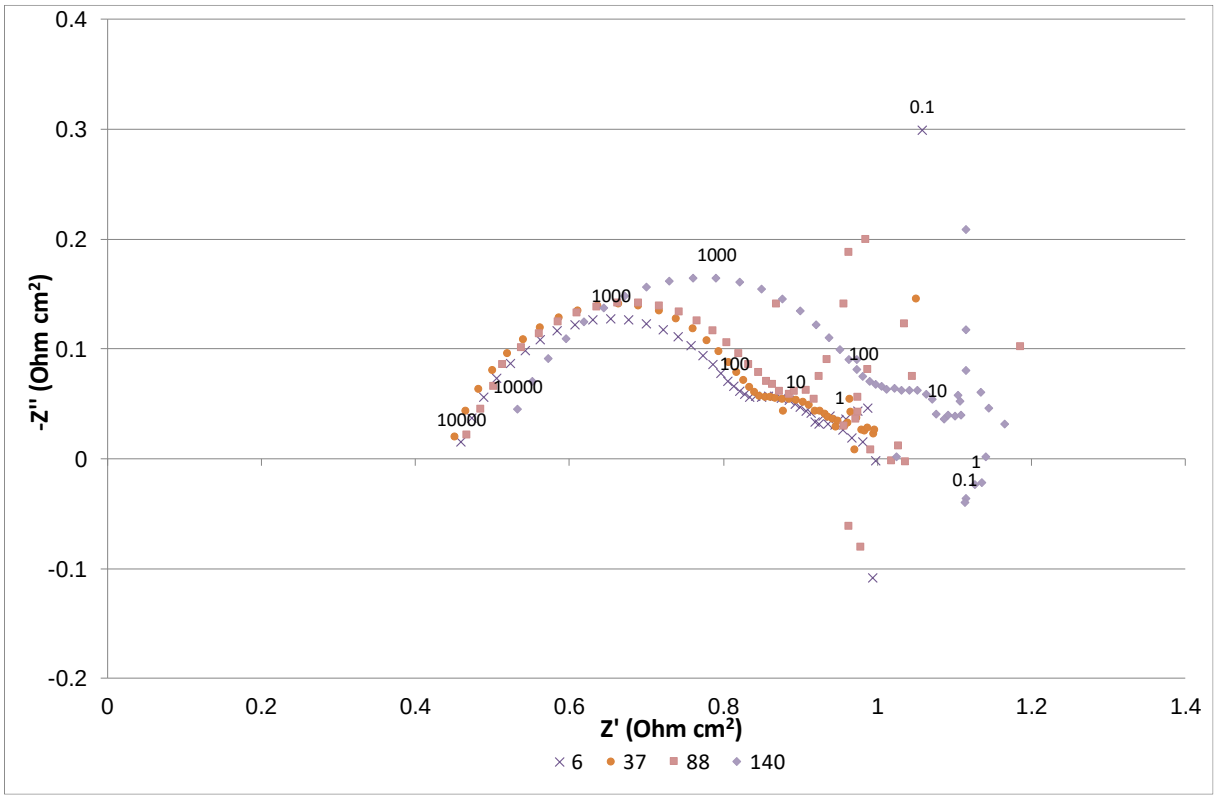


**Figure 81: Ningbo 44 electrolysis impedance spectra. Labels indicate time since start of experiment. Performed at 800°C with 1:1:2 $H_2$:$H_2O$:$N_2$ total flow rate 240ml $min^{-1}$. Frequency markers provided for 6 and 140 hours.**

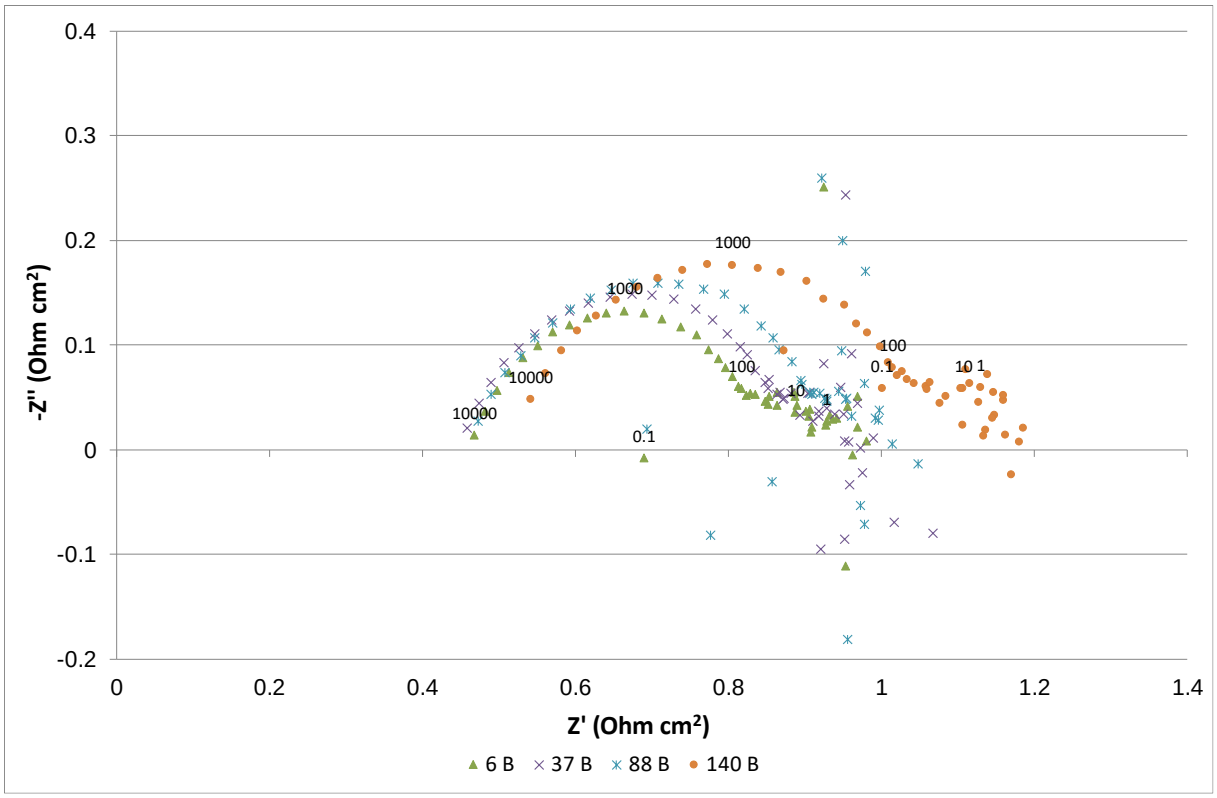


**Figure 82: Ningbo 44 fuel cell impedance spectra. Labels indicate time since start of experiment. Performed at 800ºC with 1:1:2 $H_2$:$H_2O$:$N_2$ total flow rate 240ml $min^{-1}$. Frequency markers provided for 6 and 140 hours.**

## 6.6 Discussion

### 6.6.1 Cell performance Electrolysis vs fuel cell.

In the first part of this chapter the baseline cell degradation in fuel cell (Ningbo 56) and electrolysis (Ningbo 50) operation was investigated. There are a number of observations made about the performance of the cells in electrolysis and fuel cell operation.

When the cell is operated with a 50:50 $H_2$:$H_2O$ ratio the IV curves show a slightly higher ASR for electrolysis mode than fuel cell mode. For a perfectly reversible cell the ASR would be expected to be the same for both modes of operation. The impedance spectra for Ningbo 56 and Ningbo 50 don't show the difference in performance observed in the IV curves. The impedance spectra for Ningbo 50 and Ningbo 56 were compared at 7 hours. This shows the

initial performance of the cell before changes due to operation in fuel cell or electrolysis operation. The cells show very similar total impedance for fuel cell and electrolysis operation. Ningbo 56 shows a lower electrolysis impedance than fuel cell impedance. For both Ningbo 56 and Ningbo 50 the cells show a lower high frequency for fuel cell than electrolysis. Both cell's also show a larger impedance at low frequency (100−0.1Hz) for fuel cell than electrolysis operation.

### 6.6.2 Cell conditioning

At the start of each electrolysis or fuel cell step there was an increase in the voltage of operation. In fuel cell operation this is associated with an increase in performance and in electrolysis this indicates a decrease in performance. There are a number of possible causes for this behaviour;

- During fuel cell operation the cell is operating exothermically. The cell may undergo some initial heating during operation which leads to an increase in performance. Any heating effects were below the sensitivity of the thermocouple positioned by the cell. The temperature increase would reach an equilibrium at which point the performance increase would be stabilised.
- During electrolysis the cell is operating below 1.3V therefore endothermically. There could be a decrease in cell temperature during the experiment. It was not possible to get a thermocouple close enough and with enough accuracy to measure a change in cell temperature during the experiment and it was therefore impossible to determine definitively whether the temperature change contributes to this behaviour. Ningbo 81 showed the largest cell conditioning at the start of the

experiment. However, the cell was operating at ~1.3V which means that the effect is unlikely to be the cause of the difference in cell performance.

- During electrolysis operation there is the formation of an oxygen ion gradient across the cell. During fuel cell operation the oxygen ion transport is with the oxygen potential across the cell. In electrolysis operation the oxygen ions are transported against the oxygen ion gradient. As the oxygen gradient across the cell increases the potential required to move oxygen will increase.

### 6.6.3 Difference in performance of Ningbo 81 and Ningbo 82

The performance of Ningbo 81 and Ningbo 82 showed different behaviour. The initial ASR of Ningbo 81 in fuel cell operation was 1.19 Ω $cm^2$ and in electrolysis operation the ASR was 1.31 Ω $cm^2$. The initial ASR of Ningbo 82 in fuel cell operation was 0.69 Ω $cm^2$ and in electrolysis operation the ASR was 0.71 Ω $cm^2$. This difference in performance is attributed to poor cell contacting for Ningbo 81 on either the hydrogen or oxygen electrode which can be seen in the impedance spectra of the cells with an ohmic resistance of 0.4 Ω $cm^2$ for Ningbo 81 and 0.15 Ω $cm^2$ for Ningbo 82.

Another difference in the performance of the cells is in the conditioning of the cell at the start of each electrolysis step. The galvanostatic data for Ningbo 81 shows much greater conditioning at the start of each electrolysis step than that is observed in Ningbo 82. The two effects are thought to be linked due to the formation of an oxygen gradient across the cell in electrolysis operation. For a cell with poor contacting such as Ningbo 81 the localised current density is higher than for a cell with good contacting such as Ningbo 82. The current density is directly linked to the oxygen ion gradient across the cell as a larger gradient will be performed in a cell with poor contacting. Therefore, it is thought that the poor cell contacting

leads to larger oxygen ion gradient across the cell which in turn leads to large initial degradation of each electrolysis step.

### 6.6.4 Degradation

In this chapter the rate of degradation was compared when the cell was operated in fuel cell, electrolysis and cyclically between fuel cell and electrolysis mode. There is a large variation in the results which are summarised in Table 4 however there are some clear trends in the data. The degradation rate for electrolysis operation was consistently double, or more, than the degradation rate observed in fuel cell operation for the same cell.

It was found that the rate of degradation is higher in electrolysis operation than fuel cell operation. Table 4 shows an overview of the degradation rates observed. The fuel cell degradation rate was between 32 and 77 mV $kh^{-1}$ while the electrolysis degradation rate was between 66 and 320 mV $kh^{-1}$.

That the electrolysis degradation rate is larger than the fuel cell degradation rate is similar to results found previously by other researchers [108,130,170,171]. The previous work has also been conducted on cells which operate at high current densities which is a major contributing factor to the overall degradation rate. In this work a very small current density has been used therefore the degradation due to the current of operation should have been minimised.

To a larger or lesser extent the cells operated in this chapter showed some initial conditioning during their operation, this occurred over the first 20 – 30 hours of operation and may result in an improvement or worsening of cell performance. There are many reasons for the improvement in performance during this period. It may be due to sintering of the oxygen electrode, especially the applied wet LSM paste. If the cell wasn't fully reduced during the reduction stage continuing cell reduction resulting in improved anode conduction. The

impedance results show that there is often a small change in the ohmic resistance of the cell, while there is normally a much larger change in the high frequency impedance of the cell. The high frequency arc is dominated by charge transfer in the TPB as discussed by Barfod et al [172]. As nickel oxide is reduced the length of TPB will be increased and therefore there will be a reduction in the high frequency arc of the cell impedance.

There has been little work which shows different rates of degradation for a cell operated cyclically between electrolysis and fuel cell modes[106,146,173]. That the degradation rate is different for the electrolysis and fuel cell degradation suggests that there are different processes contributing to each. There could be a number of reasons for the different electrolysis and fuel cell degradation rates:

- The electrolysis and fuel cell processes have different rate limiting steps therefore degradation in different areas affects the performance differently. For example, if the fuel cell performance is limited on the oxygen electrode by the rate at which oxygen can be broken down, whereas the electrolysis is limited by the diffusion of water through the hydrogen electrode, then changes on the hydrogen or oxygen electrodes would result in different degradation rates.
- The electrolysis degradation is partly reversible. During fuel cell operation the degradation experienced during electrolysis operation is reversed to some extent therefore the observed degradation rates are different. The cell condition during each electrolysis step would have to reach the state of the previous step faster after each fuel cell step for the degradation to be continual which would suggest that the degradation isn’t fully reversible. An effect like this would result in different rates of degradation for electrolysis and fuel cell operation.

- The increased electrolysis degradation rate could be an artefact of the way in which the degradation rates are measured, and each cell may be degrading at the same rate for both electrolysis and fuel cell operation. However, the way in which the electrolysis degradation is measured could be affecting the way in which the results are interpreted.

**Table 4: Overview of degradation rates in Fuel Cell Electrolysis and cyclic operation. Ningbo 39 was operated under a water starvation condition therefore the degradation rate is higher than expected for electrolysis operation.**

| Cell | Operation | Fuel Cell degradation (mV $kh^{-1}$) | Electrolysis degradation (mV $kh^{-1}$) | Initial performance | |
|---|---|---|---|---|---|
| | | | | Fuel cell ASR ($\Omega$ $cm^2$) | Electrolysis ASR ($\Omega$ $cm^2$) |
| Ningbo 56 | Fuel Cell | −53 | | 2.6 | 2.8 |
| Ningbo 50 | Electrolysis | | 143 | 1.75 | 2.3 |
| Ningbo 44 | Cyclic | −64 | 126 | | |
| Ningbo 81 | Cyclic | −77 | 145 | 1.2 | 1.3 |
| Ningbo 82 | Cyclic | −32 | 61 | 0.62 | 0.66 |
| Ningbo 39 | Cyclic | −44 | 320 | | |

### 6.6.5 Rate of cycling

Investigations on the effect of cycling rate on the cell degradation are at an early stage. Initial results on the cell performance with different cycling rates show that a short cycling period does not lead to greater degradation but the same trend with an electrolysis degradation rate twice the fuel cell degradation rate is observed. There is also evidence that the electrolysis degradation rate is much faster with low water content and this will be investigated further in the next chapter. It is interesting that with low water content the cell shows a very rapid electrolysis degradation of 320mV $kh^{-1}$ but a very slow fuel cell degradation of −44mV $kh^{-1}$.

This is interesting as it is further evidence that there is a disconnect between the degradation in fuel cell operation and the degradation in electrolysis operation. Further work is planned to investigate the effect of different rates of cycling on the performance of the cell.

## 6.7 Conclusions

In this chapter the degradation of solid oxide cells in fuel cell and electrolysis operation has been investigated. Initially the rate of degradation in just fuel cell or electrolysis operation was investigated. The fuel cell degradation rate was found to be 57 mV $kh^{-1}$, and the electrolysis degradation rate was found to be 140 mV $kh^{-1}$. Cells were then operated cyclically and it was found that the degradation rate of the cells is dependent on whether they were operated in electrolysis or fuel cell operation. A cell operated cyclically between fuel cell and electrolysis was found to have a degradation rate for fuel cell and electrolysis operation which was different.

It is thought that part of the degradation observed in electrolysis operation is reversible. During fuel cell operation the degradation observed in the electrolysis steps is reversed therefore a low degradation rate is observed. Each time the electrolysis starts there is a rapid period of degradation back to the previously degraded state. This reversal in degradation leads to a higher rate of degradation in electrolysis than fuel cell operation.

It was found that in electrolysis there was a larger conditioning period at the beginning of each electrolysis step than that was found during the fuel cell steps. The amount of conditioning is thought to be linked to ohmic resistance of the cell. The larger ohmic resistance which is a sign of poor contacting on the electrode surface creates a larger oxygen gradient over the cell which leads to a larger conditioning period of the cell.

# 7 Electrolysis degradation as a function of water partial pressure

## 7.1 Introduction

In this chapter the degradation and performance of solid oxide cells operated in electrolysis mode will be discussed. The degradation in electrolysis operation has been less widely studied than in fuel cell operation; however a lot of work is currently looking at SOE degradation, especially degradation at high current densities [26,105,108,113,135,174]. This work attempts to investigate the effect of water concentration on performance and degradation. It was previously found that the water content can have a severe effect on cell degradation [113]. However, this is also associated with operation at a higher current density.

In an ideal situation the fuel supply to the cell would be pure water (as steam). Under this environment nickel would oxidise, therefore hydrogen is added to the fuel. No information on the $H_2O$:$H_2$ ratio required to prevent nickel oxidation on the hydrogen electrode could be found. Most authors use a mixture of hydrogen, water and inert carrier gas in the fuel stream of a solid oxide cell. It is assumed that a carrier gas is used to prevent issues with water condensing before entering the high temperature environment in the fuel stream at high water concentrations. Due to the equipment being used in this work there are limits on the maximum water flow rate to the cell, the steam generators also require a minimum gas flow rate to generate a stable steam supply. Therefore 100% water concentrations have not been possible. In the majority of the work presented in this chapter a large quantity of Nitrogen was

required as there was not perfect sealing of the cell. Reducing the nitrogen supply was attempted but resulted in the re−oxidation of the cell.

During the experiments the degradation was monitored from the galvanostatic performance of the cell. IV curves and impedance spectra were collected during breaks in the galvanostatic operation of the cell. These were used to monitor the degradation of the cell. It is expected that changing the water concentration will have a major effect on the hydrogen electrode and a minimal effect on the oxygen electrode, however other effects may play a role in degradation on the oxygen electrode. The degradation mechanisms which are expected to be taking place in each area of the cell with changing water content are explained in more detail below.

### 7.1.1 Expected oxygen electrode degradation

It is expected that the effect of oxygen electrode degradation should not be dependent on the water content of the hydrogen electrode as the conditions which the oxygen electrode experiences should be very similar for each experiment. There was no direct contact between the steam supply and the oxygen electrode. The experiments were performed at the same and constant current density and the oxygen electrode should experience very similar conditions throughout the experiments. A major source of oxygen electrode degradation in electrolysis operation is due to the delamination of the electrode caused by pore formation in the electrolyte−oxygen electrode interface, which is due to the high oxygen partial pressure at the interface as a result of high operational current of the cell [120,127]. It is expected that the degradation of the oxygen electrode will be small because the current density of operation is low −0.166A $cm^{-2}$ which should minimise the degradation due to the delamination or pore formation in the electrolyte − oxygen electrode interface.

While efforts were made to ensure that the oxygen electrode degradation is minimised and conditions are identical for each experiment, the conditions of the oxygen electrode will not have been identical for each experiment. As the cells had different gas mixtures the OCV will change and the overpotentials, especially the mass transport overpotential, will be different for each experiment. A change in OCV and overpotential will result in differences to the operational voltage. This may result in a different cell temperature and polarisation of the oxygen electrode for each experiment. It is not expected that small differences in cell temperature will play a major role in the cell degradation. No large differences in cell temperature were observed during cell operation, however measurements cannot identify the temperature difference inside the electrode which may be greater. The difference in polarisation of the cell should be small, however influence on the degradation of the cell is currently unknown. Under cathodic polarisation the surface of an LSM catalyst has been shown to undergo changes which lead to an improvement in performance [101]. However, the applied potentials were much greater in that work. Nevertheless, it demonstrates the changes which can occur with different applied potentials.

### 7.1.2 Expected electrolyte degradation

As for the oxygen electrode the electrolyte should experience a very similar environment for each of the experiments as the temperature and oxygen flux through the electrolyte should be the same for each experiment. However, there will be different potentials acting across the cell and the electrolyte conditions close to the anode will be different. The electrolyte can break down at high potentials, over 1.8–1.9V [139,175], which leads to poor oxide ion conduction through the electrolyte.

Electrolyte breakdown can lead to electronic conduction through the electrolyte. The resulting short circuiting would reduce the hydrogen production of the cell. Short−circuiting of the cell would reduce the cell OCV. However, if this occurs during cell operation the effect will be observed as a decrease in the cell's ohmic resistance and an increase in performance. The presence of short circuiting should be observed as a reduction of the cell's ohmic resistance in the impedance spectra.

Large cell operating potentials could result in an increased rate of electrolyte breakdown. During cell operation an oxygen gradient is induced across the YSZ electrolyte, and oxygen ions are transported from the hydrogen to oxygen electrodes. This gradient is the opposite of the gradient formed in fuel cell operation and is against the natural gradient potential of the cell. If there is insufficient oxygen available from $H_2O$ on the hydrogen side this can lead to the removal of oxygen from the YSZ structure. Damage to the YSZ structure would lead to increased ohmic resistance in the cell. The degradation may be reversible, if the oxygen gradient is reversed, there is an increase in water supply to the hydrogen electrode, or there is a reduction in current density across the cell; the cell may undergo recovery as oxygen is reincorporated into the YSZ structure. However, the extent of the recovery will depend on the ability of the YSZ structure to undergo redox cycling without structural change.

The voltages of operation will generally be minimised as the current density is small. It is reported that electronic conduction through the electrolyte occurs above 1.8−1.9V which is well above the cell operating voltage in these experiments [139,175]. The extent to which breakdown of the YSZ electrolyte is due to oxygen stripping from the structure is unknown.

### 7.1.3 Expected hydrogen electrode degradation

In these experiments it is expected that the hydrogen electrode will suffer the majority of the cell degradation. The cell will be in contact with high water contents, and it is widely acknowledged that high water partial pressures can lead to degradation for a variety of reasons:

- Nickel Oxidation
- Nickel evaporation / nickel agglomeration
- Contaminants in the fuel supply or from the cell sealing.

The degradation due to nickel oxidation should be small even with a relatively small quantity of hydrogen entering the cell, it has been found that ~1% hydrogen is required to prevent degradation [130] in this work a large quantity of hydrogen is added to the fuel supply so oxidation shouldn't be an issue for the cell. However, this may be dependent on the setup of the cell, presence of any leaks and other experimental factors.

It has been shown that high water partial pressures lead to an increased rate of Ostwald ripening for nickel particles [176,177]. Ostwald ripening is a combined effect of particle agglomeration by particle dissolution and redepositing onto the surface of another particle. Increasing the water content of the fuel increases the ability of Nickel to dissolve and leads to increased agglomeration.

Work performed by a number of groups [174,178–180] has found that one of the major degradation mechanisms during SOE operation is caused by reduction in the nickel available for reaction through agglomeration of particles. This leads to a loss of nickel percolation and reduced nickel surface area.

Silica evaporation is known to cause the degradation of solid oxide cells during electrolysis. Silica is present in the sealing pastes used in solid oxide cells. With increasing $H_2O$ content, the silica becomes more volatile which has been shown to lead to silica being deposited within the hydrogen electrode. Silica causes blocking of the TPB leading to a loss of performance [113,150].

Other contaminants can also play a role in cell degradation [150]. Much of the study on cell degradation at different water partial pressures has been performed in fuel cell operation. The effect of high water partial pressures on degradation during electrolysis operation may be very different to that observed in fuel cell operation. During electrolysis operation at high water partial pressures contaminants can become oxidised and travel to the TPB as the cell is attempting to transfer oxygen to the oxygen electrode. The contaminants may become reduced. If this occurs, the contaminants will be preferentially deposited in areas of high activities in the cell which will reduce the total length of TPB for water reduction and increase the polarisation overpotential of the cell.

The aim of this chapter is to investigate the various degradation mechanisms which are occurring during electrolysis operation and determine the effect to which these are affected by the concentration of water entering the cells.

## 7.2 Experimental

The experimental setup has been discussed in more detail in the experimental chapter 4 and will be briefly summarised here:

For these tests the Ni−YSZ /YSZ / LSM−YSZ SOCs produced by Ningbo Institute were used. Hydrogen electrode contacting was made using a silver mesh with two 0.71mm silver wires

as current collectors and voltage sense wires. Oxygen electrode contacting was performed using a gold mesh pressed into an LSM paste hand painted to the surface, with two 0.71mm wires soldered to leads off the gold mesh. Gas and water were controlled with the Bronkhorst CEM gas mixer and evaporator. The cell was compressed horizontally between two MACOR holders with gaskets made from Thermiculite 866 (Flexitallic).

The cell was heated to 800 $^{o}$C at 5 $^{o}$C min$^{-1}$ with 120 ml min$^{-1}$ $N_2$ and 60 ml min$^{-1}$ $H_2$ to the hydrogen electrode and 1L min$^{-1}$ air on the oxygen side. Once at 800$^{o}$C the cell was left to reduce for 1 hour before performing an initial IV curve and impedance measurements. The hydrogen electrode gas mixture was then changed to the experimental gas composition; the oxygen electrode gas flow rate was 1L min$^{-1}$ throughout the experiment. The cell was then left for a further 2 hours for the steam supply to stabilise before a second IV curve and impedance measurements were performed and the rest of the experiment continued. Once finished the cell was cooled under the experimental gas conditions at 5$^{o}$C min$^{-1}$.

Five different gas compositions were used. The water : hydrogen ratios were; 5:95, 50:50, 80:20, 95:5, 100:0; with a total flow rate of 120 ml min$^{-1}$. In each case a carrier gas of 120ml min$^{-1}$ $N_2$ was used to avoid water condensing on the tubes. Experiments without the carrier gas were attempted however the cells failed due to catastrophic re−oxidation of the cells.

### 7.2.1 Electrochemical tests

All electrical measurements were made using a potentiostat/galvanostat (Solatron Model 1470E) with impedance measured on an FRA (Solatron Model 1455A). This was controlled with multistat software. Initial IV curve fuel cell operation only was performed from OCV – 0.4V – OCV. Subsequent IV curves in fuel cell and electrolysis operation were performed from OCV – 0.4V – OCV – 1.6V – OCV. The IV curves were performed as a potential

stair−step with a stair length of 30s and a step size of 25mV. IV data was recorded at 1 sample per second and the average value for the 30s reported. Impedance measurements were performed with an applied potential of ±0.1 V and a 10mV AC amplitude at frequencies between 10,000Hz (some measurements were made up to 100,000Hz) and 0.1Hz at 10 steps per decade. Short automatic averaging was applied within the multistate software. For each test the initial IV curve and impedance measurements were made with the same gas composition. All subsequent IV and impedance measurements were made under the experimental gas composition. During the galvanostatic stage of the experiment a constant current of −0.166 A $cm^{-2}$ was applied to the cell. Galvanostatic data was recorded at 1 sample per second and the average value over 200 seconds is presented. In each experiment galvanostatic operation was performed for 20 hours then an IV curve and impedance were performed. This was repeated 7 times for a total galvanic duration of 140 hours. Between each step in the experiment the cell was at OCV for 5 mins, this allows temperatures and the cell to return to a similar state before measurement of IV curves and impedance is made.

## 7.3 Results

In this section results from each of the experiments will be presented separately with discussion of the results. Each experiment consisted of a galvanostatic period consisting of 7 steps of 20 hours. IV curves and impedance spectra were taken throughout the experiment, and the results will be presented in this order. Experiments are arranged in order from least water content to highest water content.

### 7.3.1 2.5 vol% $H_2O$ Ningbo 54

#### 7.3.1.1 Ningbo 54 galvanostatic operation

The galvanostatic data for Ningbo 54 is shown in Figure 83. The cell was heated under a nitrogen hydrogen mixture (120ml $min^{-1}$ $N_2$ and 60ml $min^{-1}$ $H_2$). The cell was allowed to reduce, and initial IV and impedance spectra were performed (labelled 4h). The cell was operated for 140 hours in electrolysis operation at −0.166 A $cm^{-2}$ at 800ºC with 6ml $min^{-1}$ $H_2O_{(g)}$ (0.3g $h^{-1}$ $H_2O_{(l)}$), 114 ml $min^{-1}$ $H_2$ and 120ml $min^{-1}$ the volumetric gas ratios were 47.5 : 2.5 : 50 $H_2$ : $H_2O$ : $N_2$. With a total current of 0.5A in electrolysis the cell was operating with at utilisation of 58%, calculated as shown in Section 2.2.1. Over the course of the experiment the voltage increased by about 72mV with an average degradation rate of 512 mV $kh^{-1}$ and the cell resistance increased from 6.9 Ω $cm^2$ to 7.8 Ω $cm^2$.

Every 20 hours the galvanic operation was stopped and IV curve and impedance steps were performed. Between the galvanostatic periods during the impedance and IV curves there was a slight decrease in the voltage of operation which indicates a slight increase in performance. This then decayed quickly to a point where the degradation continued in a linear fashion after the previous galvanostatic period. There were also many upwards spikes in the voltage. These were at random points during the galvanostatic period. They are thought to be due to a problem with the water supply. The water supply was operating at the low end of its possible range and occasionally the valve would close completely which reduced the steam supply causing a brief increase in the voltage due to fuel ($H_2O$) starvation of the cell. While the average degradation rate appears to be constant the effect on degradation of the unstable water supply is unknown. At the end of the test after ~130 hours, there was a large increase in the instability of the voltage. The cause of the instability at the end of the experiment cannot be

determined from the galvanostatic data. However, it is thought to be linked to further problems with the water supply and has been further discussed with the IV and impedance data.

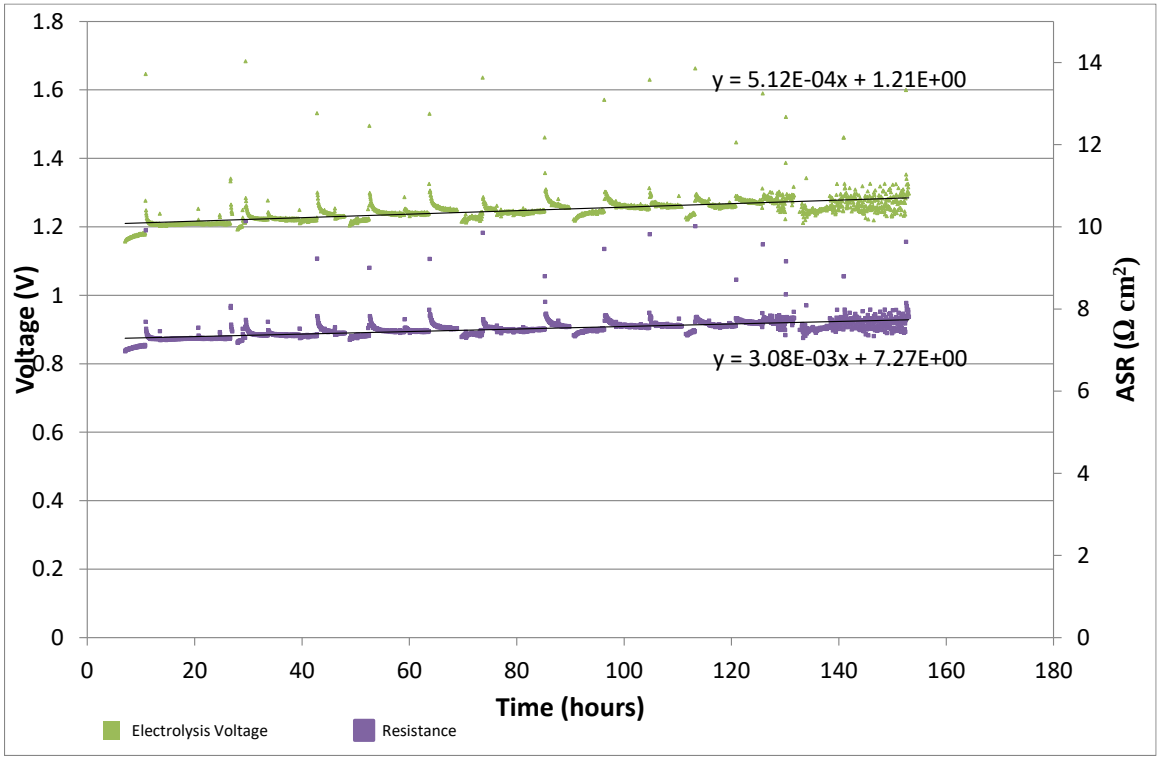


**Figure 83: Shows the galvanostatic data for Ningbo 54 which had 47.5:2.5:50 $H_2$:$H_2O$:$N_2$ ratio with a total flow rate of 240ml $min^{-1}$. The degradation rate was 512mV $kh^{-1}$. The fuel utilisation was 58% at the current during galvanostatic operation. The green line shows the cell voltage. The purple line shows the cell resistance.**

### 7.3.1.2 Ningbo 54 IV curves

The IV curves taken throughout the experiment are shown below in Figure 84. At maximum current the utilisation for fuel cell operation was 77% and in electrolysis the utilisation at maximum current was 107%, the ability of the cell to operate over 100% efficiency is likely to be due to the fact that cell is within a relatively large chamber so there will be excess fuel available for brief periods during the IV curve. As the cell is operating in electrolysis mode there could also be some utilisation of oxygen within the Ni (if there are parts not fully reduced) or YSZ structure; if operated for long periods this would be damaging to the cell.

The cell does not show any flattening of the IV curve which would indicate that electronic conduction through the electrolyte was taking place.

The initial fuel cell only IV curve at 4 hours gives an ASR based on the linear part of the IV curve of 0.81 Ω $cm^2$. Once the gas mixture is altered for the next IV curve at 6 hours there is a decrease in ASR to 0.63 Ω $cm^2$ and there is no further sign of mass transport loss. This is expected as the hydrogen flow rate has increased. After the first galvanostatic period at 27 hours the cell performance decreases significantly to an ASR of 0.87 Ω $cm^2$ which is higher than the initial ASR for fuel cell operation of the cell, from 27 hours to the end of the experiment at 153 hours. The ASR increases to a maximum of 0.94 Ω $cm^2$ at 132 hours before there is a slight decrease to 0.91 Ω $cm^2$ at 156 hours, the end of the experiment. The ASR for the cell is plotted in Figure 85, this was used to calculate the ASR degradation rate. The ASR degradation rate in fuel cell operation is 0.4 Ω $cm^2$ $kh^{-1}$ and for electrolysis is 0.66 Ω $cm^2$ $kh^{-1}$. The fuel cell regression line shows a much closer fit to the data than the electrolysis ASR degradation rate, which has a large scatter as discussed below. The electrolysis degradation rate is of a similar value as the fuel cell degradation rate which has a much lower scatter.

The ASR degradation rate measured in the IV curves is similar to the resistance degradation rate measured from the galvanostatic data in Figure 83 of 0.31 Ω $cm^2$ $kh^{-1}$.

In electrolysis operation the mass transport losses are large due to the high fuel utilisation. The loss in performance observed in fuel cell operation between 6 and 27 hours is not as evident in the electrolysis region of the IV curve. The change in electrolysis performance is partly masked by the mass transport losses however there is some loss in performance present. The mass transport losses make it difficult to assess the ASR as there is a very small

linear region in the IV curve. The ASR for each has been calculated and is plotted in Figure 85. The ASR of electrolysis is much greater than the ASR in fuel cell operation. The ASR for electrolysis at 6 and 27 hours respectively are 1.13 Ω $cm^2$ and 1.29 Ω $cm^2$.

The instability observed in the cell operation at the end of the experiment is present in the final two IV curves. However, this only appears to affect the electrolysis portion of the IV curves, while the fuel cell portion shows no instability. This leads to the conclusion that there were problems with the water supply to the cell. No obvious problems were noticed with the experimental equipment. However, the steam supply was operating at its lowest setting. One possible cause of greater instability at the end of the experiment is that there was a blockage in the valve, or the flow controller closed off too much. An extra filter was added before the water mass flow meter to prevent future issues.

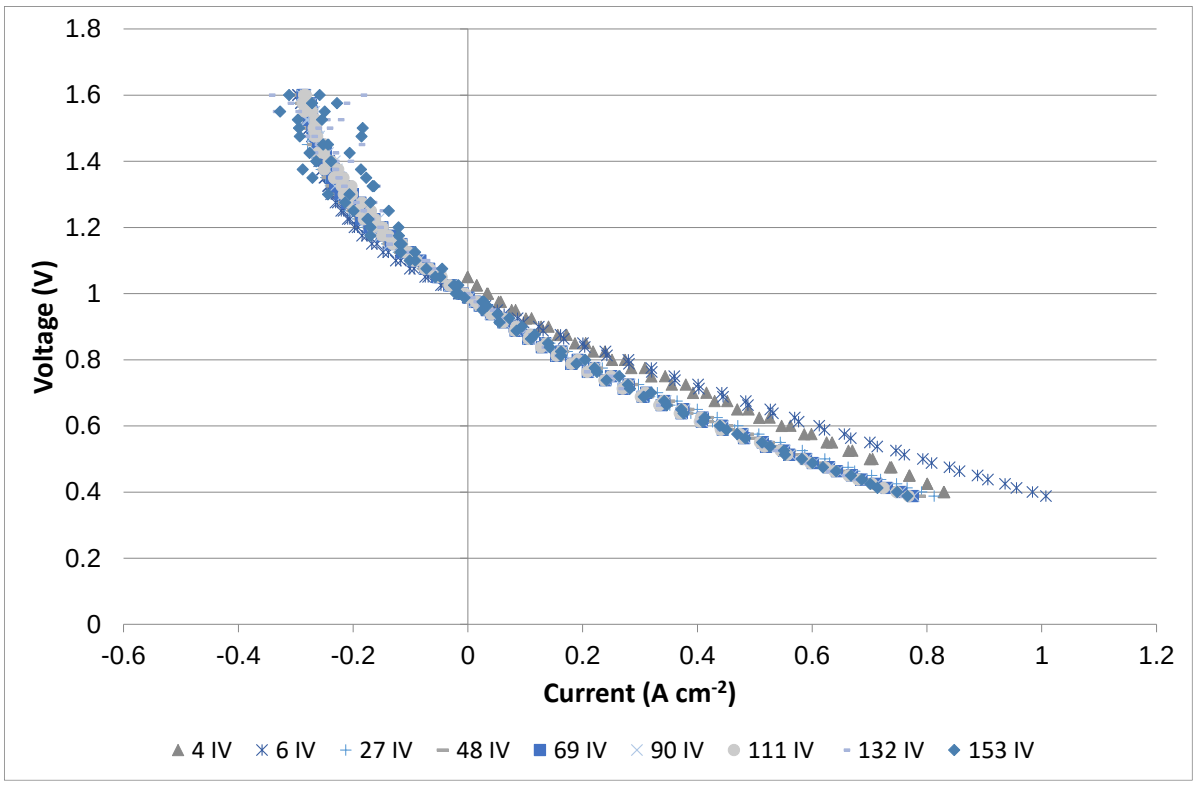


**Figure 84: Ningbo 54 IV curves. The initial IV curve at 4h was performed with 1:1 $H_2$:$N_2$ volumetric ratio with a total flow rate of 120 ml $min^{-1}$. After the initial IV curve the rest of the IV curves were performed in electrolysis and fuel cell operation with a gas mixture in a 47.5:2.5:50 $H_2$:$H_2O$:$N_2$ ratio with a total flow rate of 240ml $min^{-1}$**

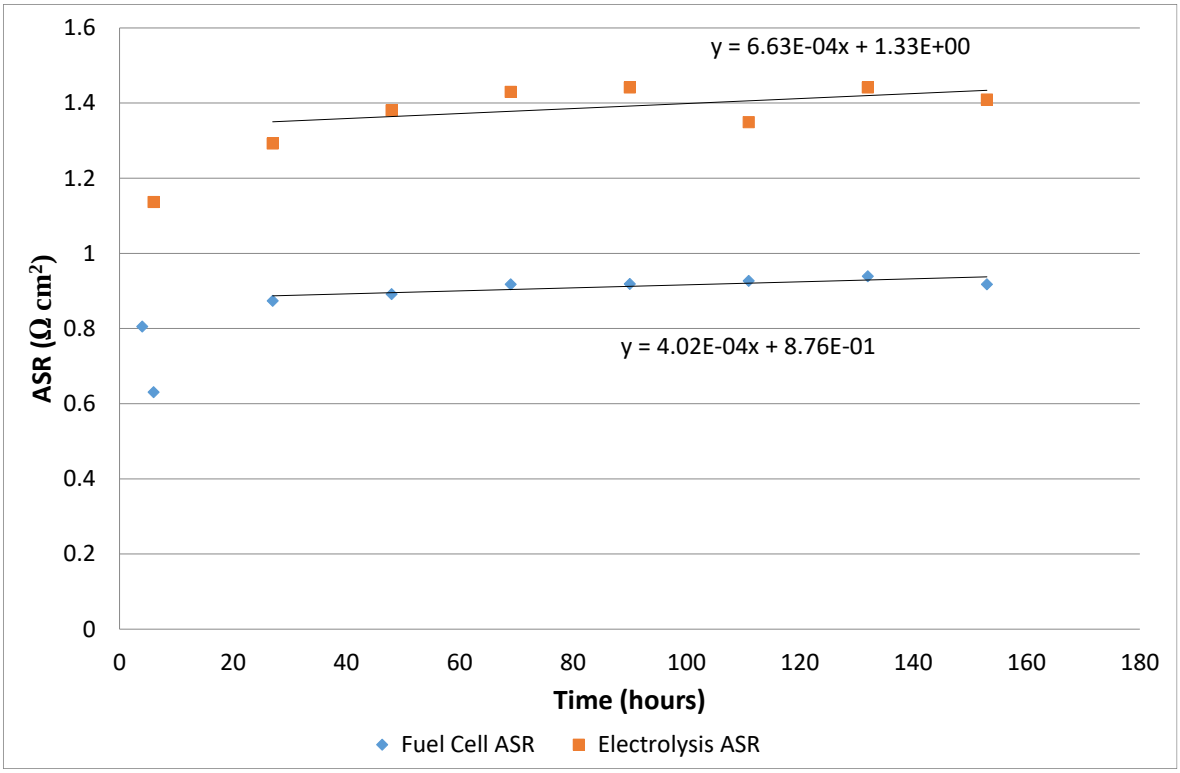


**Figure 85: ASR for Ningbo 54, calculated from the linear part of the IV curve. For electrolysis operation (shown by orange squares) the linear part of the IV curve is very short which increases the error associated with the value. The fuel cell ASR is shown by blue diamonds, as there was a large linear region in the fuel cell data the values are more accurate. The low point in the electrolysis data at 110 hours is due to a temporary increase in the water supplied to the cell, this is likely due to the water flow controller opening too much for a brief period and creating a lower ASR.**

### 7.3.1.3 Ningbo 54 Impedance analysis:

The total impedance for electrolysis operation is greater than the impedance for fuel cell operation. This is expected as the electrolysis suffers severe fuel limitation. The initial resistance measured from the impedance spectra (once the water supply has started, labelled 7) was 0.78 Ω $cm^2$ for fuel cell operation and 1.05 Ω $cm^2$ for electrolysis operation. This is expected as the cell is operating with a much greater quantity of hydrogen than water. After this there was a large jump in the impedance for both fuel cell and electrolysis operation. In fuel cell operation the increase between 7 and 28 hours was 0.21 Ω $cm^2$ and for electrolysis was 0.12 Ω $cm^2$.

The ohmic component to the cell resistance for fuel cell and electrolysis operation is almost the same. Throughout the experiment there was an increase in the ohmic resistance of 0.03 Ω $cm^2$ from 0.195 Ω $cm^2$ to 0.225 Ω $cm^2$ for the cell. The increase in ohmic resistance was the same for both fuel cell and electrolysis operation.

Between 7 and 25 hours there is an increase in the high frequency resistance of the cell, which occurs for both fuel cell and electrolysis operations. There is also a much larger increase in the low frequency <100Hz resistance of the cell.
The high frequency impedance shows no further increase for the rest of the experiment while the low frequency impedance shows a further increase between 28 and 49 hours after which the instability in the readings dominates any further differences. For electrolysis operation there is a large increase in the scatter at low frequencies from 112 hours which indicates that there is instability in the mass transport of the cell. This is thought to be due to the instability in water supply discussed earlier.

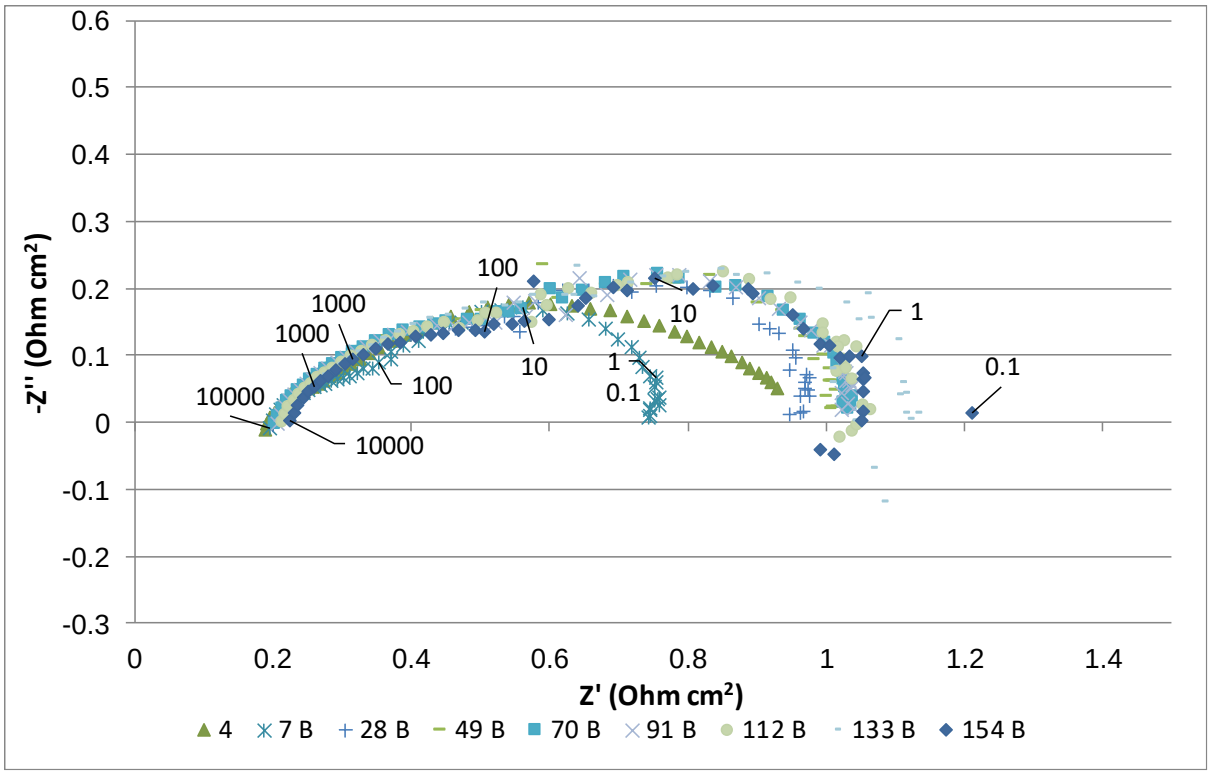


**Figure 86: Ningbo 54 fuel cell impedance spectra. The reading at 4h was performed without water. From 7 hours onwards the water supply was started. The initial IV curve at 4h was performed with 1:1 $H_2$:$N_2$ volumetric ratio with a total flow rate of 120 ml $min^{-1}$. After the initial IV curve the rest of the IV curves were performed in electrolysis and fuel cell operation with a gas mixture in a 47.5:2.5:50 $H_2$:$H_2O$:$N_2$ ratio with a total flow rate of 240ml $min^{-1}$. Frequency markers for 7 and 154 hours.**

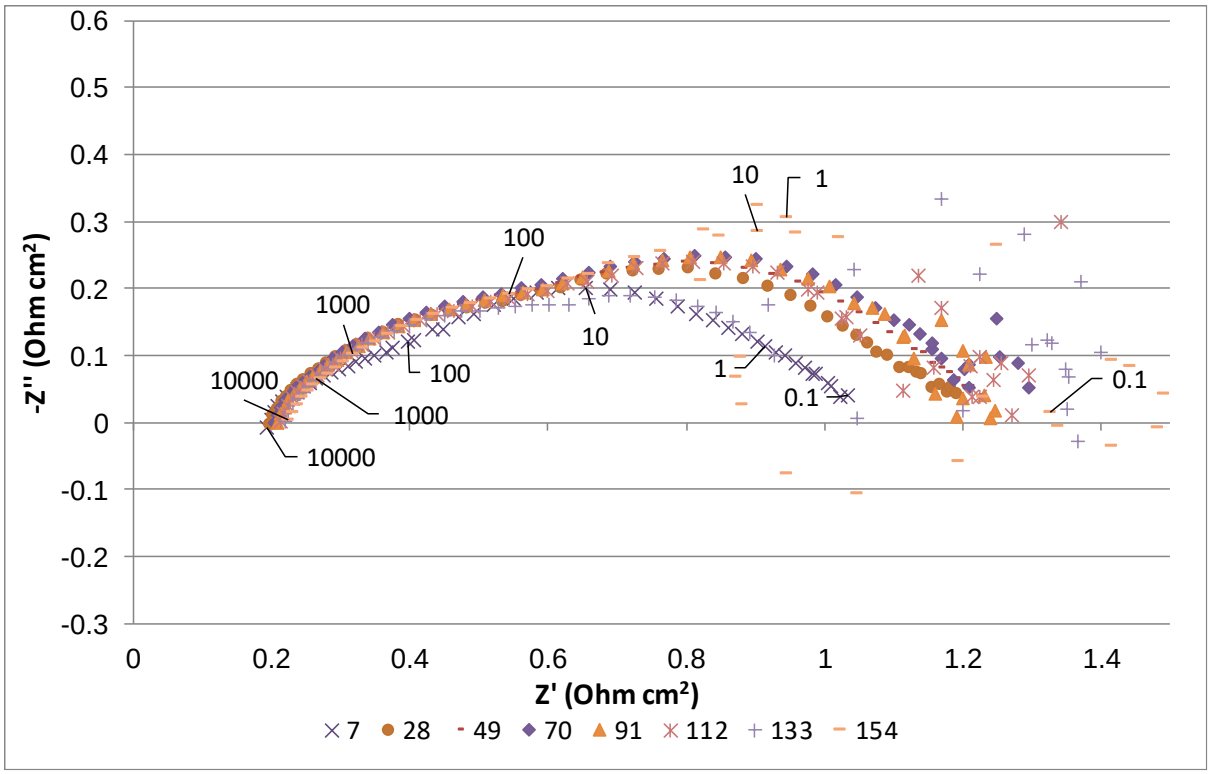


**Figure 87: Ningbo 54 electrolysis impedance spectra. The initial IV curve at 4h was performed with 1:1 $H_2$:$N_2$ volumetric ratio with a total flow rate of 120 ml $min^{-1}$. After the initial IV curve the rest of the IV curves were performed in electrolysis and fuel cell operation with a gas mixture in a 47.5:2.5:50 $H_2$:$H_2O$:$N_2$ ratio with a total flow rate of 240ml $min^{-1}$. Frequency markers for 7 and 154 hours.**

## 7.3.2 7.5 vol% $H_2O$ Ningbo 83

### 7.3.2.1 Ningbo 83 galvanostatic operation

Ningbo 83 was heated under a nitrogen hydrogen mixture (120ml $min^{-1}$ $N_2$ and 60ml $min^{-1}$ $H_2$). The cell was allowed to reduce and initial IV and impedance spectra were performed (labelled 4h). The cell was operated for 140 hours, however due to data collection issues the last 20 hours of data was lost. The cell was operated in electrolysis operation at −0.166 A $cm^{-2}$ at 800 °C with 20ml $min^{-1}$ $H_2O_{(g)}$ (0.95g $h^{-1}$ $H_2O_{(l)}$), 100 ml $min^{-1}$ $H_2$ and 120ml $min^{-1}$ the volumetric gas ratios were 0.425 : 0.075 : 0.5 $H_2$ : $H_2O$ : $N_2$. With a total current of 0.5 A in electrolysis the cell was operating with at utilisation of 17%. Over the course of the experiment the voltage increased by about 60mV with an average degradation rate of 250 mV $kh^{-1}$, and the cell ASR increases by 0.07 Ω $cm^2$. The galvanostatic data is shown in Figure 88.

Over the course of the experiment the cell degraded at an average rate of 250mV $kh^{-1}$. During each step there were two periods of degradation: an initial rapid degradation of 5500 mV $kh^{-1}$ followed by a slower degradation at 500 mV $kh^{-1}$. During each step the degradation rate is higher than the overall rate of degradation for the cell. Therefore, during the IV curve and impedance steps there must have been some improvement in performance. This may be due to the IV curve reversing the cell polarity as discussed earlier. The cell degradation is not completely reversible as the initial starting point for each galvanostatic step increases at almost the same rate as the overall cell degradation of 300mV $kh^{-1}$. If the degradation were fully reversible the initial performance of each step should show no degradation.

There is some small fluctuation in the data. This is thought to be due to the water mass flow controller operating towards the bottom end of its range and struggling to keep a steady flow rate. Small changes in water flow rate may make large differences to the cell performance when the water available is a severely limiting factor in the cell performance.

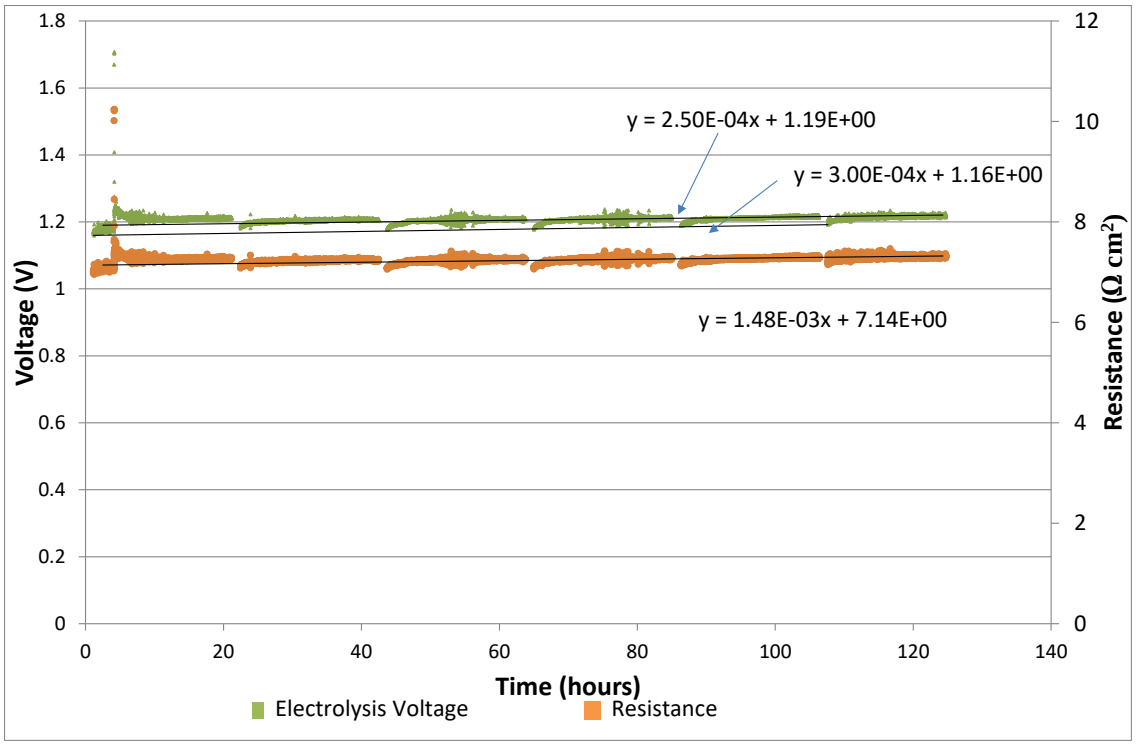


**Figure 88: Galvanostatic data for Ningbo 83 with 42.5:7.5:50 $H_2$:$H_2O$:$N_2$ ratio with a total flow rate of 240ml $min^{-1}$ at −0.166 A $cm^{-2}$. The degradation rate was 250 mV $kh^{-1}$. The green line shows the cell voltage. The orange line shows the cell resistance.**

### 7.3.2.2 Ningbo 83 IV curves

The IV curves showing the performance of Ningbo 83 are plotted in Figure 89. The OCV stays very steady at 0.99V throughout the experiment which is in good agreement with the theoretical Nernst of 1.02V for this fuel composition. There is fuel starvation of the electrolysis portion of the IV curve. This is expected with the limited fuel supply to the cell. There is no observable performance loss due to mass transport in the fuel cell portion of the IV curve. The ASR for each curve has been calculated and is presented in Figure 90. Due to the mass transport limitations in electrolysis operation a small section of the IV curve has been used to calculate the electrolysis ASR. In fuel cell operation the initial ASR is 0.59 Ω $cm^2$. This undergoes an improvement to 0.50 Ω $cm^2$ at 7 hours when the experimental gas mixture is introduced after which it continues to degrade in a linear manner reaching a maximum of 0.58 Ω $cm^2$ at 0.66 Ω $cm^2$ $kh^{-1}$. The electrolysis ASR at 7 hours is 1.10 Ω $cm^2$. It

also degrades in a linear manner reaching a maximum of 1.17 Ω $cm^2$ at a rate of 0.47 Ω $cm^2$ $kh^{-1}$. The rate of fuel cell ASR degradation is greater than the rate of electrolysis ASR degradation however both are very similar. These values are smaller than the resistance degradation measured from the galvanostatic data of 1.48 Ω $cm^2$ $kh^{-1}$.

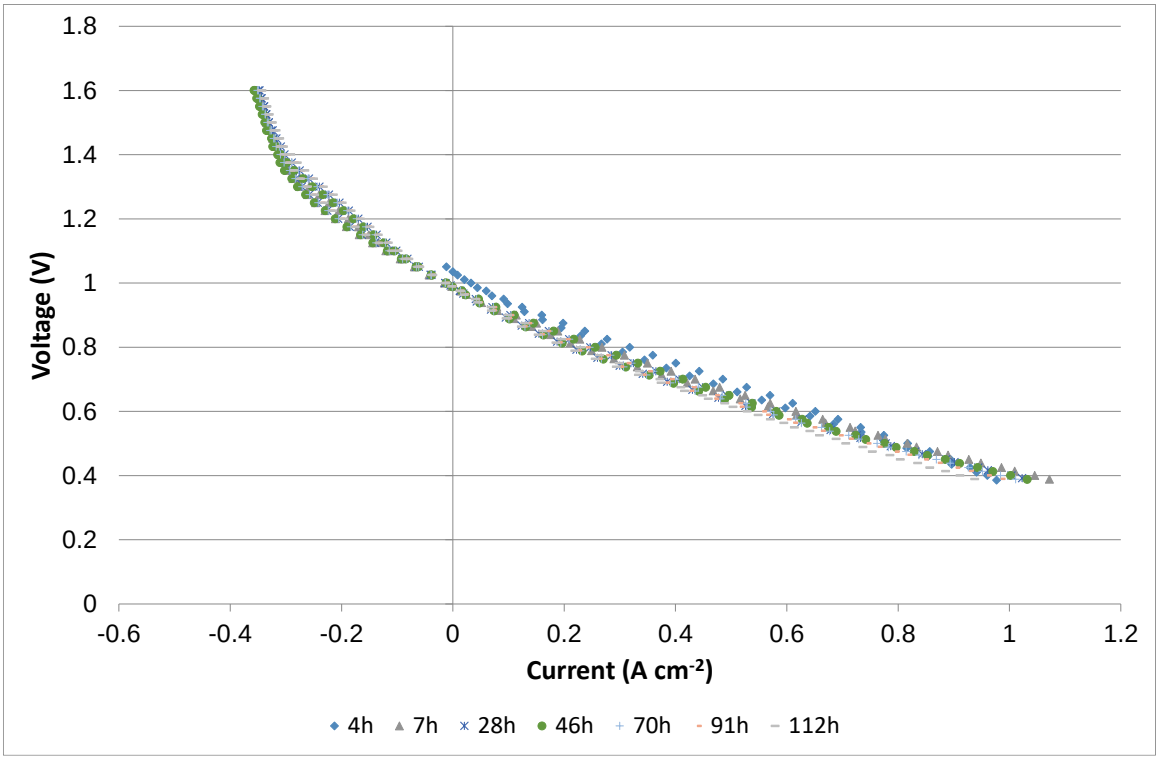


**Figure 89: The IV curves for Ningbo 83. All performed with 0.425:0.075:0.5 $H_2$:$H_2O$:$N_2$ volumetric gas ratio with a total flow rate of 240 ml $min^{-1}$ at 800°C. The initial curve at 4h (blue diamonds) was performed with a 1:3 $H_2$:$N_2$ volumetric ration with a total flow rate of 120 ml $min^{-1}$.**

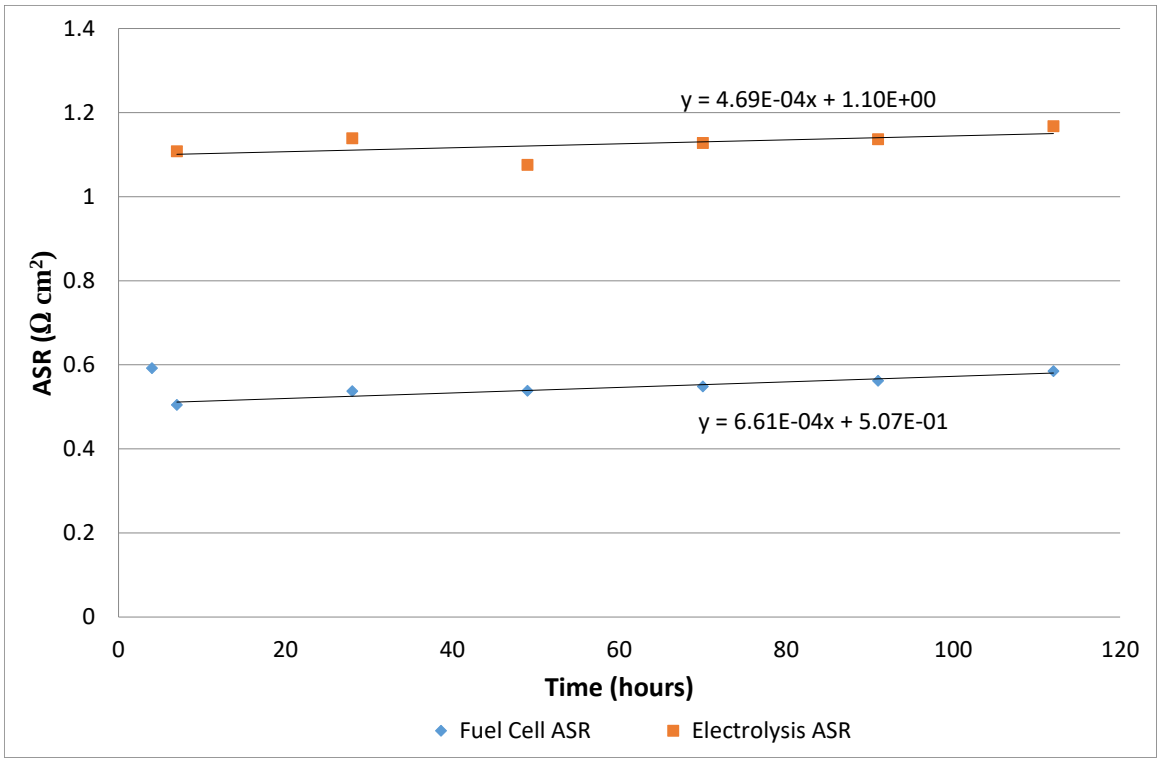


**Figure 90: ASR for Ningbo 83 calculated from the linear region of the IV curves shown in Figure 89. All performed with; 0.425:0.075:0.5 $H_2$:$H_2O$:$N_2$ volumetric gas ratio with a total flow rate of 240ml $min^{-1}$ at 800°C; apart from the first blue point at 4h which was performed with a 1:3 $H_2$:$N_2$ volumetric ration with a total flow rate of 120 ml $min^{-1}$.**

### 7.3.2.3 Ningbo 83 impedance data

The impedance curves for Ningbo 83 are shown below for fuel cell operation (Figure 91) and electrolysis (Figure 92). The ohmic resistance for both fuel cell and electrolysis operation are the same. The initial ohmic resistance at 4 hours is 0.16 Ω $cm^2$. After switching to the experimental gas mixture the ohmic resistance significantly decreases to 0.11 Ω $cm^2$ at 7 hours and over the course of the experiment increases back to 0.16 Ω $cm^2$ at 113 hours (end of impedance data). The magnitude of the increase in ohmic resistance is the same for fuel cell and electrolysis operation. After 71 hours there is a change in the inductance of the cell. There are a number of possible causes for a change in the ohmic resistance. The initial drop in ohmic resistance between 4 and 7 hours may be due to reduction of nickel in the hydrogen electrode leading to increased electrical conduction through the electrode.

For fuel cell operation between the initial IV curve at 4 hours and the first IV curve under the experimental gas mixture at 7 hours there is a large increase in the high frequency impedance of 0.25 Ω $cm^2$. After 7 hours there is little apparent change in the high frequency impedance for the rest of the experiment for either fuel cell operation or electrolysis operation. The high frequency portion of the impedance spectra is larger for electrolysis operation than for fuel cell operation.

It is in the low frequency region of the impedance spectra where most of the changes occur. Due to the scatter in the plots it is difficult to accurately fit the low frequency region. While there is instability in the readings there appears to be an increase throughout the experiment of 0.06±0.01 Ω $cm^2$ in both fuel cell and electrolysis operation.

The scatter is due to instability of the cell voltage; this could be due to slight changes in the gas flows to the cell or temperature fluctuations. As this is happening between 10 and 1 Hz it is unlikely that there are large fluctuations in the cell's operating temperature. Therefore, it is assumed that the fluctuations are caused by small changes in gas composition, flow rate or pressure.

There is less scatter in the low frequency region for fuel cell operation than for electrolysis operation. This is due to the high $H_2$ and low $H_2O$ flow rates to the cell. As can be seen in the IV curves there is large mass transport limitation for the electrolysis operation which is not observed for the fuel cell operation. Therefore, a small change in gas flow rate will have a large effect on the electrolysis performance while the fuel cell performance will have some buffer and remain stable to small fluctuations.

The impedance data shows that while the electrolysis operation has a higher impedance than fuel cell operation the changes in the cell's performance throughout the experiment are very similar for both fuel cell and electrolysis operation.

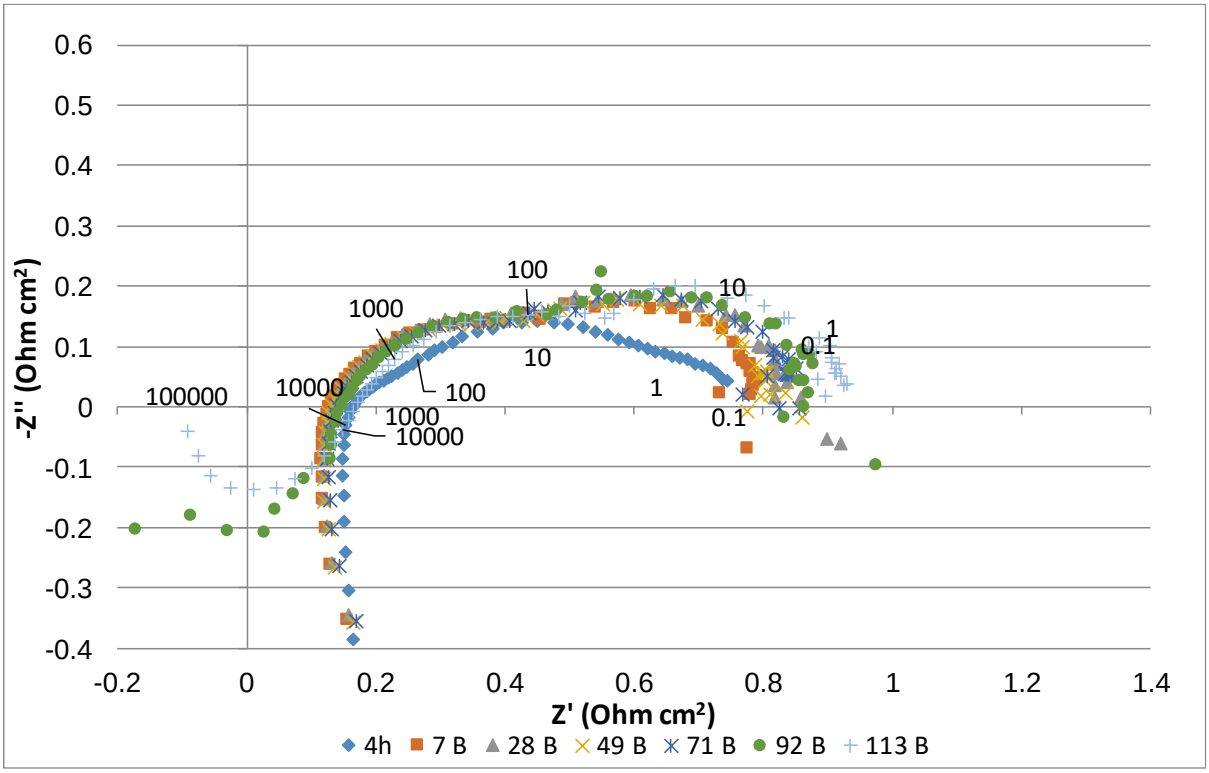


**Figure 91: Ningbo 83 fuel cell impedance. Labels indicate time since start of experiment. All performed with 0.425:0.075:0.5 $H_2$:$H_2O$:$N_2$ volumetric gas ratio with a total flow rate of 240ml $min^{-1}$ at 800°C, apart from the initial curve at 4h (blue diamonds) was performed with a 1:3 $H_2$:$N_2$ volumetric ration with a total flow rate of 120 ml $min^{-1}$. Frequency markers are shown for 4h and 113h.**

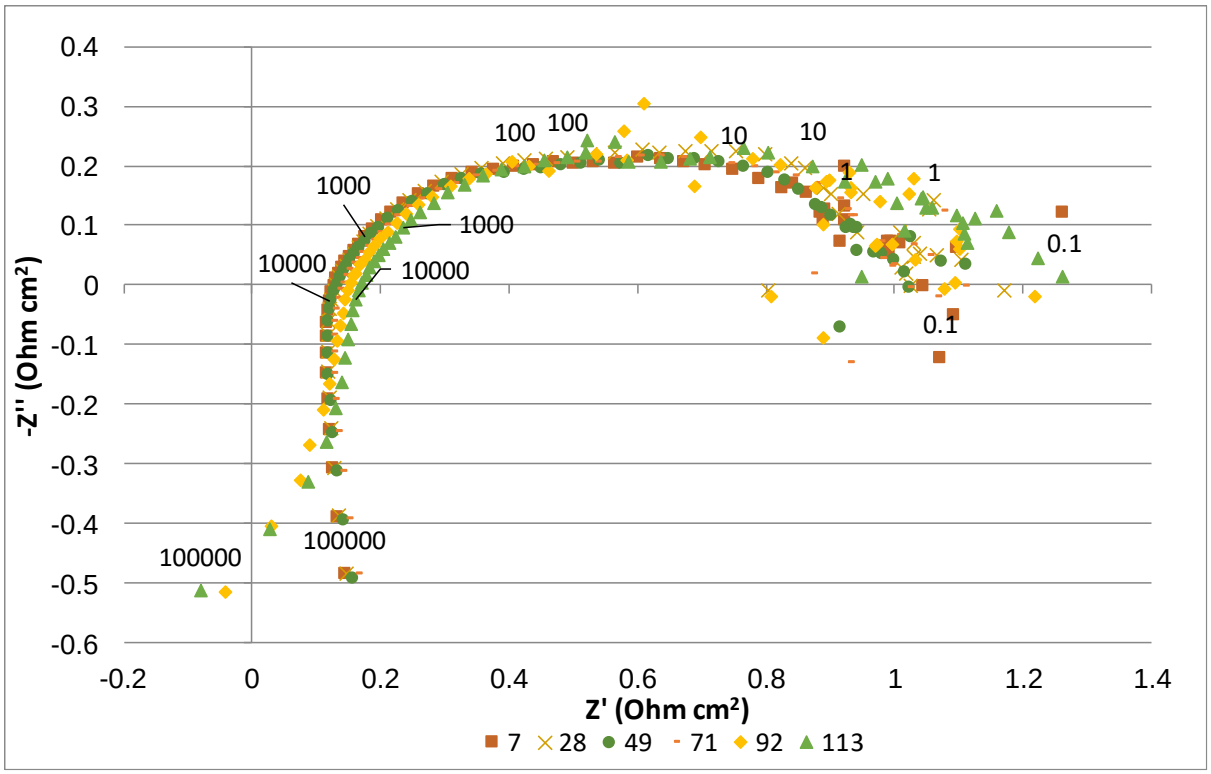


**Figure 92: Ningbo 83 electrolysis impedance. Labels indicate time since start of experiment. All performed with 0.425:0.075:0.5 $H_2$:$H_2O$:$N_2$ volumetric gas ratio with a total flow rate of 240ml $min^{-1}$ at 800ºC. Frequency markers are shown for 4h and 113h.**

### 7.3.3 25 vol% $H_2O$ Ningbo 50

Analysis on this cell has been performed in the previous chapter, please refer back to section 6.3.1 for a full analysis of the cells performance. The cell performance will nevertheless be given here.

#### 7.3.3.1 Ningbo 50 summary:

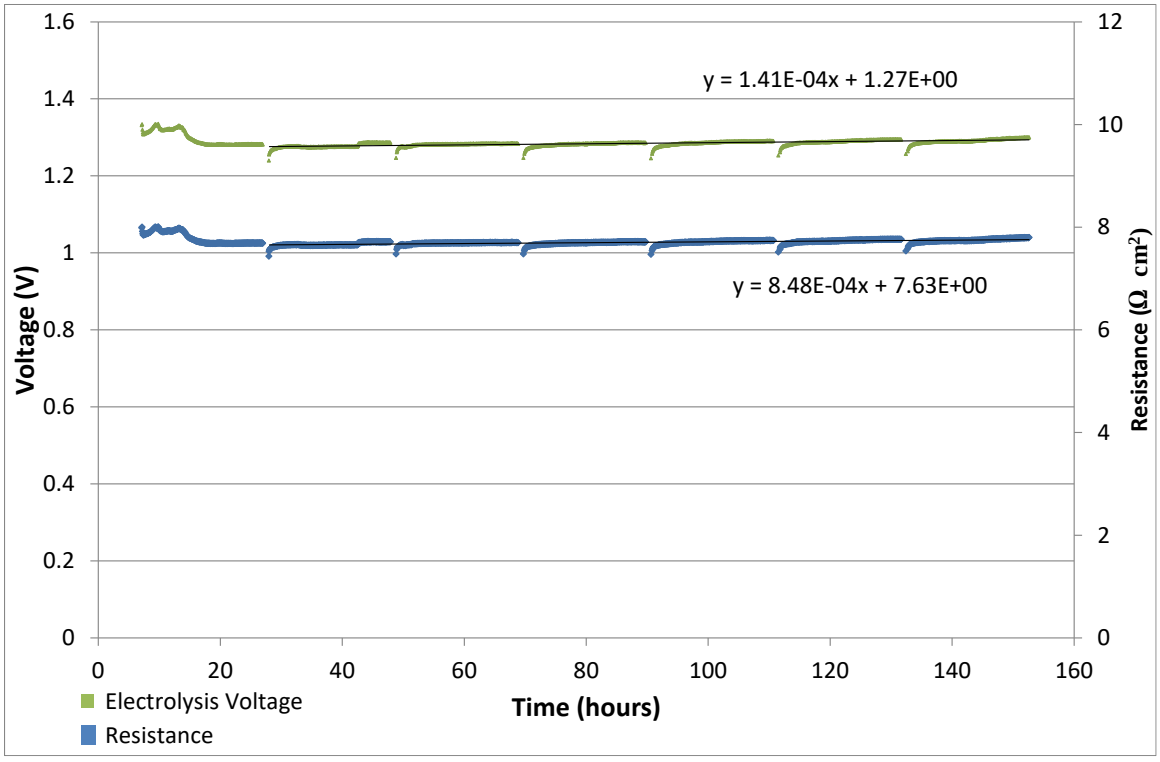


**Figure 93: Ningbo 50 electrolysis degradation rate performed at 800°C 1:1:2 $H_2$:$H_2O$:$N_2$ total flow rate 240ml $min^{-1}$ at −0.16 A $cm^{-2}$. The cell has an average degradation rate of 141 mV $kh^{-1}$. The green line shows the voltage evolution with time, the blue line shows the resistance evolution with time.**

- The cell was operated with a 50:20 $H_2$:$H_2O$ ratio. (0.25:0.25:0.5 $H_2$:$H_2O$:$N_2$ partial pressure with a total flow rate of 240 ml $min^{-1}$ at 800°C with −0.166 A $cm^2$.)
- The cell showed an average degradation rate of 141 mV $kh^{-1}$.
- Each galvanostatic step showed a very rapid increase in the voltage at the start of each step and the degradation of the rest of the step was 400 mv $kh^{-1}$, which is greater than the average degradation rate for the cell.

- The IV curve appears to be almost linear between electrolysis and fuel cell operation. The ASR in fuel cell operation was 1.85 Ω $cm^2$ and ASR in electrolysis operation was 2.21 Ω $cm^2$.
- The total impedance for both fuel cell and electrolysis operation was very similar, and due to scatter at low frequencies no differences could be established.
- The ohmic resistance is the same for fuel cell and electrolysis operation. After an initial improvement in ohmic resistance there is no further change observed throughout the experiment. The improvement in ohmic resistance is thought to be the cause of the instability and improvement at the start of the galvanostatic data which is due to either continuing reduction of the anode leading to an improvement in electronic conductivity or improved electrode/current collection contacting.
- The impedance for electrolysis operation was higher than fuel cell operation at intermediate frequencies between 1000 and 100 Hz.
- The impedance for electrolysis was lower than fuel cell operation at low frequencies below 100Hz.
- In fuel cell and electrolysis operation there is a small increase in the impedance between 1000 and 100 Hz. Otherwise the impedance spectra remain the same throughout the experiment.

### 7.3.4 40 vol% $H_2O$ Ningbo 87

#### 7.3.4.1 Ningbo 87 galvanostatic data

Ningbo 87 was heated under a nitrogen hydrogen mixture (120 ml $min^{-1}$ $N_2$ and 60 ml $min^{-1}$ $H_2$) at 5°C $min^{-1}$. The cell was allowed to reduce, and initial IV and impedance spectra were performed (labelled 4h). The cell was operated for 160 hours, however, issues with the data collection computer lost the last half of the data and there was insufficient time available to repeat the experiment. The galvanostatic operation of Ningbo 87 is shown in Figure 94. The cell was operated in electrolysis operation at −0.166 A $cm^{-2}$ at 800 °C with 96 ml $min^{-1}$ $H_2O_{(g)}$ (4.65 g $h^{-1}$ $H_2O_{(l)}$), 24 ml $min^{-1}$ $H_2$ and 120ml $min^{-1}$ $N_2$ the volumetric gas ratios were 0.1 : 0.4 : 0.5 $H_2$ : $H_2O$ : $N_2$. With a total current of 0.5 A in electrolysis mode the cell was operating with at utilisation of 3.6%. Over the course of the experiment the voltage increased by about 7mV with an average degradation rate of 94 mV $kh^{-1}$.

#### 7.3.4.2 Ningbo 87 IV curve data

The IV curves for Ningbo 87 are shown in Figure 95. The cell OCV is 0.85V and remains constant throughout the experiment. The IV curves show mass transport limitation in fuel cell operation which is consistent with the limited hydrogen supplied to the cell. The IV curves show no limitation due to fuel flow in electrolysis operation. The ASR for each IV curve has been calculated and is presented in Figure 96. The initial ASR for the cell in fuel cell operation at 4 hours is 0.89 Ω $cm^2$. Under the experimental gas conditions at 7 hours the fuel cell ASR increases to 0.95 Ω $cm^2$, and the electrolysis ASR was lower at 0.79 Ω $cm^2$.

The electrolysis performance shows a decrease in performance between 7 and 49 hours after which the cells performance remains constant. In electrolysis operation the cells ASR

increases by 0.15 Ω $cm^2$ between 7 and 49 hours to 0.94 Ω $cm^2$ at which remained constant for the rest of the experiment. The degradation rate of the ASR from the IV data is 0.69 Ω $cm^2$ $kh^{-1}$ in electrolysis operation and 0.22 Ω $cm^2$ $kh^{-1}$ in fuel cell operation which is similar to the resistance degradation rate observed in the galvanostatic data of 0.56 Ω $cm^2$ $kh^{-1}$.

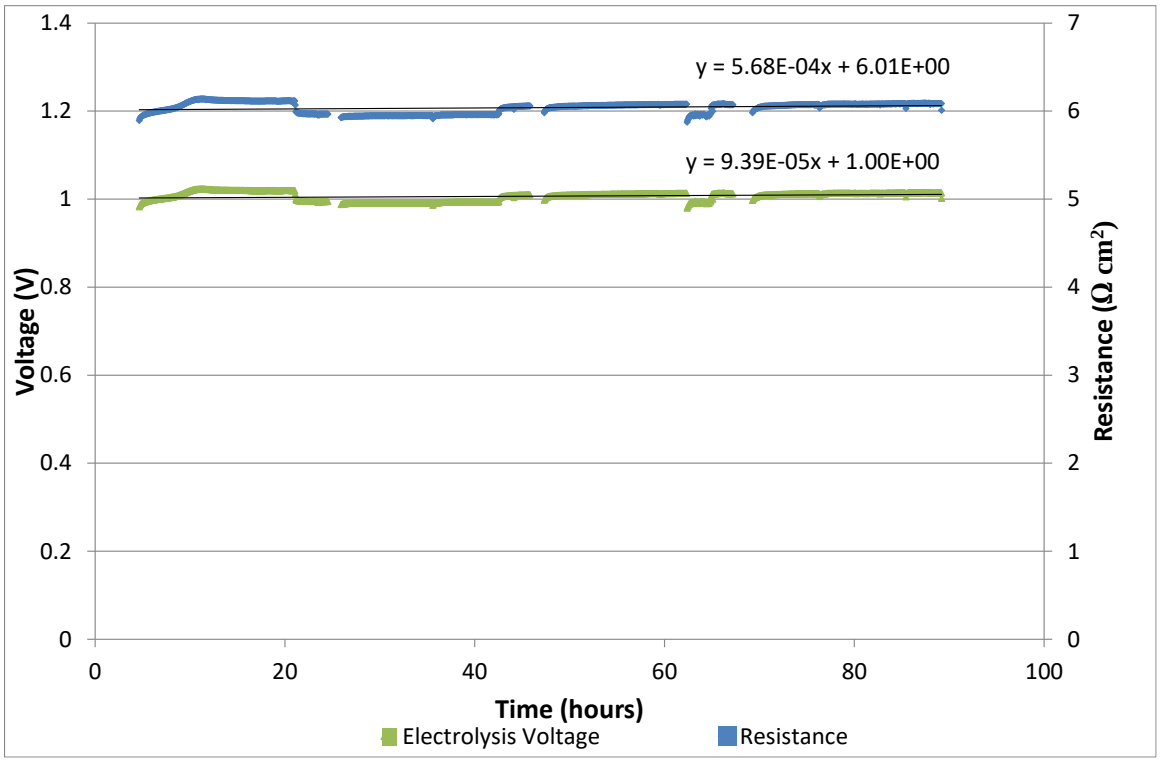


**Figure 94: Galvanostatic data for Ningbo 87 with 10:40:50 $H_2$:$H_2O$:$N_2$ ratio with a total flow rate of 240ml $min^{-1}$. The degradation rate was 94mV $kh^{-1}$. The green line shows the cell voltage. The blue line shows the cell resistance.**

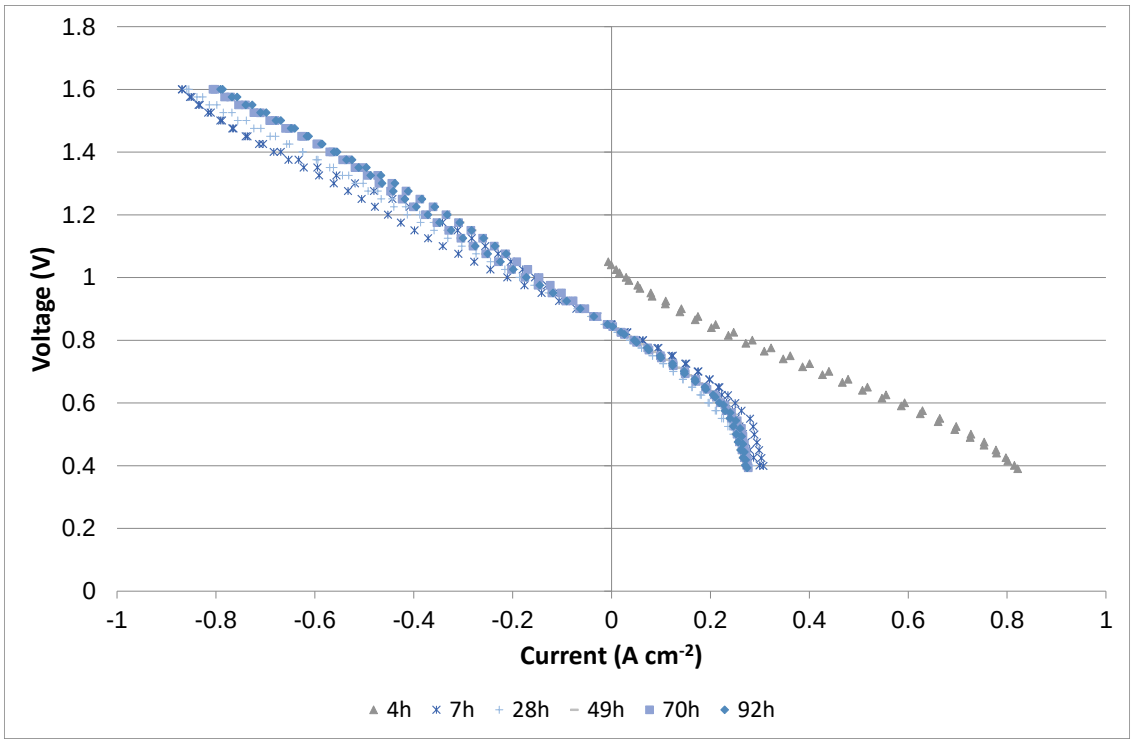


**Figure 95: The IV curves for Ningbo 87. All performed with 0.1:0.4:0.5 $H_2$:$H_2O$:$N_2$ volumetric gas ratio with a total flow rate of 240ml $min^{-1}$ at 800ºC. The initial curve at 4h (blue diamonds) was performed with a 1:3 $H_2$:$N_2$ volumetric ration with a total flow rate of 120 ml $min^{-1}$.**

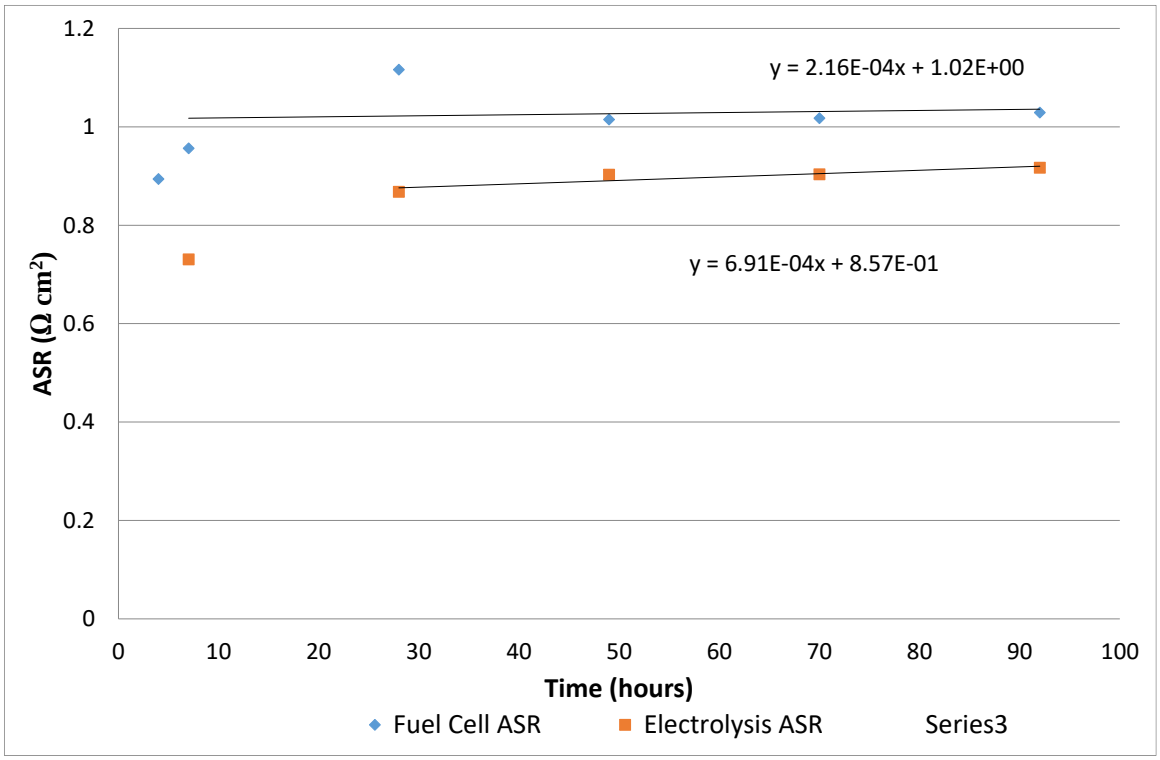


**Figure 96: ASR for Ningbo 87 calculated from the linear region of the IV curves shown in Figure 95. The large resistance at 28h for fuel cell operation may be due to the gas conditions. The cell is operating with a low hydrogen flow rate and a temporary loss in supply during the fuel cell IV curve would should as a higher resistance.**

### 7.3.4.3 Ningbo 87 impedance data

The impedance data for Ningbo 87 is shown in Figure 97 and Figure 98 for fuel cell and electrolysis operation respectively. The cells ohmic resistance is the same for both fuel cell and electrolysis operation. There is an increase in the ohmic resistance of 0.004 Ω $cm^2$ throughout the experiment and this increase is the same for both fuel cell and electrolysis operation.

In electrolysis operation there is an increase in the high frequency impedance between 7 and 25 hours. The increase in the fuel cell operation of the cell is much smaller. In fuel cell operation there is a large increase in the low frequency, <100Hz, area of the cell between 4 and 7 hours when the experimental gas composition is changed to include the water. This is expected as the hydrogen content of the gas is reduced and there is an increase in mass transport in the cell.

The low frequency behaviour of the cell for electrolysis and fuel cell operation is very similar, however the effects are bigger in electrolysis than fuel cell operation. There is an increase in the low frequency impedance of the cells between 7 and 47 hours, after 47 hours the impedance for the cells remains the same.

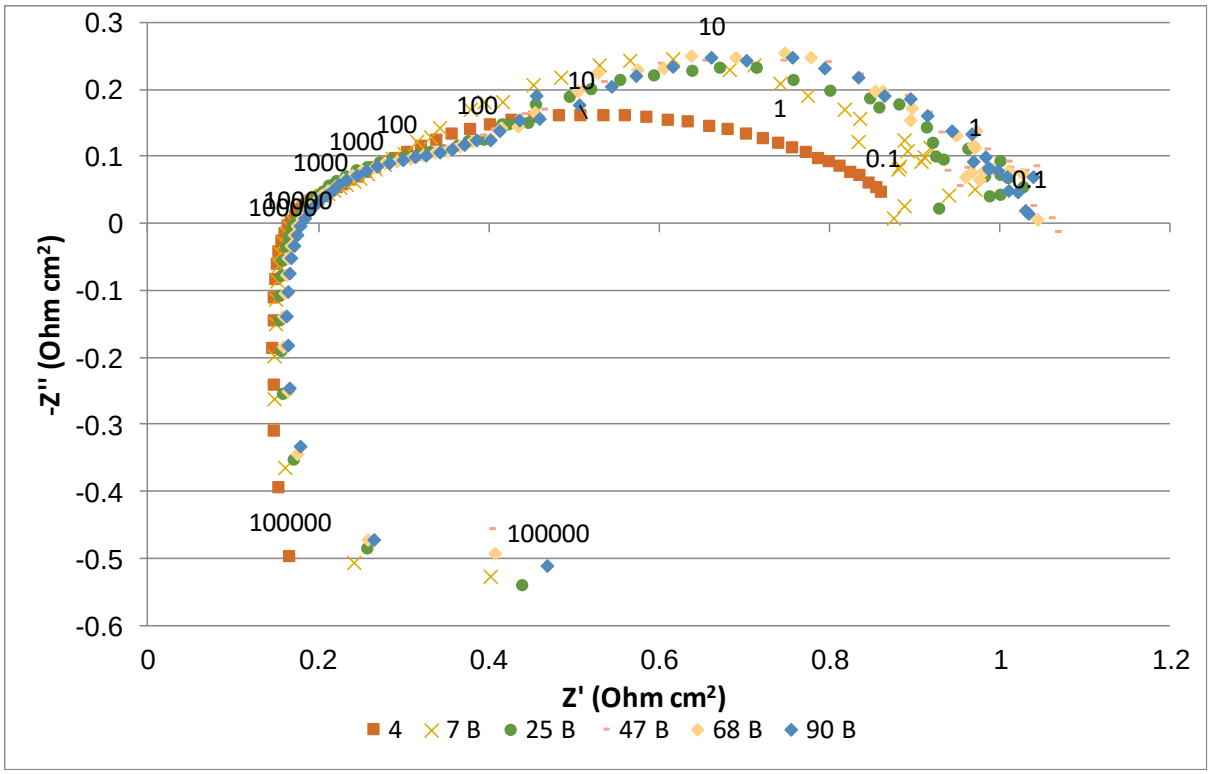


**Figure 97: Fuel cell impedance spectrum for Ningbo 87. Markers indicating frequency are positioned for the curves taken at 4 hours and 90 hours. The initial curve at 4h (blue diamonds) was performed with a 1:3 $H_2$:$N_2$ volumetric ration with a total flow rate of 120 ml $min^{-1}$. All others performed with 0.1:0.4:0.5 $H_2$:$H_2O$:$N_2$ volumetric gas ratio with a total flow rate of 240ml $min^{-1}$ at 800°C.**

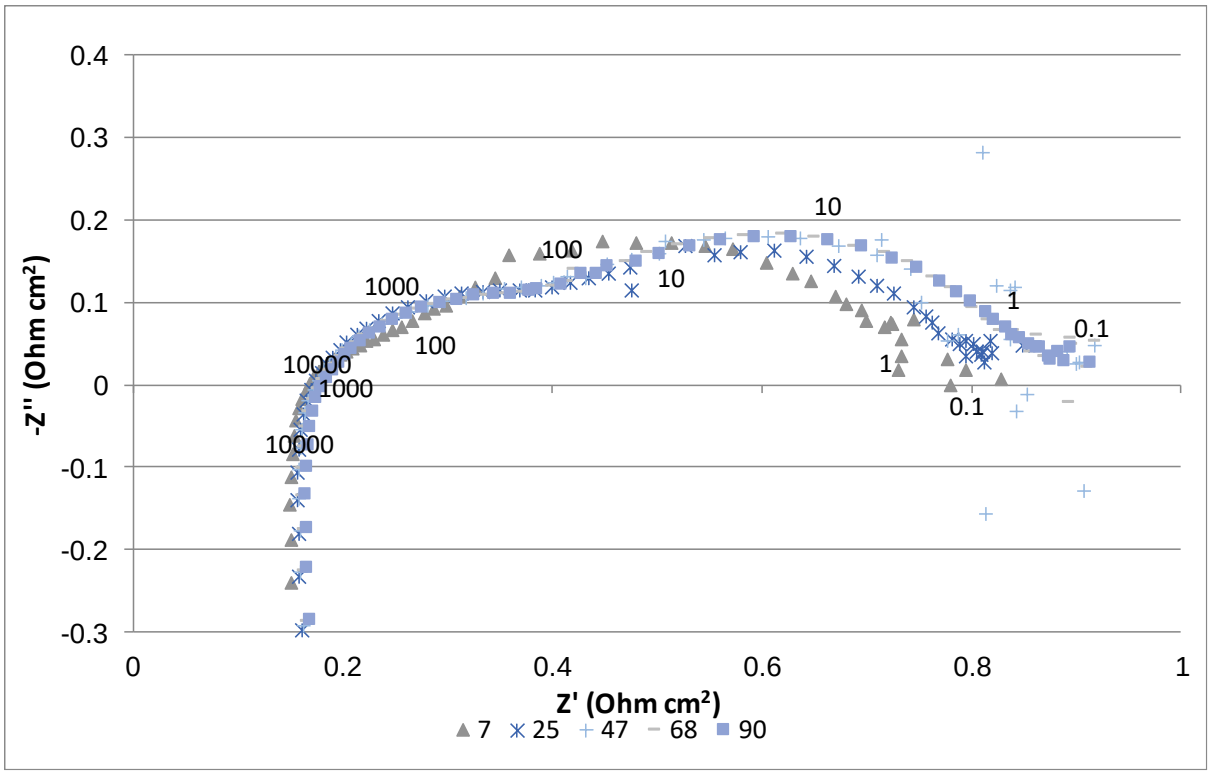


**Figure 98: Electrolysis impedance spectrum for Ningbo 87. Markers indicating frequency are positioned for 7 hours (bottom) and 90 hours (top) All performed with 0.1:0.4:0.5 $H_2$:$H_2O$:$N_2$ volumetric gas ratio with a total flow rate of 240ml $min^{-1}$ at 800°C.**

## 7.3.5 47.5 vol% $H_2O$ Ningbo 52

### 7.3.5.1 Ningbo 52 galvanostatic

Ningbo 52 was heated under a nitrogen hydrogen mixture (120ml $min^{-1}$ $N_2$ and 60ml $min^{-1}$ $H_2$) at 5°C to 800°C. The cell was allowed to reduce and initial IV and impedance spectra were performed (labelled 4h). The cell was operated in electrolysis operation for 140 hours at 0.166 A $cm^{-2}$, 800°C with 114ml $min^{-1}$ $H_2O_{(g)}$ (5.5g $h^{-1}$ $H_2O_{(l)}$), 6 ml $min^{-1}$ $H_2$ and 120ml $min^{-1}$ $N_2$ the volumetric gas ratios were 0.025 : 0.475 : 0.5 $H_2$ : $H_2O$ : $N_2$. With a total current of 0.5A in electrolysis the cell was operating with at utilisation of 3%. Over the course of the experiment the voltage increased by 6mV with an average degradation rate of 45 mV $kh^{-1}$, and the cells ASR increases by 0.03 Ω $cm^2$. The galvanostatic data for this cell is shown in Figure 99.

During galvanostatic operation there appeared to be an initial period of settling over the first 20−30 hours, and after this the degradation rate appeared very constant at 45 mV $kh^{-1}$, however there was some slight improvement in performance over the final two periods of galvanostatic operation. There were some spikes in the voltage, which were generally towards lower voltages and it is thought that these spikes indicate either a sudden increase in water concentration in the cell or increase in pressure in the cell. This may either be due to the formation of a water droplet somewhere in the pipes leading to the cell; this will lead to an increase in the water concentration reaching the cell and a drop in the OCV leading to a reduced operational voltage; or the formation of a water droplet on the cells outlet which causes a brief increase in the cell's operational pressure and therefore a drop in the OCV.

Each of the galvanostatic periods, apart from the final two, shows two regions of degradation: an initial very brief degradation lasting 1–2 hours which had a degradation rate of 8700 mV $kh^{-1}$, the next part lasted for the rest of the galvanostatic step and had a degradation rate of 100 mV $kh^{-1}$. The overall degradation rate for the experiment is lower than the degradation rate for each step, therefore there must be some improvement in performance during the IV curve and impedance stages.

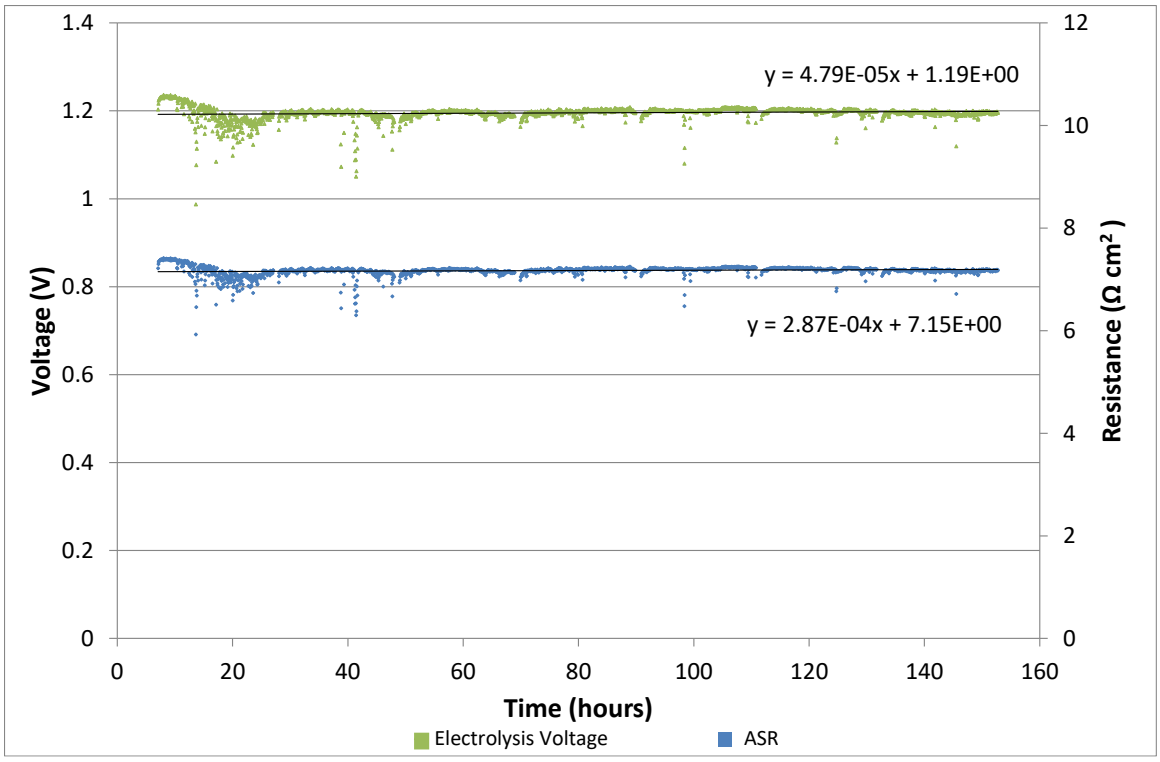


**Figure 99: Galvanostatic data for Ningbo 52 with 2.5:47.5:50 $H_2$:$H_2O$:$N_2$ ratio with a total flow rate of 240ml $min^{-1}$. The degradation rate was 48mV $kh^{-1}$. The green line shows the cell voltage. The blue line shows the cell resistance.**

### 7.3.5.2 Ningbo 52 IV curves:

The IV curves for Ningbo 52 are shown in Figure 100. The initial performance of the cell at 4 hours is poor, the cell at 4 hours with a hydrogen nitrogen mixture has a fuel cell ASR of 2.87 Ω $cm^2$, and this is higher than any of the other cells tested in this chapter. After the gas mixture is switched to the experimental gas mixture at 6 hours the fuel cell ASR increases to 3.45 Ω $cm^2$ and the electrolysis ASR is 2.55 Ω $cm^2$. The fuel cell operation shows mass transport limitation due to the limited hydrogen flow rate. The evolution of ASR calculated from the IV curves is shown in Figure 101. The rate of fuel cell ASR increase from the IV curve is 0.14 Ω $cm^2$ $kh^{-1}$, and the rate of electrolysis degradation is 0.33 Ω $cm^2$ $kh^{-1}$.

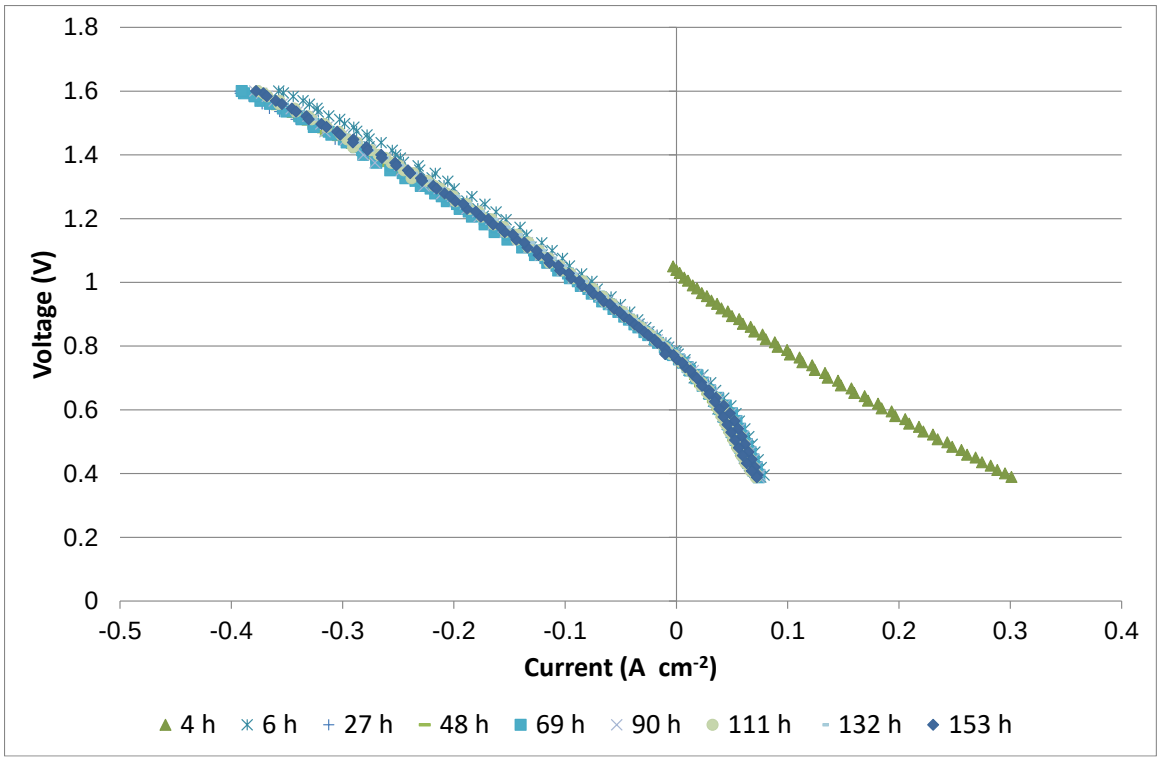


**Figure 100: The IV curves for Ningbo 52. The initial curve at 4h (green triangles) was performed with a 1:3 $H_2$:$N_2$ volumetric ratio with a total flow rate of 120 ml $min^{-1}$. All other curves performed with 2.5:47.5:50 $H_2$:$H_2O$:$N_2$ volumetric gas ratio with a total flow rate of 240ml $min^{-1}$ at 800°C.**

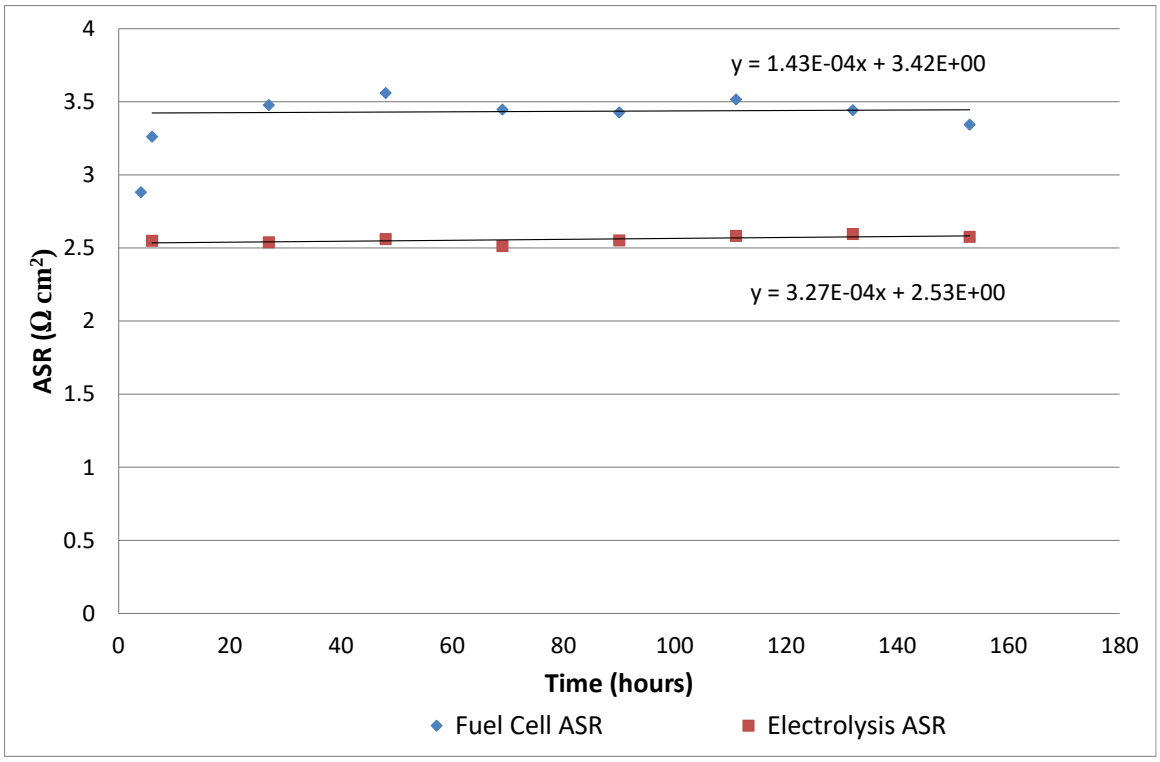


**Figure 101: ASR for Ningbo 52 calculated from the IV curves. The first fuel cell data point 4h was performed with a 1:3 $H_2$:$N_2$ volumetric ratio with a total flow rate of 120 ml $min^{-1}$. All other performed with 2.5:47.5:50 $H_2$:$H_2O$:$N_2$ volumetric gas ratio with a total flow rate of 240ml $min^{-1}$ at 800°C.**

### 7.3.5.3 Ningbo 52 Impedance:

The impedance data for Ningbo 52 is shown in Figure 102 and Figure 103 for fuel cell and electrolysis operation respectively. For both fuel cell and electrolysis impedance spectra there is a 0.12 Ω $cm^2$ decrease in ohmic resistance between 7 and 28 hours. This is accompanied by an increase in the high frequency impedance for the cell. After this there is no measureable change in the impedance spectra for either fuel cell or electrolysis operation. The low frequency, below 100 Hz, impedance of the cell appears to be very similar throughout the experiment. There is a large amount of scatter in the data, especially at 28, 91 and 133 hours. The scatter in the data is disguising any changes occurring at low frequency.

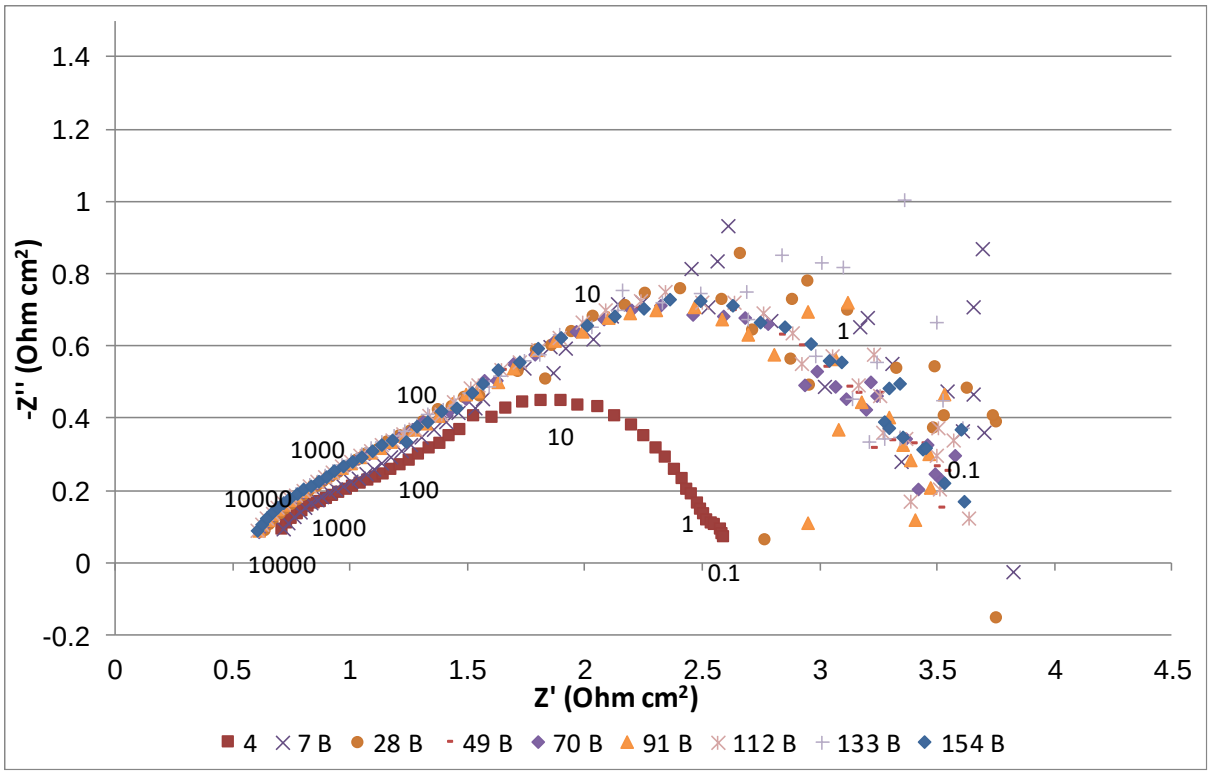


**Figure 102: Ningbo 52 fuel cell impedance. The first curve (red squares) 4h was performed with a 1:3 $H_2$:$N_2$ volumetric ratio with a total flow rate of 120 ml $min^{-1}$. All other performed with 2.5:47.5:50 $H_2$:$H_2O$:$N_2$ volumetric gas ratio with a total flow rate of 240ml $min^{-1}$ at 800°C. Frequency markers provided for 4 and 154 hours.**

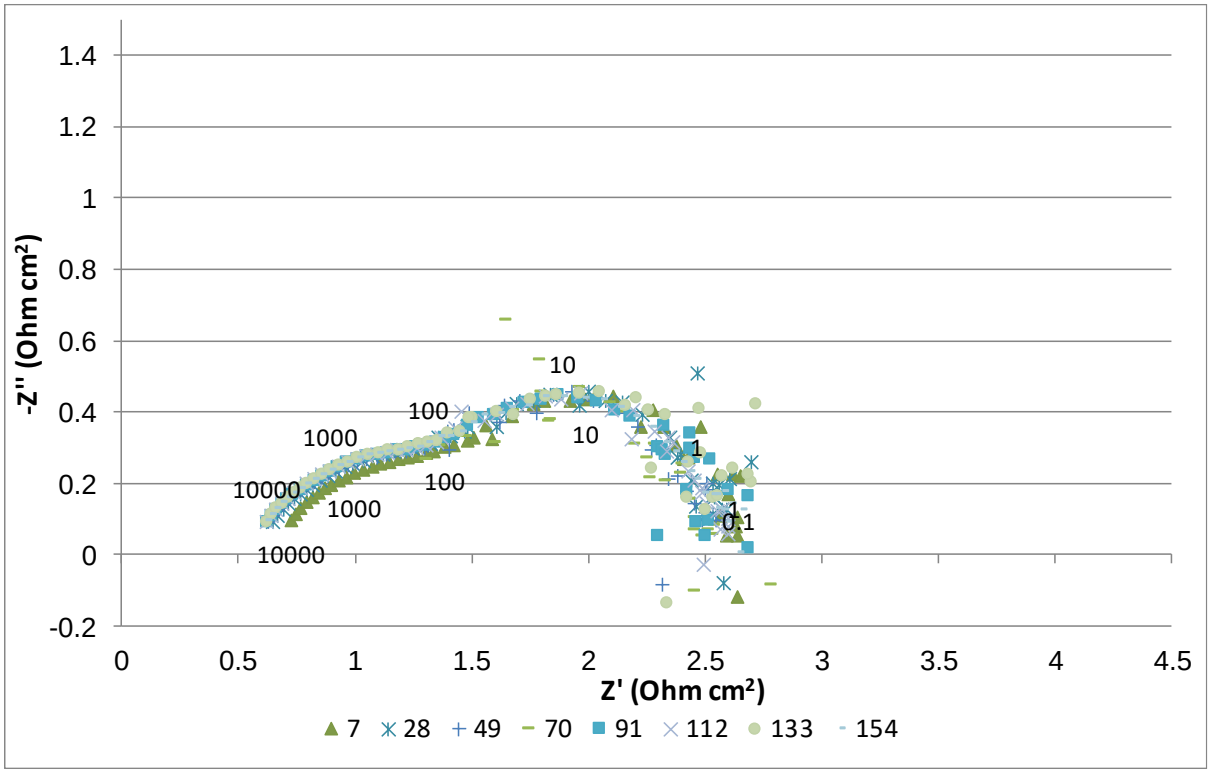


**Figure 103: Ningbo 52 Electrolysis impedance All performed with 2.5:47.5:50 $H_2$:$H_2O$:$N_2$ volumetric gas ratio with a total flow rate of 240ml $min^{-1}$ at 800°C. Frequency markers provided for 4 and 154 hours.**

## 7.4 SEM imaging

In this section post mortem analysis of the cells studied in this chapter has been performed. The main focus of the imaging has been on the hydrogen electrode as this electrode experienced differences in the water to the cell. It was expected that there would be morphological changes in the hydrogen electrode due to the different water partial pressure on the electrode. With exposure to steam at high temperature nickel particles can agglomerate which reduces the surface area at the TPB available for reactions, this therefore leads to a loss of performance[178–180].

### 7.4.1 Experimental

#### 7.4.1.1 Polishing of cells:

Care needs to be taken to ensure that the cross section of the cell imaged is true to the bulk sample, therefore the use of polishing materials was carefully selected to ensure a representative area was imaged. Manual polishing produced inconsistent results, with apparent cracks in the electrolyte. The cracks in the electrolyte disappeared with an automated polishing machine. In the presented results the samples were polished using a polishing wheel (MetaServ 250, Buehler) with automatic polishing head attached (Vector LC 250, Buehler), the samples were polished according to the schedule shown in Table 5.

**Table 5: Polishing regime used for samples. All materials obtained from Buehler.**

| Polishing support material | Diamond Size (µm) | Load (N) | Speed (rpm) | Time |
|---|---|---|---|---|
| Abrasive Paper | 75 | 36 | 300 | Until flat and roughness removed |
| Abrasive Paper | 45 | 36 | 300 | Until plane |
| Cloth | 9 | 27 | 150 | 5 mins |
| Cloth | 3 | 27 | 150 | 4mins |
| Cloth | 1 | 27 | 150 | 3 mins |
| Cloth | 0.05 | 27 | 150 | 2 mins |

### 7.4.1.2 Imaging:

Imaging was performed using a Hitachi TM3030 Desktop SEM, images were taken at 15 kV with back scatter detection. The samples had no coating applied to the surface. Images were taken of the whole cell and at three separate points in the hydrogen electrode to obtain a representative sample of the cell. Each hydrogen electrode image also had energy dispersive x−ray (EDX) spectroscopy was also performed on the samples for phase analysis. EDX was performed using a Quantax70 EDX detector (Bruker Nano GmbH), with detection performed for 60 seconds.

### 7.4.1.3 Image processing:

The images obtained were analysed using the imaging analysis software Fiji [163,181]. There were three methods of data analysis performed on the cell, two of thresholding and one of particle size measurement.

#### 7.4.1.3.1 Thresholding:

## BSE thresholding

The first thresholding method was performed on the BSE images to get a value for the pore and solid fraction of the cells. The thresholding is performed by pixel intensity; the operator chose a value for pixel intensity which they felt corresponded with void areas. This is a subjective analysis and the value depends on the contrast of the image. While errors should be reduced by the use of multiple images from different areas the error associated with this method is high.

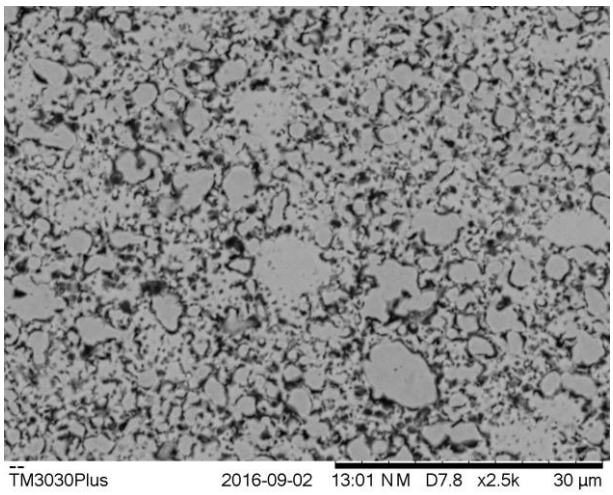


**Figure 104A**

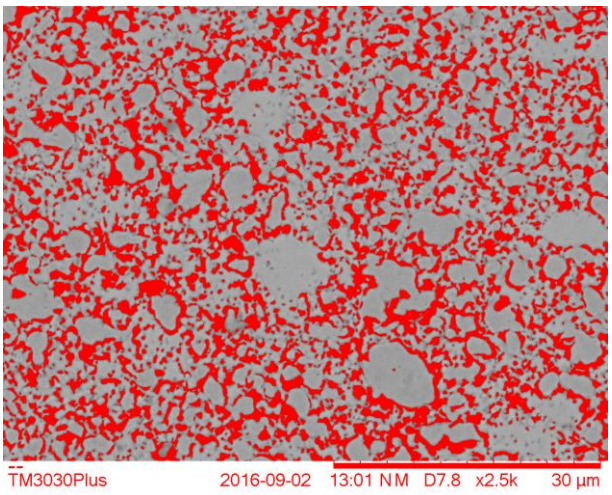


**Figure 104B**

**Figure 104: Shows the thresholding analysis performed on the BSE images. Figure 104A shows the original image. Figure 104B shows the image with voids highlighted.**

## EDX thresholding

Thresholding was also performed on the EDX images. Figure 105 shows the process of determining the phase composition for the EDX images. The porosity of these images is less than that observed through the BSE images, therefore the analysis should not be thought of as quantitative but comparisons between cells can be made. The void is lower due to the resolution of the EDX image being lower than the BSE image.

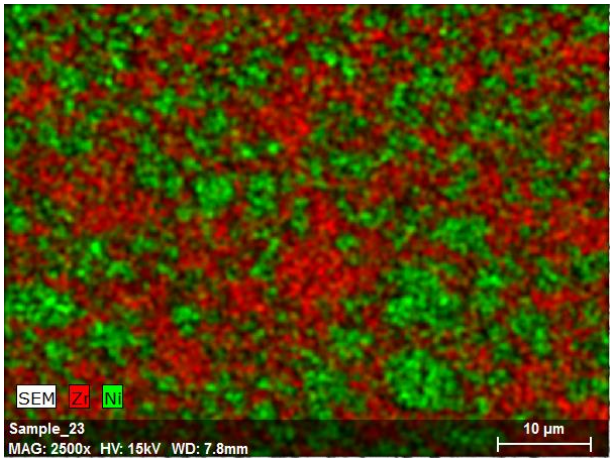


**Figure 105A**

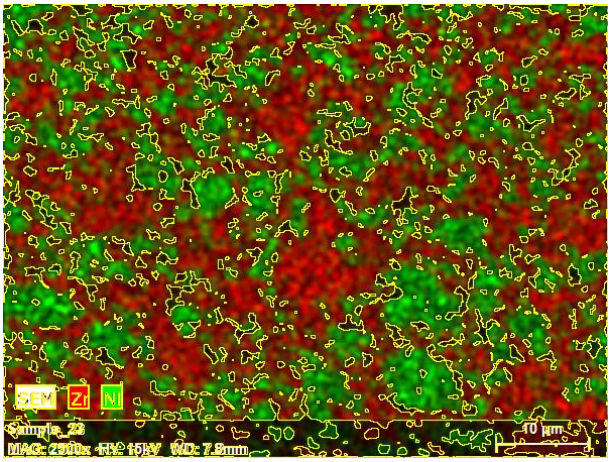


**Figure 105B**

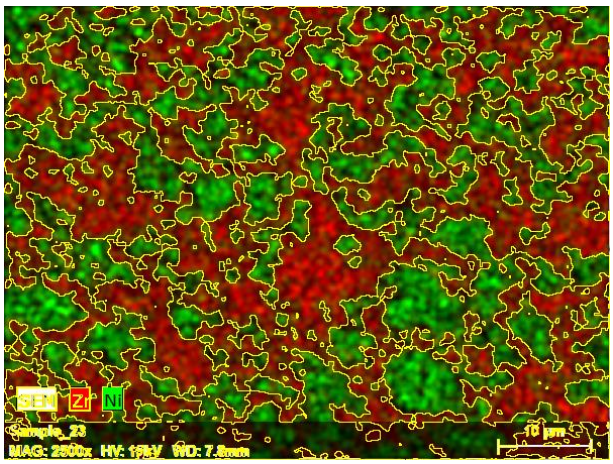


**Figure 105C**

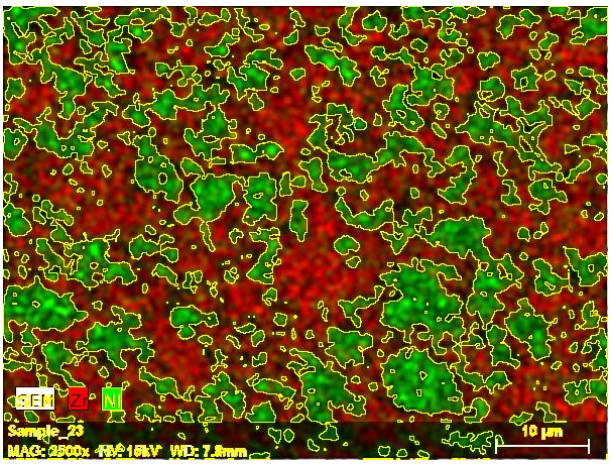


**Figure 105D**

**Figure 105: Images show thresholding of EDX images for measurement of different phases. Figure 105A shows the original image. Figure 105B shows the image with sections of void highlighted for measurement. Figure 105C shows the zirconia phase highlighted. Figure 105D shows the Nickel phase highlighted.**

The final analysis method has been used to determine the average nickel particle size. This is based on the line analysis method by Hauch described in [130]. For this a grid was placed over the image, as shown in Figure 106B. For the central 10 lines the length of intersection between each nickel particle and the line is measured. For each cell three images are analysed in this way and the average length has been used as the particle diameter.

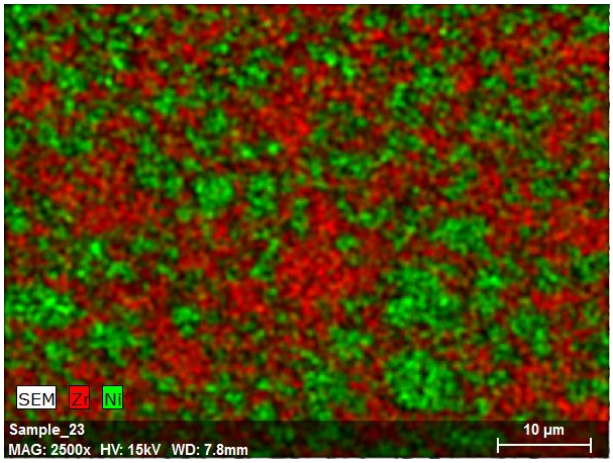


**Figure 106A**

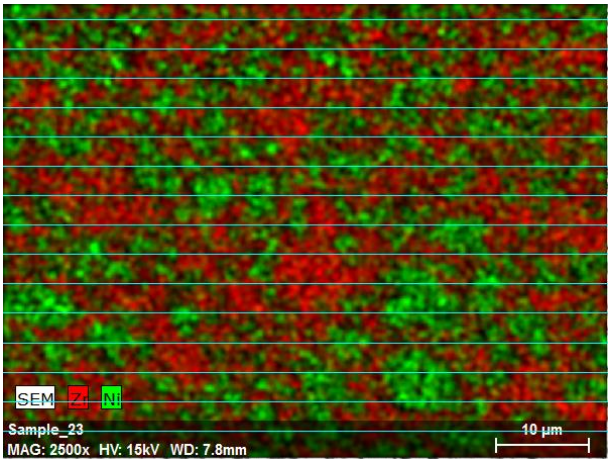


**Figure 106B**

**Figure 106: Line analysis used to determine the average nickel particle diameter. The length of the intersection between each nickel particle and the line is used to give an average value.**

## 7.4.2 Results

An overview of some of the images used in the analysis of cells in this work is shown in Figure 107 (the whole cell), Figure 108 (hydrogen electrode close up), and Figure 109 (EDX of hydrogen electrode). The majority of the focus has been on the hydrogen electrode as this was the only electrode which was experiencing a difference in conditions during the experiment therefore thought to be the source of differences in the cell degradation.

In the images shown in Figure 107 there are four distinct regions observable. The largest region at the bottom of the image is the hydrogen electrode at 392−395µm thick. The region above this is the electrolyte which is 9−10µm thick. The next region is the oxygen electrode which is 23−25 µm thick. These layers are consistent in thickness between the cells as they were the as received manufactured cell. Above these there is the oxygen electrode contacting layer which is of a very inconsistent thickness. The contacting layer was applied by hand and the inconsistency in this layer is a possible cause of inconsistent cell performance.

There are differences observable in the hydrogen electrodes of the cells. These differences are mainly in the different amount of void observable in the images notably in for 47.5 vol%

water (Figure 107E) which shows a large amount of black voids in the structure of the hydrogen electrode. However, the other cells show little differences in the porosity of the samples which doesn't allow a firm conclusion on the causes of the change to be confirmed. The void in the structure could have been present before the cell was tested further tests are required to identify that this is caused by differences in the water partial pressure. While some of the images show areas of light and dark in the hydrogen electrode it isn't possible to determine different phases using the SEM imaging.

Figure 108 shows a close up of the hydrogen electrode for each of the cells. EDX of the same areas at the same magnification is shown in Figure 109 which allows the areas of nickel and zirconia to be distinguished. In the analysis 3 images from different areas of the cell have been used to give an overview of the whole cell. It isn't possible to draw any conclusions on any differences between the images in Figure 108 or Figure 109, the differences between the images are too small to make any meaningful conclusions.

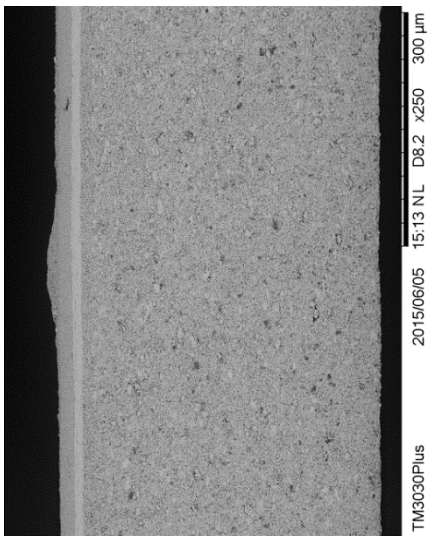


**Figure 107A: 2.5 vol% $H_2O$**

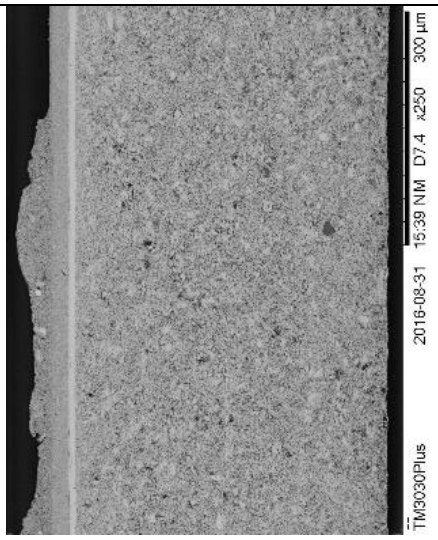


**Figure 107B: 7.5 vol% $H_2O$**




**Figure 107C: 25 vol% $H_2O$**

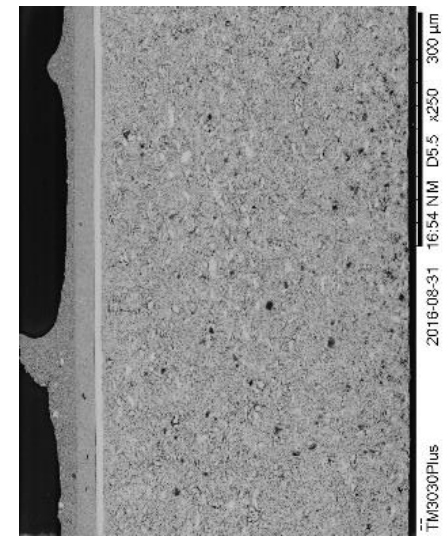


**Figure 107E: 47.5 vol% $H_2O$**

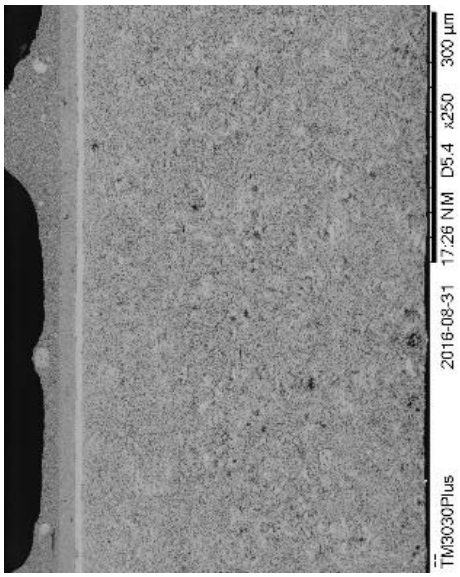


**Figure 107D: 40 vol% $H_2O$**

**Figure 107: Images showing the cross section of the whole cell at 250x magnification.**

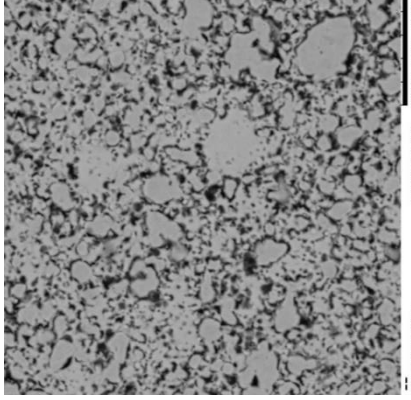


**Figure 108: 25 vol% $H_2O$**

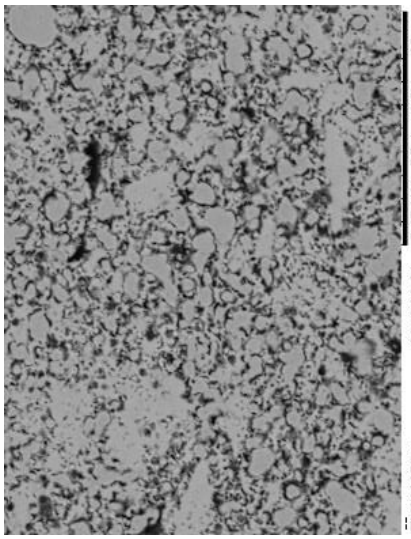


**Figure 108: 7.5 vol% $H_2O$**

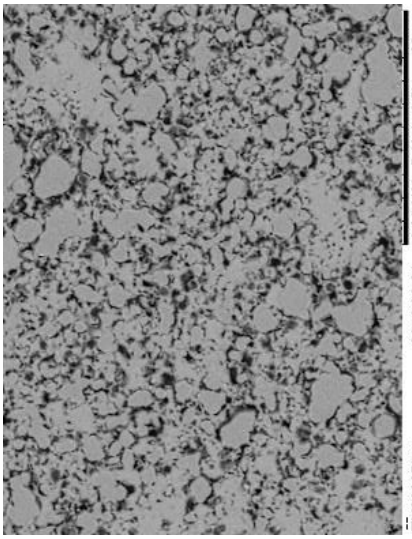


**Figure 108: 2.5 vol% $H_2O$**

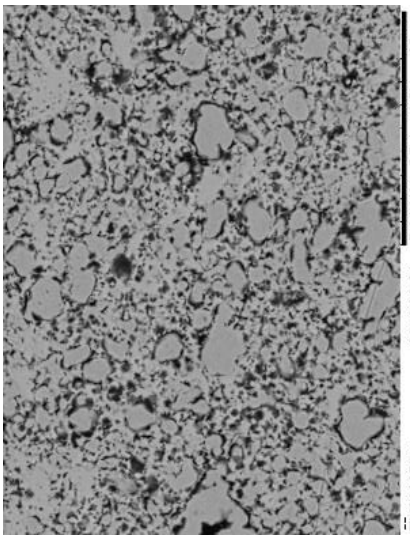


**Figure 108: 47.5 vol% $H_2O$**

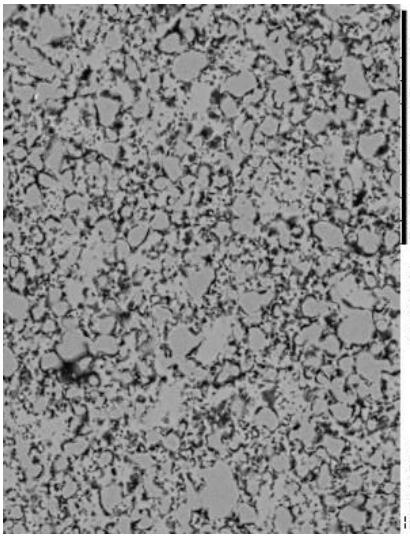


**Figure 108: 40 vol% $H_2O$**

**Figure 108: A selection of the SEM images of the hydrogen electrode at 2500x magnification used for particle analysis.**

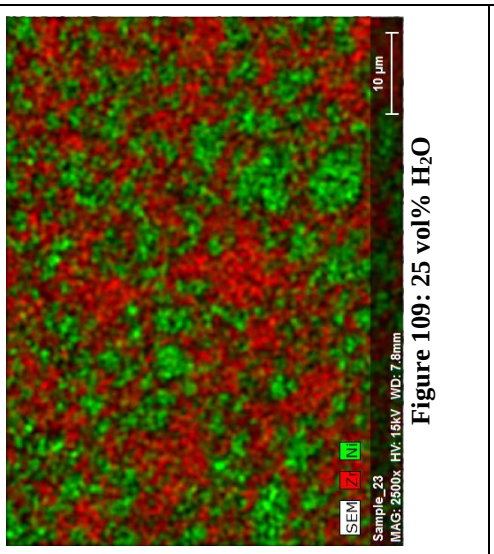


Figure 109: 25 vol% $H_2O$

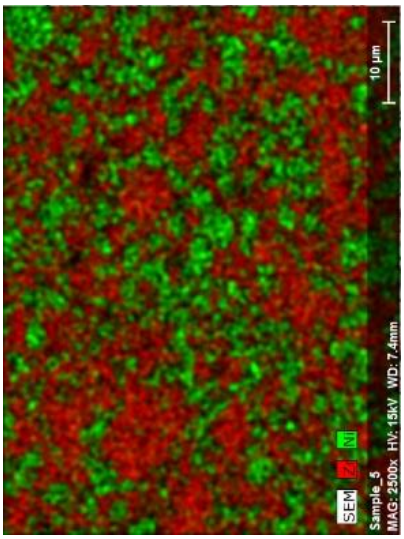


Figure 109: 7.5 vol% $H_2O$

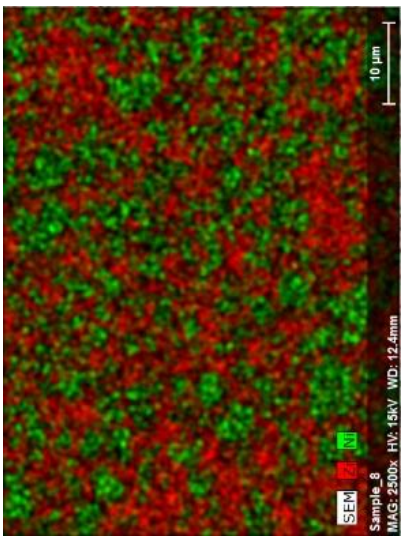


Figure 109: 2.5 vol% $H_2O$

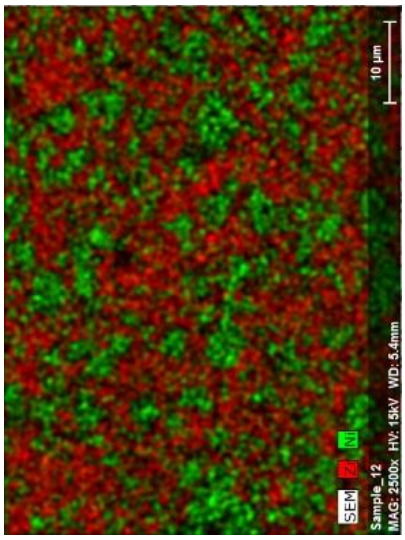


Figure 109: 47.5 vol% $H_2O$

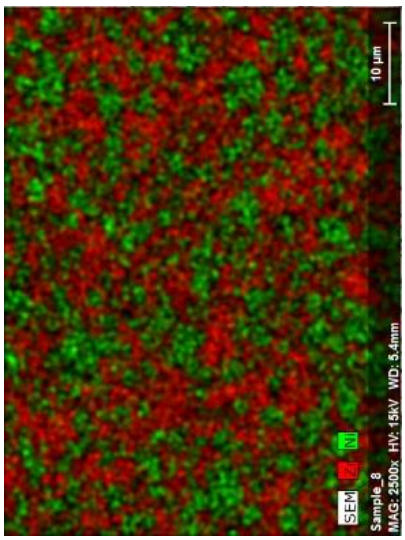


Figure 109: 40 vol% $H_2O$

**Figure 109; EDX showing areas of nickel and zirconia of the areas of the cell shown in Figure 108.**

The visual analysis of the cells didn't provide any insight into the degradation mechanisms present in the cell. While there are differences in the cells the differences are small and don't appear to follow a pattern or be linked to the water content or the degradation rate of the cells. On a single image there is no guarantee that the effects observed are due to the conditions of testing as opposed to localised defects induced during manufacturing. As single images aren't able to provide an insight into the evolution of the cell the analysis images taken for a number of different areas has been performed in an attempt to prevent localised differences playing a part in the analysis. Images from three randomly selected areas of the cell have been taken, these have then been analysed, the results are shown in Figure 110, Figure 111, and Figure 112.

Figure 110 shows the average particle length against the water ratio in the feed gas. There appears to be a slight downward trend in the nickel particle size which would be expected if nickel agglomeration was taking place. However, this trend is not strong enough to prove definitive as the errors associated with the measurement of the particles is large. Further experiments at a longer time scale and with higher water ratio in the feed gas are required to provide a more comprehensive analysis and further evidence for the agglomeration.

Figure 111 shows the phase ratios of pore nickel and zirconia detected in the EDX analysis. There are no distinct trends in the data. The cell with 25% water at the inlet shows a slight reduction in zirconia and pore fractions with a slight increase in the nickel fraction. This could be due to the manufacturing of the cell leading to a slight difference in nickel particle size. It could also be that the areas of the cell studied was not representative of the bulk. It would be expected that nickel agglomeration would lead to a decrease in the apparent nickel fraction as the agglomeration would lead to a decrease in the apparent surface coverage of the nickel, this was not observed in this work. It is possible that longer duration or higher water partial

pressures are required for this to occur. The pore fraction observed through the EDX analysis isn't a reliable measure as the EDX masks the true porosity of the sample through blurring of the image.

Figure 112 shows the average pore fraction for the cells using the BSE image of the surface. This allows a better analysis of the cell porosity as the edges of the particles are more clearly defined. There is still some error associate with the results as determination of the particle edge is still dependant on the operator's judgment. In this work no significant changes in the pore fraction of the cells was observed and there were no trends observable.

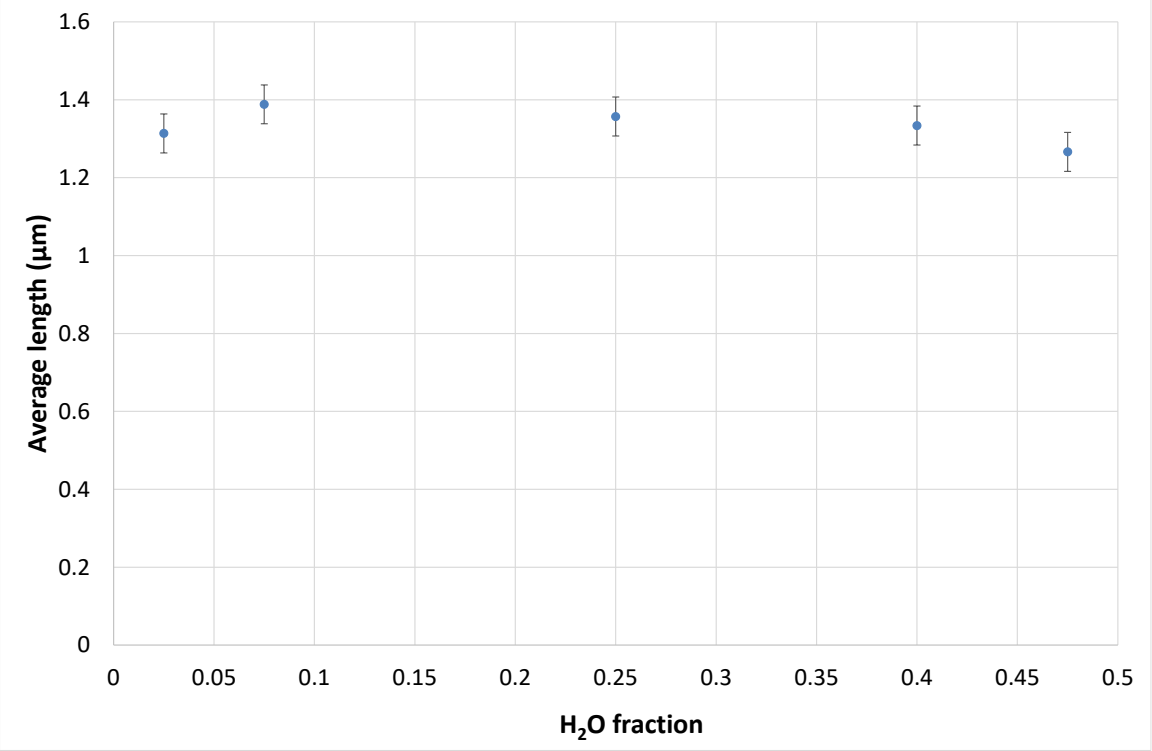


**Figure 110: Showing the variation in average particle diameter vs the $H_2O$ ratio in the feed gas (the rest of the fuel gas was 50% nitrogen with the remainder $H_2$), the total gas flow rate was 240 ml $min^{-1}$ performed at 800ºC.**

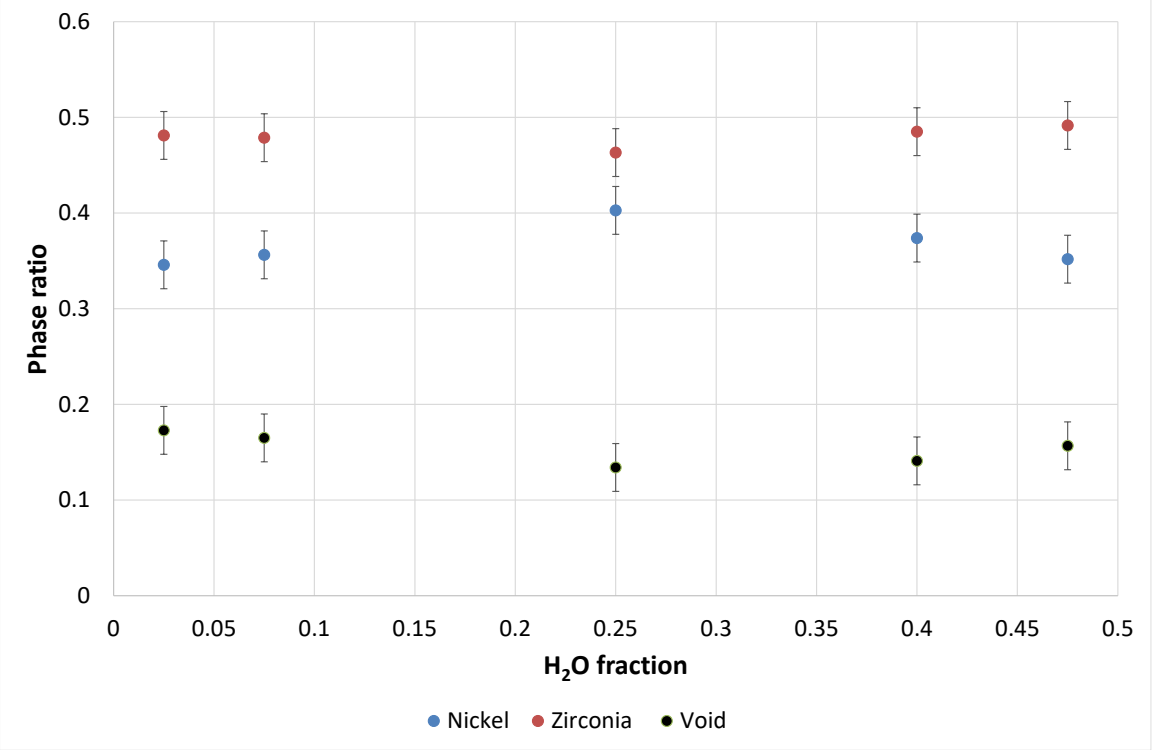


**Figure 111: Showing the fraction of void, Zirconia and Nickel in the samples vs the water content in the feed gas (the rest of the fuel gas was 50% nitrogen with the remainder $H_2$) the total gas flow rate was 240 ml $min^{-1}$ performed at 800ºC.**

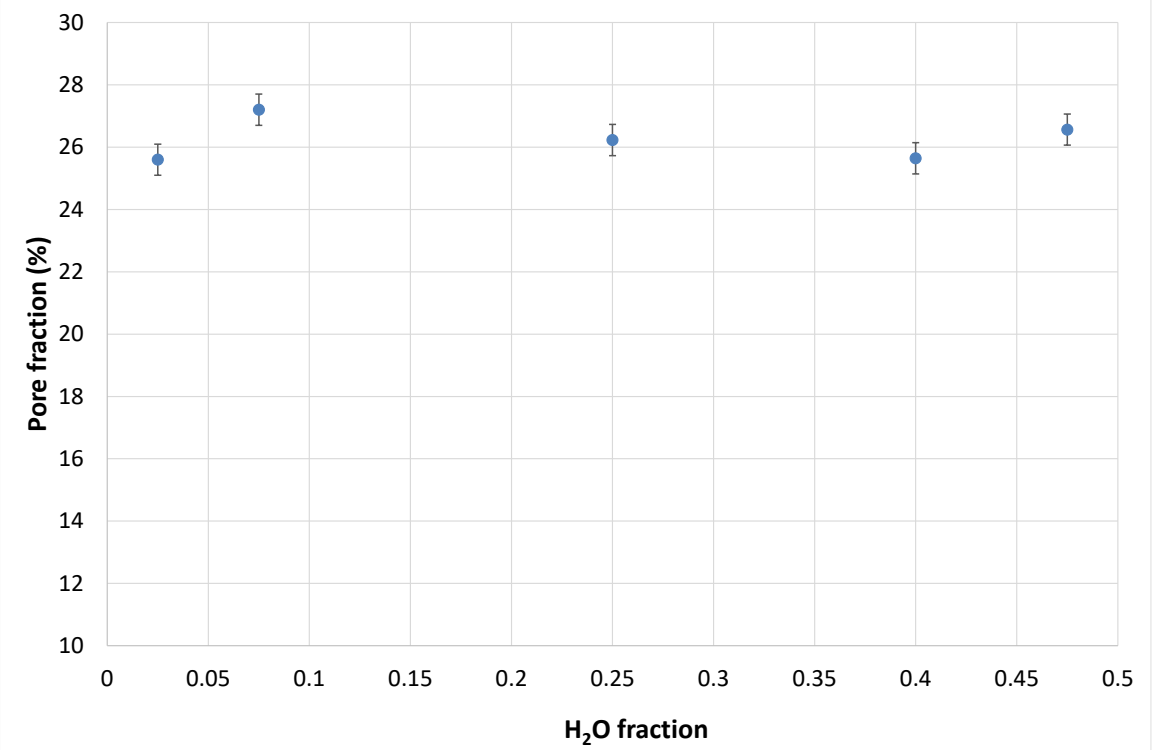


**Figure 112: Average pore fraction for the cells tested with different water partial pressure to the hydrogen electrode (the rest of the fuel gas was 50% nitrogen with the remainder $H_2$). the total gas flow rate was 240 ml $min^{-1}$ performed at 800ºC.**

## 7.5 Discussion:

In Table 6 the results for the galvanostatic degradation have been summarised, and in Figure 113 the degradation rate for the cell vs water content is plotted. It was expected that the degradation rate would increase as the water content in the cells increased. However as can be seen in Figure 113 this is not the case as there is a decrease in electrolysis degradation rate with increasing water content in the cell. It was expected that an increase in the water content would result in an improvement in cell performance during electrolysis but an increase in the water content in the fuel would also lead to an increase in the cell degradation rate.

**Table 6: Summary of the results for each cell.**

| H2:H2O:N2 Volumetric ratio | | | OCV with water | Electrolysis Degradation rate ($mV\ kh^{-1}$) | Cell Name | Initial ASR ($\Omega\ cm^2$) | IV ASR degradation ($\Omega\ kh^{-1}$) | | Resistance degradation from galvanostatic data ($\Omega\ kh^{-1}$) |
|---|---|---|---|---|---|---|---|---|---|
| $H_2$ | $H_2O$ | $N_2$ | | | | | FC | EL | |
| 47.5 | 2.5 | 50 | 0.99 | 512 | Ningbo 54 | 0.737 | 0.40 | 0.66 | 1.03 |
| 42.5 | 7.5 | 50 | 0.99 | 250 | Ningbo 83 | 0.63 | 0.66 | 0.67 | 0.49 |
| 25 | 25 | 50 | 0.91 | 143 | Ningbo 50 | 1.79 | −0.27 | 0.47 | 0.28 |
| 10 | 40 | 50 | 0.85 | 94.1 | Ningbo 87 | 0.89 | 0.22 | 0.13 | 0.18 |
| 2.5 | 47.5 | 50 | 0.77 | 45.3 | Ningbo 52 | 2.88 | 0.14 | 0.32 | 0.09 |

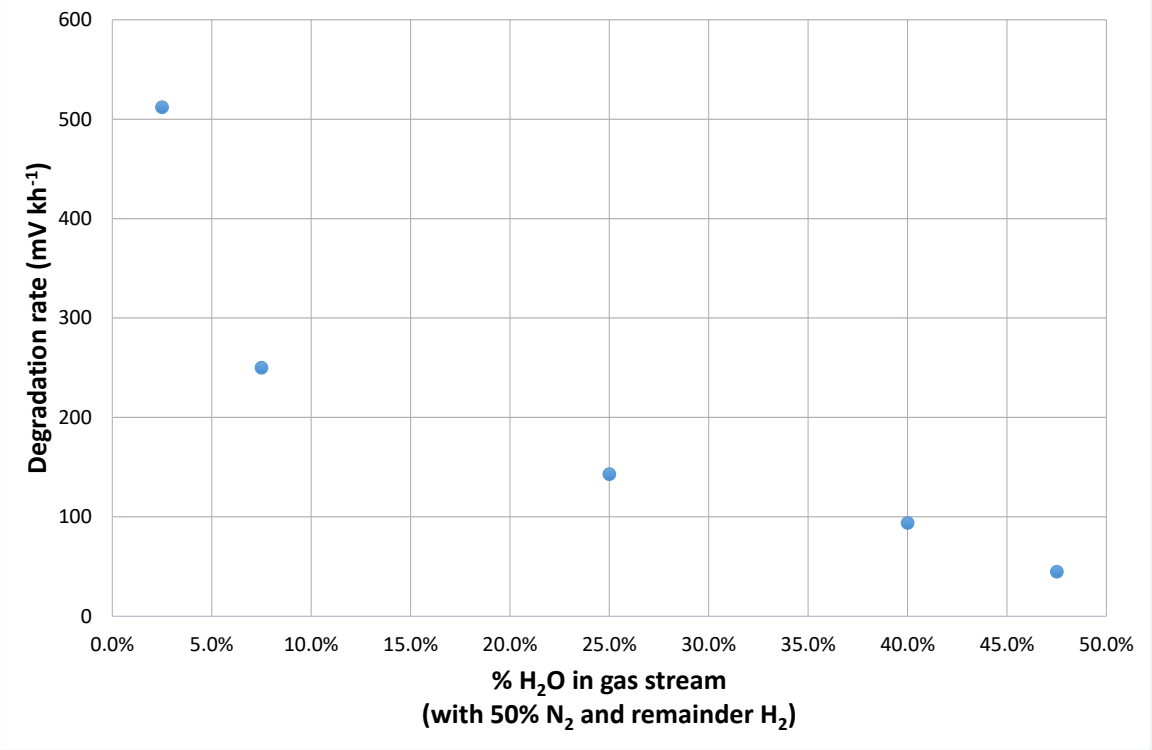


**Figure 113: Graph showing voltage degradation rate vs water content in the cell fuel supply, the rest gas was 50% $N_2$ with the balance $H_2$.**

The rate of degradation was also monitored via impedance spectroscopy and through IV measurements. The trend in the degradation measured via the IV curves does not seem to be related to the degradation measured via the galvanostatic data.

Interpretation of the degradation via impedance spectroscopy has been very difficult as no clear trends in the data have been identifiable. There is some evidence at low water content 2.5Vol% and 7.5Vol% of an increase in the ohmic resistance and increase in low frequency impedance of the cell; however these don't appear to account for the full degradation observed in the cell. There are three reasons why no trend in the impedance data has been evident. The degradation of the cells has been too small which is resulted in very small differences in the impedance spectra. The scatter within the impedance data is too large and obscures any trends within the data. The improvement in the cell performance observed during the IV curve is masking the degradation process. It is likely that it is a combination of

all three processes which is occurring to prevent interpretation of the degradation mechanism via impedance spectroscopy.

The rate of ASR degradation measured from the IV data does not appear to be related to the rate of degradation observed during galvanostatic operation of the cell. This may indicate that the degradation is reversible. After each break in the galvanic operation there was also an improvement in performance which indicated that some temporary reversal of the degradation was occurring. Possible reasons are outlined below;

- The degradation is reversible, and a period of OCV or polarisation during the IV curve is enough to partially restore the cell. As the degradation rates were constant it appears likely that upon resumption of galvanostatic operation the cell quickly returns to the previous state of degradation.
- The rate of degradation during galvanostatic operation may be artificially high due to the formation of oxide ion gradients across the cell appearing as cell degradation. This degradation is temporary and is reversed during OCV of fuel cell operation (i.e. during the IV curve).
- If the cell is displaying an improvement in performance and shows improvement during the IV curves it is also likely that the impedance measurements which was performed directly after the IV curves measurements would also fail to show the full extent of the degradation.

At low degradation rates there were some initial changes in the start of the galvanostatic data, which lasted 20−40 hours and is due to some conditioning of the cell. This region is associated with a change in the ohmic resistance of the cell and increases in the high frequency impedance of the cell. After the cell conditioning has occurred there is no further

indication of degradation in the impedance spectra or the IV curves. At low rates of degradation a much greater period of time would be required to identify the causes.

Some possible causes of the increased degradation at low water content are discussed below.

- Degradation is higher at higher voltages in electrolysis operation. High voltage operation is known to cause breakdown of the cell. This was expected to cause degradation at much higher operational voltages >1.6V for electrolysis operation. This was ruled out as being the cause as the degradation with 47.5% water was low but the cell showed a poor initial performance causing the voltage of operation to be very similar to that of 2.5Vol% and 7.5Vol% which both had very high rates of degradation. Therefore, degradation due to cell breakdown caused by operation at high voltages is not thought to be the main reason why degradation is occurring at a greater rate with lower water content.
- As the degradation is greatest when the cell is operating at low water partial pressure it was thought that the cell could be damaging itself due to the lack of water. During electrolysis operation the potential across the cell causes oxygen ions to be pulled towards the oxygen electrode. The oxygen ions should be supplied by the water in the cell. When the water partial pressure is low the water may not be able to provide oxygen at the rate the cell is consuming it. While this will cause a loss in performance the cell may also get oxygen ions from other sources. The only other available source of oxygen is from within the YSZ structure. During operation oxygen from YSZ within either the anode, cathode or electrolyte may be consumed. This would lead to structural damage of the cell due to the YSZ reduction. It was thought that this would only occur with operation at very high potentials.

- As discussed previously the cell is undergoing mass transport losses due to removal of the water at a greater rate than it can be replaced. It is not possible to accurately measure the mass transport losses via impedance spectroscopy as there is a large amount of scatter in the data at low frequency.

The range of water contents tested in the work is lower than is ideal. In future more studies on degradation at higher water contents will be made. It is expected that the rate of degradation will grow as the water content increases closer to 100%.

In this work it has not been possible to determine a link between the observed cell degradation rates and the microstructural changes observed in the cell. The cell imaging has focused on the degradation of the hydrogen electrode and it hasn't been possible to identify any trends in the changes to cell structure. It is possible that the changes occurring in the cell are too small to be observed over the time scales used in this work. The use of more detailed imaging of the hydrogen electrode may show differences in the individual nickel particles which hasn't been possible with the equipment available in this work. Further investigation of the cell using a microscope with greater resolution is required to identify changes in the hydrogen electrode. The performance of more long term degradation studies would allow larger changes in the cell to become observable.

## 7.6 Conclusions:

Solid oxide cells have been tested in galvanostatic operation with a range of water contents from 2.5−47.5 vol% water. The galvanostatic data shows that there is much greater degradation occurring with low water content than with high water content, at 2.5 vol% the cell degrades at 512mV $kh^{-1}$, and at 47.5 vol% the cell degrades at 45 mV $kh^{-1}$. This is the

opposite of what was expected as increased water content was expected to cause increased degradation of the cell. A clear interpretation of the causes of the degradation using impedance analysis and IV curves is difficult as they don't indicate the degradation observed in the galvanostatic data.

Between the galvanostatic periods the cells underwent some improvement in performance, which may be due to the cell undergoing an IV curve which cycles the cell between fuel cell and electrolysis operation or due to the cell resting at OCV. Either of these may cause a change in the oxide ion gradient across the cell which leads to a temporary increase in performance upon resumption of galvanostatic operation. The improvement in performance may disguise the degradation in the IV and impedance data when the cell is operating at low water partial pressures. At low water partial pressure, 2.5 vol% and 7.5 vol% there was evidence of increases in ohmic resistance and increases in the low frequency resistance of the cell however quantification of the results is difficult as the scatter in the impedance results is large.

# 8 Conclusions and future work

## 8.1 Overview

In this thesis testing of solid oxide cells in fuel cell and electrolysis operation has been performed, and attempts were also made to fabricate cells and these attempts have been described. Equipment for testing solid oxide electrolysis cells has been set up and the development process for this was described.

Cells of a number of different types were tested. Initial work was performed using microtubular cells, the supply of these became limited and a new source of cells was required. Attempts were made to fabricate solid oxide cells however problems were experienced in the application of a dense electrolyte which means that a reliable OCV could not be achieved. A number of testing parameters were used to achieve a dense electrolyte. However, leak testing results showed that the performance was an order of magnitude worse than should be achievable. Due to the issues in the manufacture of cells the bulk of the results described in this thesis have been performed on cells purchased from a commercial supplier.

Degradation studies were performed in two ways, with cyclic operation and varying water content. The degradation of the cells was studied using the galvanostatic, IV and impedance data collected from the cell during its operation. It is thought that some of the degradation of the cells is reversible. Therefore, it is suspected that the degradation observed in the IV and impedance data may not fully correspond to the degradation observed in the galvanostatic data.

## 8.2 Cyclic testing (reversible operation)

Current cyclic testing on solid oxide cells was performed between fuel cell and electrolysis operation. The cyclic testing was aimed at investigating the degradation rate in both fuel cell and electrolysis operation. It was also aimed at gaining an understanding of the different degradation rates experienced when a cell undergoes cyclic operation. The cells used in this work showed a higher rate of degradation in electrolysis operation than fuel cell operation. The rate was approximately double for electrolysis operation than fuel cell operation. One possibility is that there are multiple degradation pathways in progress in the same cell. The main degradation pathway for fuel cell operation may be different to the main degradation pathway for electrolysis operation. If each of these independently changed the degradation rate, different degradation rates may be observed. Another possibility is that the degradation which occurs in electrolysis operation is a reversible, or partially reversible, process. During the fuel cell steps the cell may undergo a recovery stage during which the damage is reversed. Other researchers have found that a cell operated cyclically does not show signs of degradation [106], however the time period over which each electrolysis step was performed was shorter than in this work. They reported that an electrolysis time period shorter than the fuel cell time period was required to prevent degradation.

## 8.3 Varying water content

Cells were also tested with varying water concentration to the hydrogen electrode. Instability and poor sealing meant that water contents over 50 vol% $H_2O$ were not achievable. When the cell was operated with low humidity (2.5 vol% and 7.5 vol%) very high rates of degradation were observed. The rate of degradation rapidly reduced when the cell was operated with

increasing water supply to the hydrogen electrode. The degradation of the cell was not, as was expected, due to high water content on the hydrogen electrode.

As with the work in the cyclic testing chapter there were difficulties with the identification of degradation mechanism via impedance spectroscopy. There were no clear trends in the impedance data throughout the experiments and further studies are required to establish the cause of degradation in the cell. The impedance results for the cells with the lowest water content 2.5 vol% and 7.5 vol%, show increases in the low frequency impedance, and there is also an increase in the ohmic resistance of the cell. The low frequency region is associated with mass transport limitations of the cell therefore it is possible that the cell is suffering from fuel limitations. Damage to the hydrogen electrode at low water flow rates may result in reduction of porosity which would lead to increasing mass transport resistance, however no evidence of this was observed in the imaging performed.

It has not been possible to draw conclusion on the links between the cell degradation observed and the differences in the cell microstructure. More imaging work is required to identify the changes in cell microstructure occurring.

## 8.4 Future Work

### 8.4.1 Increasing degradation length

The timescale over which the experiments will be performed will be extended. The current experiments have been performed over a time scale which hasn't shown clear evidence of the cause of the cell degradation. Increasing the timescale would provide clearer evidence of the

degradation mechanisms and would enable structural investigation of the cell to reveal any changes to the cell microstructure occurring over the experiment.

### 8.4.2 Investigating electrolysis and fuel cell period

In this work initial experiments on changing the period of the fuel cell and electrolysis periods has been performed. In further work this will be expanded to gain a deeper understanding on the influence on the different process of the overall degradation rate. In each electrolysis galvanostatic step there is an initial period of very rapid degradation which is followed by a longer period of slower degradation. It is unknown if the initial degradation is more damaging to the cell or if the rate of degradation would become less severe with longer testing. Therefore, longer and shorter time periods for each galvanostaic step will be investigated.

# 9 References

[1] Brown A, Simon M, Zuzana D. Markets and Prospects by Technology. 2011.

[2] Cho J, Jeong S, Kim Y. Commercial and research battery technologies for electrical energy storage applications. Prog Energy Combust Sci 2015;48:84. doi:http://dx.doi.org/10.1016/j.pecs.2015.01.002.

[3] Carrasco JM, Franquelo LG, Bialasiewicz JT, Member S, Galván E, Guisado RCP, et al. Power-Electronic Systems for the Grid Integration of Renewable Energy Sources : A Survey. Ieee Trans Ind Electron 2006;53:1002–16. doi:10.1109/TIE.2006.878356.

[4] Dehamna A, Jerram L. Market Data : Hydrogen Infrastructure. UK: Navigant Research; 2013.

[5] Richards M, Shenoy A. $H_2$-MHR Pre-Conceptual Design Summary for Hydrogen Production. Nucl Eng Technol 2007;39:1–8. doi:http://article.nuclear.or.kr/jknsfile/v39/JK0390001.pdf.

[6] Gainer K. Hydrogen as a Chemical Constituent and as an Energy Source. U.S.: BCC Research; 2011.

[7] Persistence Market Research. Global hydrogen market will reach $141.4 bn by value, in 2020 by Persistence Market Research. Focus Catal 2015;2015:2. doi:10.1016/j.focat.2015.07.049.

[8] UK Parliament. Climate Change Act 2008. UK: The National Archives; 2008. doi:10.1136/bmj.39469.569815.47.

[9] HM Government. 2050 Pathways Analysis. UK: HM Government; 2010. doi:Ref: 10D/764.

[10] Sinden G. Characteristics of the UK wind resource: Long-term patterns and relationship to electricity demand. Energy Policy 2007;35:112–27. doi:10.1016/j.enpol.2005.10.003.

[11] Goater A. Intermittent Electricity Generation. UK: Houses of Parliament, Office of Science and Technology; 2014.

[12] Dunn B, Kamath H, Tarascon J-M. Electrical Energy Storage for the Grid: A Battery of Choices. Science 2011;334:928–35. doi:10.1126/science.1212741.

[13] The Energy Research Partnership. The future role for energy storage in the UK -- Main Report. UK: The Energy Research Partnership; 2011.

[14] Grid N. Gas Transmission Operational Data 2015. http://www2.nationalgrid.com/UK/Industry-information/Gas-transmission-operational-data/ (accessed June 25, 2015).

[15] Grid N. Electricity Transmission Operational Data 2015. http://www2.nationalgrid.com/uk/industry-information/electricity-transmission-operational-data/ (accessed June 25, 2015).

[16] Newton J. Power-to-gas & methanation - Pathways to a “hydrogen economy.” 14th Anu. APGTF Work. London 12-13th March, 2014.

[17] Gahleitner G. Hydrogen from renewable electricity: An international review of power-to-gas pilot plants for stationary applications. Int J Hydrogen Energy 2013;38:2039–61. doi:10.1016/j.ijhydene.2012.12.010.

[18] Gotz M, Lefebvre J, Friedemann M, Graf F, McDaniel Koch A, Bajohr S, et al. Renewable Power-to-Gas : A technological and economic review. Renew Energy 2015;85:1371–90. doi:10.1016/j.renene.2015.07.066.

[19] De Saint Jean M, Baurens P, Bouallou C, Couturier K. Economic assessment of a power-to-substitute-natural-gas process including high-temperature steam electrolysis. Int J Hydrogen Energy 2015;40:6487–500. doi:10.1016/j.ijhydene.2015.03.066.

[20] Zhang X, Chan SH, Ho HK, Tan S-C, Li M, Li G, et al. Towards a smart energy network: The roles of fuel/electrolysis cells and technological perspectives. Int J Hydrogen Energy 2015;40:6866–919. doi:10.1016/j.ijhydene.2015.03.133.

[21] Melaina MW, Antonia O, Penev M. Blending Hydrogen into Natural Gas Pipeline Networks : A Review of Key Issues. US: NREL; 2013.

[22] ITM Power | Hydrogen n.d. http://www.itm-power.com/ (accessed April 1, 2015).

[23] Hydrogenics. Power-to-Gas n.d. http://www.hydrogenics.com/hydrogen-products-solutions/energy-storage-fueling-solutions/power-to-gas (accessed August 15, 2015).

[24] Wang W, Vohs J, Gorte R. Hydrogen Production Via $CH_4$ and CO Assisted Steam Electrolysis. Top Catal 2007;46:380–5.

[25] Graves C, Ebbesen SD, Mogensen M. Co-electrolysis of $CO_2$ and $H_2O$ in solid oxide cells: Performance and durability. Solid State Ionics 2011;192:398–403.

doi:10.1016/j.ssi.2010.06.014.

[26] Ebbesen SD, Høgh J, Nielsen KA, Nielsen JU, Mogensen M. Durable SOC stacks for production of hydrogen and synthesis gas by high temperature electrolysis. Int J Hydrogen Energy n.d.;In Press,. doi:10.1016/j.ijhydene.2011.03.130.

[27] Milliken JA. Roadmap on Manufacturing R&D for the Hydrogen Economy. US: DOE Hydrogen Program; 2005.

[28] Holladay JD, Hu J, King DL, Wang Y. An overview of hydrogen production technologies. Catal Today 2009;139:244–60. doi:10.1016/j.cattod.2008.08.039.

[29] Scholz WH. Processes for industrial production of hydrogen and associated environmental effects. Gas Sep Purif 1993;7:131–9. doi:10.1016/0950-4214(93)80001-D.

[30] Spath PL, Mann MK. Life Cycle Assessment of Hydrogen Production via Natural Gas Steam Reforming 2001.

[31] Balat H, Kırtay E. Hydrogen from biomass – Present scenario and future prospects. Int J Hydrogen Energy 2010;35:7416–26. doi:10.1016/j.ijhydene.2010.04.137.

[32] Malaika A, Kozlowski M. Hydrogen production by propylene-assisted decomposition of methane over activated carbon catalysts. Int J Hydrogen Energy 2010;35:10302–10. doi:10.1016/j.ijhydene.2010.07.176.

[33] Ni M, Leung DYC, Leung MKH, Sumathy K. An overview of hydrogen production from biomass. Fuel Process Technol 2006;87:461–72. doi:10.1016/j.fuproc.2005.11.003.

[34] Yilmaz F, Balta MT, Selbaş R. A review of solar based hydrogen production methods. Renew Sustain Energy Rev 2016;56:171–8. doi:10.1016/j.rser.2015.11.060.

[35] Miller EL, Rocheleau RE, Deng XM. Design considerations for a hybrid amorphous silicon/photoelectrochemical multijunction cell for hydrogen production. Int J Hydrogen Energy 2003;28:615–23. doi:10.1016/S0360-3199(02)00144-1.

[36] Mingyi L, Bo Y, Jingming X, Jing C. Thermodynamic analysis of the efficiency of high-temperature steam electrolysis system for hydrogen production. J Power Sources 2008;177:493–9. doi:10.1016/j.jpowsour.2007.11.019.

[37] Konrad T. Hydrogen and Fuel Cell Stocks. Forbes 2013. http://www.forbes.com/sites/tomkonrad/2013/12/11/twelve-hydrogen-and-fuel-cell-stocks/#122d987326df (accessed August 26, 2016).

[38] EERE. Types of Fuel Cells | Department of Energy n.d. http://energy.gov/eere/fuelcells/types-fuel-cells (accessed August 26, 2016).

[39] O'Brien JE, Stoots CM, Herring JS, McKellar MG, Sohal MS, Condie KG. High Temperature Electrolysis for Hydrogen Production from Nuclear Energy - Technology Summary 2010.

[40] Lide DR, editor. CRC Handbook of Chemistry and Physics 80th Edition. 80th ed. U.S.: CRC Press; 1999.

[41] Donitz W. High-temperature electrolysis of water vapor--status of development and perspectives for application. Int J Hydrogen Energy 1985;10:291–5. doi:10.1016/0360-3199(85)90181-8.

[42] Schefold J, Brisse a., Tietz F. Nine Thousand Hours of Operation of a Solid Oxide Cell in Steam Electrolysis Mode. J Electrochem Soc 2012;159:A137. doi:10.1149/2.076202jes.

[43] Cai Q, Haw AWV, Adjiman CS, Brandon NP. Hydrogen production through steam electrolysis: a model-based study. Comput. Aided Chem. Eng., vol. 30, 2012, p. 257–61. doi:10.1016/B978-0-444-59519-5.50052-6.

[44] Nechache A, Mansuy A, Petitjean M, Mougin J, Mauvy F, Boukamp BA, et al. Diagnosis of a cathode-supported solid oxide electrolysis cell by electrochemical impedance spectroscopy. Electrochim Acta 2016;210:596–605. doi:10.1016/j.electacta.2016.05.014.

[45] GrinHy project demos high-temp electrolysis in steel production. Fuel Cells Bull 2016;2016. doi:10.1016/S1464-2859(16)30218-8.

[46] Cinti G, Frattini D, Jannelli E, Desideri U, Bidini G. Coupling Solid Oxide Electrolyser (SOE) and ammonia production plant. Appl Energy 2016;In Press. doi:10.1016/j.apenergy.2016.09.026.

[47] Koumi Ngoh S, Njomo D. An overview of hydrogen gas production from solar energy. Renew Sustain Energy Rev 2012;16:6782–92. doi:10.1016/j.rser.2012.07.027.

[48] Graves C, Ebbesen SD, Mogensen M, Lackner KS. Sustainable hydrocarbon fuels by recycling $CO_2$ and $H_2O$ with renewable or nuclear energy. Renew Sustain Energy Rev 2011;15:1–23. doi:10.1016/j.rser.2010.07.014.

[49] Hosseini SE, Wahid MA. Hydrogen production from renewable and sustainable energy resources: Promising green energy carrier for clean development. Renew Sustain

Energy Rev 2016;57:850–66. doi:10.1016/j.rser.2015.12.112.

[50] O'Brien JE, McKellar MG, Harvego EA, Stoots CM. High-temperature electrolysis for large-scale hydrogen and syngas production from nuclear energy – summary of system simulation and economic analyses. Int J Hydrogen Energy 2010;35:4808–19. doi:10.1016/j.ijhydene.2009.09.009.

[51] Zhang H, Su S, Chen X, Lin G, Chen J. Configuration design and performance optimum analysis of a solar-driven high temperature steam electrolysis system for hydrogen production. Int J Hydrogen Energy 2013;38:4298–307. doi:10.1016/j.ijhydene.2013.01.199.

[52] Roeb M, Monnerie N, Houaijia A, Sattler C, Sanz-bermejo J, Romero M, et al. Coupling Heat and Electricity Sources to Intermediate Temperature Steam Electrolysis 2013;7:2068–77.

[53] Manage MN, Hodgson D, Milligan N, Simons SJR, Brett DJL. A techno-economic appraisal of hydrogen generation and the case for solid oxide electrolyser cells. Int J Hydrogen Energy 2011;36:5782–96. doi:10.1016/j.ijhydene.2011.01.075.

[54] Hino R, Haga K, Aita H, Sekita K. R&D on hydrogen production by high-temperature electrolysis of steam. Nucl Eng Des 2004;233:363–75. doi:10.1016/j.nucengdes.2004.08.029.

[55] Shin Y, Park W, Chang J, Park J. Evaluation of the high temperature electrolysis of steam to produce hydrogen. Int J Hydrogen Energy 2007;32:1486–91. doi:10.1016/j.ijhydene.2006.10.028.

[56] Yildiz B, Kazimi M. Efficiency of hydrogen production systems using alternative

nuclear energy technologies. Int J Hydrogen Energy 2006;31:77–92. doi:10.1016/j.ijhydene.2005.02.009.

[57] Bo Y, Wenqiang Z, Jingming X, Jing C. Status and research of highly efficient hydrogen production through high temperature steam electrolysis at INET. Int J Hydrogen Energy 2010;35:2829–35. doi:16/j.ijhydene.2009.05.037.

[58] Wang Z, Mori M, Araki T. Steam electrolysis performance of intermediate-temperature solid oxide electrolysis cell and efficiency of hydrogen production system at 300 Nm3 h-1. Int J Hydrogen Energy 2010;35:4451–8. doi:10.1016/j.ijhydene.2010.02.058.

[59] Harvego E, McKellar M, Sohal M. Economic Analysis of a Nuclear Reactor Powered High-Temperature Electrolysis Hydrogen Production Plant. J Energy Resour Technol 2008;132:1–0. doi:10.1115/1.4001566.

[60] U.S. Doe. Hydrogen Production Technical Plan — Production. Multi-Year Res Dev Demonstr Plan 2010;5013:1–47.

[61] Muellerlanger F, Tzimas E, Kaltschmitt M, Peteves S. Techno-economic assessment of hydrogen production processes for the hydrogen economy for the short and medium term. Int J Hydrogen Energy 2007;32:3797–810. doi:10.1016/j.ijhydene.2007.05.027.

[62] Dönitz W, Erdle E. High-temperature electrolysis of water vapor--status of development and perspectives for application. Int J Hydrogen Energy 1985;10:291–5. doi:16/0360-3199(85)90181-8.

[63] Stoots CM, O'Brien JE, Condie KG, Hartvigsen JJ. High-temperature electrolysis for large-scale hydrogen production from nuclear energy – Experimental investigations. Int J Hydrogen Energy 2010;35:4861–70. doi:10.1016/j.ijhydene.2009.10.045.

[64] Brisse A, Schefold J, Zahid M. High temperature water electrolysis in solid oxide cells. Int J Hydrogen Energy 2008;33:5375–82. doi:10.1016/j.ijhydene.2008.07.120.

[65] Pergolesi D, Fabbri E, D'Epifanio A, Di Bartolomeo E, Tebano A, Sanna S, et al. High proton conduction in grain-boundary-free yttrium-doped barium zirconate films grown by pulsed laser deposition. Nat Mater 2010;9:846–52. doi:10.1038/nmat2837.

[66] Enoki M, Yan J, Matsumoto H, Ishihara T. High oxide ion conductivity in Fe and Mg doped $LaGaO_3$ as the electrolyte of solid oxide fuel cells. Solid State Ionics 2006;177:2053–7. doi:10.1016/j.ssi.2006.01.015.

[67] Bi L, Boulfrad S, Traversa E. Steam electrolysis by solid oxide electrolysis cells (SOECs) with proton-conducting oxides. Chem Soc Rev 2014;43:8255–70. doi:10.1039/c4cs00194j.

[68] Sadykov V a., Eremeev NF, Sadovskaya EM, Bobin a. S, Fedorova YE, Muzykantov VS, et al. Cathodic materials for intermediate-temperature solid oxide fuel cells based on praseodymium nickelates-cobaltites. Russ J Electrochem 2014;50:669–79. doi:10.1134/S1023193514070131.

[69] Bi L, Boulfrad S, Traversa E. Reversible solid oxide fuel cells (R-SOFCs) with chemically stable proton-conducting oxides. Solid State Ionics 2015;275:101–5. doi:10.1016/j.ssi.2015.03.006.

[70] Berger CM, Tokariev O, Orzessek P, Hospach A, Fang Q, Bram M, et al. Development of storage materials for high-temperature rechargeable oxide batteries. J Energy Storage 2015;1:54–64. doi:10.1016/j.est.2014.12.001.

[71] Laguna-Bercero M a. Recent advances in high temperature electrolysis using solid

oxide fuel cells: A review. J Power Sources 2012;203:4–16. doi:10.1016/j.jpowsour.2011.12.019.

[72] Malavasi L, Fisher CAJ, Islam MS. Oxide-ion and proton conducting electrolyte materials for clean energy applications: structural and mechanistic features. Chem Soc Rev 2010;39:4370–87. doi:10.1039/b915141a.

[73] Hashimoto S, Liu Y, Mori M, Funahashi Y, Fujishiro Y. Study of steam electrolysis using a microtubular ceramic reactor. Int J Hydrogen Energy 2009;34:1159–65. doi:10.1016/j.ijhydene.2008.11.037.

[74] Laguna-Bercero M a., Skinner SJ, Kilner J a. Performance of solid oxide electrolysis cells based on scandia stabilised zirconia. J Power Sources 2009;192:126–31. doi:10.1016/j.jpowsour.2008.12.139.

[75] O'Brien JE, Stoots CM, Herring JS, Hartvigsen J. Hydrogen Production Performance of a 10-Cell Planar Solid-Oxide Electrolysis Stack. J Fuel Cell Sci Technol 2006;3:213. doi:10.1115/1.2179435.

[76] Mahmood A, Bano S, Yu JH, Lee K-H. High-performance solid oxide electrolysis cell based on ScSZ/GDC (scandia-stabilized zirconia/gadolinium-doped ceria) bi-layered electrolyte and LSCF (lanthanum strontium cobalt ferrite) oxygen electrode. Energy 2015;90:344–50. doi:10.1016/j.energy.2015.06.109.

[77] Schefold J, Brisse A, Poepke H. Long-term Steam Electrolysis with Electrolyte-Supported Solid Oxide Cells. Electrochim Acta 2015;179:161–8. doi:10.1016/j.electacta.2015.04.141.

[78] Lee KJ, Seo JW, Yoon JS, Hwang HJ. Electrode Performance in a Solid Oxide

Electrolyzer Cell (SOEC). ECS Trans 2013;57:3255–60. doi:10.1149/05701.3255ecst.

[79] Chen T, Zhou Y, Liu M, Yuan C, Ye X, Zhan Z, et al. High performance solid oxide electrolysis cell with impregnated electrodes. vol. 54. 2015. doi:10.1016/j.elecom.2015.02.015.

[80] Chen T, Liu M, Yuan C, Zhou Y, Ye X, Zhan Z, et al. High performance of intermediate temperature solid oxide electrolysis cells using $Nd_2NiO_{4+\delta}$ impregnated scandia stabilized zirconia oxygen electrode. J Power Sources 2015;276:1–6. doi:10.1016/j.jpowsour.2014.11.042.

[81] Ni M, Leung MKH, Leung DYC. Theoretical analysis of reversible solid oxide fuel cell based on proton-conducting electrolyte. J Power Sources 2008;177:369–75. doi:10.1016/j.jpowsour.2007.11.057.

[82] Ni M, Leung MKH, Leung DYC. Technological development of hydrogen production by solid oxide electrolyzer cell (SOEC). Int J Hydrogen Energy 2008;33:2337–54. doi:10.1016/j.ijhydene.2008.02.048.

[83] Jiang SP, Chan SH. A review of anode materials development in solid oxide fuel cells. J Mater Sci 2004;39:4405–39. doi:10.1023/B:JMSC.0000034135.52164.6b.

[84] Klemenso T, Chung C, Larsen PH, Mogensen M. The Mechanism Behind Redox Instability of Anodes in High-Temperature SOFCs. J Electrochem Soc 2005;152:A2186–92. doi:10.1149/1.2048228.

[85] El Gabaly F, McCarty KF, Bluhm H, McDaniel AH. Oxidation stages of Ni electrodes in solid oxide fuel cell environments. Phys Chem Chem Phys 2013. doi:10.1039/c3cp50366f.

[86] Payne BP, Biesinger MC, McIntyre NS. The study of polycrystalline nickel metal oxidation by water vapour. J Electron Spectros Relat Phenomena 2009;175:55–65. doi:10.1016/j.elspec.2009.07.006.

[87] Uchida H, Osada N, Watanabe M. High-Performance Electrode for Steam Electrolysis. Electrochem Solid-State Lett 2004;7:A500. doi:10.1149/1.1819864.

[88] Xu S, Chen S, Li M, Xie K, Wang Y, Wu Y. Composite cathode based on Fe-loaded LSCM for steam electrolysis in an oxide-ion-conducting solid oxide electrolyser. J Power Sources 2013;239:332–40. doi:10.1016/j.jpowsour.2013.03.182.

[89] Xie K, Zhang Y, Meng G, Irvine JTS, Vasireddy S, Morreale B, et al. Direct synthesis of methane from $CO_2$/$H_2O$ in an oxygen-ion conducting solid oxide electrolyser. Energy Environ Sci 2011;4:2218. doi:10.1039/c1ee01035b.

[90] Xu S, Dong D, Wang Y, Doherty W, Xie K, Wu Y. Perovskite chromates cathode with resolved and anchored nickel nano-particles for direct high-temperature steam electrolysis. J Power Sources 2014;246:346–55. doi:10.1016/j.jpowsour.2013.07.082.

[91] Leah R, Lankin M, Bone A, Selcuk A, Pierce R, Rees L, et al. Towards a Fully REDOX Stable SOFC: Cell Development at Ceres Power. ECS Trans 2013;57:849–56.

[92] Faes A, Wuillemin Z, Tanasini P, Accardo N, Van Herle J. Redox stable Ni-YSZ anode support in solid oxide fuel cell stack configuration. J Power Sources 2011;196:3553–8. doi:10.1016/j.jpowsour.2010.11.047.

[93] Xiao G, Chen F. Redox Stable Anodes for Solid Oxide Fuel Cells. Front Energy Res 2014;2:1–13. doi:10.3389/fenrg.2014.00018.

[94] Ishihara T, Jirathiwathanakul N, Zhong H. Intermediate temperature solid oxide electrolysis cell using $LaGaO_3$ based perovskite electrolyte. Energy Environ Sci 2010;3:665. doi:10.1039/b915927d.

[95] Sengodan S, Choi S, Jun A, Shin TH, Ju Y-W, Jeong HY, et al. Layered oxygen-deficient double perovskite as an efficient and stable anode for direct hydrocarbon solid oxide fuel cells. Nat Mater 2014;14:205–9. doi:10.1038/nmat4166.

[96] Tao S, Irvine JTS. A redox-stable efficient anode for solid-oxide fuel cells. Nat Mater 2003;2:320–3.

[97] Pu T, Tan W, Shi H, Na Y, Lu J, Zhu B. Steam/$CO_2$ electrolysis in symmetric solid oxide electrolysis cell with barium cerate-carbonate composite electrolyte. Electrochim Acta 2016;190:193–8. doi:10.1016/j.electacta.2015.12.220.

[98] Hosoi K, Sakai T, Ida S, Ishihara T. $Ce_{0.6}Mn_{0.3}Fe_{0.1O2-\delta}$ as an Alternative Cathode Material for High Temperature Steam Electrolysis Using $LaGaO_3$-based Oxide Electrolyte. Electrochim Acta 2016;194:473–9. doi:10.1016/j.electacta.2016.02.121.

[99] Chen S, Xie K, Dong D, Li H, Qin Q, Zhang Y, et al. A composite cathode based on scandium-doped chromate for direct high-temperature steam electrolysis in a symmetric solid oxide electrolyzer. J Power Sources 2015;274:718–29. doi:10.1016/j.jpowsour.2014.10.103.

[100] Wang W, Jiang S. A mechanistic study on the activation process of (La, Sr)$MnO_3$ electrodes of solid oxide fuel cells. Solid State Ionics 2006;177:1361–9. doi:10.1016/j.ssi.2006.05.022.

[101] Backhaus-Ricoult M, Adib K, Clair TS, Luerssen B. In-situ study of operating SOFC

LSM/YSZ cathodes under polarization by photoelectron microscopy. Solid State Ionics 2008;179:891–5. doi:10.1016/j.ssi.2008.02.033.

[102] Laguna-Bercero MA, Kilner JA, Skinner SJ. Performance and Characterization of (La, Sr)MnO3 /YSZ and La0.6Sr0.4Co0.2Fe0.8O3 Electrodes for Solid Oxide Electrolysis Cells. Chem Mater 2010;22:1134–41. doi:10.1021/cm902425k.

[103] Yamamoto O, Takeda Y, Kanno R, Noda M. Perovskite-type oxides as oxygen electrodes for high temperature oxide fuel cells. Solid State Ionics 1987;22:241–6. doi:10.1016/0167-2738(87)90039-7.

[104] Wang W, Huang Y, Jung S, Vohs JM, Gorte RJ. A Comparison of LSM, LSF, and LSCo for Solid Oxide Electrolyzer Anodes. J Electrochem Soc 2006;153:A2066. doi:10.1149/1.2345583.

[105] Tietz F, Sebold D, Brisse a., Schefold J. Degradation phenomena in a solid oxide electrolysis cell after 9000 h of operation. J Power Sources 2013;223:129–35. doi:10.1016/j.jpowsour.2012.09.061.

[106] Graves C, Ebbesen SD, Jensen SH, Simonsen SB, Mogensen MB. Eliminating degradation in solid oxide electrochemical cells by reversible operation. Nat Mater 2014;14:239–44. doi:10.1038/nmat4165.

[107] Hauch A, Mogensen M, Hagen A. Ni/YSZ electrode degradation studied by impedance spectroscopy — Effect of p($H_2O$). Solid State Ionics 2011;192:547–51. doi:10.1016/j.ssi.2010.01.004.

[108] Moçoteguy P, Brisse A. A review and comprehensive analysis of degradation mechanisms of solid oxide electrolysis cells. Int J Hydrogen Energy 2013;38:15887–

902. doi:10.1016/j.ijhydene.2013.09.045.

[109] Laguna-Bercero MA, Campana R, Larrea A, Kilner JA, Orera VM. Electrolyte degradation in anode supported microtubular yttria stabilized zirconia-based solid oxide steam electrolysis cells at high voltages of operation. J Power Sources n.d.;In Press,. doi:10.1016/j.jpowsour.2011.01.015.

[110] Knibbe R, Traulsen ML, Hauch A, Ebbesen SD, Mogensen M. Solid Oxide Electrolysis Cells: Degradation at High Current Densities. J Electrochem Soc 2010;157:B1209. doi:10.1149/1.3447752.

[111] Lay-Grindler E, Laurencin J, Villanova J, Cloetens P, Bleuet P, Mansuy a., et al. Degradation study by 3D reconstruction of a nickel-yttria stabilized zirconia cathode after high temperature steam electrolysis operation. J Power Sources 2014;269:927–36. doi:10.1016/j.jpowsour.2014.07.066.

[112] SECA. NETL: Solid State Energy Conversion Alliance (SECA) - Minimum Requirements for Industrial Team n.d. http://www.netl.doe.gov/technologies/coalpower/fuelcells/seca/minrequire.html (accessed July 12, 2013).

[113] Hauch A, Ebbesen SD, Jensen SH, Mogensen M. Solid Oxide Electrolysis Cells: Microstructure and Degradation of the Ni/Yttria-Stabilized Zirconia Electrode. J Electrochem Soc 2008;155:B1184. doi:10.1149/1.2967331.

[114] Schefold J, Brisse A, Zahid M. Long Term Testing of Solid Oxide Fuel Cell Stacks with Yttria Stabilized Zirconia Electrolyte in the H. ECS Trans., vol. 28, The Electrochemical Society; 2010, p. 357–67. doi:10.1149/1.3495860.

[115] Hjalmarsson P, Sun X, Liu Y-L, Chen M. Durability of high performance Ni–yttria stabilized zirconia supported solid oxide electrolysis cells at high current density. J Power Sources 2014;262:316–22. doi:10.1016/j.jpowsour.2014.03.133.

[116] Mougin J, Chatroux A, Couturier K, Petitjean M, Reytier M, Gousseau G, et al. High Temperature Steam Electrolysis Stack with Enhanced Performance and Durability. Energy Procedia 2012;29:445–54. doi:10.1016/j.egypro.2012.09.052.

[117] Sohal MS, O'Brien JE, Stoots CM, Hartvigsen JJ, Larsen D, Elangovan S, et al. Critical Causes of Degradation in Integrated Laboratory Scale Cells during High Temperature Electrolysis. Idaho National Laboratory (INL); n.d.

[118] Hjalmarsson P, Sun X, Liu Y-L, Chen M. Influence of the oxygen electrode and inter-diffusion barrier on the degradation of solid oxide electrolysis cells. J Power Sources 2013;223:349–57. doi:10.1016/j.jpowsour.2012.08.063.

[119] Virkar A V. Mechanism of oxygen electrode delamination in solid oxide electrolyzer cells. Int J Hydrogen Energy 2010;35:9527–43. doi:10.1016/j.ijhydene.2010.06.058.

[120] Keane M, Mahapatra MK, Verma A, Singh P. LSM–YSZ interactions and anode delamination in solid oxide electrolysis cells. Int J Hydrogen Energy 2012;37:16776–85. doi:10.1016/j.ijhydene.2012.08.104.

[121] Chen K, Jiang SP. Failure mechanism of (La,Sr)$MnO_3$ oxygen electrodes of solid oxide electrolysis cells. Int J Hydrogen Energy 2011;36:10541–9. doi:10.1016/j.ijhydene.2011.05.103.

[122] Chen K, Ai N, Jiang SP. Performance and stability of (La,Sr)$MnO_3$–$Y_2O_3$–$ZrO_2$ composite oxygen electrodes under solid oxide electrolysis cell operation conditions.

Int J Hydrogen Energy 2012;37:10517–25. doi:10.1016/j.ijhydene.2012.04.073.

[123] Kim J, Ji H-I, Dasari HP, Shin D, Song H, Lee J-H, et al. Degradation mechanism of electrolyte and air electrode in solid oxide electrolysis cells operating at high polarization. Int J Hydrogen Energy 2013;38:1225–35. doi:10.1016/j.ijhydene.2012.10.113.

[124] Sohal MS, Virkar AV, Rashkeev SN, Glazoff MV. Modeling Degradation in Solid Pxide Electrolysis Cells. 2010.

[125] Rashkeev SN, Glazoff M V. Atomic-scale mechanisms of oxygen electrode delamination in solid oxide electrolyzer cells. Int J Hydrogen Energy 2012;37:1280–91. doi:10.1016/j.ijhydene.2011.09.117.

[126] Laguna-Bercero MA, Campana R, Larrea A, Kilner JA, Orera VM. Performance and Aging of Microtubular YSZ-based Solid Oxide Regenerative Fuel Cells. Fuel Cells 2011;11:116–23. doi:10.1002/fuce.201000069.

[127] Li N, Keane M, Mahapatra MK, Singh P. Mitigation of the delamination of LSM anode in solid oxide electrolysis cells using manganese-modified YSZ. Int J Hydrogen Energy 2013;38:6298–303. doi:10.1016/j.ijhydene.2013.03.036.

[128] Steinberger-Wilckens R, Lehnert W, editors. Innovations in Fuel Cell Technologies, Cambridge: Royal Society of Chemistry; 2010, p. 271–86. doi:10.1039/9781849732109.

[129] Hansen JB. Solid oxide electrolysis – a key enabling technology for sustainable energy scenarios Early developments. Faraday Discuss 2015;0:1–40. doi:10.1039/C5FD90071A.

[130] Hauch A. Solid Oxide Electrolysis Cells – Performance and Durability. Technical University of Denmark, 2007.

[131] Matsui T, Fujii H, Ozaki A, Takeuchi T, Kikuchi R, Eguchi K. Degradation Behavior of Ni–ScSZ Cermet Anode under Various Humidified Conditions for Solid Oxide Fuel Cells. J Electrochem Soc 2007;154:B1237. doi:10.1149/1.2783771.

[132] Osinkin D a., Kuzin BL, Bogdanovich NM. Effect of oxygen activity and water partial pressure to degradation rate of Ni cermet electrode contacting $Zr_{0.84}Y_{0.16}O_{1.92}$ electrolyte. Russ J Electrochem 2010;46:41–8. doi:10.1134/S1023193510010052.

[133] Kim S-D, Seo D-W, Dorai AK, Woo S-K. The effect of gas compositions on the performance and durability of solid oxide electrolysis cells. Int J Hydrogen Energy 2013;38:6569–76. doi:10.1016/j.ijhydene.2013.03.115.

[134] Hauch A, Jensen SH, Bilde-Sorensen JB, Mogensen M. Silica Segregation in the Ni/YSZ Electrode. J Electrochem Soc n.d.;154:A619–26. doi:10.1149/1.2733861.

[135] Hauch A, Brodersen K, Chen M, Mogensen MB. Ni/YSZ electrodes structures optimized for increased electrolysis performance and durability. Solid State Ionics 2016;293:27–36. doi:10.1016/j.ssi.2016.06.003.

[136] Knibbe R, Hauch A, Hjelm J, Ebbesen S. Durability of Solid Oxide Cells. Green 2011;1:141–69. doi:10.1515/GREEN.2011.015.

[137] Tietz F, Sebold D, Brisse A, Schefold J. Degradation phenomena in a solid oxide electrolysis cell after 9000 h of operation. J Power Sources 2013;223:129–35. doi:10.1016/j.jpowsour.2012.09.061.

[138] Laguna-Bercero MA, Campana R, Larrea A, Kilner JA, Orera VM. Steam Electrolysis Using a Microtubular Solid Oxide Fuel Cell. J Electrochem Soc 2010;157:B852. doi:10.1149/1.3332832.

[139] Schefold J, Brisse A, Zahid M. Electronic Conduction of Yttria-Stabilized Zirconia Electrolyte in Solid Oxide Cells Operated in High Temperature Water Electrolysis. J Electrochem Soc 2009;156:B897. doi:10.1149/1.3138701.

[140] Weppner W. Formation of intermetallic Pt-Zr compounds between Pt electrodes and $ZrO_2$-based electrolytes, and the decomposition voltage of yttria-doped $ZrO_2$. J Electroanal Chem Interfacial Electrochem 1977;84:339–50. doi:10.1016/S0022-0728(77)80384-7.

[141] Laguna-Bercero MA, Campana R, Larrea A, Kilner JA, Orera VM, Laguna-Bercero M. Performance and Aging of Microtubular YSZ-based Solid Oxide Regenerative Fuel Cells. Fuel Cells 2011;11:116–23. doi:10.1002/fuce.201000069.

[142] Marina OA, Pederson LR, Williams MC, Coffey GW, Meinhardt KD, Nguyen CD, et al. Electrode Performance in Reversible Solid Oxide Fuel Cells. J Electrochem Soc 2007;154:B452. doi:10.1149/1.2710209.

[143] Ni M, Leung MKH, Leung DYC. A modeling study on concentration overpotentials of a reversible solid oxide fuel cell. J Power Sources 2006;163:460–6. doi:10.1016/j.jpowsour.2006.09.024.

[144] Ferrero D, Lanzini A, Leone P, Santarelli M. Reversible operation of solid oxide cells under electrolysis and fuel cell modes: Experimental study and model validation. Chem Eng J 2015;274:143–55. doi:10.1016/j.cej.2015.03.096.

[145] Hughes GA, Yakal-Kremski K, Barnett SA. Life testing of LSM-YSZ composite electrodes under reversing-current operation. Phys Chem Chem Phys 2013;15:17257–62. doi:10.1039/c3cp52973h.

[146] Brown C. Progress on the Development of Reversible SOFC Stack Technology Presented by : Casey Brown 2011.

[147] Hauch A, Jensen SH, Ramousse S, Mogensen M. Performance and Durability of Solid Oxide Electrolysis Cells. J Electrochem Soc 2006;153:A1741. doi:10.1149/1.2216562.

[148] Petipas F, Fu Q, Brisse A, Bouallou C. Transient operation of a solid oxide electrolysis cell. Int J Hydrogen Energy 2013;38:2957–64. doi:10.1016/j.ijhydene.2012.12.086.

[149] Nguyen VN, Fang Q, Packbier U, Blum L. Long-term tests of a Jülich planar short stack with reversible solid oxide cells in both fuel cell and electrolysis modes. Int J Hydrogen Energy 2013;38:4281–90. doi:10.1016/j.ijhydene.2013.01.192.

[150] Ebbesen SD, Graves C, Hauch A, Jensen SH, Mogensen M. Poisoning of Solid Oxide Electrolysis Cells by Impurities. J Electrochem Soc 2010;157:B1419. doi:10.1149/1.3464804.

[151] Cai Q, Brandon NP, Adjiman CS. Modelling the dynamic response of a solid oxide steam electrolyser to transient inputs during renewable hydrogen production. Front Energy Power Eng China 2010;4:211–22. doi:10.1007/s11708-010-0037-6.

[152] Cumming DJ, Elder RH. Thermal imaging of solid oxide cells operating under electrolysis conditions. J Power Sources 2015;280:387–92. doi:10.1016/j.jpowsour.2015.01.109.

[153] Petipas F, Brisse A, Bouallou C. Model-based behaviour of a high temperature electrolyser system operated at various loads. J Power Sources 2013;239:584–95. doi:10.1016/j.jpowsour.2013.03.027.

[154] Yoon KJ, Lee S, An H, Kim J, Son J-W, Lee J-H, et al. Gas transport in hydrogen electrode of solid oxide regenerative fuel cells for power generation and hydrogen production. Int J Hydrogen Energy 2014;39:3868–78. doi:10.1016/j.ijhydene.2013.12.142.

[155] Dhir A. Improved Microtubular Solid Oxide Fuel Cells. Doctoral Thesis. The University of Birmingham, 2008.

[156] Howe KS, Clark ER. A Novel Water-Based Cathode Ink Formulation. Int J Hydrogen Energy 2013;38:1731–6.

[157] Howe KS. Design Improvements of Micro-Tubular Solid Oxide Fuel Cells for Unmanned Aircraft Applications. The University of Birmingham, 2013.

[158] Pihlatie M, Ramos T, Kaiser A. Testing and improving the redox stability of Ni-based solid oxide fuel cells. J Power Sources 2009;193:322–30. doi:10.1016/j.jpowsour.2008.11.140.

[159] Nechache A, Cassir M, Ringuedé A. Solid oxide electrolysis cell analysis by means of electrochemical impedance spectroscopy: A review. J Power Sources 2014;258:164–81. doi:10.1016/j.jpowsour.2014.01.110.

[160] Hauch A, Jensen SH, Ramousse S, Mogensen M. Performance and Durability of Solid Oxide Electrolysis Cells. J Electrochem Soc 2006;153:A1741. doi:10.1149/1.2216562.

[161] Nakajima H, Kitahara T, Konomi T. Electrochemical Impedance Spectroscopy Analysis of an Anode-Supported Microtubular Solid Oxide Fuel Cell. J Electrochem Soc 2010;157:B1686. doi:10.1149/1.3486805.

[162] Chatzichristodoulou C, Chen M, Hendriksen PV, Jacobsen T, Mogensen MB. Understanding degradation of solid oxide electrolysis cells through modeling of electrochemical potential profiles. Electrochim Acta 2016;189:265–82. doi:10.1016/j.electacta.2015.12.067.

[163] Schindelin J, Rueden CT, Hiner MC, Eliceiri KW. The ImageJ ecosystem: An open platform for biomedical image analysis. Mol Reprod Dev 2015;in press:DOI: 10.1002/mrd.22489. doi:10.1002/mrd.22489.

[164] Schindelin J, Arganda-Carreras I, Frise E, Kaynig V, Longair M, Pietzsch T, et al. Fiji: an open-source platform for biological-image analysis. Nat Meth 2012;9:676–82.

[165] Alan Hobby D printing machines L. PRINTING THICK FILM HYBRIDS 1997. http://www.gwent.org/gem_thick_film.html (accessed January 16, 2016).

[166] Pfeiffer Vaccuum. Leakage rate n.d. https://www.pfeiffer-vacuum.com/en/know-how/leak-detection/general/leakage-rate/.

[167] Hagen A, Hendriksen P V., Frandsen HL, Thyden K, Barfod R. Durability Study of SOFCs Under Cycling Current Load Conditions. Fuel Cells 2009;9:814–22. doi:10.1002/fuce.200900013.

[168] Wendel CH, Kazempoor P, Braun RJ. Novel electrical energy storage system based on reversible solid oxide cells: System design and operating conditions. J Power Sources 2015;276:133–44. doi:10.1016/j.jpowsour.2014.10.205.

[169] Fan H, Keane M, Singh P, Han M. Electrochemical performance and stability of lanthanum strontium cobalt ferrite oxygen electrode with gadolinia doped ceria barrier layer for reversible solid oxide fuel cell. J Power Sources 2014;268:634–9. doi:10.1016/j.jpowsour.2014.03.080.

[170] Ebbesen SD, Sun X, Mogensen MB. Understanding the processes governing performance and durability of solid oxide electrolysis cells. Faraday Discuss 2015;182:393–422. doi:10.1039/c5fd00032g.

[171] Ebbesen SD, Jensen SH, Hauch A, Mogensen MB. High temperature electrolysis in alkaline cells, solid proton conducting cells, and solid oxide cells. Chem Rev 2014;114:10697–734. doi:10.1021/cr5000865.

[172] Barfod R, Mogensen M, Klemenso T, Hagen A, Liu Y-L, Vang Hendriksen P. Detailed Characterization of Anode-Supported SOFCs by Impedance Spectroscopy. J Electrochem Soc 2007;154:B371. doi:10.1149/1.2433311.

[173] Hansen JB, Ebbesen SD, Jensen SH, Hauch A, Mogensen MB, Laguna-Bercero MA, et al. Solid oxide electrolysis – a key enabling technology for sustainable energy scenarios. Faraday Discuss 2015;182:9–48. doi:10.1039/C5FD90071A.

[174] Zheng Y, Li Q, Chen T, Wu W, Xu C, Wang WG. Comparison of performance and degradation of large-scale solid oxide electrolysis cells in stack with different composite air electrodes. Int J Hydrogen Energy 2015;40:2460–72. doi:10.1016/j.ijhydene.2014.12.101.

[175] Biers DM. Regenerative and Fuel Flexible Anodes for Solid Oxide Fuel Cells. 2011.

[176] Sehested J, Gelten JAP, Helveg S. Sintering of nickel catalysts: Effects of time,

atmosphere, temperature, nickel-carrier interactions, and dopants. Appl Catal A Gen 2006;309:237–46. doi:10.1016/j.apcata.2006.05.017.

[177] Sehested J. Four challenges for nickel steam-reforming catalysts. Catal Today 2006;111:103–10. doi:10.1016/j.cattod.2005.10.002.

[178] Tao Y, Ebbesen SD, Mogensen MB. Degradation of solid oxide cells during co-electrolysis of steam and carbon dioxide at high current densities. J Power Sources 2016;328:452–62. doi:10.1016/j.jpowsour.2016.08.055.

[179] Keane M, Fan H, Han M, Singh P. Role of initial microstructure on nickel-YSZ cathode degradation in solid oxide electrolysis cells. Int J Hydrogen Energy 2014;39:18718–26. doi:10.1016/j.ijhydene.2014.09.057.

[180] The D, Grieshammer S, Schroeder M, Martin M, Al Daroukh M, Tietz F, et al. Microstructural comparison of solid oxide electrolyser cells operated for 6100 h and 9000 h. J Power Sources 2015;275:901–11. doi:10.1016/j.jpowsour.2014.10.188.

[181] Schindelin J, Arganda-Carreras I, Frise E, Kaynig V, Longair M, Pietzsch T, et al. Fiji: an open-source platform for biological-image analysis. Nat Methods 2012;9:676–82. doi:10.1038/nmeth.2019.